



THE UNIVERSITY *of* EDINBURGH

This thesis has been submitted in fulfilment of the requirements for a postgraduate degree (e.g. PhD, MPhil, DClinPsychol) at the University of Edinburgh. Please note the following terms and conditions of use:

This work is protected by copyright and other intellectual property rights, which are retained by the thesis author, unless otherwise stated.

A copy can be downloaded for personal non-commercial research or study, without prior permission or charge.

This thesis cannot be reproduced or quoted extensively from without first obtaining permission in writing from the author.

The content must not be changed in any way or sold commercially in any format or medium without the formal permission of the author.

When referring to this work, full bibliographic details including the author, title, awarding institution and date of the thesis must be given.

DEVELOPMENT OF REGISTRATION METHODS FOR CARDIOVASCULAR ANATOMY AND FUNCTION USING ADVANCED 3T MRI, 320-SLICE CT AND PET IMAGING



Chengjia Wang

Thesis submitted for the degree of Doctor of Philosophy

School of Clinical Science

College of Medicine and Veterinary Medicine

The University of Edinburgh

2016

Author's Declaration

I declare that this thesis has been composed solely by myself and that it has not been submitted, either in whole or in part, in any previous application for a degree or professional qualification. Except where otherwise acknowledged, the work presented is entirely my own.

Any included publications are my own work, except where indicated throughout the thesis and summarised and clearly identified on the declarations page of the thesis

Chengjia Wang

2016

Contents

Author's Declaration	3
Table of Contents	4
Abstract	i
Lay Summary	i
Acknowledgments	iii
Publications related to work presented in this thesis	v
List of Figures	viii
List of Tables	xxiv
List of Abbreviations	xxix
List of Abbreviations	xxix
1 Introduction	1
1.1 Background and Study Objectives	1
1.2 Progress of The Work	4
2 Literature Review of Image Registration	7
2.1 Introduction	8
	5

Contents

2.2	Imaging Modalities	10
2.2.1	CT Imaging	10
2.2.2	MR Imaging	11
2.2.3	Image Contrast of CT and MR Data	12
2.3	Image Registration	16
2.3.1	Subject and Modality	18
2.3.2	Dimensionality	20
2.3.3	Classification	20
2.4	Pre-processing and Feature Selection	22
2.4.1	Extrinsic Registration	22
2.4.2	Intrinsic Registration	23
2.5	Transformation	27
2.5.1	Euclidean Transformation	28
2.5.2	Similarity Transformation	29
2.5.3	Affine Transformation	30
2.5.4	Projective and Perspective Transformation	31
2.5.5	Curved Transformation	32
2.5.6	More Complex Transformations	33
2.5.7	Mapping by Radial Basis Functions	34
2.5.8	Non-parametric Registration	38
2.5.9	Optical Flow based Methods and Other Methods	39
2.5.10	Summary	40
2.6	Similarity Measurements	42
2.6.1	Distance Measures	44
2.6.2	Correlation Measures	45
2.6.3	Mutual Information based Methods	48
2.6.4	Other Similarity Measures	51
2.6.5	Summary	52

2.7	Optimization	54
2.8	Other Implementation Issues	57
2.9	Discussion and Conclusion	59
3	3D Inter-modality Registration of Axial Aortic Images	61
3.1	Introduction	62
3.2	The MA ³ RS Clinical Trial	64
3.2.1	Clinical Background	64
3.2.2	Imaging and Analysis Protocol	66
3.3	Registration Methodology	72
3.3.1	3D ROI Generation based on Axial Aorta Tracking	72
3.3.2	ROI Correction based on modified implicit shape model	76
3.3.3	Initial Alignment	79
3.3.4	Voxel Intensity Based Registration	89
3.3.5	Registration Schedule	97
3.4	Graphical User Interface	98
3.5	Evaluation criteria of Registration Results	107
3.5.1	Evaluation using manual corrections	108
3.5.2	Evaluation using pure manual registrations	109
3.6	Results	112
3.6.1	Visualization	112
3.6.2	Qualitative Evaluation Results	112
3.6.3	Quantitative Evaluation Results	113
3.7	Conclusion and Discussion	123
4	Intensity Inhomogeneity Correction	127
4.1	Introduction	128
4.1.1	Sources of MR intensity inhomogeneity	134
4.2	Related Works	137

Contents

4.2.1	Correction Methods	137
4.2.2	Evaluation Criteria	139
4.3	Compared Methods	142
4.3.1	N3 and N4	142
4.3.2	SPM	145
4.3.3	Wavelet-based method	147
4.3.4	Polynomial surface fitting	148
4.4	Assessment Methodology	150
4.4.1	Evaluation datasets	150
4.4.2	Assessment metrics	151
4.5	Results	155
4.5.1	Qualitative Evaluation	155
4.5.2	Quantitative Evaluation	155
4.5.3	Quantitative Analysis of the polynomial method	160
4.6	Discussion and Conclusion	163
5	MR Registration using Adaptive Asymmetric K-means Binning	165
5.1	Introduction	167
5.2	Re-arranged Histogram based Intensity Distribution Correction	169
5.3	Registration Framework Implementation	186
5.4	Experiments and Validation	191
5.4.1	Cardiac Data	191
5.4.2	Neonatal Data	192
5.5	Results	198
5.5.1	Cardiac Data	198
5.5.2	Neonatal Data	198
5.6	Discussion and Conclusion	201

6	Review of Particle Swarm Optimizer	207
6.1	Introduction	208
6.2	Original PSO Algorithm and Common Improvements	212
6.2.1	The Original Formulae	212
6.2.2	Common Extensions	213
6.3	Modified Speed and Position Update Mechanisms	216
6.3.1	Neighbourhood and Population Information	216
6.3.2	Quantum Behaved PSO	218
6.3.3	Hybridizations	220
6.4	Applications to Registration	223
6.5	Inspiring Methods	227
6.5.1	Gaussian Extensions and Bare Bones PSO	227
6.5.2	Kalman Filter PSO	228
6.5.3	Bayesian Interpretation	230
6.6	Conclusion and Discussion	235
7	Registration Oriented UKF-PSO Method	237
7.1	Introduction	238
7.2	Theory Derivation	240
7.3	The UKF-PSO Method	247
7.4	The Nested UKF-PSO	260
7.5	Experiments	262
7.5.1	Benchmark Functions	262
7.5.2	Registering Benchmark Datasets	264
7.5.3	Registering Data from A Real Clinical Trial	265
7.6	Results	269
7.6.1	Benchmark Functions	269
7.6.2	RIRE Data	270
7.6.3	Neonatal Data	270

Contents

7.7	Conclusion and Discussion	278
8	Conclusion and Future Work	279
8.1	Introduction	279
8.2	Multi-modality and Multi-parametric Registration of Clinical Data . . .	280
8.3	Strengths of This Project	283
8.4	Limits and Weaknesses of This Study	285
8.5	Future Directions	287
	Appendices	333
A	Appendix 1	335
A.1	Conference abstract of ISMRM2014	336
A.2	Electronic poster presented in ISMRM2014	338
A.3	Conference paper published of IEEE ISBI2015	344
A.4	Poster presented in IEEE ISBI2015	349
A.5	Posters presented in ESMRMB2015	351

Abstract

Different medical imaging modalities provide complementary anatomical and functional information. One increasingly important use of such information is in the clinical management of cardiovascular disease. Multi-modality data is helping improve diagnosis accuracy, and individualize treatment. The Clinical Research Imaging Centre at the University of Edinburgh, has been involved in a number of cardiovascular clinical trials using longitudinal computed tomography (CT) and multi-parametric magnetic resonance (MR) imaging. The critical image processing technique that combines the information from all these different datasets is known as image registration, which is the topic of this thesis. Image registration, especially multi-modality and multi-parametric registration, remains a challenging field in medical image analysis. The new registration methods described in this work were all developed in response to genuine challenges in on-going clinical studies. These methods have been evaluated using data from these studies.

In order to gain an insight into the building blocks of image registration methods, the thesis begins with a comprehensive literature review of state-of-the-art algorithms. This is followed by a description of the first registration method I developed to help track inflammation in aortic abdominal aneurysms. It registers multi-modality and multi-parametric images, with new contrast agents. The registration framework uses a semi-automatically generated region of interest around the aorta. The aorta is aligned based on a combination of the centres of the regions of interest and intensity matching. The method achieved sub-voxel accuracy.

The second clinical study involved cardiac data. The first framework failed to register many of these datasets, because the cardiac data suffers from a common artefact of magnetic resonance images, namely intensity inhomogeneity. Thus I developed a new preprocessing technique that is able to correct the artefacts in the functional data using data from the anatomical scans. The registration framework,

with this preprocessing step and new particle swarm optimizer, achieved significantly improved registration results on the cardiac data, and was validated quantitatively using neuro images from a clinical study of neonates. Although on average the new framework achieved accurate results, when processing data corrupted by severe artefacts and noise, premature convergence of the optimizer is still a common problem. To overcome this, I invented a new optimization method, that achieves more robust convergence by encoding prior knowledge of registration. The registration results from this new registration-oriented optimizer are more accurate than other general-purpose particle swarm optimization methods commonly applied to registration problems.

In summary, this thesis describes a series of novel developments to an image registration framework, aimed to improve accuracy, robustness and speed. The resulting registration framework was applied to, and validated by, different types of images taken from several ongoing clinical trials. In the future, this framework could be extended to include more diverse transformation models, aided by new machine learning techniques. It may also be applied to the registration of other types and modalities of imaging data.

Lay Summary

Diagnosis and treatment of cardiovascular diseases often requires us to combine all of the information that can be acquired from different types of medical images. Combining the information that we can obtain from these different imaging techniques, helps our understanding of different diseases and aid in treatment. Several cardiovascular research projects conducted in the Clinical Research Imaging Centre, University of Edinburgh, involve a mixture of images and information acquired by computed tomography and magnetic resonance imaging. To combine this information, the data needs to be spatially aligned first. The technology that transforms one image to allow it to be combined with another image is called image registration. This is a challenging topic in the field of medical image analysis due to the fact that images from these techniques can look very different, and are therefore very difficult to align. A typical registration method for two images searches for the best transformation of the first image based on the resulting similarity between the first and second image once they are aligned. This assessment is based on any important features that can be extracted from the two images by the registration method. It is often necessary to pre-process the images prior to them being registered, in order to extract these similar features which are used for the alignment.

Various registration methods have been proposed in the past two decades. All these methods can be classified based on several criteria, including the pre-processing steps used to enhance the image features before registration, the type of spatial transformations used in the registration, the type of measures used to assess how similar the images are after registration, and the mathematical methods used to search for the best transformation. In this thesis, I investigate several specific applications where registration can benefit the clinical care of patients and help to develop new imaging techniques. New registration methods are invented in the thesis while solving practical registration problems for several cardiovascular clinical projects

currently being run in Edinburgh. A registration software package is first developed for a clinical trial about a new diagnostic protocol of aortic aneurysm, a swelling of the main blood vessel that can cause fatal internal bleeding when it bursts. This software only requires minimal human interaction and achieved results comparable to similar techniques performed by highly trained human operators. To deal with heart images acquired in another project, I had to improve the software with new pre-processing steps. Performances of registration are further improved by adding some novel steps which were designed to help the software decide on the best registration transformation more quickly, and more reliably. This allows the software to be used to solve a much wider range of problems. The registration techniques described in this thesis point out a possible direction of more intelligent automatic software for more complicated problem solving in the future.

Acknowledgments

First of all, all my results and innovations are achieved under supervision of Dr. Scott Semple and Dr. Keith Goatman who led me through the academic word of medical image analysis. They have provided better supervisions than the best I can imagine, which transforming me gradually from a newbie PhD student to a qualified researcher. This work can never be finished without them. In this long, but joyful, journey to a doctorate degree, I learnt from them not only about how to thrill the academic world, but also the knowledge and wisdom that can help me in my future life.

To my gorgeous dear wife, Peng, who is my life partner and my real “boss”, no words can express how much I’m relying on your cares, supports, your accompany, your love, as well as the mind-blowing delicious food that you cooked for me. There has never been, and will not be, a better thing happened in my life than travelling thousands of miles to this beautiful city to meet you. I can achieve nothing for this work without you.

I also want to give a big emotional thank to my parents, who devoted most of their lives to research and made me enjoy myself in the academic world. No matter what happens in my life, you’ve always help me through the hard times with sapiential advices and unconditional supports. You not only gave me my life, but also the mental powers that I value the most.

Special thanks to my colleagues and friends in CRIC and TMVSE. Thanks to Dr. Tom Macgillivray, Dr. Calum Gray and Prof. David Newby for all your professional advices and directions. Thank you to Mrs. Clair Young who always have my visa documents ready in a second like a magician. Best wishes to you and Simon. Many thanks to our clinical researchers Olivia McBride, Rachael Forsythe, Alex Vesey, Colin Stirrat, Noel Conlisk, Shirjel Alam, Marc Dweck, Calvin Chin, Rozalia Pataky, James Boardman, Sarah Sparrow, Emma Moore, Jennifer Richards, Jenny Robson, and Peter

Hoskins. Without the data, registration results and gold standards you provided, I'll have no directions, feedbacks, or even a target for my PhD study. I also want to thank all my colleagues of TMVSE image analysis research and image analysis teams. You are all smart researchers and programmers, I can learn so much even just from a little warm chatting with you guys during a cup of tea in the kitchen. You also helped me on so many issues I cannot handle while based in TMVSE. Thanks to Yamagata-san for all the help with my publications, Dominic Ashmole who helped a lot for patent application, and Erin Beveridge who provided the critical material for evaluation of my registration methods. Thanks to my fellow PhD and EngD students for those inspiring discussions and your generous advices. Special thanks to our radiographers who brought high quality images to me. Thanks to my good childhood friends whose success story gave me a lot of encouragements. Also thanks to my teammates and good friends who regularly enjoy a relaxing time after a whole day work in badminton and basketball.

Great acknowledgements to organizations funding my study. This PhD project is funded by Medical Research Council, British Heart Foundation, Toshiba Medical Visualization System and the Scottish Universities Physics Alliance INSPIRE award. The neonatal data used for quantitative evaluation were acquired with funding from Theirworld.

Finally, I want to use a few sentences from the Jackie Chan's movie, *Around the World in 80 Days*, as a summary of this fulfilling period. "I saw the world, learnt about new cultures, . . . , flew across the ocean, made friends, and fell in love," and I have no regrets.

Publications related to this thesis

Some of the material presented in chapter 3 has been published as a conference abstract and presented as an electronic poster at the International Society for Magnetic Resonance in Medicine (ISMRM) annual scientific meeting 2014, Milan, Italy. A patent (US 9275432) was published in May 2015, and was granted in March 2016. The image analysis method and results presented in chapter 5 were published at The Institute of Electrical and Electronics Engineers (IEEE) International Symposium on Biomedical Imaging (ISBI) 2015, New York, USA. The application of the image analysis software to cardiac and neonatal MR data was presented separately at the European Society for Magnetic Resonance in Medicine and Biology (ESMRMB) annual meeting 2015, Edinburgh, UK. Journal papers about analysis methods and results presented in chapter 3 and chapter 7 are still in print and not yet published. The published works are summarized as follows and the copies of them are included in the thesis appendices.

Patent:

C Wang, KA Goatman and SIK Semple. (2016). *Method of, and apparatus for, registration of medical images*. US Patent: us 9275432.

Author's Contributions: Design the registration procedure by generalising the method presented in chapter 3; implement the image analysis algorithm using MATLAB; Evaluate performance of registration software using clinical research data; Collect statistics of results.

Contribution by others: KAG and SIS supervised the project, control the quality of the software, communicating intelligent property teams in Toshiba and the University, helped collecting experiment data and scripting the patent files.

Conference Paper:

C Wang, KA Goatman, TJ MacGillivray, E Beveridge, Y Koutraki, J Boardman, C Stirrat, S Sparrow, E Moore, R Paraky, S Alam, MR Dweck, C. Chin, C Gray, DE Newby, and SIK Semple. Automatic multi-parametric MR registration method using mutual information based on adaptive asymmetric k-means binning. In *Biomedical Imaging (ISBI)*, 2015 IEEE 12th International Symposium on, pages 1089–1092. IEEE, 2015.

Author Contributions: Design the image registration framework; Develop novel preprocessing method; Implement the algorithm; Evaluating performances of the proposed method using the available clinical data.

Contribution by others: KAG, SIKS and TJM supervised the project, provide advices for improving the registration method, and perform proof reading for the paper draft. YK and CG contributed code for the image registration software. CS, SA, MRD and CC acquired the cardiac MR data and provide manual registration results. JPB, SS, EM and RP provided the neonatal data and gave feedbacks about the data alignments. EB manually select over 1900 anatomical landmarks which were used for quantitative evaluation of the registration algorithms.

Conference Abstracts:

C Wang, YG Koutraki, O McBride, A Vesey, TJ MacGillivray, C Gray, DE Newby, KA Goatman, and SIK Semple. A robust automated multi-modality registration tool applied to abdominal aortic aneurysm. ISMRM-ESMRMB Joint Annual Meeting Proceedings, 2014, Milan, Italy.

YG Koutraki, C Wang, J Robson, O McBride, RO Forsythe, TJ MacGillivray, C Gray, K

Goatman, J Camilleri-Brennan, DE Newby, and SIK Semple. Automatic detection of inflammatory ‘hotspots’ in abdominal aortic aneurysms to identify patients at risk of aneurysm expansion and rupture. ISMRM 23rd Annual Meeting Proceedings, 2015, Toronto, Canada.

C Wang, C Stirrat, S Alam, MR Dweck, C Chin, TJ Macgillivray, C Gray, R Pataky, and SIK Semple. Robust registration software of multi-parametric cardiac MR data with presence of motion-related artefacts and intensity non-homogeneity. ESMRMB 32nd Annual Scientific Meeting Proceedings, 2015, Edinburgh, UK.

C Wang, T Macgillivray, YG Koutraki, JP Boardman, S Sparrow, E Moore, R Pataky, and SIK Semple. A robust automated multi-parametric registration software applied to neonatal MR neuro data. ESMRMB 32nd Annual Scientific Meeting Proceedings, 2015, Edinburgh, UK.

YG Koutraki, O McBride, J Robson, RO Forsythe, C Wang, TJ MacGillivray, C Gray, K Goatman, J Camilleri-Brennan, J Jegadeeson, DE Newby, and SIK Semple. Automatic classification of abdominal aortic aneurysms to identify patients at risk of aneurysm expansion and rupture. ESMRMB 32nd Annual Scientific Meeting Proceedings, 2015, Edinburgh, UK.

List of Figures

2.1	Echoes acquired in an MR scan are stored in k-space which is transformed with a mathematical Fast Fourier Transform (FFT) to image space [1].	11
2.2	General Image Registration Procedure.	18
2.3	Basic Set of 2D Linear Transformations [2]	28
3.1	Study Flow of MA ³ RS Clinical Trial	65
3.2	Example of axial MA ³ RS data acquired from the same patient in the baseline and reproducibility assessments: from left to right is pre- and post-contrast T2* weighted (T2*W) images, T2 weighted (T2W) image, and CT image. White arrows point to the aorta in different images. T2*W images shown in all figures of this chapter are acquired with shortest TE.	67
3.3	The classification of patients based on USPIO uptake from the pilot study [3]: (a) The distinctive patterns of USPIO-positive voxels for each patient group; (b) The relationship of the diameter and growth rate with patient group. The group C patients shown in (a) exhibit detectable focal hotspots (pointed by the red arrow) of USPIO uptake associated with faster growth of aneurysm, while the average diameter shown in (b) has no obvious difference with other two groups.	70

- 3.4 An example of the registration process in the baseline assessment: the T2* weighted (T2*W) images acquired within the two days are both co-registered to the T2 weighted (T2W) images. 71
- 3.5 Example of spatially aligned data with the reference and floating slices shown in red and blue color channels. A pair of corresponding MR T2* weighted (T2*W) data acquired in two successive scans is shown on the left and a pair of CT-MR data on the right. The relatively stable area is included in the green contours. The aortic aneurysm of interest in the clinical assessment is included within the red contours. 74
- 3.6 Rectangle ROI generated by the seed point roughly located at the aortic centre 75
- 3.7 An example of 2D ROI correction using the simplified implicit shape model circle detection method: 1. a 2D ROI is initialized from its neighbouring slice; 2. the gradient of the ROI is then calculated; 3. the 3D accumulator matrix which stores the probability of a circle with radius r , and centred (x,y) ; 4. the aorta is detected by searching for the highest score in the accumulator matrix shown by the red arrows; 5. the centre of the 2D ROI is relocated to the centre of aorta. 80
- 3.8 Manually segmented aorta (left) on CT data (centre) compared with automatic ROI (right): the manual segmentation is generated by thresholding a sub-volume that include the whole aorta. The coordinate systems of left and right images shown here are not aligned as the segmentation and ROI are generated using different software. 81

3.9	Calculating correspondence between 2D ROI centres using the triangulation topology feature: within a large neighbourhood of a point, the edges of a few predefined triangles were used to form the feature vector; the correspondence between the 2D ROI centres can be found by searching for the nearest neighbours; the correspondence between slices are calculated first with a RANSAC-least-square scheme to exclude the outliers shown as dash lines; if the statistic error of this correspondence is bigger than 1, the correspondence is recalculated using the ICP method.	85
3.10	Example of initial alignment of two T2* weighted (T2*W) data: (a) Initial alignment process using the automatically tracked region of interest (ROI) centres; (b) the ROI selected on a slice of the pre-contrast T2*W image; (c) the ROI selected on a slice of the post-contrast T2*W image; (d) the initially aligned ROIs of the post- and pre-contrast T2*W data visualized in red and green colour channels.	88
3.11	Example of a pre-contrast T2* weighted image clustered by the bottom-up k -means while K were initialized as 10 but converged to 6.	93
3.12	Creation of low resolution data from an example CT volume.	95
3.13	Registration Procedure	96
3.14	The GUI used for semi-automatic registration	100
3.15	The GUI used for observing results and manual registration	101
3.16	An example of aligned multi-contrast T2* weighted data visualized by overlapped red-green colour channels.	102
3.17	An example of chessboard visualization of aligned multi-contrast T2* weighted data.	103
3.18	An example of aligned multi-contrast T2* weighted data visualized by overlapping the edge image of the floating data with the reference data.	104

3.19	Example of aligning R2* weighted data using the transformation matrix obtained by registering the T2* weighted data: (a), (b), (e), (f) show the ROI and full image of T2*W data before and after registration; (c), (d), (g), (h) show the R2*Map data before and after applying the transformation. Data is visualized using overlapped red-green colour channels, overlapped parts tend to be yellow.	105
3.21	Evaluation of registration	111
3.22	A pre-contrast T2* weighted volume overlapped with anatomical structures manually segmented from a T2 weighted data before registration visualized in green and red colour channels: (a) ROIs; (b) full volumes.	114
3.23	A pre-contrast T2* weighted volume overlapped with anatomical structures manually segmented from a T2 weighted data after automatically registered using the proposed method visualized in green and red colour channels: (a) ROIs; (b) full volumes.	115
3.24	A pre-contrast T2* weighted volume overlapped with anatomical structures manually segmented from a T2 weighted data after manually registered visualized in green and red colour channels: (a) ROIs; (b) full volumes.	116
3.25	Visualization of the edge image of post-contrast T2* weighted (T2*W) data overlapped with pre-contrast T2*W data before registration: (a) ROIs; (b) full volumes.	117
3.26	Visualization of the edge image of post-contrast T2* weighted (T2*W) data overlapped with pre-contrast T2*W data after automatically registered by the proposed method: (a) ROIs; (b) full volumes.	118
3.27	Visualization of the edge image of post-contrast T2* weighted (T2*W) data overlapped with pre-contrast T2*W data after manual registrations: (a) ROIs; (b) full volumes.	119

3.28	A pre-contrast T2* weighted volume overlapped with CT data before registration visualized in green and red colour channels: (a) ROIs; (b) full volumes.	120
3.29	A pre-contrast T2* weighted volume overlapped with CT data after automatically registered by the proposed method visualized in green and red colour channels: (a) ROIs; (b) full volumes.	121
3.30	A pre-contrast T2* weighted volume overlapped with CT data after manual registration visualized in green and red colour channels: (a) ROIs; (b) full volumes.	122
3.31	Histograms of number of registrations verses translational and rotational errors of the post- to pre-contrast T2* weighted (T2*W) registration and T2 weighted (T2W) to T2*W registration: the results of T2*W-T2*W registration are shown at the top, results of T2W-T2*W registration at the bottom; the translational errors measured in <i>mm</i> are shown on the left, rotational errors measured in <i>degree</i> on the right. . . .	125
4.1	Demonstration of short-axis imaging planes of the heart and examples of short-axis T1 weighted delayed enhancement images that are used to visualize the interested structures (left and right ventricles) [4].	130
4.2	Example T2*W data from <i>MA³RS</i> and <i>IRNMAN</i> clinical trials: (a) <i>MA³RS</i> data, with the white arrow pointing to the aorta; (b) <i>IRNMAN</i> data, with the white arrow pointing to the left ventricle.	131
4.3	An example of a failed registration caused by intensity inhomogeneity: (a) T1 weighted delayed enhancement data; (b) pre-contrast T2* weighted data with severe intensity inhomogeneity; (c) alignment of the T2* weighted data and T1 weighted delayed enhancement data after registration visualized in overlapped red and green colour channels. The horizontal and vertical white arrows separately point to the centre of the left ventricle in the T2* weighted and delayed enhancement data.	132

List of Figures

4.4	Devices and patient setup for acquiring cardiac T1 weighted delayed enhancement and T2* weighted data.	133
4.5	Classification of existing correction methods [5].	136
4.6	N3 Bias Field Correction Framework from [6]	146
4.7	SPM Bias Field Correction Procedure [7].	147
4.8	Polynomial surface fitting bias field correction procedure	149
4.9	Example of simulated data: on the left is the original image without intensity nonuniformity and additive noise; in the middle is the image affected by 40% bias field and 3% noise; the image with bias field FWHM = 80% and 5% noise is on the right.	152
4.10	Example of intensity inhomogeneity generated using the BrainWeb simulator: the spatial domain of the image represented in number of pixels is placed in the horizontal plane, and the height of a point on the surface represents the strength of the inhomogeneity that affect a pixel of the image.	153
4.11	Example of simulated data before after correction: strength of bias field is 40% with no noise. The bias-corrupted data was labelled as "Corrupted"; "WD7" is the result from wavelet decomposition correction; "VY" represents the result using the polynomial surface method. N3 and N4 methods, with shrink factor setted as 2 and 4, are labelled as "N3F2" "N3F4" "N4F2" "N3F4".	156
4.12	Example of simulated data before after correction: strength of bias field is 80 with 5 % noise. The bias-corrupted data was labelled as "Corrupted"; "WD7" is the result from wavelet decomposition correction; "VY" represents the result using the polynomial surface method. N3 and N4 methods, with shrink factor setted as 2 and 4, are labelled as "N3F2" "N3F4" "N4F2" "N3F4".	157

- 4.13 SSD between the corrected data from all 7 methods and the data corrupted by the simulated bias field and noises: Noise from left to right is 0%, 3% and 5%; the strength of the bias field from top to bottom is 0%, 20%, 40% and 80%. The true signal without bias field and noise is shown on the left in the upper left subplot. 158
- 4.14 Correlation coefficients between the corrected data from all 7 methods and the data corrupted by the simulated bias field and noises: Noise from left to right is 0%, 3% and 5%; the strength of the from top to bottom is 0%, 20%, 40% and 80%. The true signal without bias field and noise is shown on the left in the upper left subplot. 159
- 4.15 SSD between the data corrected by the polynomial method, when changing the order of polynomial model from 1 to 5 and the data corrupted by the simulated bias field and noises: Noise from left to right is 0%, 3% and 5%; the strength of the bias field from top to bottom is 0%, 20%, 40% and 80%. The true signal without bias field and noise is shown on the left in the upper left subplot. 161
- 4.16 Correlation coefficients between the data corrected by the polynomial method when changing the order of the polynomial model from 1 to 5 and the data corrupted by the simulated bias field and noises: Noise from left to right is 0%, 3% and 5%; the strength of the bias field from top to bottom is 0%, 20%, 40% and 80%. The true signal without bias field and noise is shown on the left in the upper left subplot. 162
- 5.1 Examples of short axis cardiac images with different intensity inhomogeneity artefacts processed by different binning methods: at the top is the T1 weighted delayed enhancement data, at the bottom is the T2* weighted data which suffered more severe intensity inhomogeneity. 170

- 5.2 Visualizations of the failed registration caused by histogram dispersion: the edge image of the transformed T2*W data overlapped with the original T1W delayed enhancement data are shown on the left; the overlapped red-green visualizations are shown on the right, where the T2*W data is shown in red and T1W delayed enhancement data shown in green. The left ventricle, as the object of interest in our study, is shown by the vertical arrows in T1W delayed enhancement data, and by the horizontal arrows in the T2*W data. 171
- 5.3 Synthesized data contain four rectangles of different sizes and represented by different ranges of intensity used to observe the histogram dispersion effects on the performance of registration: (a) and (d) the reference image, and its histogram, that has a 255-level dynamic grayscale; (b) and (e) the floating image, and its histogram, that has a 100-level dynamic grayscale; (c) and (f) the floating image, and its histogram, corrupted by an intensity inhomogeneity with a strength equal to 40% of the intensity range. 174
- 5.4 Clustered images obtained by applying the *k*-means method to the synthesized data: (a) and (d) the original and clustered reference image; (b) and (e) the original and clustered floating image without intensity inhomogeneity; (c) and (f) the original and clustered floating image corrupted by the intensity inhomogeneity. 175

- 5.5 Results of affine registration obtained from the synthesized data visualized by overlapped red and green colour channels: (a) the results of registering the original floating image without intensity inhomogeneity to the clustered reference image; (b) the results of registering the floating image corrupted by inhomogeneity to the clustered reference image; (c) the results of registering the clustered floating image corrupted by the inhomogeneity to the original reference image. 176
- 5.6 The images used in the simulation experiment and their histograms shown with the “dynamic” ranges: the reference image which is chosen to be clustered and its histogram are shown in (a) and (d); the floating image without intensity inhomogeneity and its histogram are shown in (b) and (e); the floating image with intensity inhomogeneity and its histogram are shown in (c) and (f). The “dynamic” ranges of these images are marked by the black arrows, and the range define on (f) is the same with (e). 179
- 5.7 The range of normalized intensity values decided by two thresholds define on the histograms of each image in the simulated experiment. From top to bottom: the reference image (selected to be clustered), the floating image without intensity inhomogeneity, and the floating image corrupted by intensity inhomogeneity. 180
- 5.8 An example of cardiac MR data before and after being processed by ranked histogram specification: (a) the T2*W image before being processed using RHS; (b) the delayed enhancement image used to correct intensity distribution of the T2*W image; (c) the T2*W image after being processed using RHS. 184

5.9	The intensity distribution correction based on rearranged histogram specification and k -means binning process: μ and ν are the reference and floating images, $\hat{\mathcal{H}}_\mu$ and $\hat{\mathcal{H}}_\nu$ is the intensity histograms between two thresholds $b_{\mathcal{L}}$ and $b_{\mathcal{U}}$. In the case of registering T2* weighted data to T1 weighted delayed enhancement data, $\text{HDIR} > 1$ indicates that the T1 weighted delayed enhancement data has better visibility of the anatomical structures while suffering less inhomogeneity. Thus the intensity of the T2* weighted data is corrected using the rearranged histogram specification method.	185
5.10	Examples of ROIs selected on the T1 weighted delayed enhancement data (left) and pre-contrast T2* weighted image (right). The blue boxes show the regions of interest in both reference and floating images. A region of interest includes the left ventricle (LV) shown by the horizontal arrows, and the right ventricle (RV) shown by the vertical arrows.	188
5.11	An example of a T2* weighted cardiac data initially aligned to a delayed enhancement data achieved using automatically tracked ROI centres: (a) and (b) ROI centres on the reference and floating data (c) Alignment of 2D ROI centres (b) and (e) Visualization of overlapping the edge image of the delayed enhancement data over the T2* weighted data before and after the initial alignment.	189
5.12	Example of data down-sampled to 0.25 of the original resolution obtained from Gaussian pyramid and wavelet pyramid: (a) the original delayed enhancement data; (b) the down-sampled data from Gaussian pyramid; (c) the down-sampled data from wavelet pyramid.	190

5.13	Example of the pre-contrast T2* weighted image aligned to the T1 weighted delayed enhancement data, visualized by overlapping the edge image of the T2* weighted data to the T1 weighted data, after registration using the proposed method, and after the registration result being manually corrected: (a) data registered by the proposed method; (b) the manually corrected registration result.	194
5.14	Imaging devices (12-channel Siemens head matrix coil) and patient location for acquiring the neonatal MR data used to evaluate the performance of the proposed registration framework.	195
5.15	Examples of neonatal data used for validation of registration: (a) T1 weighted MPRAGE; (b) T2 weighted; (c) T2 weighted STIR; (d) T2 weighted Dark-fluid.	196
5.16	Illustration of landmarks picked on the 3D neonatal data: (a) sagittal view; (b) coronal view; (c) axial view.	197
5.17	An example of the results of registering the pre-contrast T2* weighted data to the T1 weighted delayed enhancement data, visualized using overlapped red and green colour channels. White arrows pointed to the left ventricle.	199
5.18	An example of the results of registering the pre-contrast T2* weighted data to the T1 weighted delayed enhancement data, visualized by edge image of the T2* weighted data to the T1 weighted data.	200
5.19	Example results of registering T2W-T2W neonatal data visualized by overlapped red and green colour channels: (a) before registration; (b) after registration.	203
5.20	Boxplots of registration results obtained from neonatal data.	204
5.21	Data from the failed registration (patient No.2956): (a) a slice of T1 MPRAGE data; (b) a slice of T2 Dark-fluid data which suffers from severe motion artefact as shown by white arrows and noise.	205

5.22	The T2 weighted Dark-fluid image aligned with the T1 weighted MRPAGE data of patient No.2956, visualized by overlapped red and green colour channels, before and after registered using the proposed method: (a) before registration; (b) failed registration.	206
6.1	Example of data from a failed registration: (a) a slice of T1 MRPAGE data; (b) a slice of T2 dark fluid data which suffers from severe motion artefact and shown by white arrows and noise; (c) a plot of mutual information values when transforming the T2W data along one dimension of the searching space.	210
7.1	Fitting Gaussian function to distribution of mutual information within three different searching ranges. The fitted Gaussian function tends to give a more accurate estimation of the distribution within a smaller searching range.	245
7.2	Estimation of the global optimum using the weighted mean of all particles within different searching ranges. The estimation of the global optimum tends to be closer to the real global optimum within a smaller searching range.	245

7.3	Information available at the t th iteration of PSO: in a dynamic Bayesian network, the hidden state θ represents an optimal estimation \mathbf{x}^{g*} of the true global optimum; the observed state ξ is defined as the average position of all particles $\hat{\mathbf{x}}^g$ weighted by the measured fitness function \hat{f} of each particle. An estimation of the hidden state \mathbf{x}^g is produced by fitting \hat{f} to a Gaussian function in each iteration of the optimization process. For the t -th iteration, $\mathbf{x}^g(t)$ can be obtained by combining $\mathbf{x}^g(t-1)$ and $\hat{\mathbf{x}}^g(t)$. When solving the optimization problem using a linear Kalman filter as reviewed in chapter 6, $\mathbf{x}^g(t-1)$ is treated as the output of <i>time – update</i> stage, $\hat{\theta}^-$, and $\mathbf{x}^g(t)$ is the output of the <i>measurement – update</i> stage, $\hat{\theta}$	246
7.4	Hidden Markov model [8]: θ and ξ are the hidden and observed states. .	247
7.5	The non-linear state transition model \mathcal{F} used to evolve the optimal estimation \mathbf{x}^{g*} of the true global optimum	248
7.6	The <i>predict – correct</i> circle of Kalman filter and its extensions	249
7.7	Brief workflow of the original particle swarm optimizer	253
7.8	Brief workflow of the unscented Kalman filter particle swarm optimizer (UKFPSO)	254
7.9	Estimations of global optimum when placing the searching range to different positions of the problem space	255

7.10	Information available at each iteration when solving the optimization process using a Kalman filter: the hidden state θ represents an optimal estimation \mathbf{x}^{g*} of the true global optimum. An estimation of the hidden state \mathbf{x}^g is produced by fitting the measured fitness function value \hat{f} to a Gaussian function in each iteration of the optimization process. The output of the <i>time – update</i> stage of the Kalman filter, $\hat{\theta}^-$, is defined as the mean value $\hat{\mathbf{x}}^g$ of all the particle positions weighted by \hat{f} . The population of particles is then moved to be centred on $\hat{\mathbf{x}}^g$. The observed state ζ is then defined as the mean $\tilde{\mathbf{x}}^g$ of all the new particle positions. The up-to-date estimation of the global optimum, $\mathbf{x}^g(t)$, is then provided by the output of the Kalman filter, $\hat{\theta}$, combining $\hat{\mathbf{x}}^g$ and $\tilde{\mathbf{x}}^g$	256
7.11	Workflow of the unscented Kalman filter particle swarm optimizer with “shift particles observation” (SPO-UKFPSO).	257
7.12	Workflow of nested unscented Kalman filter particle swarm optimizer (UKFPSO)	258
7.13	Axial views of the data chosen from patient_001 of <i>the Retrospective Image Registration Evaluation (RIRE) Project</i> : (a) CT; (b) MR_PD; (c) MR_T2; (d) PET.	268
7.14	Example of the overlapped T2 weighted image and CT image from <i>the Retrospective Image Registration Evaluation (RIRE) Project</i> , visualized using overlapped red and green colour channels: (a) before registration; (b) after being registered; (c) after being registered using the ground truth.	273
7.15	Example of the overlapped PET and MR_PD images from <i>the Retrospective Image Registration Evaluation (RIRE) Project</i> , visualized using overlapped red and green colour channels: (a) before registration; (b) after being registered; (c) after being registered using the ground truth.	274

-
- 7.16 Registration results obtained using original particle swarm optimizer (PSO), the linear dynamic system Kalman filter PSO (LDS-KFPSO) and the nested unscented Kalman filter PSO (UKFPSO): (a) before registration; (b) registered using original PSO; (c) registered using LDS-KFPSO; (d) registered using nested UKFPSO. The registration is performed to align the T2 weighted dark fluid and T1 MRPAGE images of the patient (No. 2956) which makes all the registration methods tested in chapter 5 fail. The results are visualized in overlapped red and green colour channels. 275
- 8.1 Example of a pair of carotid images registered by the registration method presented in chapter 5 integrated in the GUIs, visualized by overlapped red and green colour channels. The GUIs and ROI tracking method are slightly modified to locate the central “frog face” structure. . 284
- 8.2 Example of registration results of a triple-slice short-axis T1 weighted (T1W) CMR data, visualized by overlapped red and green colour channels: the results obtained using single transformation matrix is at the bottom, and the results obtained using the triple matrices transformation model is shown at the top. The white arrows point to the visual clues that indicate the difference between the registration results. 288

List of Tables

2.1	Comparison of CT and MR [9, 10, 11, 12, 13, 14, 15, 16, 17, 18, 19]	15
2.2	Commonly Used Similarity Measures [20, 21, 22, 23, 24, 25].	43
2.3	Some Optimization methods reviewed with its classification [24, 26, 27]	56
3.1	MR image registration errors, including translational and rotational errors in x, y, z directions, and the mean Euclidean errors and rotational errors calculated as the equivalent single rotation by the rotational errors. Translational error presented as millimetres and number of pixels (shown within brackets), and rotational error in degrees where all images were down sampled to 1.5625mm per voxels.	124
3.2	Statistics of target registration errors measured in mm	124
4.1	Brief Information of the Methods to Compare	143
5.1	Critical points proposed for landmark selection.	193
5.2	Average Translational and Rotational Errors of Cardiac Registration: voxels and degrees of manual correction. The standard deviation of the errors are shown within the brackets.	198

5.3	Registration accuracy evaluated by median and standard deviation (STD) of target registration error (TRE) calculated with the neonatal data: The method proposed in this work is underlined. Gaussian-pyramid method replaces wavelet image pyramid with Gaussian pyramid. No-Kmeans method simply uses linear binning when calculating mutual information. No-RHS method does not perform rearranged histogram specification (RHS). I also tried to use DIRECT to replace the particle swarm optimization (PSO) searching. Finally, the previous framework was also evaluated. The PSO method is applied with parametric setup recommended by Eberhart and Kennedy [28]: 10 particles are used for each dimension; both the social and self acceleration coefficients are initialized as 2.0; the inertia weight is initialized as 1.1, and vary between 0.1 and 1.1; when the change of the optimal value similarity measure is less than 10^{-6} , the optimization converges; the maximum number of iterations is 300. For the DIRECT search, the same standard is used to detect convergence, and the maximum number of iterations is also 300.	204
6.1	The Rule of Changing Acceleration Coefficients [29]	217
7.1	Benchmark Functions	267
7.2	Performances of the selected particle swarm optimizers applied to the chosen benchmark functions: the performances are measured by the average distances between the global optima they found to the ground truths obtained from 100 times of experiments with random initialization. The best result of each benchmark function is shown in bold font, and the standard deviations of results obtained from the 100 runs of this experiments are shown within parenthesis.	271

7.3	Comprehensive evaluation of the particle swarm optimizers applied to the chosen benchmark functions: the optimal results are shown in bold font.	272
7.4	Comprehensive evaluation of the particle swarm optimizers applied to the <i>Retrospective Image Registration Evaluation (RIRE) Project</i> data using target registration errors measured in <i>mm</i> : best results are shown in bold font. The right column shows the average runtime measured in <i>second</i>	276
7.5	Registration quality evaluation for CRIC Neonatal Data. Statistics of target registration errors (TRE) is measured in <i>mm</i> and calculated from succeeded registrations. Registrations with TRE larger than <i>8mm</i> is considered as failures as they can be easily detected by visual assessments. The average run time of each registration is measured in <i>second</i>	277

List of Abbreviations

AAA	Abdominal aortic aneurysm
ACO	Ant colony optimization
APSO	Adaptive particle swarm optimization
ARPSO	Attractive and repulsive particle swarm optimization
BOM	Bayesian optimization model
CC	Cross-correlation/correlation coefficient
CDF	Cumulative density function
CDR	Corrected detected rate
CHT	Circular Hough transform
CLPSO	Comprehensive learning particle swarm optimization
CMI	Conditional mutual information
CMR	Cardiac magnetic resonance
CP	Control point
CR	Correlation ratio
CRIC	Clinical Research Imaging Centre
CT	X-ray computed tomography
CJV	Coefficient of joint variance
CV	Coefficient of variance
DBN	Dynamic Bayesian network
DCT	Discrete cosine transformation
DRQPSO	Diversity controlled revised quantum behaved particle swarm optimization
DWT	Discrete wavelet transformation
ECC	Entropy correlation coefficient
ECG	Electrocardiogram

EKF	Extended Kalman filter
ELS	Elitist learning strategy
EM	Expectation-maximization
EPS	Elastic body spline
ESE	Evolutionary state estimation
FCM	Fuzzy-C-means
FFT	Fast Fourier transform
FLAIR	Fluid attenuation inversion recovery
fMRI	Functional MR imaging
FWHM	Full-width-half-maximum
GA	Genetic algorithms
GC	Gradient correlation
GCC	Gradient cross correlation
GD	Gradient difference
GPU	Graphics processing unit
GUI	Graphic user interface
HDIR	Homogeneous dynamic intensity ratio
HMM	Hidden Markov model
ICP	Iterative closest point
IDR	Incorrect detection rate
IRNMAN	Iron nanoparticle enhanced MRI in the assessment of inflammation after myocardial infarction
ISM	Implicit shape model
ISMRM	the International Society for Magnetic Resonance in Medicine
KF	Kalman filter
KPSO	Kalman filter particle swarm optimization
LI-CQPSO	Chaotic quantum behaved particle swarm optimization based on Lateral inhibition

LDS	Linear dynamic system
MA³RS	MRI for abdominal aortic aneurysms to predict rupture or surgery
MAD	Maximum of absolute difference
MAP	Maximum a posteriori
MDS	Multi-dimensional scaling
MI	Mutual information
ML	Maximum likelihood
MQ	Multiquadrics
MR	Magnetic resonance
MRF	Markov random field
MRI	Magnetic resonance imaging
MSE	Mean square error
N3	non-parametric non-uniform intensity normalization
NCC	Normalized cross correlation
NCQPSO	Niche chaotic mutation quantum behaved particle swarm optimization
NMI	Normalized mutual information
PAKS	p Approximate Kalman Swarm
PC	Phase correlation
PDE	Partial differential equation
PDF	Probability density function
PET	Positron emission tomography
PGM	Probabilistic graphic model
PI	Pattern intensity
PIU	Partitioned intensity uniformity
PSNR	Peak signal to noise ratio
PSO	Particle swarm optimizer/particle swarm optimization
QDPSO	Quantum Delta-Potential-Well-based particle swarm optimization
QPSO	Quantum behaved particle swarm optimization

RANSAC	Random sample census
ROI	Region of interest
RF	Radiofrequency
RHS	Re-arranged histogram specification
RIRE	Retrospective Image Registration Evaluation
RIU	Ratio-image uniformity
RQPSO	Revised quantum behaved particle swarm optimization
SA	Simulated annealing
SAD	Sum of absolute differences
SHT	Standard Hough transformation
SNR	Signal-to-noise ratio
SPECT	Single-photon emission computed tomography
SPM	Statistical parametric mapping
SPO	Shift particles observation
SSD	Sum of square difference
SSDA	Similarity detection algorithms
STD	Standard deviation
STIR	Short tau inversion recovery
SVD	Singular value decomposition
SWT	Stationary wavelet transformation
T1W	T1-weighted
T2W	T2-weighted
T2*W	T2*-weighted
TMVSE	Toshiba Medical Visualization System – Europe
TPS	Thin-plate splines
TRE	Target registration error(s)
UKF	Unscented Kalman filter

UoE	The University of Edinburgh
USPIO	Ultrasmall superparamagnetic particles of iron oxide
VIR	Variation of intensity ratios
VNS-PSO	Variable neighborhood selection particle swarm optimization
VOI	Volume of interest

CHAPTER 1

Introduction

1.1 Background and Study Objectives

Multi-modality imaging is increasingly being used in the assessment of cardiovascular imaging to provide information on a combination of anatomy and function in the healthy and pathological states. Different imaging modalities are able to provide complementary information which may benefit the clinical management of various diseases. For example, X-ray computed tomography (CT) imaging can outline bony structures inside the body accurately, and can provide good differentiation of vascular structures with the application of intravenous contrast agents [30]. Magnetic resonance (MR) imaging, acquired with a variety of imaging parameters, displays more versatile contrast information about a variety of soft tissues, and has been used to examine a large variety of medical conditions. Positron emission tomography (PET) scan is particularly useful for capturing information on specific metabolic activities and measuring specific aspects of body functions using targeted imaging radiotracers. Besides these differences in the type of provided information, different types of medical images also exhibit different imaging qualities and spatial/temporal resolutions.

Remarkable developments of medical imaging techniques have been seen in the past few decades. New generations of image acquisition systems have been focussed on improving the acquisition speed, resolution and quality of images, for great clinical benefit. For example, the 320-slice Toshiba Aquilion ONE CT scanner is able to

1.1 Background and Study Objectives

acquire a 16 cm field of view in less than half a second and incorporates new low dose technology making perfusion measurements feasible. Similarly, MR scanners now have improved spatial and temporal resolution allowing tissue characterization through measurement of tissue properties. Furthermore, simultaneous acquisition of PET and CT data using PET/CT scanners is now widely used in many centres. However, these improvements cannot diminish the content differences between the images from different modalities. Furthermore, multiple images acquired at different times from a single modality may be also required for supervision of pathologies or treatment response monitoring. To draw useful conclusions in many clinical scenarios, the combination of information from different imaging techniques is a vital step in the further development of non-invasive imaging as a tool for the progression and individualization of the treatment for various diseases.

Combination of multiple types of medical images and data acquired at different times requires spatial alignment of the data. This has previously been achieved by manually minimising changes in subject position between scans. A computing technique, called image registration, was developed and widely deployed to align the data by establishing correspondence between features seen on different imaging modalities or between images and physical space. It also aims to assist monitoring of subtle changes in size and intensity over time or across a population [30]. However, image registration, especially alignment of multi-modality and multi-parametric data, is a challenging topic in the field of medical image analysis. First, different types of data provide non-linear intensity correspondences with different contrast distributions, for example, a tissue that has enhanced visibility in one modality may be specifically suppressed in another. Second, data acquired with different imaging techniques and parameters have different imaging qualities and suffer from completely different types of noise and artefacts. Also, patient motion happens between or even during scans or changes of pathological information between scans (such as growth or reduction in tumour size) can lead to large deformations of image

contents. This requires the registration methods to integrate complicated image transformations and introduces increased computational cost into the registration algorithms. Furthermore, evaluation of the registration results requires intense user interactions and precise “gold standards” in order to enable full validation of new processes. Nowadays, image registration receive a special attention from both clinical and technical research groups.

Several clinical research projects ongoing in the Clinical Research Imaging Centre (CRIC), the University of Edinburgh (UoE), involve state-of-the-art multi-modality and multi-parametric imaging of cardiovascular and neural systems before and after application of novel contrast agents and throughout disease monitoring. The aim of this PhD project is to develop novel registration applications whereby image registration can immediately benefit not only the clinical care, but also the development of novel non-invasive imaging techniques, specifically focused around these clinical trial data. This thesis presents mathematical and software solutions for multi-modality and multi-parametric image registration problems involved in several cardiovascular clinical research projects. The proposed registration methods were evaluated with up-to-date benchmark datasets, as well as clinical data acquired within three clinical trials where the imaged objects include abdominal aortic aneurysm (AAA), heart and neonate, and the performances were compared against state-of-the-art methods.

1.2 Progress of The Work

To provide application-specific image registration solutions for different clinical research projects, I first reviewed a wide range of fundamental mathematical tools used in image registration algorithms based on contrasting characters of different imaging modalities, as shown in chapter 2. The reviewed methods are all applicable to multi-modality and multi-parametric image alignment problems from CT and MR imaging. Based on this literature review a novel multi-resolution registration method based on the classical four-step registration procedure was developed for a clinical trial. This clinical research project aims to develop novel diagnostic protocol for abdominal aortic aneurysm (AAA) through CT and MR imaging with application of a novel contrast agent. Details of the involved clinical data and the provided registration software is described in chapter 3.

The AAA registration framework was validated against data acquired from over 400 patients. However, when the framework was applied to multi-parametric cardiac MR (CMR) data from another clinical trial, it failed for almost half of the registrations. The reason for the failure was the presence of severe intensity inhomogeneities in the CMR data. Thus, an additional preprocessing step was necessary to correct the inhomogeneity before the registration was performed. To gain an insight into state-of-the-art intensity inhomogeneity correction methods, and to prepare for the development of a preprocessing step for the proposed registration framework for the CMR data, a comparison was made of inhomogeneity correction methods, which is described in chapter 4. Following a brief review of typical methods, four representative correction methods were selected for comparison experiments, with a widely used benchmark Brain MR data simulator. The conclusions were obtained from simulated data with different parametric settings about the performance of the difference methods under different levels of intensity inhomogeneity and additive noise.

Based on the comparison study presented in chapter 4, in chapter 5, a new preprocessing method, based on the homogeneous dynamic intensity ratio and rearranged histogram specification, was developed. Besides this preprocessing step, the registration framework was further improved by a new multi-resolution particle swarm optimization (PSO) [28] strategy. The proposed framework was validated using multi-parametric MR cardiac datasets. For more reliable calculation of the registration error, neonatal datasets were also used for assessment with manually picked landmarks. The new registration framework has shown superior performances in these applications than the algorithm shown in chapter 3. However, this new registration framework still failed to register the neonatal data from one patient due to severe motion artefacts and noise present in the data. These artefacts and noise introduce multiple local optima in the problem space of registration, and thus lead to premature convergence of the optimization process. To register data with worse imaging qualities, the optimizer, PSO, used in this method needs to be modified for better robustness to noise and artefacts.

Chapter 6 presents a comprehensive literature review of various modified PSO models that have been applied to image registration problems. This review was performed for possible improvements that could be applied to the optimization module of my registration framework. From this review, I concluded that most current PSO methods are still classified as general purpose optimization processes, and none of the reviewed methods were specialized for registration applications, thus a novel PSO method specifically developed for image registration is needed. A few reviewed PSO models provide possible solutions to encode registration-oriented prior knowledge of the problem space.

In chapter 7, based on the review presented in chapter 6, I propose a novel type of registration-oriented PSO model, guided by an unscented Kalman filter (UKF). Three newly implemented optimizers displayed better robustness to local optima in the searching space with less computational complexity in the comparison experiments

1.2 Progress of The Work

performed using both benchmark and real data. This new PSO model provides a new efficient mechanism to integrate prior knowledge of a registration problem into the optimization process, which obviously enhanced the performance of the image registration algorithms.

Finally, chapter 8 summarizes results and technological innovations achieved by works presented in each chapter, and discusses possible further extensions and future directions of the proposed methods.

Literature Review for Image Registration Techniques of CT and Multi-parametric MRI Data

ABSTRACT

Image registration, which allows us to combine complimentary anatomical and functional information, is a vital step for the progression and individualization of the treatment of cardiovascular disease. Several ongoing cardiovascular research projects in the Clinical Research Imaging Centre, the University of Edinburgh, require comprehensive analysis of X-ray computed tomography and magnetic resonance imaging. Registration of multi-modality and multi-parametric images is challenging due the different image contrasting properties and non-stationary artefacts. Performances of image registration methods are not only affected by different properties of image acquisition, but also choices of image features, similarity measure, transformation model, and optimization strategy. It is a popular area of image analysis research, and various registration algorithms have been invented in the past few decades. In this chapter, I first briefly compared the imaging properties of CT and MR cardiovascular imaging techniques, followed by a comprehensive investigation of basic computational components and state-of-the-art developments of image registration methods.

2.1 Introduction

As introduced in the last chapter, modern medical imaging captures complementary information using different modalities [31]. Integration of complementary information obtained by different modalities, acquisition techniques, or preparation and pre-processing of the object being imaged are vital steps in gathering knowledge about healthy and diseased cells, tissues and organs. Imaging data co-registration is a critical technique in this process which brings the images into best possible spatial correspondence with respect to each other [32]. This registration of data can allow the complimentary information from each imaging dataset to be combined spatially, leading to a more complete understanding of the pathology being imaged. Several ongoing cardiovascular clinical imaging research projects in the Clinical Research Imaging Centre (CRIC), the University of Edinburgh (UoE), involve developing novel imaging and analysis methods to combine the information from computed tomography (CT) and magnetic resonance (MR) images acquired by state-of-the-art scanners to produce novel clinical decision-making tools. Part of the requirements of these studies is to combine the information gathered by the different imaging modalities, such that image registration becomes a required step in the analysis pipeline for each study. Specific information about each of these studies is included in subsequent chapters together with the associated registration resolution. In this chapter, I review basic mathematical models and methods used in the four basic steps of image registration, 1) preprocessing and feature extraction, 2) similarity measure (or feature matching), 3) transformation and resampling, and 4) optimization, which are helpful to develop optimized image registration algorithms for these specific clinical projects. As the objective of this chapter is to gain an overview of multi-modal and multi-parametric registration methods applicable to specific clinical data, fundamental physical backgrounds of the involved imaging techniques are out of the scope of this thesis. Details about imaging physics can be found in the reviews

and introductions conducted by Herman [33], Kalender [17], Hajnal and Hill [30], Cunningham [34], Bernstein et al. [35], McRobbie et al. [18], and Hashemi et al. [36].

This chapter starts with a brief comparison of CT and MR imaging techniques in section 2.2, as well as a comparison of the complementary information displayed by CT and MR images that can affect the performance of the registration process. A general introduction of the structure and classification of registration algorithms, and their application to medical images, are shown in section 2.3. Sections 2.4, 2.5, 2.6 and 2.7 look into each of the four components of registration listed above. Common implementation issues of registration, such as interpolation and resampling, are discussed in section 2.8. Finally, based on the reviewed techniques, the strategy to build up my own registration algorithms for our specific clinical research projects are discussed in section 2.9. Then a comprehensive literature review of state-of-art multi-modality image registration algorithms is presented. An insight into the common building blocks is gained in this review, as well as the fundamental differences, of various common registration methods applied to cardiovascular imaging.

2.2 Imaging Modalities

The clinical imaging research projects in CRIC discussed in detail in later chapters of this thesis, require spatial alignment of multi-modality (CT-MR) and multi-parametric MR-MR images obtained with and without novel types of contrast agents, sometimes with specific tissue contrasts according to anatomy or function in mind. Some positron emission tomography (PET) images were also acquired using a 128-multidetector PET-CT scanner. As the output PET images are considered spatially aligned with the associated CT data, alignments between these PET images and other data can be achieved by registering the CT data. Thus in this PhD project I mainly deal with developing solutions for MR-CT co-registration, and MR-MR co-registration using data acquired with various parametric settings, with or without assistance of contrast agents, or different voxel sizes. The involved modalities and acquisition techniques are briefly reviewed in this section.

2.2.1 CT Imaging

An in-depth description of the theory of CT imaging is beyond the scope of this thesis. Please refer to [33] and [17] for a more comprehensive description. In brief, CT scanners utilise x-ray tubes which rotate around the patient. Detectors on the opposite side of the patient to the x-ray emission from the tube receive the x-ray beam which is sampled, digitised and then sent to the reconstruction processor [37][38]. Cross sectional images of human body can be generated by combination of the x-rays received by the detectors through the body, correcting for attenuation caused by tissue of the body between the x-ray emitters and the detectors [33]. The main difference of CT imaging compared to the traditional x-ray imaging mode is that the x-ray tube and detectors rotate around the patient who is kept stationary. The images of cross sections of the patient are computed through the image reconstruction techniques from the line integrals of the x-ray attenuation coefficient between the corresponding x-ray sources

and detectors. Increment of detector row numbers and speed of gantry rotation make CT scanning applicable not only to static organs but also the ones under constant motion, such as the heart [38][17].

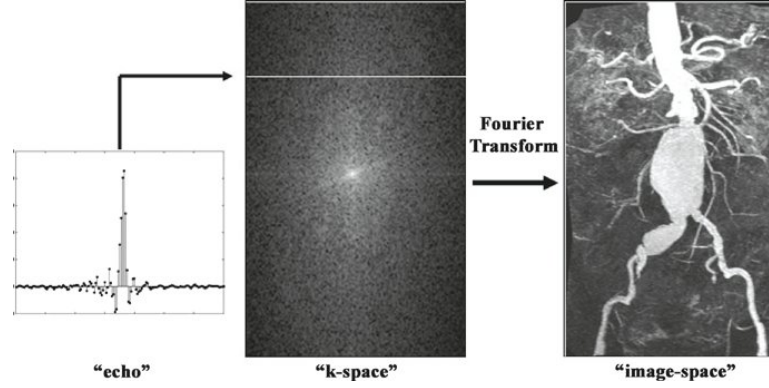


Figure 2.1: Echoes acquired in an MR scan are stored in k -space which is transformed with a mathematical Fast Fourier Transform (FFT) to image space [1].

2.2.2 MR Imaging

An in-depth description of the theory of MR imaging is beyond the scope of this thesis. Please refer to [18], [1] and [36] for a more comprehensive description. In brief, MRI aligns magnetization of atomic nuclei in the body using strong magnetic fields measured in the units of tesla (T) [39]. The net, bulk magnetization of the object being imaged, which aligns along the main magnetic field of the scanner, is excited by application radiofrequency (RF) waves. These RF pulses temporarily perturb the water proton's spins. As they recover, they emit a resonant frequency of energy which is used to produce the raw MR signal. Additional magnetic gradient are applied to the main magnetic field to manipulate the frequency and phase of the signals given out by the nuclei, to provide spatial information. A Fourier transformation is then applied to the signal to convert the frequency encoded signal in order to generate MR images with spatial information about the nuclei's position. This process is shown in Figure 2.1 [39] [1] [40]. What the receiver coil detects as the MR signal is the magnetization as it goes through the process of "relaxation" back to its original equilibrium orientation

2.2 Imaging Modalities

aligned to the main magnetic field, through several relaxation processes. These relaxation processes vary between tissues, and may be further manipulated through application of exogenous contrast agents with suitable magnetic properties. Tissue contrast may also be generated through the application of targeted MRI acquisition “sequences” which involve manipulation of the available magnetization using a combination of RF pulses and magnetic gradients [41]. The main relaxation processes which dictate the tissue contrasts used in this thesis are spin-lattice relaxation, referred to as T1 weighted (T1W) scans (mainly reflecting exchange of proton spin energy to local chemical lattice, and spin-spin relaxation time T2 weighted (T2W) scans which reflect exchange of magnetization between neighbouring protons (a much faster than the T1 thermal exchange). Additionally the decay of magnetisation which combines the effect of T2 spin-spin interaction and local inhomogeneity of the main magnetic field is described as T2* relaxation. Several of the projects discussed in this thesis specifically make use of scans which target this process in the form of T2* weighted (T2*W) scans, in order to attempt to detect applied exogenous imaging contrast agents which target inflammation (discussed in more detail in chapters 3, 4 and 5).

2.2.3 Image Contrast of CT and MR Data

CT image contrast between tissues is formed only by X-ray attenuation, such that it is suitable for examining tissues which have differing X-ray attenuation characteristics which strongly relates to tissue density, for example differentiating bony and soft tissues. MR tends to be better at providing contrast between different soft tissues [41], which may present little variation in X-ray attenuation.

In MR images the contrast between different tissues can be modified by applying different types of pulse sequences (a combination of RF pulse and magnetic field gradient applications) [9] [10]. Two of the main classifications of techniques used for MR imaging are “spin-echo” and “gradient-echo” imaging. These are discussed in more detail in [41]. In terms of the characteristic of these images that are important

to image registration approaches, it is important to note that images obtained with spin-echo sequences tend to have better imaging quality in terms of higher signal-to-noise ratio (SNR) and generally lower sensitivity to imaging artefacts. Spin-echo imaging can be used to provide high contrast between the blood pool (often shown as dark when blood is flowing through the imaging plane), and the relatively brighter heart tissue in cardiovascular imaging applications. T1W spin echo images give high fat signal and low fluid signal, and thus are useful to visualize anatomical structures with high contrast between fat, muscle and fluid. T2W spin echo sequences brighten the fluid signal, and are useful for the characterisation of cardiac masses and oedema with fluid collections. When soft tissue contrast is not required, proton density (PD) spin echo sequences can be used for depiction of anatomical structures. Gradient-echo sequences can achieve higher imaging speed and are therefore very well suited to cardiovascular applications (where organs tend to be moving), but can lead to loss of signal at the boundaries between tissues with different magnetic susceptibilities and tend to be more sensitive to both magnetic field inhomogeneity and movement. Fast moving blood flow through the imaging plane often have enhanced signal compare to surrounding tissues (although this can be manipulated using specific imaging sequences). Contrast in T2*W gradient echo images is strongly influenced by susceptibility effects caused by local inhomogeneity of the main magnetic field, but sensitive to haemorrhage or iron loading of tissue [42]. Many of the projects discussed in this thesis use imaging protocols specifically designed to make use of T2* sensitivity to presence of iron, in order to target inflammation processes in image contrast (as discuss in detail in subsequent chapters).

This PhD project focuses on solving the image co-registration problems for several clinical research projects which involve imaging of heart and abdominal aortic aneurysm (AAA). In addition, some brain image data is used to test some of the proposed registration algorithms. For cardiac imaging, electrocardiogram (ECG) synchronization techniques are used to ensure that the CT and MR signal is acquired

2.2 Imaging Modalities

at a particular time of cardiac cycle [41]. A detailed introduction of the rapid pulse sequences used in cardiac MR (CMR) imaging is provided by Ridgway [41]. For imaging of both cardiovascular and brain, fat suppression sequences are commonly used to suppress or detect signal from adipose tissue [43]. For example, short tau inversion recovery (STIR), is a commonly used technique to homogeneously attenuate fat signal for contrast enhancement [18]. Similarly, in brain imaging cerebrospinal fluid also can be attenuated to enhance parenchymal oedema or subtle changes at the periphery of the hemispheres. A popular “dark fluid” pulse is called fluid attenuation inversion recovery (FLAIR).

Both CT and MR images may also be enhanced using contrast agents. For CT the contrast agents contain elements of higher atomic number, such as barium or iodine. In MR, contrast agents are used which have paramagnetic properties, such as gadolinium, to control relaxation times [9]. In the clinical trial introduced in chapter 3, which involves multi-modality and multi-parametric imaging of AAA, a contrast agent is used to introduce iron particles which is highlighted in T2*W images. Detailed instructions for selecting CT and MR in different applications is provided by many international guidelines, such as the European Commission [13]. Table 2.1 compares some of the pros and cons of CT and MR.

Table 2.1: *Comparison of CT and MR [9, 10, 11, 12, 13, 14, 15, 16, 17, 18, 19]*

	CT Scan	MR Scan
Imaging Principle	X-ray attenuation; Back projection model [17]	The precession of magnetization induced by a strong magnetic field; FFT transformation [18]
Scope of application	Objects that have high atomic numbers	More versatile than X-ray; Used to examine a large variety of medical conditions
Type of details	Better details for bony structure, less soft tissue contrast	Much higher soft tissue details, less details in hard tissue
Radiation exposure	Moderate to High	None, so very good for paediatrics, healthy control imaging, and repeated scanning in the same subject
Resolution	Better spatial resolution	Better temporal resolution
Artefacts	Streaking, Shading, Rings, Distortions, etc . [44]	More artefacts than CT caused by patient motions, external magnetic field (bias field), etc . [19]
Time taken per scan	Usually completed within 5 minutes [16]	Typically 30 minutes [14, 15]
Cost	Usually less than MR	Usually higher than CT and most other imaging modalities [45]

2.3 Image Registration

Image registration is an important analysis strategy for integrating useful data obtained from separate images in medical diagnosis, especially for motion correction and follow-up study comparison. Such applications can be found within the routine clinical pathway of events such as radiotherapy planning, surgical evaluation, and radiotherapeutical procedures [46]. In the field of medical image analysis, image registration is generally described as the process of transforming and aligning the floating image (or sensed image) to the reference image (or source image) [27]. A general model of image registration can be expressed as following equation:

$$T' = \arg \max_{T \in E} S(I_1, I_2 \diamond T) \quad (2.1)$$

where I_1 and I_2 are two images represented as functions of a location in the image space, T is the transformation applied to I_2 from the admissible transformation set E and S is the similarity measure of the transformed I_2 and I_1 , and T' is the optimal transformation. In this case, I_1 is the reference image which is kept fixed, and I_2 is the floating image which is transformed during the registration process. Given a voxel position $\mathbf{v} = (v_x, v_y, v_z)$, the intensity value of the reference image at \mathbf{v} is $I_1(\mathbf{v})$. There is no requirement for I_1 and I_2 to have the same size and intensity ranges.

A number of broad surveys focusing on particular aspects of registration were published back to the year of 1992 [2, 23, 27, 47, 48, 49, 50]. Brown [47] proposed the first major review in 1992. More comprehensive and detailed descriptions of image registration algorithms can be found in [2, 27]. Deshmukh [50]'s brief review emphasized entropy, spectral and wavelet based methods. Other brief surveys have been conducted by Fischer and Modersitzki [23], Salvi et al. [48], Wyawahare et al. [49].

Registration methods applied to medical imaging were initially investigated

by Maintz [20, 46], and Hawkes [51] reviewed different algorithms for radiological image registration and their clinical applications. A detailed survey of hierarchical algorithms was later proposed by Lester and Arridge [52]. As a critical technique for comparing different registration algorithms, methods of evaluating registration quality were reviewed by Christensen et al. [53]. Algorithms for registering low resolution functional imaging to high resolution structural modalities were reviewed in [54]. A comprehensive and complete survey of cardiac image registration methods applicable to all major imaging modalities was provided by Mäkelä et al. [55], and Kostelec and Periaswamy [56]’s review paper concentrates specifically on MR images. Shams et al. [24] provided a report specific to multicore/GPU parallel implementations for image registration.

Diverse registration algorithms have been designed for various types of images, degradations and geometric deformations. No universal method applicable to all imaging application tasks is currently possible [27]. Nevertheless, most registration methods follow similar procedures, as shown in Figure 2.2, and consist of four main steps: 1) pre-processing, 2) similarity metric design, 3) optimization and 4) spatial transformation. A similar schedule was defined by Brown [47] where the registration process was divided into four components: 1) feature space, 2) search space, 3) search strategy and 4) similarity metric, and by Zitová and Flusser [27]: 1) feature detection, 2) feature matching, 3) mapping function design, and 4) image transformation and resampling. In this thesis, the registration technique is discussed based on the schedule given by Brown [47] as shown in Figure 2.2. Algorithms are classified according to the nature of registration basis and criteria extracted from each step. In clinical diagnosis using medical images, registration is mainly used to assist integration of data obtained from images taken at different times, using different imaging protocols or from different imaging perspectives [49]. Early medical image registration algorithms pre-dated the 1980s [47]. More realistic automated methods were proposed from mid 1990s onwards [57]. In this survey, I concentrate on the

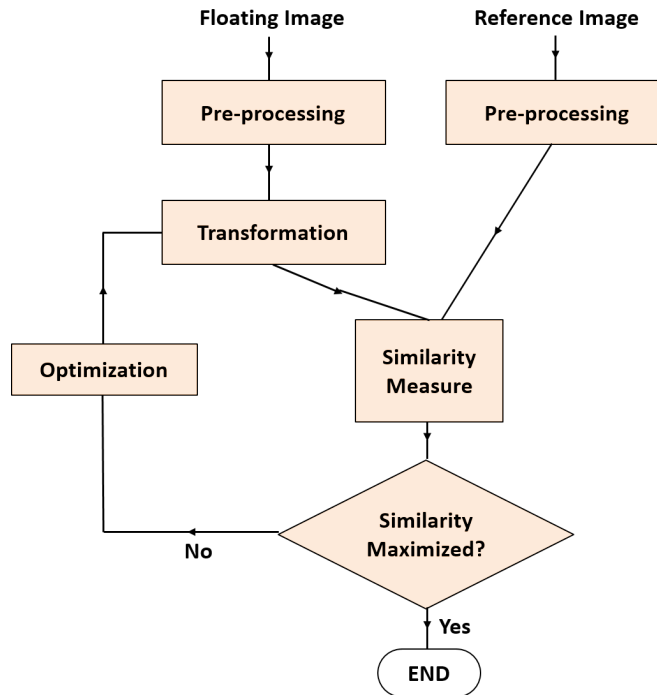


Figure 2.2: *General Image Registration Procedure.*

multi-modality and multi-parametric methods that can be possibly used to register CT-MR image pairs or different types of MR images. Dean et al. have evaluated four co-registration techniques for radiotherapy treatment planning of prone rectal cancer patients [58]. Sannazzari et al. and Rasch et al. discussed delineation of volumes in conformal radiation therapy for treatment of localized prostate cancer [59, 60] and the available multi-modal image fusion software was assessed by Kagawa et al. [61]. Due to the objectives of our ongoing clinical research projects, these reviewed methods are applicable to cardiovascular analysis. In most of the reviewed publications, the registration methods in literature are evaluated also using brain images as a variety of landmarks can be selected for quantitative evaluation.

2.3.1 Subject and Modality

Registration tasks involved in practical clinical research can be differentiated by the study application (such as body area being imaged) and imaging modalities.

Generally there are different registration problems which can be summarised as follows.

Same subject and same modality Registration can be used for finding changes in images taken at different times or under different conditions, specifically [47]:

- Images acquired at different times within short interval, for example, motion correction for ultrasound cine sequences, perfusion studies in CT and nuclear medicine;
- Images acquired at different times with long interval, for example, serial study follow-up for tumour growth or regression measurement;
- Images acquired under different conditions for example, before and after contrast injection, ventilation and perfusion nuclear medicine scans.

Same subject but different modalities In medical diagnosis, the same clinical application or object can be imaged using different modalities. Thus a structural modality recording anatomical body structure, such as CT, or ultrasound, is often combined with a functional modality monitoring functional or metabolic body activities, for example, single-photon emission computed tomography (SPECT), positron emission tomography (PET) or functional MR imaging (fMRI). Alignment of multi-parametric MR images can use similar post-processing methods as multi-modality images due to the fact that the MR imaging parameters (sequences) can be modified to highlight different anatomical and functional content.

Different subjects but same modality This type of application can address *scene to model registration* [27]. The model can be a computer generated virtual atlas or a different subject that has similar contents with the transformed subject. The aims of this type of registration include:

- creating a standard atlas to align all subjects into the same space;

2.3 Image Registration

- automatic labelling and segmentation;
- detecting average changes across subjects to study very small functional changes in functional brain studies (PET/fMRI).

2.3.2 Dimensionality

The same subject may be imaged from different viewpoints using different modalities to gain a larger 2D view or 3D representation of the imaged subject [27]. The problem space of image registration applications is built up by dimensions of spatial transformation. In special cases, for example, registrations performed to supervise growth of a tumour, time can be an added dimension of the problem space.

In the simplest case, separate slices from tomographic data, or intrinsically 2D images, require 2D/2D registration which is less complex than 3D/3D registration in terms of the size of parameter space and volume of data. 3D/3D registration can also be applied to align two tomographic datasets, as well as to register a single tomographic dataset to spatially defined models [46]. 2D/3D registration is a special case of medical image registration which has particular applications, including direct alignment between spatial data and projective data, for example, aligning a pre-operative CT image to an intra-operative X-ray image, or aligning single tomographic slices to spatial data, for example, registering sparse MR slices to CT 3D data. This type of registration is usually applied to image guided navigation or by surgeons, for example radiotherapy planning and treatment verification, spinal surgery, hip replacement, neurointerventions, or aortic stenting [62].

2.3.3 Classification

A variety of classification criteria have been proposed in the past decades based on properties of different steps in registration algorithms. Most publications classify the algorithms based on features used in registration (feature based or intensity

based), nature of transformations (linear, similarity, affine, projective, and non-rigid), operating domains (spatial or frequency), level of automation (manual, interactive, semi-automatic and automatic), similarity measures, etc. [23, 27].

For medical images, den Elsen et al. [63] gave widely recognized classification standards of registration methods back to 1993 and Maintz [46] later proposed more detailed and augmented classification based on nine separate criteria. Chmielewski and Kozinska [64] summarized earlier classification standards in earlier publications [47][46, 63] and similar classification was mentioned by Rui and Minglu [65] based on dimensionality, domain and type of transformation, tightness of feature coupling, measure of registration quality, method of parameter determination, subject of registration, type of data, source of features and automation level [49]. Salvi et al. [48] further developed Maintz's [46] classification based on the accuracy evaluation and summarized the registration to two general categories, coarse and fine registration.

2.4 Pre-processing and Feature Selection

Typically, medical images suffer from one or more imperfections [66]: such as low spatial and spectral resolution, inadequate contrast, high levels of noise, geometric deformation or presence of imaging artefacts. So before any transformation models can be generated, some pre-processing methods may be applied to the images, such as a noise and artefact removal step. Intensity inhomogeneity, or “bias field” is a type of frequently encountered artefact in MR images, the correction methods of which will be reviewed in chapter 4.

Most publications, following den Elsen et al.’s standard [63], classified the algorithms as extrinsic, intrinsic and non-image based methods according to the source of features of the registration algorithms [46, 47, 49, 63]. Non-image based registration mainly uses camera calibration techniques to bring the images into a uniform coordinate system [49]. This type of method can be sufficiently used in applications related to ultrasound [49, 67, 68], or applications of registering the position of surgical tools mounted on a robot arm to images [49, 69, 70].

The extrinsic and intrinsic registration methods are based on salient and distinctive objects, or statistics of intensity distribution, extracted from the image contents [27]. Feature extraction is the first step of these methods. Zitová and Flusser [27] summarized the common properties of features: user-demanded physical interpretability, enough common elements in both images, good localization accuracy of detection and finally being robust to assumed image degradation. Ideally, the same features of the same imaged object should be detected. The features are often represented by their point representatives, which are named control points (CP).

2.4.1 Extrinsic Registration

Extrinsic methods use features from objects that are artificially introduced specifically for registration purposes by attaching these marker objects that are specifically

visible and detectable by the imaging modalities used [24, 46]. This means that the registration parameters can be explicitly computed. This type of method is comparatively fast, easy, usually can be automated, and often has no requirement for complicated optimization algorithms. The attached objects are however often invasive, which is one drawback of extrinsic registration [46, 49]. A stereoscopic frame is an example of an object screwed rigidly to the patient's outer skull table [46], which can then be used as the best reference for registration accuracy in a long period [71, 72, 73, 74, 75, 76, 77]. Other invasive objects, such as screw-mounted markers have been used for localisation and registration purposes [49, 78, 79, 80, 81]. Non-invasive markers can lead to less accurate registration than invasive markers. Examples of popular non-invasive objects are markers glued to skin and larger devices [80, 82, 83, 84, 85, 86] that can be fitted snugly to the patient [46].

Another disadvantage of extrinsic methods is that patient specific information can be difficult to include in the extrinsic methods [46], and the transformation is often limited to translation and rotation due to the rigid nature of the objects used for registration purposes. Because of this constraint of transformation, as well as a variety of practical considerations, multi-modality and multi-parametric registrations extrinsic methods are largely limited to specific applications in orthopedic and brain images. However, in special cases like studies of animal motion, this type of methods may obtain non-rigid registration [46]. Most extrinsic methods reviewed were proposed early in the 1990s.

2.4.2 Intrinsic Registration

2.4.2.1 Landmark Based Method

Different from extrinsic methods, intrinsic methods only make use of patient generated image contents defined as "features", thus they are non-invasive and can be used retrospectively [24]. These features can be landmarks which are sets of manually identified salient objects, or segmented binary structures and surfaces [27, 46]. Some

2.4 Pre-processing and Feature Selection

methods directly measure the intensity values and are then classified as area-based, voxel property or intensity-based methods in the reviewed publications [27, 49, 55, 65]. The optimization, or searching strategy, is relatively dependent on the type of features selected in the intrinsic methods. Detailed introduction of each optimization process of transformation is discussed in section 2.7.

Landmarks can be either manually identified anatomical points or automatically localized geometrical features. Maintz [46] described anatomical landmarks as salient and accurately locatable points of the morphology of the visible anatomy. A great number of papers published in early 1990s [83, 87, 88, 89, 90, 91, 92, 93] described various methods applicable to multi-modality and multi-parametric registrations. Local curvature extrema and corners are typical examples of geometric features. Landmark based methods have a wide range of applications, theoretically applicable to any image. The defined point sets are relatively sparse compared to raw image data, so simple and thus fast optimization procedure is possible [46]. Because of this characteristic, landmark based methods are mostly applied to rigid and affine registration. More complicated forms of transformation can be realized if the selected point set is large enough. When combined with a different registration basis, for example, Wahl et al. [85]’s method which mixes point features with extrinsic fiducial markers, it is possible for the optimization process to get stuck in local optima and to result in largely mismatch if the optimization parameter space is not constrained to be quasi-convex. Another frequently encountered drawback of landmark based method is the requirement for relatively intense user interaction as part of the registration pathway [49].

2.4.2.2 Segmentation Based Method

By technical definition, segmentation based methods are highly related to landmark based methods as some studies [46, 49, 65] pointed out that landmark identification is a segmentation on data of lower order. Segmentation based methods extract the same

anatomical structures from both the reference and the floating images, such as curves, surfaces or volumes, and use them as the sole input of rigid registration [94, 95, 96]. The extracted anatomical structure may also be applied to elastic deformation models [97, 98]. All segmentation based methods have a common disadvantage which is that the registration accuracy is limited by segmentation accuracy. The hierarchical Chamfer matching method [99], which matches an object to a pre-defined contour, significantly contributes to the popularity of segmentation based methods [46]. Maintz compared different kinds of edge and ridge feature extraction methods for CT-MR and other inter-modality registration problems [46].

Segmentation based registration suits applications in intra-subject registration well when using rigid transformation models, and is also well-suited for inter-subject and atlas registration with a deformation model [46]. When applied to elastic registration with a deformation model, matching of features is computed locally with some constraints given by a regularization term. The registration process is usually iteratively performed with small deformations in each iteration. A template should be defined in this case, either to match a segmented structure in the second image or to an unsegmented image, for example, an edge region area. Early literature mainly applied these methods to CT bone contours and MR brain images [97, 98, 100].

2.4.2.3 Intensity Based Method

Intensity based methods directly make use of pixel (or voxel) values. A number of papers [46, 55] called these voxel property based methods. Intensity based methods either select representative scalars and orientations of intensity value content, called principal axes and moments based methods, or utilize full image content, which are voxel property based methods.

Principal axes and moments based methods compute and align center of gravity and principal axes from zeroth and first order moments of the image. Higher order moments can also be used in special cases. Low accuracy and inability to handle

2.4 Pre-processing and Feature Selection

volume differences are main drawbacks of this type of algorithm. So some algorithms use principal axes and moments based registration as a coarse initial alignment [101].

Relatively less distinctive and easily detectable objects can be found in medical images compared to others [27] thus voxel property based methods are more commonly used. This type of method has theoretically high temporal complexity (will perform slow), although this is limited by considerable computational costs in clinical applications. Various similarity measures, resampling, optimization and searching strategies have been used in this type of method.

2.5 Transformation

Transformation, also called mapping function [27], is the essential step to align the images. A transformation can be either applied to the entire floating image, which is called global transformation, or to subsections of the image, which is local transformation [47]. The designed mapping function should be able to align the floating and reference image so that the distance between the corresponding corresponding image points is minimized [27].

Transformation can be either linear or non-linear. The linear transforming process of a point in 3D space can be represented as the product of a coordinate vector and a 4×4 transformation matrix

$$\mathbf{v}' = \mathbf{T}\mathbf{v} \quad (2.2)$$

where \mathbf{v} and \mathbf{v}' are vectors representing the coordinate value of a point and its transformed correspondence, $(v_x, v_y, v_z, 1)'$ or $(v'_x, v'_y, v'_z, 1)'$ in the case of 3D space, and \mathbf{T} the transformation matrix.

As a commonly expressed example, basic linear transformations include: translation, linear displacement on coordinate axes; rotation, angular offset; shearing, effective rotation of one axis in the coordinate system; scaling, enlarging or diminishing the objects with the same scale factor in all directions; reflection, a map of an object into its mirror image; and projection and/or decomposition of a distance to another direction. Based on these basic displacements, different types of transformation between images are defined allowing different degrees of freedom, including rigid, similarity, affine, projective, curved transformation, etc. Definitions of different types of transformation are slightly different in different literature. A demonstration of different linear transformations given by Szeliski [2] is shown in Figure 2.3.

2.5 Transformation


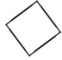
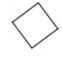


Name	Matrix	Number of d.o.f.	Preserves	Icon
Translation	$\begin{bmatrix} \mathbf{I} \mathbf{t} \end{bmatrix}_{2 \times 3}$	2	Orientation + ...	
Rigid (Euclidean)	$\begin{bmatrix} \mathbf{R} \mathbf{t} \end{bmatrix}_{2 \times 3}$	3	Lengths + ...	
Similarity	$\begin{bmatrix} s\mathbf{R} \mathbf{t} \end{bmatrix}_{2 \times 3}$	4	Angles + ...	
Affine	$\begin{bmatrix} \mathbf{A} \end{bmatrix}_{2 \times 3}$	6	Parallelism + ...	
Projective	$\begin{bmatrix} \tilde{\mathbf{H}} \end{bmatrix}_{3 \times 3}$	8	Straight lines	

Figure 2.3: Basic Set of 2D Linear Transformations [2]

2.5.1 Euclidean Transformation

Considering the case of a 2D image, Euclidean transformation preserves the Euclidean distance between two coordinate locations by allowing translation along each major axis of the image plane and a rotation, three degree of freedom totally, which can be expressed as

$$\mathbf{v}' = \mathbf{R}\mathbf{v} + \mathbf{t}, \quad (2.3)$$

where \mathbf{R} is a matrix representing rotation and \mathbf{t} is a vector that represents translation. Written in the form of equation 2.2:

$$\begin{pmatrix} v'_x \\ v'_y \\ 1 \end{pmatrix} = \begin{pmatrix} \cos(\theta) & -\sin(\theta) & t_x \\ \sin(\theta) & \cos(\theta) & t_y \\ 0 & 0 & 1 \end{pmatrix} \begin{pmatrix} v_x \\ v_y \\ 1 \end{pmatrix}, \quad (2.4)$$

where θ is the rotation angle, and t_x and t_y are the translation elements on each axis.

Extended to 3D space, by allowing six degrees of freedom the transformation can be composed by three translations and three rotations, expressed in the form of a

matrix as follows

$$\begin{pmatrix} v'_x \\ v'_y \\ v'_z \\ 1 \end{pmatrix} = \begin{pmatrix} \mathbf{R} & \mathbf{t} \\ \mathbf{0} & 1 \end{pmatrix} \begin{pmatrix} v_x \\ v_y \\ v_z \\ 1 \end{pmatrix}, \quad (2.5)$$

where \mathbf{t} is the translation vector (t_x, t_y, t_z) , and \mathbf{R} is the rotation matrix. \mathbf{R} is the product of the three matrices expressing three basic rotation transformation [26], considering clockwise as positive and looking in the positive direction along the axis:

$$\mathbf{R}_z = \begin{pmatrix} \cos(\theta) & -\sin(\theta) & 0 \\ \sin(\theta) & \cos(\theta) & 0 \\ 0 & 0 & 1 \end{pmatrix} \quad (2.6)$$

$$\mathbf{R}_y = \begin{pmatrix} \cos(\varphi) & 0 & \sin(\varphi) \\ 0 & 1 & 0 \\ -\sin(\varphi) & 0 & \cos(\varphi) \end{pmatrix} \quad (2.7)$$

$$\mathbf{R}_x = \begin{pmatrix} 1 & 0 & 0 \\ 0 & \cos(\psi) & -\sin(\psi) \\ 0 & \sin(\psi) & \cos(\psi) \end{pmatrix} \quad (2.8)$$

$$\mathbf{R} = \mathbf{R}_z \cdot \mathbf{R}_y \cdot \mathbf{R}_x. \quad (2.9)$$

θ , φ and ψ are the angles rotated along each axis. The rotation \mathbf{R} of image transformation can also be expressed in axis-angle or quaternion specification, which can be found in [26].

2.5.2 Similarity Transformation

Similarity transformation preserves angles and curvatures by allowing rotation, translation and a uniform scaling on all axes. To find the transformation parameters

2.5 Transformation

for 2D images, the following equation pair needs to be solved:

$$\begin{aligned}v'_x &= s(v_x \cos(\theta) - v_y \sin(\theta)) + t_x \\v'_y &= s(v_x \sin(\theta) + v_y \cos(\theta)) + t_y.\end{aligned}\tag{2.10}$$

Four variables, s, θ, t_x, t_y need to be calculated, so the transformation can be determined by two pairs of CPs [27]. Extended to the situation of 3D volumes, considering all degrees of freedom (7 dimensions), 4 pairs of CPs are required to define the transformation. This type of transformation preserves angles and curvatures thus some literature refers to this method as shape-preserving mapping [27]. To sum up, similarity transformation can be expressed as,

$$\mathbf{v}' = s\mathbf{R}\mathbf{v} + \mathbf{t},\tag{2.11}$$

where s is the uniform scaling parameter.

2.5.3 Affine Transformation

Affine transformation preserves the straight lines, straight line parallelism and ratio of distance between points lying on a straight line [102] by loosening the constraint of shape-preserving. It allows shearing transformation along each axis and can be represented in 2D form:

$$\begin{aligned}v'_x &= a_0 + a_1v_x + a_2v_y \\v'_y &= b_0 + b_1v_x + b_2v_y.\end{aligned}\tag{2.12}$$

The shearing transformation in 3D case can be further expressed as

$$\mathbf{R} = \begin{pmatrix} 1 & m & 0 \\ 0 & 1 & 0 \\ 0 & 0 & 1 \end{pmatrix}, \quad (2.13)$$

where m is the shearing parameter, and \mathbf{R} is the rotation matrix describing shearing in one plane only. Shearing transformation can be understood as keeping one dimension unchanged while any of other dimensions is the linear composition of all dimensions.

Affine transformation can be expressed as

$$\begin{pmatrix} v'_x \\ v'_y \\ v'_z \\ 1 \end{pmatrix} = \begin{pmatrix} a_{11} & a_{12} & a_{13} & t_x \\ a_{21} & a_{22} & a_{23} & t_y \\ a_{31} & a_{32} & a_{33} & t_z \\ 0 & 0 & 0 & 1 \end{pmatrix} \begin{pmatrix} v_x \\ v_y \\ v_z \\ 1 \end{pmatrix}, \quad (2.14)$$

where no restriction is defined on any element a_{ij} . The use of homogeneous coordinates does not produce extra power for rigid transformations.

2.5.4 Projective and Perspective Transformation

Affine transformation is a special case of projective transformation which preserves the straightness of lines and planarity of surfaces. Similarly, perspective projection is a special case of projective transformation that projects a 3D object to its 2D projection. Projective transformation generally has the following form [26, 102]

$$\mathbf{v}' = (\mathbf{A}\mathbf{v} + \mathbf{t}) / (p\mathbf{v} + \alpha), \quad (2.15)$$

2.5 Transformation

where A is the projective transformation matrix. This equation can be written in homogeneous coordinates as

$$\begin{pmatrix} u'_1 \\ u'_2 \\ u'_3 \\ u'_4 \end{pmatrix} = \begin{pmatrix} a_{11} & a_{12} & a_{13} & t_x \\ a_{21} & a_{22} & a_{23} & t_y \\ a_{31} & a_{32} & a_{33} & t_z \\ p_1 & p_2 & p_3 & 1 \end{pmatrix} \begin{pmatrix} v_x \\ v_y \\ v_z \\ 1 \end{pmatrix}, \quad (2.16)$$

where u'_i is transformed coordinates before normalization as u'_4 is no longer necessarily equal to 1. The normalized coordinates $v'_i = u'_i / u'_4$.

To solve general projective problems, as well as in special cases, usually a larger number of CPs is required than the minimum requirement to solve equation (2.16). In this case, least-square fit [103] can be used to minimize the sum of squared errors of the transformation [27].

2.5.5 Curved Transformation

Curved transformation violates the straight-line constraint, which means the transformation does not preserve the straightness of lines and allows mapping a straight line to a curve. The simplest expression of this transformation can be a polynomial in the coordinate:

$$\mathbf{v}' = \sum_{i,j,k=0}^{I,J,K} \mathbf{c}_{ijk} v_x^i v_y^j v_z^k \quad (2.17)$$

where \mathbf{c}_{ijk} is a vector of coefficients for i, j, k term in the polynomial expression for \mathbf{v}' . Usually, high order polynomial of transformation with i, j, k value bigger than 2 is rarely used because of spurious oscillation which can warp the floating image in areas away from CPs [26, 27, 104].

2.5.6 More Complex Transformations

Division of rigid and non-rigid registration has not been defined explicitly in all reviewed publications. Usually the term “rigid transformation” refers to Euclidean deformation, while a number of literature include affine transformation when discussing rigid registration. A widely accepted standard of rigid registration is transformation of an object that preserve the length between any two points. In this case, similarity transformation and models with more degrees of freedom should not be classified as rigid. Zagorchev and Goshtasby [105] proposed a comparative study of transformation models for non-rigid image registration. Most literature terms registration problems which have more complex transformations than affine transformation as elastic registration while in some other literature “elastic registration” represents one particular type of method which models the transformation as elastic surface objects with influence of external forces [27, 30, 106].

Global polynomial mapping cannot commonly solve local (non-global) image registration. When the registration results in non-linear deformation, local, or at least locally sensitive, transformation models are superior above global registration methods. For example, spurious oscillations can be reduced or eliminated by employing piecewise polynomials. The image space can be partitioned into a set of rectangles by a set of cut planes perpendicular to each Cartesian axis [26]. Goshtasby [107] introduced a modified least square and weighted mean method to register images locally. A number of local registration methods are based on interpolation techniques [27], for example, Goshtasby’s piecewise linear [108] and cubic mapping methods, and Wiemker et al.’s quintic method [109].

Image transformation becomes more complex than the linear models by violation of constraints on the number of degrees of freedom. In the most extreme case, any object or shape is theoretically possible to be registered to another. Such a transformation model is usually viewed as a “warp field”, or “force field”, of a vector analogous to a distribution of deformation forces. The non-rigid registration problems

can be solved by radial function based, spline based and elastic model based methods, or by modelling the transformation using fluid models or optical flow which are introduced in this section [27].

2.5.7 Mapping by Radial Basis Functions

This type of mapping function is a linear combination of a set of radial basis functions and a low-degree polynomial. In 2D cases it can be modelled as:

$$\begin{aligned} v'_x &= a_0 + a_1 v_x + a_2 v_y + \sum_{i=1}^N c_i g(\mathbf{v}, \mathbf{v}_i) \\ v'_y &= b_0 + b_1 v_x + b_2 v_y + \sum_{i=1}^N d_i g(\mathbf{v}, \mathbf{v}_i), \end{aligned} \quad (2.18)$$

where g is a radial basis function the value of which is dependent on the distance of the point to the set of CPs [27], and \mathbf{v}_i is the coordinate of each CP. Different radial basis functions were proposed in the past decades, for example, multiquadrics [110], Wendland's functions [111], Gaussian, thin-plate splines (TPS) [112, 113, 114] and various other type of spline functions. A comprehensive review of different types of radial basis functions can be found in [115].

In image registration, monotonically decreasing radial basis functions are more appropriate to be used because the CPs tend to have more influence on the points nearby than the farther ones. A typical example of monotonically decreasing functions is the Gaussian basis function as follows,

$$g(\mathbf{v}, \mathbf{v}_i) = \exp \left(-\frac{(v_x - v_{ix})^2 + (v_y - v_{iy})^2}{2\delta_i^2} \right). \quad (2.19)$$

However, based on Franke's experiments [116], monotonically decreasing functions do not lead to better registration results than the ones that monotonically increase when CPs are randomly or uniformly distributed within the image space. As the sum of basis functions quickly approaches zero, the registration errors are large around the

image borders.

Multiquadrics Function Multiquadrics (MQ) function was introduced into medical image processing by Little et al. [110]. Using $g(\mathbf{v}, \mathbf{v}_i)$ as in equation 2.18, for 2D space the multiquadrics radial function is,

$$g(\mathbf{v}, \mathbf{v}_i) = \left[(v_x - v_{ix})^2 + (v_y - v_{iy})^2 + d^2 \right]^{\frac{1}{2}}, \quad (2.20)$$

where d^2 is the smoothing parameter. A smoother surface is created as d^2 increases [105]. Some comparative studies [116] pointed out that MQ can sometimes provide comparable results to TPS interpolation [105].

Spline Based Methods If a mapping function in the form of equation 2.18 is n times polynomial and at least $n - 1$ times continuously differentiable, it is called a spline. In image registration, several types of spline based transformation functions have been found useful for non-rigid registration problems. The one that is most widely used is Thin-plate spline [26, 27, 105, 117].

Harder and Desmarais introduced the mathematical definition of TPS [113]. Goshtasby firstly introduced it to image registration using to describe the deformation within a 2D plane as follows [107],

$$\mathbf{v}' = \mathbf{A}\mathbf{v} + \mathbf{t} + \sum_i^N \mathbf{c}_i r_i^2 \ln r_i^2 \quad (2.21)$$

where $r_i = \|\mathbf{v} - \mathbf{v}_i\|$ is the distance to the i th CP which is placed arbitrarily. Extended to a 3D space, the $r_i^2 \ln r_i^2$ is simply replaced by r_i . The affine component $\mathbf{A}\mathbf{v} + \mathbf{t}$ in equation 2.21 is necessary to ensure a solution exists for any arrangement of points decided by the set of side conditions \mathbf{c}_i . Bookstein firstly applied TPS to medical image registration [118]. The optimal mapping function using TPS should minimize the quadratic variation function of potential energy [27]. TPS can realise either exact or approximated interpolation. By defining a stiffness parameter d^2 and let

2.5 Transformation

$r_i^2 = \|(v_x - v_{ix})^2 + (v_y - v_{iy})^2 + d^2\|$, the shape of the interpolation surface and the registration accuracy can be controlled [105]. As d^2 increases, a smoother surface will be produced, and when $d^2 = 0$ the surface is considered fully rigid. To reduce errors of the points far from the CPs, Rohr et al. [120] added a smooth term when $d^2 = 0$ to control the smoothness, fluctuation, and the distance between the spline surfaces and CPs. When the CPs are irregularly located, approximation methods are preferred.

Because TPS is based on a monotonically increasing logarithmic function which spreads the local deformation over the entire image domain, it can lead to better results for global deformation, but worse results for local transformation [26, 105]. A comprehensive comparison study of TPS based image registration methods was proposed by Rohr [121].

Besides TPS, other kinds of spline functions have also been used as transformation functions in medical image registration, for example, B-spline which is derived from a piecewise polynomial. B-spline functions use three sets of cutting planes, perpendicular to each axis, to partition the 3D space into a set of rectangles. Within each rectangle represented by its cutting plane (i, j, k) of dimensions u_i, v_j, w_k , the piecewise transformation τ is modelled by,

$$\tau = P_{ijk}^{(x)}(x) + P_{ijk}^{(y)}(y) + P_{ijk}^{(z)}(z) \quad (2.22)$$

where (x, y, z) is the coordinate and each $P(\cdot)$ is a univariate polynomial defined over each rectangle [26]. A “cubic spline” is defined when the polynomial has a degree equals to 3.

In the 3D case, a B-spline deformation field is defined as [26]

$$\mathbf{x}' = \sum_{ijk} B_{i-l}(\alpha) B_{j-m}(\beta) B_{k-n}(\gamma) \mathbf{c}_{ijk}, \quad (2.23)$$

where the \mathbf{c}_{ijk} has the same definition in equation 2.18, and the coordinate \mathbf{x} of each point is calculated as $(u_i(l + \alpha), v_j(m - \beta), w(k - \gamma))$ when $0 < \alpha, \beta, \gamma < 1$. The term

presented in the form of $B_q(t)$ in equation 2.23 represents a segmentation of cubic B-spline with $B_q(t) \neq 0$ only when $-1 < t < 2$. Shikin and Plis described some simple methods to determine $B_q(t)$ [122].

Another example of spline based mapping function is elastic body spline (EPS) [123] which is motivated by deformation of elastic bodies influenced by external forces. The external force is modeled by Gaussian-shaped functions centered at the CPs. The EPS is closely related to elastic surface deformation and Wendland functions which are described in the following part of this section. Different from TPS and Wendland functions, local transformations modeled by Gaussian EBS are not radially symmetric [117].

Wendland Function When using MQ and spline based functions, one CP pair will have global influences on the registration results. Although a variety of methods have been proposed to deal with this requirement, for example Goshtasby added local weight functions to reduce this global deformation effect, the CPs are required to be well distributed over the image [107]. Otherwise the radial basis functions will have difficulty to describe the local deformations [111]. Forness et al. summarized the important properties that should be considered when choosing a radial basis function, locality, solvability and efficiency and compared the frequently used radial basis function, such as MQ, inverse MQ, TPS and Gaussian [111]. Based on these discussion they propose use of ψ -function of Wendland [124] as the radial basis for medical image registration. A general form of Wendland function is

$$\psi(r) \begin{cases} \left(1 - \frac{r}{a}\right)_+^4 \left(4\frac{r}{a} + 1\right) & r < a \\ 0 & r > a \end{cases} \quad (2.24)$$

where r is the distance to the CPs and acts as a the support radius which limits the spatial influence induced by particular CP pairs [117]. For image registration, affine transformation parameters should be estimated before deformation registration where the Wendland function is applied because of its invariance to affine transformations

[111, 117].

2.5.8 Non-parametric Registration

Elastic Body Registration The transformation models introduced above are parametric. Some non-parametric transformations relying on physical properties are proposed which provide better flexibility but may be less efficient [117]. The basic idea of non-parametric registration was proposed by Bajcsy and Kovačič [125] for registering brain x-ray images. The feature matching process for the elastic transformations are performed simultaneously while the transformation function is being optimized. One difference between elastic deformation and deformation modeled by an elastic body spline is that the image is viewed as piece of rubber sheet affected by both external forces (which stretch the image) and internal forces (which are defined by stiffness constraints) [27]. External forces can be defined based on similarity measures of intensity, or other geometric features. The energy function derived from the two types of forces should be minimized during the optimization process [117]. With different definitions of the energy function, Kaus and Brock generalized elastic transformation models into three levels based on Hooke's law, including linear elastic, viscoelastic and hyperelastic models [117].

Viscous Fluid To deal with the situation that the image deformation is very localized, the image transformation can be controlled by a viscous fluid model. Kaus and Brock [117] described this model based on Navier-Stokes equation which is used to describe the deformation of a linear elastic object [30],

$$\mu \nabla^2 \mathbf{u} + (\mu + \lambda) \nabla (\nabla \cdot \mathbf{u}) + \mathbf{F} \cdot (\mathbf{x}, \mathbf{u}) = 0, \quad (2.25)$$

where the vector \mathbf{u} represent the displacement, \mathbf{F} is the force on the object at location \mathbf{x} that depends on the deformation \mathbf{u} , and μ and λ are Lames coefficients which can be obtained by solving the equation pair of Young's Modulus and Poisson's ratio [117].

∇ is the vector differential operator. In some publications, \mathbf{u} , \mathbf{F} and \mathbf{x} are written as \vec{u} , \vec{F} and \vec{x} to emphasize that they represent displacement fields. When used to describe a viscous fluid, $\mu = 1$ and $\lambda = 0$. The optimal transformation can be found by modifying the force fields \mathbf{F} and \mathbf{x} [117]. Viscous fluid has been widely used in medical image registration. A main disadvantage of this type of method is the blurring it introduces to the registered image. Bro-Nielsen and Gramkow [126] proposed a fast fluid registration and a comparison of three fluid registration methods based on the computational cost which can be found in [127].

Partial Differential Equation Kaus and Brock generalised the elastic and fluid transformation problem using the partial differential equation (PDE) [117]. Thirion proposed another transformation which models the features in the image as membranes to set geometric constraints [128]. This method is called diffusion based registration, or Demon's algorithm, and the transformation field is defined as [117],

$$\mathbf{u} = \frac{(\mathbf{m} - \mathbf{s}) \nabla \mathbf{s}}{\|\nabla \mathbf{s}\|^2 + \|\mathbf{m} - \mathbf{s}\|^2} = \frac{\mathbf{F} \nabla \mathbf{s}}{\|\nabla \mathbf{s}\|^2 + \mathbf{F}^2} \quad (2.26)$$

where \mathbf{s} is the gradient of the image, \mathbf{u} is displacement, and $\mathbf{F} = (\mathbf{m} - \mathbf{s})$ is the external force. Kaus and Brock [117] describe two methods, finite element and finite difference, to solve the PDE based registration.

2.5.9 Optical Flow based Methods and Other Methods

In image registration, optical flow represent a popular type of method used for modelling deformation of medical images, especially for intra-modality registration tasks [128]. The optical flow approach was proposed to recover the relative motion field between frames of a video by directly measuring intensity differences of local data [129]. Popular optical flow methods include Lucas-Kanade [130], Horn-Schunck [131], Buxton [132], Black-Jepson [133], etc.. A comparison of 9 optical flow methods was given in Barron et al. [134]. Various optical flow methods have been applied to

2.5 Transformation

medical image registration [27, 135]. But instead of tracking the object across video frames, optical flow is used to model the deformation of the corresponded objects between the reference and floating images. Cooper and Ritter [136] introduced optical flow to validate registration results of retina images. Pock et al. [137] used TV-L1 optical flow to register CT lung data and inter-subject brain MR images. Urschler et al. [138] use optical flow with two different regularization standards to register CT thorax images. Comprehensive reviews of this type of method can be found in several review papers [46, 131, 134, 139]

Beside the methods discussed above, other types of transformation estimation methods also appeared. For example, Glocker et al. [140] proposed a method to formulate the registration problems using discrete Markov random field (MRF) and linear programming. Vemuri et al. [141] introduced a medical image registration method which is applicable to atlas-based segmentation by modelling the transformation as motions along model of level sets.

2.5.10 Summary

Transformation estimation has always been one of the most challenging topics in image registration. The transformation models vary from the simplest similarity transformation to complex piecewise non-rigid transformation, either globally or locally. Some methods model the image deformation exactly while others are just approximations. Zagorchev and Goshtasby [105] evaluated the computational complexity of different transformation methods for registering 2D $n \times n$ images with N CPs. More complicated transformation models give more degrees of freedom of image deformation, but due to the increments of adjustable parameters they are more computationally costly. Furthermore, deformation which has too much “freedom” to deform the image may change the pathological information contained in the image, and thus mislead the follow up clinical assessment works. So when designing an image registration algorithm to align a particular clinical imaged object,

the transformation model with the least number of effective degrees of freedom should be used. For example, for our ongoing clinical research projects using brain and abdominal aorta images where the imaged objects are soft-tissue structures but didn't demonstrated non-linear deformations, the linear transformation model with 6 degrees of freedom is preferred for efficient registration. This is also applicable to the ECG-gated cardiac data where the heart is imaged approximately at the same point of the cardiac cycle.

2.6 Similarity Measurements

Optimal transformation or deformation of the images, which is treated as the output of registration algorithms, is determined by optimization of certain similarity, or distance measures [22]. These measures can be obtained either directly from intensity values or indirectly from some abstract features extracted from image contrast. In the ideal situation, the output transformation should lead to the maximum value of a similarity measure, a minimum of a distance measure, when the images are perfectly aligned [25]. Damas et al. [25] model the similarity measure as a function $F(\cdot)$ of reference image \mathbf{I}_r , floating image \mathbf{I}_f and transformation function $T(\cdot)$:

$$F(\mathbf{I}_r, \mathbf{I}_f, T) = \psi(T(\mathbf{I}_f), \mathbf{I}_r), \quad (2.27)$$

where $\psi(\cdot, \cdot)$ is the mathematical definition of similarity function based on voxel values, such as sum of square difference (SSD), cross-correlation (CC), mutual information (MI), etc.. Some publications classified different similarity measures as geometric based approaches, which explicitly model the anatomical elements in the images, and intensity approaches, which match intensity patterns in each image using mathematical or statistical criteria [20]. Zitová and Flusser [27] reviewed several types of similarity measures and divided them into correlation-like methods, Fourier methods and mutual information methods. Different similarity measures are associated with different features and transformation models, and cooperate with different optimization approaches.

Popular similarity measures that appear frequently in the reviewed literature include SSD, sum of absolute differences (SAD), maximum of absolute difference (MAD), normalized cross correlation (NCC), CC, gradient correlation (GC), mutual information (MI), normalized mutual information (NMI), correlation ratio (CR), pattern intensity (PI), gradient difference (GD), etc. Some of these measure

Table 2.2: Commonly Used Similarity Measures [20, 21, 22, 23, 24, 25].

Measure	Type	Usage	Formula
Sum of square differences (SSD)	Distance	Intra-modality	$D_{SSD}(I_r, I_f) = \sum_{\mathbf{v} \in \Omega_{rf}} (I_r(\mathbf{v}) - I_f(\mathbf{v}))^2$
Sum of absolute differences (SAD)	Distance	Intra-modality	$D_{SAD}(I_r, I_f) = \sum_{\mathbf{v} \in \Omega_{rf}} I_r(\mathbf{v}) - I_f(\mathbf{v}) $
Maximum of absolute differences (MAD)	Distance	Intra-modality	$D_{MAD}(I_r, I_f) = \max_{\mathbf{v} \in \Omega_{rf}} I_r(\mathbf{v}) - I_f(\mathbf{v}) $
Normalized cross correlation (NCC)	Similarity	Intra-modality	$S_{NCC}(I_r, I_f) = \sum_{\mathbf{v} \in \Omega_{rf}} \frac{I_r(\mathbf{v})I_f(\mathbf{v})}{\sqrt{(E[I_r(\mathbf{v})^2]E[I_f(\mathbf{v})^2])}}$
Correlation coefficients (CC)	Similarity	Intra-modality	$S_{CC}(I_r, I_f) = \frac{(I_r(\mathbf{v}) - E(I_r(\mathbf{v}))) (I_f(\mathbf{v}) - E(I_f(\mathbf{v})))}{\sum_{\mathbf{v} \in \Omega_{rf}} \frac{\sigma(I_r) \sigma(I_f)}{\sigma(I_r) \sigma(I_f)}}$
Gradient correlation (GC)	Similarity	Intra-modality	$S_{GC}(I_r, I_f) = \frac{1}{d} \sum_{i=1}^d S_{CC} \left(\frac{\partial I_r}{\partial v_i}, \frac{\partial I_f}{\partial v_i} \right)$
Mutual information (MI)	Similarity	Inter-modality	$S_{MI}(I_r, I_f) = \sum_i \sum_j P_{r,f}(i, j) \log \frac{P_{r,f}(i, j)}{P_r(i) P_f(j)}$
Normalized mutual information (NMI)	Similarity	Inter-modality	$S_{NMI}(I_r, I_f) = \frac{2S_{MI}(I_r, I_f)}{H(I_r) + H(I_f)}$
Correlation ratio (CR)	Similarity	Inter-modality	$S_{CR}(I_r, I_f) = \frac{\sigma^2(E[I_f/I_r])}{\sigma^2(I_r)}$

2.6 Similarity Measurements

the similarity directly while others measure distance between the images. The mathematical definitions of these measures and their suitability for specific types of registration problems are shown in table 2.2. In table 2.2, I_r and I_f represent reference and floating images as functions of input voxel coordinates. D and S are the distance and similarity measures respectively, and \mathbf{v} denotes a coordinate in the image. P is the probability of voxel values which can be reflected by image histograms. $\omega_{r,f}$ is the overlap domain of fields of view ω_r and ω_f between the two images.

2.6.1 Distance Measures

SSD, SAD and MAD are typical distance measures utilized in image registration. These measures assume that the intensity of the reference and floating images only differs by Gaussian noise. Optimal transformations lead to minimization of these three measures, and large values indicate poor alignments. SSD is very sensitive to a small portion of pixels that present larger differences than other pixels. SAD and MAD are designed to reduce this impact. Ulysses [22] reported comparison results of these three simplest distance measures applied to a MR brain image registration task. They were evaluated against mean square error (MSE), CC and peak signal to noise ratio (PSNR) and demonstrated that SSD and MAD give similar results in this application [22]. Measures like SAD and MAD can be generalized in the form of robust error metrics (SRD) as follows,

$$D_{SRD}(I_r, I_f) = \sum_{\mathbf{v} \in \Omega_{rf}} \rho(I_r(\mathbf{v}) - I_f(\mathbf{v})), \quad (2.28)$$

where $\rho(\cdot)$ is a robust function that is designed for enhancing the robustness to outliers [2].

To further enhance the robustness of the distance measures, and to deal with the points that lie outside the original image boundaries, a spatially varied weight can be

added to the formulae, which leads to a weighted SSD function:

$$D_{WSSD}(I_r, I_f) = \sum_{\mathbf{v} \in \Omega_{rf}} \omega_r \omega_f (I_r(\mathbf{v}) - I_f(\mathbf{v}))^2, \quad (2.29)$$

where ω_r and ω_f are the weighting function of the reference and floating images respectively. Both of them are 0 outside the spatial scope of the images [2]. Approaches to determine the weighting functions can be found in [2].

2.6.2 Correlation Measures

Distance measures like SSD assume that the intensities of the reference and floating images should be deferred only by Gaussian noise, which is seldom true when registering multi-modality and multi-contrast images. Cross correlation slightly violates this assumption by allowing linear relation of intensity values in the images [20]. The simplest definition of cross-correlation is just a product of intensity values of the two images:

$$S_C(I_r, I_f) = \sum_{\mathbf{v} \in \Omega_{rf}} I_r(\mathbf{v}) I_f(\mathbf{v}). \quad (2.30)$$

CC should be maximized by optimal transformation, and I_r and I_f can also represent be sub-images. To reduce the sensitivity to variance of image intensity values, a more popular measure called normalized cross correlation, or NCC, is used [20], as shown in Table 2.2. NCC scores are guaranteed to be in the range $[-1, 1]$.

Inspired by NCC, another measure called sequential similarity detection algorithms (SSDA) was proposed by Barnea and Silverman [142]. A threshold criterion is added to accumulated SAD, which returns faster but less accurate results. To speed up the searching process in a problem space with a lot of local optima, hierarchical motion estimations can be used based on different types of multi-resolution techniques which build up a “pyramid” of different resolutions of the data. This enables a coarse-to-fine estimation of image transformations [2].

Two main drawbacks of correlation based similarity measures are high

2.6 Similarity Measurements

computational complexity and flat local maxima [27]. The computational load can be reduced by calculating CC in Fourier domain. The signal transformed to the Fourier domain has the same information as the original spatial signal. However, a spatial convolution of two images can be more efficiently achieved by multiplication in the Fourier domain [2]. Defining the formulae of CC as shown by equation 2.30, the Fourier transformation \mathcal{F} of CC is

$$\mathcal{F}(S_{cc}) = \mathcal{F}\left(\sum_{\Omega_{rf}} I_r(\mathbf{v}) I_f(\mathbf{v})\right) = \mathcal{F}(I_r \otimes I_f) = I_r(\omega) I_f^*(\omega), \quad (2.31)$$

where \otimes represent convolution, $I_f^*(\omega)$ is the complex conjugate of the floating image contrast function $I_f(\omega)$, and ω is a conjugate variable defined in the frequency domain. Similarly, correspondence of SSD in Fourier domain is also used for reduction of the computational complexity [2].

When the overlapping area of the two images is relatively small compared to the spatial range of images, CC does need to be calculated over the whole image domain. In this case, a windowing function which is similar to the weighting function used to calculated weighted SSD can be applied. The windowing functions are zero outside spatial domains of images.

Another similarity measure derived from CC in the Fourier domain is phase correlation (PC) [143]. It is calculated with a frequency normalisation process as follows,

$$\mathcal{F}(S_{PC}(I_r, I_f)) = \frac{I_r(\omega) I_f^*(\omega)}{\|I_r(\omega)\| \|I_f(\omega)\|}, \quad (2.32)$$

where $\|I_r(\omega)\|$ and $\|I_f(\omega)\|$ are the signal magnitudes of both images within the Fourier domain [143]. PC promises effective performance if the images are only affected by noise limited in a narrow frequency band. However, it is not able to deal with images which have a very low signal-to-noise ratio, or SNR [2]. In this case, the gradient cross correlation (GCC) can be used as a promising alternative [144].

Correlation-based measures are often compared to the entropy-based measures,

such as MI. Entropy correlation coefficient (ECC) was proposed by Maes et al. [145] to mix these two types of measures which increases the alignment accuracy but requires extra computational cost.

Correlation Ratio Correlation-based measures were once only applicable to intra-modality registration problems because of assumptions about a linear relationship of voxel intensities of the two images [117]. Recently, however, special interest has been paid to a measure called correlation ratio, or CR [146] for inter-modality applications [27]. Roche et al. [146] proposed and compared CR with other kinds of inter-modality similarity measures. CR only requires a functional relationship between voxels. The simplest form of CR is shown in Table 2.2. CR is inspired by the orthogonality principle of the Kalman filter, based on which Roche et al. [146] gave an alternative formula:

$$S_{CR} = \eta(I_f/I_r) = 1 - \frac{\sigma^2(I_f - E(I_f/I_r))}{\sigma^2(I_f)}, \quad (2.33)$$

where σ^2 is the variance of the image. One advantage of CR is lower computational complexity compared to other correlation-based measures. Classical mutual information measures have $O(n_r, n_f)$ complexity and Roche et al.'s implementation of RC [146] has only $O(n_r)$ complexity. However, Collignon et al. [57] pointed out that CR may lead to less accurate registrations than MI.

Correlation Methods with Function Intensity Limit Using the marginal probability distribution, two criteria similar to CR that can also work with a functional intensity relationship are Woods' criterion and weighted neighbour likelihood [146]. Woods criterion $W(I_f/I_r)$ [147] express the same basic idea as CR, but instead of using the sum of the variance, it sums normalised standard deviation (STD) [146]:

$$W(I_f/I_r) = \frac{1}{N} \sum_i N_i \frac{\sigma_i}{m_i}, \quad (2.34)$$

2.6 Similarity Measurements

where N is the number of voxels in the overlapped area, N_i , m_i and σ_i are the number of voxels, mean and STD in an area Ω_i which are defined within the domain $\{\mathbf{v} \in \Omega_i, I_r(\mathbf{v}) = i\}$. Viola and Wells proposed weighted neighbour likelihood criterion using a weighted likelihood approximation and log-likelihood estimation [148] as follows,

$$L(I_f/I_r) = -k\sigma^2 [I_f - E(I_f/\hat{I}_r)], \quad (2.35)$$

where \hat{I}_r is a random variable whose probability density distribution (PDF) is a Parzen window estimation of I_r . Because CR added the division term $\sigma^2(I_f)$, it performs better than the neighbourhood weighing measures in registration problems which require to prevent image contrast disconnections [146].

Roche et al. [146] compares CR, Wood's criterion and weighted neighbour likelihood with MI by registering a range of multi-modality and multi-parametric brain data. This study shows that CR gives better results when registering T1W MR images to T2W images, and registering PET images to T1W MR images compared to other three measures. These methods also lead to performances comparable to MI for CT-MR registration. The flat local maxima of correlation-based measures can be sharpened by using the gradient features extracted from the image[27]. Examples of this type of method are edge-based correlation, and its extension called vector-based correlation proposed by Anuta [149].

2.6.3 Mutual Information based Methods

MI based measures were derived from the definition of entropy in information theory. Over 20 definitions of entropy were proposed over last few decades. The most widely used one is Shannon's definition as follows,

$$H = \sum_i p_i \log \frac{1}{p_i}, \quad (2.36)$$

where p_i is probability of a symbol occurring in a message and $H(\cdot)$ is Shannon's entropy function which measure the amount of definition (or uncertainty). For an image registration problem, the joint entropy of the reference and floating images can be used as a similarity measure, which can be written as,

$$H = - \sum_i P_i(\mathbf{I}_r, \mathbf{I}_f) \log P_i(\mathbf{I}_r, \mathbf{I}_f), \quad (2.37)$$

where $P_i(\mathbf{I}_r, \mathbf{I}_f)$ is the joint probability of intensity levels of images represented by matrices, \mathbf{I}_r and \mathbf{I}_f . The joint probability can be calculated by normalizing the joint histogram [26]. When the optimal registration result is found, the joint histogram should display tight clusters. This is also true when using the entropy of the difference image calculated between the reference and floating images. The entropy of the difference image should increase as the alignment becomes worse [20]. Buzug and Weese [150] proposed an iterative image registration method which minimizes entropy of the difference image. Generally speaking, joint entropy and entropy of difference image is dependent on voxel intensity [20]. This means these approaches become less reliable when dealing with images contain less anatomical content, such as background in medical images. In this case, minimized joint entropy can lead to complete misalignment [26].

MI was firstly investigated and proposed by Collignon et al. [57], Maes et al. [145] and Viola and Wells [148] to overcome this problem by considering the information contributed by each image. Optimal registration will maximize MI by seeking the alignment that has the lowest joint entropy but maximized marginal entropy. The MI is calculated by,

$$S_{MI}(I_r, I_f) = \sum_{i,j} P(I_r(i), I_f(j)) \log \frac{P(I_r(i), I_f(j))}{P(I_r(i))P(I_f(j))} = H(I_r) + H(I_f) - H(I_r, I_f). \quad (2.38)$$

Various mathematical descriptions of MI have been proposed depending on the definition of entropy. A comprehensive survey of similarity measures based on

2.6 Similarity Measurements

information theory, and their corresponding properties, are reviewed by Pluim et al. [151]. Generally, MI can be explained as how well an image can explain the other, or as the amount of information one image contains about the other image [20]. Pluim et al. [151] proposed an expression based on the conditional entropy, which is defined by,

$$H(I_f/I_r) = -\sum_i P(I_f(i), I_r(i)) \log P(I_f(i)/I_r(i)) = H(I_r, I_f) - H(I_r). \quad (2.39)$$

Then the expression of MI can be rewritten as:

$$S_{MI}(I_r, I_f) = H(I_r) - H(I_f/I_r) = H(I_f) - H(I_r/I_f). \quad (2.40)$$

MI only requires a functional intensity relationship between voxels in both image which makes it widely applied to inter-modality registration. However, the size of the overlapped spatial domain of the two images has a profound influence on performances of registration using MI. When the two images share relatively small amounts of image contents, MI may return the wrong direction of optimization [151]. To solve this problem, Studholme et al. [152] proposed a normalised mutual information (NMI) which is less sensitive to changes of the overlapping region. The NMI is calculated as follows,

$$S_{NMI}(I_r, I_f) = \frac{H(I_r) + H(I_f)}{H(I_r, I_f)}. \quad (2.41)$$

NMI has been proved to be able to distinctly improve the performance of MR-CT and MR-PET registration results [151]. In most cases, NMI has shown equivalent performances to MI, for example, 3D MR series image registration [153]. Different formulae of NMI were proposed by Maes et al. as follows,

$$S_{NMI1}(I_r, I_f) = \frac{2S_{MI}}{H(I_r) + H(I_f)}, \quad (2.42)$$

$$S_{NMI2}(I_r, I_f) = H(I_r, I_f) - S_{MI}(I_r, I_f). \quad (2.43)$$

Entropy correlation coefficient (ECC) was suggested as an alternative of NMI by Maes et al. [145] and Collignon et al. [57]. Another alternative of NMI, proposed by Loeckx et al. [154], is called conditional mutual information (CMI) which displayed better robustness to worse imaging qualities [154]. CMI is calculated between reference and floating images with a certain spatial distribution X ,

$$\begin{aligned} S_{CMI}(I_r, I_f|X) &= H(I_r|X) + H(I_f|X) - H(I_r, I_f|X) \\ &= \sum_{x \in X} P(X) \sum_{x_r \in I_r} \sum_{x_f \in I_f} P(I_r, I_f|X) \ln \left(\frac{P(I_r, I_f|X)}{P(I_r|X)P(I_f|X)} \right). \end{aligned} \quad (2.44)$$

CMI was compared to standard MI and correlation-based measures. It overcame the performance of MI in several experiments [154], including registration of CT-MR spine images.

MI-base measures are the most intensively studied measures in presently proposed method image registration algorithms. Several advanced measures have been invented by extending the calculation of MI using joint histogram, for example, Jensen-Shanon divergence [155], Kullback-Leibler divergence [156], joint intensity scatter plot [157], weighted mutual information [158] and Bhattacharyya distance [159]. The common idea behind these methods is to assign to each element in the joint histogram a weight learned from a well aligned pair of images. Compared to MI, these measures make the registration more robust to the presented noise and artefacts, but introduce extra computation loads and may require manually aligned data before they are computed.

2.6.4 Other Similarity Measures

Other similarity measures related to MI are also used in inter-modality registration problems [26]. Woods et al. proposed an alternative similarity measure for inter-modality registration called ratio-image uniformity (RIU), also known as variation of

2.6 Similarity Measurements

intensity ratios (VIR) [160]. It was originally applied to PET-MR image registration. To calculate RIU, a ratio image \mathbf{R} is calculated by dividing intensity values in the reference image with corresponding voxels in the transformed floating image. The uniformity of \mathbf{R} is determined by its normalized standard deviation. Minimization of standard deviation, which represents maximization of uniformity, is used to determine the optimal transformation [26]. This measure is non-symmetric, which means reversing the role of reference and floating images will lead to a different registration algorithm.

RIU was soon developed further by Woods et al. for MR-PET registration and named partitioned intensity uniformity (PIU) [147]. With an assumption that all voxels have similar intensity values for the same type of tissue. PIU divides the intensity histogram of images into several intensity partitions. The registration algorithm using PIU searches for the optimal transformation by minimizing the spread of the histogram [147].

Weese et al. [161] proposed a similarity measure, called pattern intensity (PI), based on difference image that is robust to large intensity differences between the reference and floating images. It assumes that a pixel belongs to a structure if it has a significantly different intensity value from a neighbourhood defined by a constant. The regional nature of PI is able to reduce the effect of differences between the images which are on a larger scale than the radius of neighbourhood [21].

2.6.5 Summary

Various criteria used to measure the difference or similarity are reviewed in this section. Choice of difference/similarity measure profoundly influence the speed and accuracy of image registration algorithms. A more effective difference/similarity measure introduces less local optima in the problem space, which leads to more efficient optimization processes. Distance measures generally have smaller computational complexities than correlation- or entropy- based similarity measures,

but they are difficult to apply to multi-modality and multi-parametric problems. MI has been the most popular similarity measure due to its robustness to contrast differences and relatively low computational cost when dealing with multi-modality and multi-parametric data. However, no evidence has been found to prove that MI has a better performance than distance measures when used for intra-modality registration. Several newer similarity measures have been proposed by extending the calculation of MI for more accurate alignment and better robustness to noise and artefacts. However, these approaches lead to slower registration performance, and none of them have been widely validated by different experiments.

2.7 Optimization

As pointed out by many published articles, image registration can be treated as an energy maximization or cost minimization problem. The purpose of optimization processes in image registration is to find the optimal transformation by maximizing the similarity or minimizing the distance measures [27]. However, unlike the transformation models and similarity measures discussed above, optimization methods used in all of the reviewed publications are not proposed specifically for registration purposes. In other words, they are general-purpose methods that can be applied to a much wider range of problems. So most of these methods will not be reviewed in this chapter. Instead, details of the optimization strategies used in the registration algorithms developed for our clinical research projects can be found in later chapters.

Most optimization methods iteratively refine the transformation by evaluating the similarity measure in each iteration. In most publications [20, 24, 26, 27], optimization methods are classified as gradient-dependent and gradient-independent methods based on whether the gradient information of the searching space is required, or local and global optimizations. Gradient-based methods are more involved in registration implementations because they can often be calculated efficiently [26]. Other than exhaustive searching which cannot be achieved due to the large, even infinite, searching spaces of image registration problems, nearly no method is claimed as a completely global solution [27]. This leads to a common problem in registration that the desired optima are often global while many algorithms tend to converge to a local optimum. In practice, especially for multi-modality and multi-parametric registrations, local optima are often inevitable in the problem spaces no matter which similarity/difference measure is used. Most methods search for the global optimal value of similarity/difference measures with an initial estimated transformation in a limited field of view [26]. The local optimization methods

have faster convergence speed but the registration results are highly dependent on choices of initial transformation parameters. The global methods are more robust to initializations and presence of local optima, but have slower convergence speed. Some methods mix these two optimization strategies to balance the trade-off between robustness and efficiency [24]. Sometimes a regularization, or penalty term is added for separating data from transformation model, especially for non-rigid registration problems. Some literature termed this type of algorithm as energy-minimization [27].

Commonly used general purpose optimization algorithms that have been applied to image registration include iterative closest point (ICP), Powell's method [162], Simplex algorithm [163], Soblex [164], multi-dimensional scaling (MDS) [165], gradient descent [162], Quasi-Newton method [162], Levenburg-Marquardt method [162], simulated annealing [162], DIRECT [166], genetic algorithm [167], and swarm intelligence based methods [168]. Comprehensive reviews and comparison studies of optimization methods have been proposed by Press and Teukolsky [169], and Sonka and Fitzpatrick [26]. Some reviewed optimization methods and their classifications are listed in Table 2.3.

Table 2.3: *Some Optimization methods reviewed with its classification [24, 26, 27]*

Optimization Method		Classification
Powell [162]	Gradient-independent	Local
Simplex [163]	Gradient-independent	Local
Soblex [164]	Gradient-independent	Combined
MDS [165]	Gradient-independent	Local
Gradient descent [162]	Gradient-dependent	Local
Quasi-Newton [162]	Gradient-dependent	Local
Levenberg-Marquardt [162]	Gradient-dependent	Local
Simulated annealing [162]	Gradient-independent	Combined
DIRECT [166]	Gradient-independent	Global
Genetic [167]	Gradient-independent	Global
Chamfer matching [26]	Gradient-independent	Global
ICP [170]	Gradient-independent	Global
Swarm intelligence [168]	Gradient-independent	Global

2.8 Other Implementation Issues

Directly registering images with high resolutions can make the algorithms computationally expensive. Hierarchical methods using different types of image pyramids are often used for this purpose from coarse to fine level. Hierarchical schemes can also reduce the computational cost due to the large image size. Two of the most common types of pyramid built up in hierarchical registration schemes are Gaussian-Laplace pyramid and Wavelet pyramid [27]. Combined with CC, methods based on the summing pyramid, median pyramid and average pyramid were proposed [27]. However, the searching spaces of registration problems often have small and multiple optima, and global optima can disappear from the problem space of low resolution versions of images used in the multi-resolution registration frameworks [26]. Thus number of levels of the image pyramid should be carefully selected.

In recent years, wavelet based multi-resolution methods have received increasing attention because of the interesting nature of different type of wavelet basis. Most methods decompose the images into sets of coarse and fine coefficients on different resolution levels. A detailed description of common wavelet basis and their applications to image registration has been reviewed by Zitová and Flusser [27].

Calculation of similarity measures often requires interpolation of the transformed image [26]. Interpolation methods are associated to different transformation models discussed in section 2.5. Commonly used interpolation methods include nearest neighbour, linear interpolation, cubic interpolation, quadratic splines, B-splines, Gaussian and thin-plate splines function. The nearest neighbour interpolation has the smallest computational cost, but it cannot differentiate translations less than 1 voxel. Thus it has been used to initially align low resolution versions of data in the multi-resolution registration methods. Spline based methods lead to more accurate interpolation and make the searching space smoother, but with much higher

2.8 Other Implementation Issues

computational complexity. Thus most registration methods use linear or cubic interpolation to achieve sub-voxel accuracy.

2.9 Discussion and Conclusion

Multi-modality and multi-parametric registrations are challenging due to the differences of imaging mechanisms and image contrasts discussed above. Most of the reviewed methods evaluated the performances of registration using brain images because of availability of multiple landmarks which are used to calculate target registration errors (TRE). For rigid registration, the performance of registration can also be measured by summarizing the output transformation to a single translation distance and a rotational angle along a single rotational axis. Registering images that have very different slice orientations and fields of view is possible, for example, registering coronal CT images with axial MR images[26]. In this case, the final transformation can be very large, and the overlapping region of the reference and the optimally transformed floating image can be relatively small [26]. A comparison of four CT-MR co-registration techniques, which are proposed to guide radiotherapy treatment planning without fiducial markers, have been conducted by Dean et al. [58].

In this chapter, I reviewed the basic components of image registration methods that can be used to build up my own image registration framework. The ongoing clinical research projects in CRIC, UoE require registration of CT-MR multi-modality, and MR-MR multi-parametric image pairs. All of these types of medical images are involved in registration methods reviewed in this section. Descriptions of modalities and imaging parameters of these data can be found in chapter 3, 4 and 5. This review raised several considerations for the development of my own novel registration algorithms.

As discussed in section 2.5, the imaged objects in our clinical research projects are either naturally rigid, such as abdominal aorta and brain, or the images are acquired with special imaging technique, such as the ECG-gated cardiac data. Thus when no obviously non-linear deformations are observed, a rigid transformation model with 6 degrees of freedom tends to be used in my registration methods to preserve important

2.9 Discussion and Conclusion

pathological information for supervision purposes. Due to its widely verified robustness, MI should be the first choice of the similarity measure as the imaged objects are presented in multi-modality data, and MR data acquired with different imaging parameters, for example before and after uptake of a contrast agent. This also leads to another problem that the softer tissue or fluids around the imaged objects can have very different contrasts and suffer from significant deformations. Furthermore, MR data suffers from various noise and artefacts, for example, artefacts caused by patient motion in neonatal imaging. These contrast changes or noise can introduce large amounts of local optima in the searching space of the optimization process. To solve this problem, a preprocessing step should be added to the registration method to remove the noise and artefacts while a robust global optimization algorithm should be used. To further speed up the registration process, the alignments of the imaged objects can be achieved by only registering the image contents included in a region-of-interest and boosted by a multi-resolution strategy. Last but not least, the performance of a new registration method should be validated against either manual alignments performed by human operators or a widely recognised “gold standard”. In the following chapters of this thesis, registration methods based on these considerations will be introduced.

3D Inter-modality Registration of Axial Aortic Images

ABSTRACT

Based on the literature review in the previous chapter, a simple semi-automatic registration method was developed, based on the common “preprocessing-similarity measure-transform-optimization” framework outlined in the last chapter. This registration framework was first used to solve the alignment problem of CT-MR multi-modality data and MR-MR multi-parametric data acquired in an ongoing clinical trial. The method uses semi-automatically generated regions of interest and a rigid transformation model. These results have been published as a conference abstract and presented at the International Society for Magnetic Resonance in Medicine (ISMRM) annual scientific meeting 2014, Milan, Italy. A patent (20150131880) was published in May 2015.

3.1 Introduction

The main motivation for producing a novel medical image analysis tool in this chapter was to assist ongoing clinical research trials taking place in the Clinical Research Imaging Centre (CRIC), University of Edinburgh (UoE). The first practical image registration framework was designed based on a clinical trial (MRI for Abdominal Aortic Aneurysms to predict Rupture or Surgery (*MA³RS*), Medical Research Council: Efficacy and Mechanism Evaluation, 11/20/03, 2012-2016.) investigating inflammatory markers for growth and rupture of abdominal aortic aneurysm (AAA) [171]. AAA is often defined as an aneurysmal abdominal aortic diameter that is ≥ 3.0 cm, which usually is more than 2 standard deviations above the mean diameter for both men and women [172]. This project involves multi-parametric and multi-contrast MR imaging using a novel contrast agent for magnetic resonance (MR) imaging, as well as X-ray computed tomography (CT) angiography. A pilot study for this project showed that the proposed novel method of targeted imaging of inflammation with MR imaging (MRI) may have merit in development as a tool to help to more accurately and reliably predict the risk of aneurysm growth in a cohort of patients with AAA than the current clinical surveillance performed using serial ultrasound measurements of aneurysm size [3]. However, the proposed method requires co-registration of images acquired on different days, and also using different imaging modalities [171]. In the pilot study, this image registration was performed manually for a relatively small patient cohort (29 subjects). Although the pilot study showed merit in the novel clinical application in AAA, the next step was to perform a larger clinical trial, for which manual registration of data would be exceptionally time-consuming and user-dependent. Based on the clinical requirements of this expanded study, a robust semi-automated algorithm was first developed to rigidly register medical images of tubular structures, especially aorta. To register large numbers of images, as well as for evaluation purposes, the algorithm was integrated into a graphic user interface (GUI)

that can be easily operated by users with different backgrounds, such as scientists and clinicians.

The reliability of the algorithm, registering both MR-CT multi-modality, and MR-MR multi-parametric images, was evaluated using data collected from over 300 patients by comparison between the automatic registration results and manual alignments performed by human operators. The validated software was then applied to other clinical trials which are discussed in later chapters.

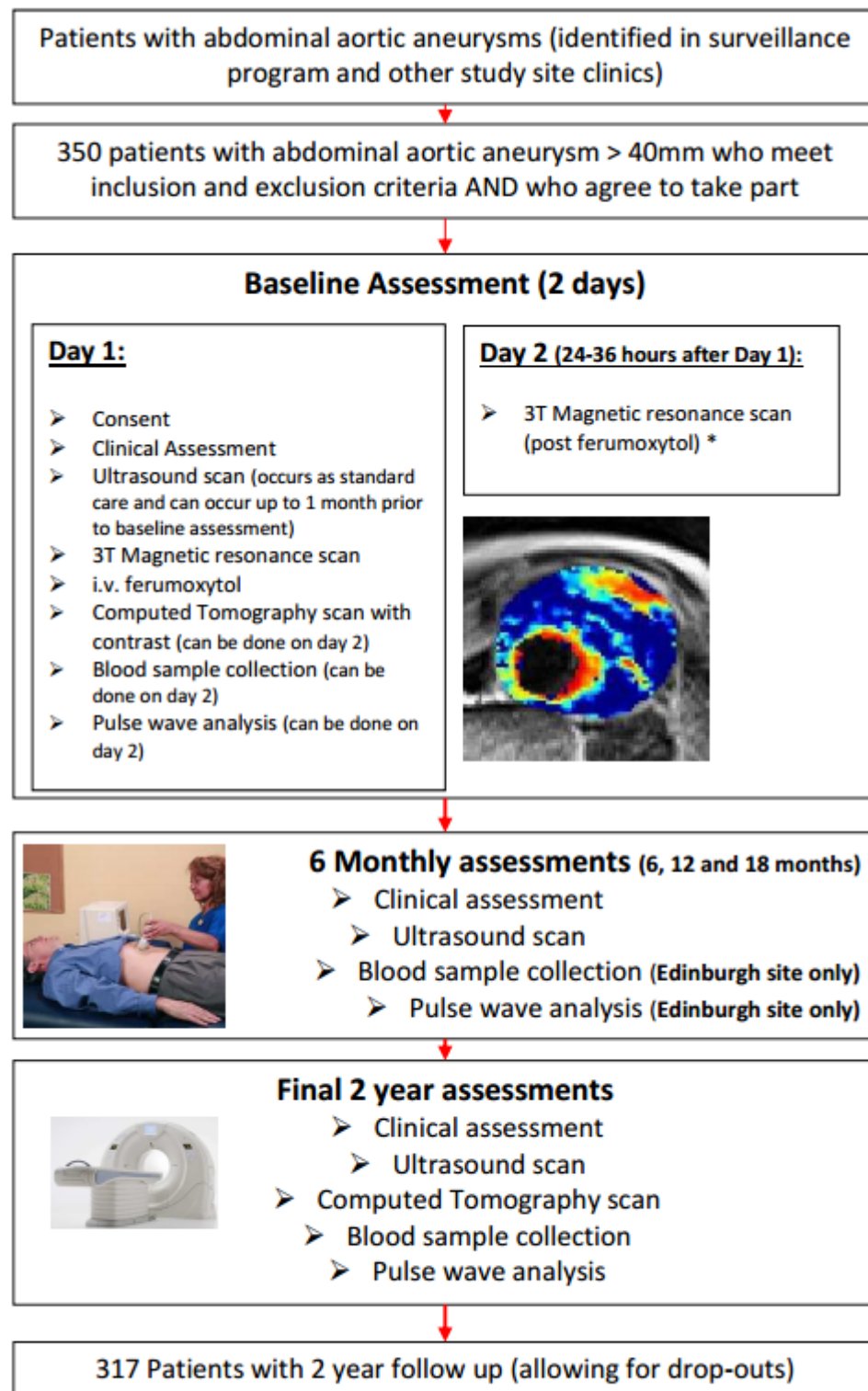
This chapter describes the simple semi-automated registration validated by our clinical trial focused on AAA imaging which provides the building blocks of our later work on developing new registration methods. I first briefly introduce relevant medical background of the clinical trial in section 3.2. Section 3.3 and section 3.4 describe my registration methodology. The performed registrations and evaluation results can be found in section 3.5 and section 3.6. Development of this registration software, as well as some extended works in the future, are summarized in section 3.7.

3.2 The MA³RS Clinical Trial

3.2.1 Clinical Background

AAA is a disease most commonly found among elderly men, and is associated with a very high mortality rate for aneurysm rupture [171]. Current conventional monitoring of aneurysm size and growth is performed by serial diameter measurements using ultrasound imaging. Aneurysm repair involves surgical intervention options which are not without risk. Aneurysm patients under surveillance are selected for surgical repair based on a threshold of aneurysm anteroposterior diameter (5.5 cm) or growth rate (1 cm/year). However, this rule is not perfect: a significant minority of ruptured AAA are less than 5.5 cm in diameter, whilst some surveillance patients who are contraindicated for surgery, due to co-morbidities, survive without aneurysm rupture whilst exhibiting aneurysms with diameters significantly greater than 5.5 cm[171].

Recently, MR imaging, which can enable distinction between different atherosclerotic plaque components, has been increasingly applied to cardiovascular disease [171]. Use of a novel class of MRI contrast agent, known as *ultrasmall superparamagnetic particles of iron oxide* (USPIO), has shown an ability to image tissue inflammation. Furthermore, a previous pilot study in patients with AAA[3], has shown that the uptake of USPIO correlated with macrophage activity in the aortic wall, visualising cellular inflammation, and predicting higher aneurysm expansion rate. The motivation of the MA³RS study is to validate within a larger multicentre cohort study that this USPIO-enhanced MRI method presented by Richards et al. [3] provides incremental prediction to conventional risk markers [171], and therefore that this approach has the potential to save lives while avoiding unnecessary surgery, i.e. to help to individualise therapy.



* 20 patients will undergo MRI reproducibility assessments at 1 month and 1 year and 60 will have the assessment at 1 year only.

Figure 3.1: Study Flow of MA³RS Clinical Trial

3.2 The MA³RS Clinical Trial

Over 300 participants were recruited over a 24-month period, from clinical surveillance programmes and databases in three centres in Scotland. All patients are over 40 years old, with AAA anteroposterior diameter larger than 4.0 cm as measured on routine clinical ultrasound scanning. The clinical assessment details, briefly shown in figure 3.1, can be found in [171].

3.2.2 Imaging and Analysis Protocol

Besides the ultrasound scanning, all patients underwent a contrast-enhanced CT using either a 320-multidetector Toshiba Aquilion ONE (Toshiba Medical, Japan), or 64-multidetector Philips Brilliance 64 (Philips Medical, The Netherlands) CT scanner, at baseline and 2 years, and a baseline MRI scan using a 3T Magnetom Verio scanner (Siemens, Germany) [171]. Following the baseline scan, the USPIO contrast agent (4.0 mg/kg of Ferumoxytol; Rienso, Takaeda) was administered intravenously. A repeat MRI scan was then acquired after 24–36 hours. All patients received 20 mg of intravenous hyoscine butylbromide (Buscopan, Boehringer Ingelheim) prior to both MRI scans to minimise bowel motion artifacts. A small group of 20 patients returned within 1 month and 1 year for an identical USPIO-enhanced MRI protocol for assessment of reproducibility of the study [171]. The CT data, reconstructed in 3D, were used for comprehensive assessment of geometry and growth of aneurysm [171]. A thorough explanation of MRI physics is outwith the scope of this thesis. For a detailed description of MRI physics, please refer to McRobbie et al. [18].

According to the imaging protocol, a respiratory gated, electrocardiographically-triggered T2 weighted (T2W) turbo-spin echo sequence was used to acquire detailed anatomical data (TR/TE 2R-R intervals/72 ms; flip angle 180 degrees; matrix 192×256 ; field of view 400×400 mm; slice width 5 mm). On the pre-contrast T2W image, the aortic wall and thrombus were manually segmented. Because of its sensitivity to the presence of iron particles, a multi-echo, gradient-echo T2* weighted (T2*W) sequence (TE 4.9, 7.7, 10.5, 13.3 ms; TR 133 ms; flip angle 15 degrees; matrix $192 \times$

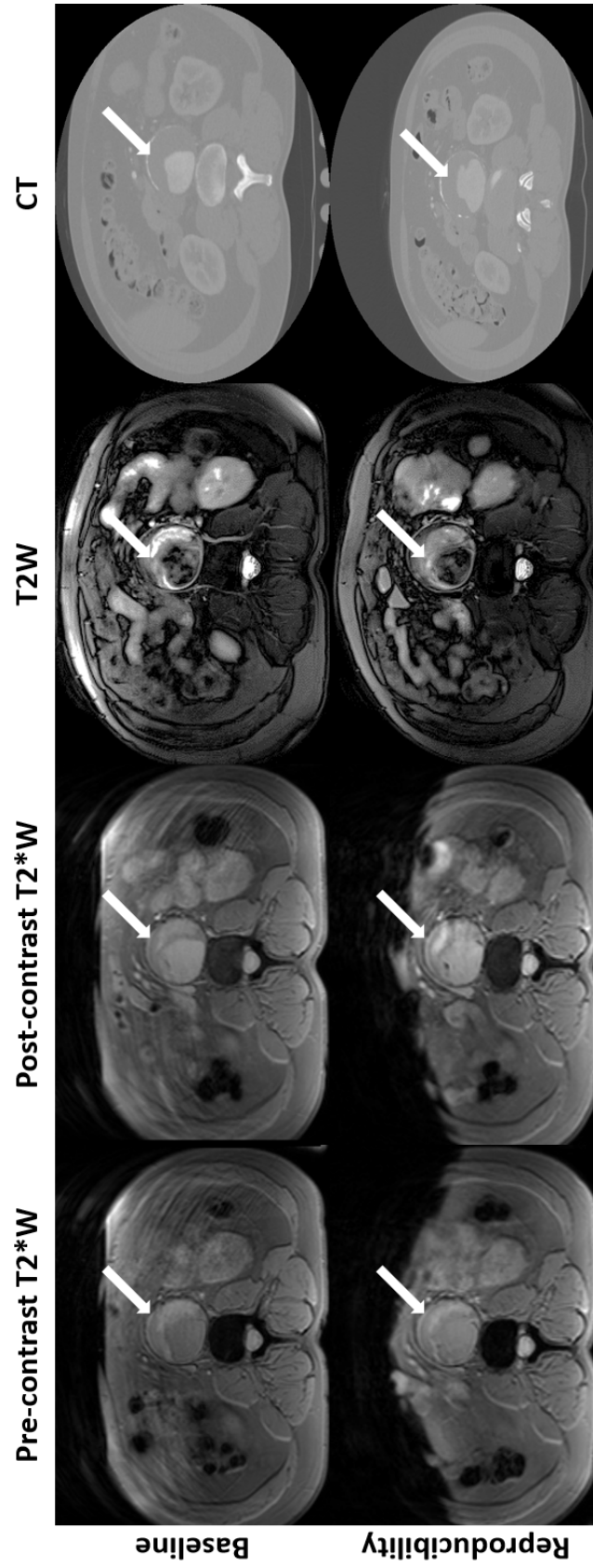


Figure 3.2: Example of axial MA³RS data acquired from the same patient in the baseline and reproducibility assessments: from left to right is pre- and post-contrast T2* weighted (T2*W) images, T2 weighted (T2W) image, and CT image. White arrows point to the aorta in different images. T2*W images shown in all figures of this chapter are acquired with shortest TE.

3.2 The MA³RS Clinical Trial

256; field of view 400×400 mm; slice width 5 mm) was used to acquire contiguous axial images of the entire aneurysm (from the neck of the aneurysm down to the iliac bifurcation) with slice positions corresponding to those of the T2W images [3]. The four echoes in the T2*W MR sequence were combined to generate post-processed data, for example, $R2^*$ (where $R2^* = 1 / T2^*$) and $T2^*$ maps based on the decay of signal magnitude values with increasing echo time [171]. $R2^*$ and $T2^*$ values are correlated to the concentration of USPIO particles. A color map for each patient was produced, based on the thresholded changes of $T2^*$ or $R2^*$ maps, to display the USPIO uptake between the pre- and post-contrast scans [171]. An example of pre- and post-contrast T2*W data (TE 4.9 ms), T2W, and CT images which were acquired in both baseline and reproducibility scans is shown in figure 3.2.

Following the requirements of clinical assessment of the data, the color maps have to be displayed along with the anatomical scans to locate the USPIO concentration within the aneurysm as shown in figure 3.3a [3]. Also based on the mural and thrombus USPIO uptake, the patients were divided into three groups. In the initial pilot study, this grouping demonstrated a clearer correlation with the aneurysm growth rate than the measured diameters as shown in figure 3.3b [3]. However, to simultaneously display the USPIO uptake information along with anatomical structure of aneurysm requires spatial alignment of the T2*W functional scans, which are used to generate the color maps, with baseline T2W and CT images. Alignment of the multi-echo T2*W images to other images can be achieved by aligning the T2*W with the shortest TE (4.9 ms) and applying the same image transformation to other echoes. Furthermore, surveillance of aneurysm growth also requires alignment of the baseline data with subsequent scans [171]. Figure 3.4 gives an example of this process in the baseline assessment. As the aorta structure was manually segmented on the T2W data acquired on the first day of baseline assessment, it was used as the reference data in the registration, while any other data were used as floating data being transformed. This registration procedure was repeated for the reproducibility

scans which were all co-registered to the baseline T2W data. As shown in our pilot study [3], the aorta suffers ignorable nonlinear deformations between scans, so the images were rigidly co-registered in 3D space [171].

This 3D rigid registration plays a critical role in the whole diagnostic process. In the following section of this chapter, a new rigid registration algorithm is proposed [173]. This algorithm was customized for the specific assessment procedure of the *MA³RS* clinical trial, thus it is able to register multi-modality MR-CT images, as well as multi-parametric MR-MR images, of the aorta.

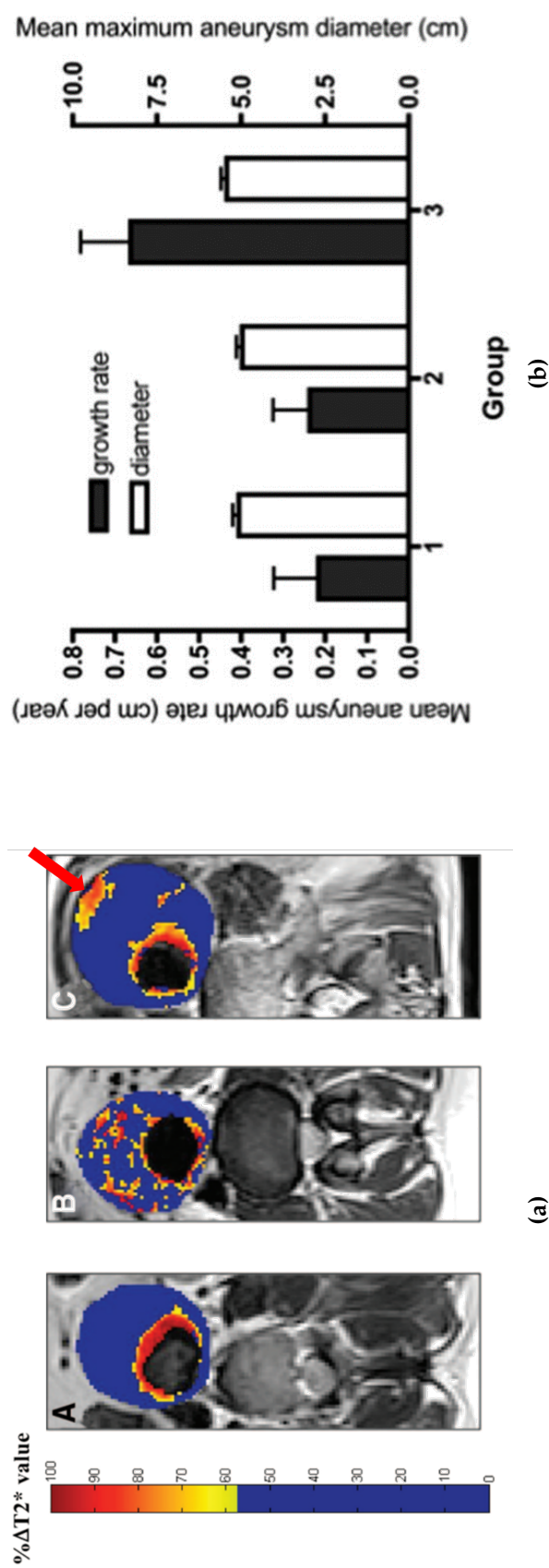


Figure 3.3: The classification of patients based on USPIO uptake from the pilot study [31]: (a) The distinctive patterns of USPIO-positive voxels for each patient group; (b) The relationship of the diameter and growth rate with patient group. The group C patients shown in (a) exhibit detectable focal hotspots (pointed by the red arrow) of USPIO uptake associated with faster growth of aneurysm, while the average diameter shown in (b) has no obvious difference with other two groups.

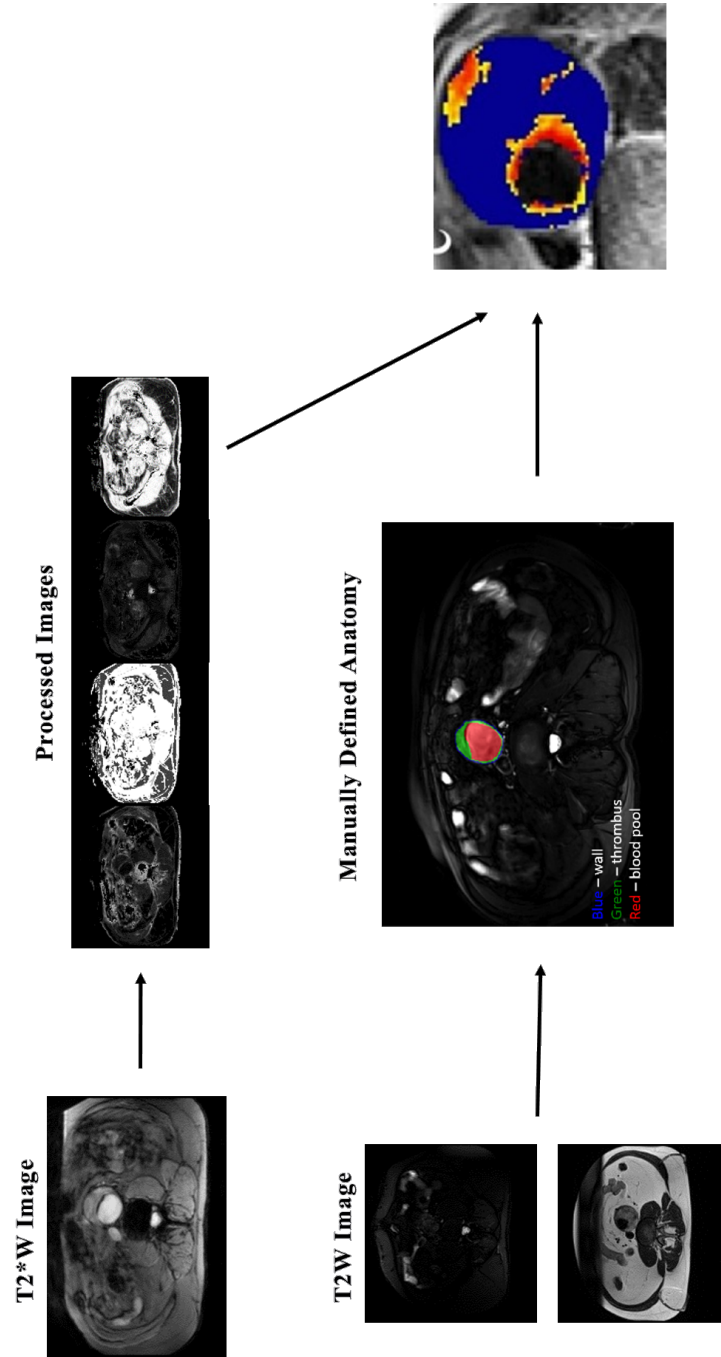


Figure 3.4: An example of the registration process in the baseline assessment: the T2* weighted (T2*W) images acquired within the two days are both co-registered to the T2 weighted (T2W) images.

3.3 Registration Methodology

In the last chapter, for a registration problem, the reference and floating images were represented by function of voxel locations. But practically, registration is performed through matrix operations. Let μ and ν be the image matrices of the reference and floating image I_r and I_f , registration aims to find the best transformation that optimizes a given similarity measure, $\mathcal{S}\{\mu, \nu \circ T\}$, where T is the transformation applied to ν . Our method constrains T to be a rigid-body transformation, thus it can be realized by a transformation matrix T . To allow reliable and convenient registration with minimum user interactions, the rigid registration algorithm was integrated into a registration-oriented GUI.

The registration procedure starts with a semi-automatic selection process of region of interest (ROI). The ROIs are then aligned through a multi-resolution registration method, based on a novel type of topological feature and mutual information. Then the transformation of the full image can be calculated from the registration result of the ROIs. Although the full images were finally registered, only the alignment of the ROIs was of interest for the clinical trial.

According to observations on AAA MR and CT images acquired at the CRIC, using the protocol described above, the shape of the aorta on corresponding axial slices was found to be relatively stable. Hence, we applied a rigid transformation model with 6 degrees of freedom (three translations and three rotations) with respect to the origin of the transformed image.

3.3.1 3D ROI Generation based on Axial Aorta Tracking

As shown in figure 3.2, data from different modalities (and different parametric settings) highlight different tissues. Furthermore, some objects may change their shapes and appearances between baseline and reproducibility scans because of, for example, the growth of the aneurysm. Only the stable image content should be used

for the rigid co-registration; unstable objects should be considered as confounding biases and noise. Figure 3.5 shows an example slice from a pair of corresponding MR data acquired in two successive scans, and a pair of CT-MR data in the baseline assessment. It can be seen that the aorta and spinal area are relatively stable structures. Other image features, such as bowel tissue and other abdominal organs can vary in size and position between scans, which introduces noise into the registration. Obvious differences between these contents can be observed, except in some relatively hard tissues, even in the well aligned images. Thus at the beginning of the co-registration process, a ROI including the clinically interesting area (the contents around aorta) is defined to exclude noisy tissue that might confound the registration.

To define this ROI throughout a 3D volume, or a stack of axial 2D data, a 2D ROI needs to be manually defined first on a “seed” slice which shows a complete axial view of the aneurysm. The rule of thumb of choosing the “seed” slice is that the typical anatomical structures, such as the aortic wall, the thrombus and the lumen, should be visible. This selected slice should be close to the middle of the 3D volume as much as possible, and must locate before the bifurcation at the bottom of aorta. The centre of the 2D ROI is located by approximately defining the centre of aorta as a seed. In the GUI developed for this work, which is introduced in Section 3.4, this can be done by a single click. A square ROI is then generated around the seed. The 2D ROIs on other slices then can be generated by locating a square of the same size above the centre of aorta. Because the square size is constant across slices, this 2D ROI should be properly sized to include the complete axial view of aorta on each slice while excluding as much other soft tissue as possible. Empirically, the side length of the 2D ROI can vary between 10cm to 15cm. An example of a $11.4 \times 11.4 \text{ cm}^2$ 2D ROI defined a “seed” slice is shown in figure 3.6. To sum up, the required user interactions in the registration framework are: selecting a “seed” slice, defining the size of the square 2D ROI, and placing a seed on the “seed” slice.

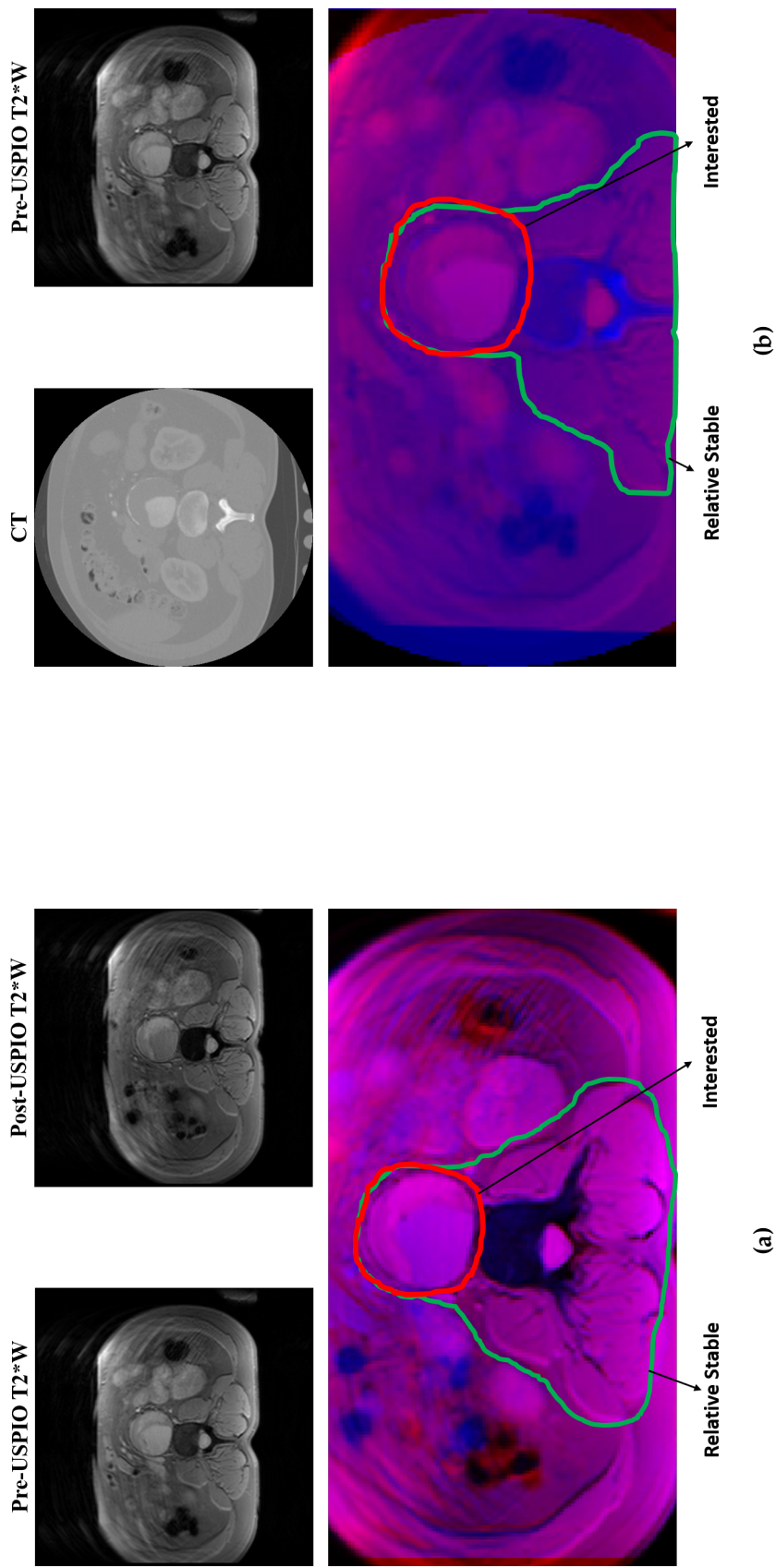


Figure 3.5: Example of spatially aligned data with the reference and floating slices shown in red and blue color channels. A pair of corresponding MR T2* weighted (T2*W) data acquired in two successive scans is shown on the left and a pair of CT-MR data on the right. The relatively stable area is included in the green contours. The aortic aneurysm of interest in the clinical assessment is included within the red contours.

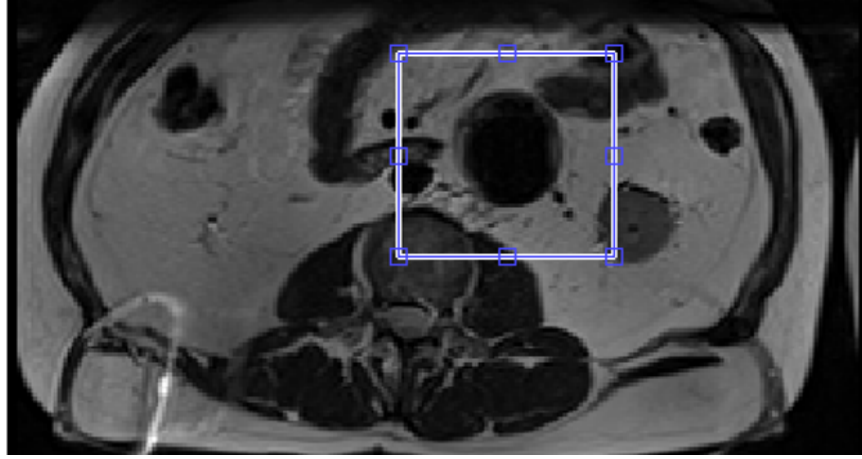


Figure 3.6: Rectangle ROI generated by the seed point roughly located at the aortic centre

The interactive process described above only produces the region of interest on one slice. The whole ROI in a 3D volume is generated by an automatic seed tracking method. Let the k th slice be the “seed” slice of a K -slice 3D data $\mu = \{\mu_k\}, k = 1, 2, \dots, K$, and $\hat{\mathcal{R}}_{\mu_k}$ be the optimal ROI on this slice, with only its size and centre manually decided. The 2D ROI of this slice can be considered as a function $\mathcal{R}_{\mu_k}(\mathbf{o}_{\mu_k})$, where \mathbf{o}_{μ_k} is the ROI centre. So $\hat{\mathcal{R}}_{\mu_k}$ is the optimal value of \mathcal{R}_{μ_k} . Once $\hat{\mathcal{R}}_{\mu_k}$ is picked, the optimal ROI $\hat{\mathcal{R}}_{\mu_j}$ on the neighbouring slice, $\mu_j, j \in \{k-1, k+1\}$, is tracked by minimizing the sum of square difference (SSD) of intensities:

$$\hat{\mathcal{R}}_{\mu_j} = \arg \min_{\mathbf{o}_{\mu_j} \in \Omega_{\mu_j}} \sum |\hat{\mathcal{R}}_{\mu_k} - \mathcal{R}_{\mu_j}(\mathbf{o}_{\mu_j})|^2, \quad (3.1)$$

where Ω_{μ_j} is a region defined on μ_j , but centred on the same coordinate with $\hat{\mathcal{R}}_{\mu_k}$ to search for possible ROI centres.

Equation 3.1 automatically extends the manually picked 2D ROI on slice μ_k to its adjacent slices μ_{k-1} and μ_{k+1} . Then the 2D ROIs on μ_{k-2} and μ_{k+2} can also be located using the same method. This results in a bi-directional growth of the 3D ROI, starting from μ_k and ending when it covers the entire 3D dataset.

3.3.2 ROI Correction based on modified implicit shape model

Each time a 2D ROI is tracked, it may then be further refined due to the fact that on the axial slices the aorta roughly exhibits a circle shape. In this work, a shape detection method based on the circular Hough transform (CHT) [174] is proposed to automatically detect objects, such as the aortic wall in abdominal data. The standard Hough transformation (SHT) based methods were proposed [175] and generalized [176] for detecting and recognizing objects with arbitrary shapes through a voting procedure in the parameter space presented in an accumulator matrix. For the CHT applied to 2D circular objects, the detection is performed in a 3D parameter space by searching for an optimal point (x_c, y_c, r) , as a circle is formulated as:

$$r^2 = (x - x_c)^2 + (y - y_c)^2, \quad (3.2)$$

where (x_c, y_c) and r denote the centre and radius of the detected circle. Peng et al. [177] modified the adaptive Hough transformation method developed by Illingworth and Kittler [178] that identifies locations and radii of multiple circles separately for storage and computational efficiency. Implicit shape model (ISM) [179] provides a probabilistic formulation of Hough transformation that has been widely applied to various recognition and detection frameworks. In this work, to refine the automatically generated 2D ROIs by detecting the aorta which shows a circular-ish shape, a simplified probabilistic CHT model is proposed. An example of the correction process of the 2D ROI using this simplified ISM circle detection is shown in figure 3.7.

To detect a set of objects \mathcal{O} that are possibly being detected at a position \mathbf{x} in an image, the implicit shape model assigns overall scores $S(\mathcal{O}, \mathbf{x})$ to \mathcal{O} and \mathbf{x} by adding up individual possibilities [179]:

$$S(\mathcal{O}, \mathbf{x}) = \sum_k p(\mathcal{O}, \mathbf{x}, \mathbf{e}_k, \mathbf{l}_k) = \sum_k p(\mathbf{e}_k, \mathbf{l}_k) p(\mathcal{O}, \mathbf{x} | \mathbf{e}_k, \mathbf{l}_k), \quad (3.3)$$

where \mathbf{e}_k is a feature observed at location \mathbf{l}_k . Assuming the prior probabilities over features \mathbf{e} and locations \mathbf{l} follow uniform distributions, the problem can be simplified by [179]:

$$S(\mathcal{O}, \mathbf{x}) \propto \sum_k p(\mathcal{O}, \mathbf{x} | \mathbf{e}_k, \mathbf{l}_k). \quad (3.4)$$

For the probability, $p(\mathcal{O}, \mathbf{x} | \mathbf{e}, \mathbf{l})$, the implicit shape model [179] uses a codebook made up of image features collected during the training process [179]. For the i 'th entry I_i of the codebook :

$$p(\mathcal{O}, \mathbf{x} | \mathbf{e}, \mathbf{l}) = \sum_i p(\mathcal{O}, \mathbf{x} | \mathbf{e}, I_i, \mathbf{l}) p(I_i | \mathbf{e}, \mathbf{l}). \quad (3.5)$$

Because $p(\mathcal{O} | \mathbf{e}, \mathbf{l})$ is actually independent from the location \mathbf{l} , and $p(\mathcal{O}, \mathbf{x} | \mathbf{e}, I_i, \mathbf{l})$ only depends on the codebook entry I_i and the location \mathbf{l} , it can be further simplified as [179]:

$$p(\mathcal{O}, \mathbf{x} | \mathbf{e}, \mathbf{l}) = \sum_i p(\mathbf{x} | \mathcal{O}, I_i, \mathbf{l}) p(\mathcal{O} | I_i, \mathbf{l}) p(I_i | \mathbf{e}). \quad (3.6)$$

To detect circular structures, although equation 3.3 can be directly used, the implicit shape model can be further simplified. This is because \mathcal{O} is just a set of circles with different radius r , position \mathbf{x} is the coordinate in the searched region of an image, and \mathbf{e} and I often become a simple feature f , such as edges and gradient [178]. As a result of this, there is only one single feature stored in the codebook. The observation-to-entry likelihood $p(I_i | \mathbf{e})$ then becomes a weight function $\mathbf{w}(\cdot)$ about f . Using the gradient at a pixel along x and y directions, $f = (g_x, g_y)$, in this work the weight function \mathbf{w} is defined as the magnitude of gradient as shown in figure 3.7:

$$\mathbf{w}(g_x, g_y) = \sqrt{g_x^2 + g_y^2}. \quad (3.7)$$

The formulation can be then rewritten as:

$$p(r, \mathbf{x} | f, \mathbf{l}) = p(\mathbf{x} | r, f, \mathbf{l}) p(r | f, \mathbf{l}) \mathbf{w}(f). \quad (3.8)$$

Thus the final score assigned to each point (r, \mathbf{x}) in the parameter space, which is

3.3 Registration Methodology

stored in an accumulator matrix as shown in figure 3.7, can be formulated as:

$$S(r, \mathbf{x}) = \sum_k p(\mathbf{x}|r, f, \mathbf{l}_k) p(r|f, \mathbf{l}_k) \mathbf{w}(f). \quad (3.9)$$

For a feature f observed at location \mathbf{l} , the probability $p(r|f, \mathbf{l})$ is decided by the number of the candidate radius N_r , where \mathbf{r} represents the set of all candidate radii. Because the registration performed in this work is based on voxel intensity, for the sake of convenient computation, sub-pixel accuracy is not required when generating 2D ROIs. In this case, N_r is a natural number less than the smallest dimension of the 2D ROIs. The $p(r|f, \mathbf{l})$ is assumed to follow a uniform distribution, thus:

$$p(r|f, \mathbf{l}) = \frac{1}{N_r}. \quad (3.10)$$

Finally, once the gradient f is calculated at $\mathbf{l} = (i, j)$, $p(\mathbf{x}|r, f, \mathbf{l})$ is evenly distributed to two points along or against the gradient direction whose distance to \mathbf{l} is r :

$$p(\mathbf{x}|r, f, \mathbf{l}) = \begin{cases} 0.5, & \text{if } \mathbf{x} = (i, j) \pm (\lfloor \frac{g_x}{\sqrt{g_x^2 + g_y^2}} \cdot i \rfloor, \lfloor \frac{g_y}{\sqrt{g_x^2 + g_y^2}} \cdot j \rfloor) \\ 0, & \text{if } \mathbf{x} \neq (i, j) \pm (\lfloor \frac{g_x}{\sqrt{g_x^2 + g_y^2}} \cdot i \rfloor, \lfloor \frac{g_y}{\sqrt{g_x^2 + g_y^2}} \cdot j \rfloor) \end{cases}. \quad (3.11)$$

As the aortic wall often displays an irregular circular shape, the accumulator matrix need to be smoothed for better robustness to less perfect circles. A 5×5 Gaussian filter was applied to each slice of the 3D accumulator. A threshold is also applied so that only the pixels with strong enough gradient are used to build up the accumulator matrix.

For space efficiency, Peng et al. [177] detect multiple circle centres first based on a 2D accumulator matrix, then look for the best radius. In this work, each 2D ROI is of relative small size, typically less than 75×75 for pixel size $1.406 \times 1.406 \text{ mm}^2 / \text{pixel}$. Furthermore, the aorta wall can be assumed to be the largest object that has a shape closest to regular circle within the 2D ROI. Thus a 3D accumulator matrix \mathbf{A} is used to

decide both the centre and radius of the aorta (\mathbf{o}, r_o) together using:

$$(\mathbf{o}, r_o) = \arg \max_{(\mathbf{x}, r) \in \Omega_A} \sum_k p(\mathbf{x}|r, f, \mathbf{l}_k) p(r|f, \mathbf{l}_k) \mathbf{w}(f), \quad (3.12)$$

where Ω_A is the definition domain of the accumulator matrix A which is decided by the size of the 2D ROIs and the range of candidate radii. Then the 2D ROI is relocated to be centred on the detected object, as shown in figure 3.7. Figure 3.8 shows an aorta manually segmented by a clinician compared to the trajectory of the automatically tracked 2D-ROI centres, from a standard contrast enhanced CT dataset acquired on an Aquilion ONE (Toshiba Medical Systems, Japan).

3.3.3 Initial Alignment

Similarity measures that are used in different registration frameworks often have limited capture ranges. Thus before the main registration steps, the floating image needs to be transformed to a relatively close position to the reference image within the problem space, which is the purpose of the initial alignment.

Because the seed points are relocated to the centres of the aorta on each slice, initial alignment can be achieved by registering the 2D-ROI centres. Generally, this can be done by using the iterative closest points (ICP) Algorithm [180] which aligns two groups of points by searching for the minimum of SSD [170]. When the correspondences between slices are known, least square methods can be applied to solve this problem analytically, using singular value decomposition (SVD)[181][182]. As the least square method can solve the alignment problem non-iteratively, in this project, a triangulation topology feature was used to find the correspondences between the two point sets formed by the 2D ROI centres. If it failed to solve the correspondence problem, then ICP was then used. Because the 3D ROIs generated for reference and floating data are unlikely to cover exactly the same area, the initial alignment is only required to align 80% of the 2D ROI centres.

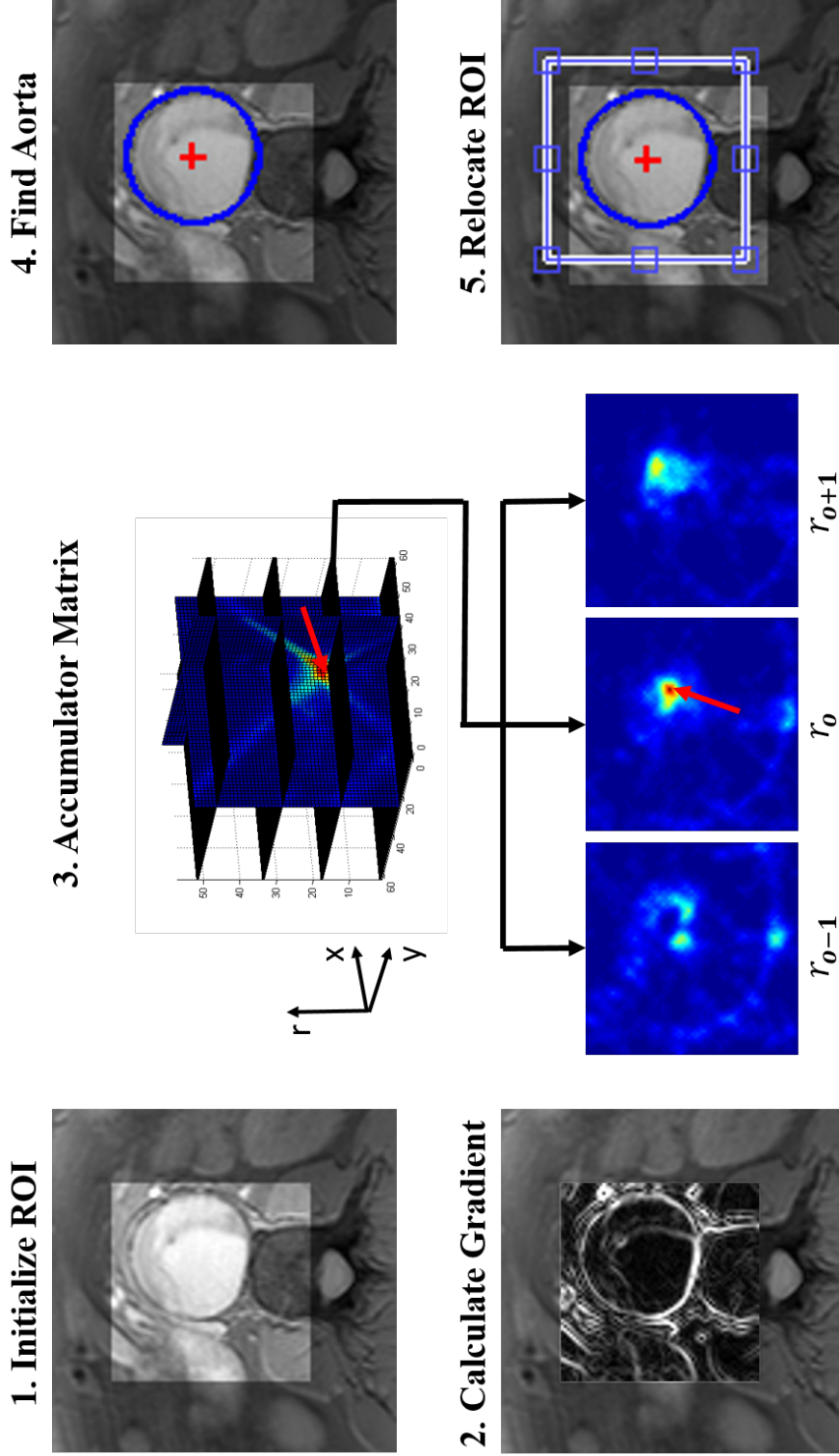


Figure 3.7: An example of 2D ROI correction using the simplified implicit shape model circle detection method: 1. a 2D ROI is initialized from its neighbouring slice; 2. the gradient of the ROI is then calculated; 3. the 3D accumulator matrix which stores the probability of a circle with radius r , and centred (x, y) ; 4. the aorta is detected by searching for the highest score in the accumulator matrix shown by the red arrows; 5. the centre of the 2D ROI is relocated to the centre of aorta.

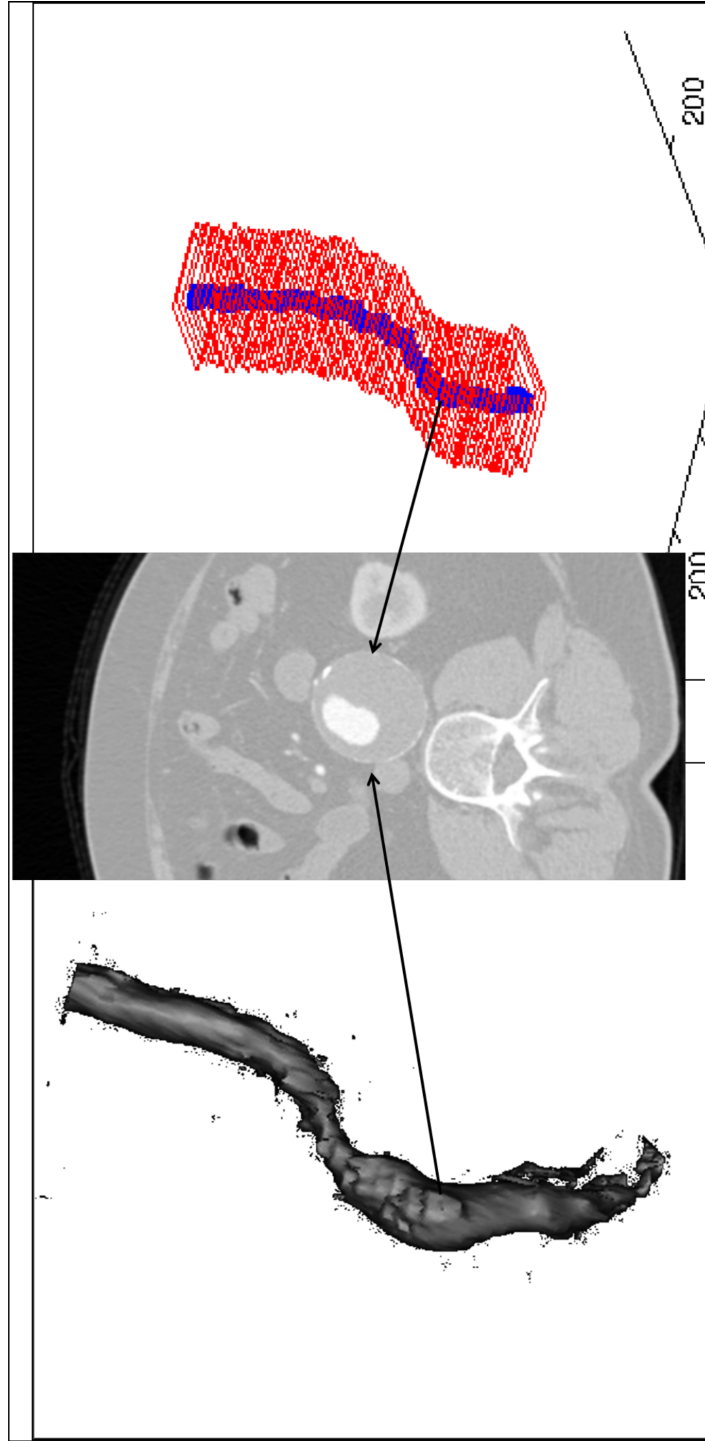


Figure 3.8: Manually segmented aorta (left) on CT data (centre) compared with automatic ROI (right): the manual segmentation is generated by thresholding a sub-volume that include the whole aorta. The coordinate systems of left and right images shown here are not aligned as the segmentation and ROI are generated using different software.

3.3 Registration Methodology

As the aorta exhibits negligible deformation between scans, the correspondence problem can be solved using features that encode the shape of the aorta, for example, local curvature. Defining $\mathbf{O}_\mu = (\cdots, \mathbf{o}_{\mu_{j-1}}, \mathbf{o}_{\mu_j}, \mathbf{o}_{\mu_{j+1}}, \cdots)$ as the vector that saves the coordinates of all 2D ROI centres in a volume where the initial ROI was first defined on slice μ_j , the curvature value at point \mathbf{o}_u can be calculated as the change of tangent direction at a point [183]. However, in a small neighbourhood, the corresponding points may have different curvature values due to the inaccuracy of the automatic 2D ROI tracking discussed above. Furthermore, to calculate the curvature feature within a large neighbourhood, \mathbf{O}_{μ_j} needs to be smoothed, which can reduce the accuracy and thus fail the solution of the correspondence problem. Alternatively, the curvature may be approximated by a second order derivative based on a finite difference approximation [184], for which the computational complexity increases and the accuracy drops with increasing neighbourhood size. In this work, a triangulation topology feature is used to describe the local shape of the aorta within a large neighbourhood that does not require smoothing of \mathbf{O}_μ . This type of triangulation features have been used in other feature based surface registration methods [185, 186]. For a neighbourhood $\mathbf{O}_{\mu_j} = (\mathbf{o}_{\mu_{j-L}}, \cdots, \mathbf{o}_{\mu_j}, \cdots, \mathbf{o}_{\mu_{j+L}})$ in \mathbf{O}_μ around a 2D ROI centre \mathbf{o}_{μ_j} , N_Δ is the predefined number of triangles used to generate the feature vector. Each triangle is decided by the point \mathbf{o}_{μ_j} and two points selected from symmetric positions with respect to \mathbf{o}_{μ_j} . Thus the largest triangle for a neighbourhood length $2L + 1$ is decided by \mathbf{o}_{μ_j} and $\mathbf{o}_{\mu_{j\pm L}}$. The lengths of the edges of this triangle are used as the first three elements in the feature vector, and the second triangle whose edges are used for the following three feature elements is defined by \mathbf{o}_{μ_j} and $\mathbf{o}_{\mu_{j\pm \lfloor \frac{L}{2} \rfloor}}$, as shown in figure 3.9. N_Δ is defined arbitrarily, based on the size of the neighbourhood, and that the side points used to generate the triangle should be equidistant to each other.

In this work, for computational efficiency, the empirical choice of feature parameters are $N_\Delta = 3$ and $L = 9$. This gives three triangles which are defined by $\mathbf{o}_{\mu_{j\pm 3}}$, $\mathbf{o}_{\mu_{j\pm 6}}$, $\mathbf{o}_{\mu_{j\pm 9}}$ and \mathbf{o}_{μ_j} . The parameters N_Δ and L are chosen empirically here, systematic

exploration of their parameter spaces will be done in the future work.

For two volumes μ and ν , the corresponding points of the ROI centres stored in the vector \mathbf{O}_ν can be quickly calculated by searching for their nearest neighbours in \mathbf{O}_μ . An example of the correspondence between ROI centres of two volumes is shown in the centre of figure 3.9. Correspondences between \mathbf{O}_μ and \mathbf{O}_ν can be expressed as a vector $\delta = (\delta_1, \delta_2, \dots)$, so that for the 2D ROI centre \mathbf{o}_{ν_j} on the j th slice of ν , the corresponding point in \mathbf{O}_μ is the 2D ROI centre on the $(j + \delta_j)$ -th slice of μ . The correspondence between slices of μ and ν are then calculated as the mean of all scalars in δ , denoted as $\bar{\delta}$, excluding some outliers, so that for all ν_j the corresponded slice in μ is $\mu_{j+\bar{\delta}}$. In this work, the outliers are detected and excluded using a simplified random sample census (RANSAC) [187] displayed by Algorithm 1. The input raw data of this RANSAC process is δ calculated for ROI centres of ν ; the model used to fit the data is simply the average of δ . For sampling the input data, the probability, p_R , decides the possibility that at least one iteration of RANSAC can avoid all outliers. This parameter was set to 0.99, as is commonly done. Importantly, the minimum number of samples used to calculate the slice correspondence is defined by the highest bin in the histogram of δ , as shown in figure 3.9. The outliers were detected using a predefined tolerance $\epsilon_R = 1$, and the RANSAC resampling process terminated when the number of detected inliers exceeds $\tau_R = 70\%$ of the slice number. Let p_O be the probability of observing an outlier, which can be obtained as shown in figure 3.9, the maximum number of iterations N_R is calculated by [187]:

$$N_R = \frac{\log(1 - p_R)}{\log(1 - (1 - p_O)^{m_R})}, \quad (3.13)$$

where p_O can be approximated by the highest bin in the histogram of δ and the error tolerance ϵ_R .

Algorithm 1 Simplified RANSAC for Slice Correspondence

Input: δ : feature correspondence vector; p_R : probability that at least one iteration observe no outliers; ϵ_R : error tolerance; τ_R : threshold on amount of inliers; m_R minimum number of sampled points used to fit the model.

Output: $\bar{\delta}$: final slice correspondence; e_R : fitting error.

```

1: Initialization:  $N_R$  and  $m_R$  using equation 3.13 and histogram of  $\delta$ ,  $N_e = 0$ 
   {number of inliers};
2: while  $i \leq N_R$  do
3:   Randomly selects  $m_R$  points from  $\delta$ ,  $\hat{\delta} = (\hat{\delta}_1, \hat{\delta}_2, \dots)$ ,  $N_e = m_R$ ;
4:    $\bar{\delta} = \frac{1}{m_R} \sum_{j=1}^{m_R} \hat{\delta}_j$ ; {estimate the mean of  $\delta$  using  $\hat{\delta}$ }
5:    $e_R = \frac{1}{N_{all}} \sum_{j=1}^{N_{all}} |\delta_j - \bar{\delta}|$ ; {calculate the error of estimation}
6:   for each  $\delta_k$  in  $\delta$  do
7:     if  $|\delta_k - \bar{\delta}| \leq \epsilon_R$  then
8:        $\hat{\delta} \leftarrow \delta_k$ ,  $N_e = N_e + 1$ ;
9:     end if
10:  end for
11:  if  $N_{inliers} > \tau_R \cdot N_{all}$  then
12:     $\hat{\delta} = \frac{1}{N_e} \sum_{j=1}^{N_e} \hat{\delta}_j$ ; {re-calculate the mean of  $\hat{\delta}$ }
13:     $\hat{e}_R = \frac{1}{N_{all}} \sum_{j=1}^{N_{all}} |\delta_j - \hat{\delta}|$ 
14:    if  $\hat{e}_R < e_R$  then
15:       $\bar{\delta} = \hat{\delta}$ ;
16:       $e_R = \hat{e}_R$ ;
17:    end if
18:  end if
19:   $i = i + 1$ .
20: end while
  
```

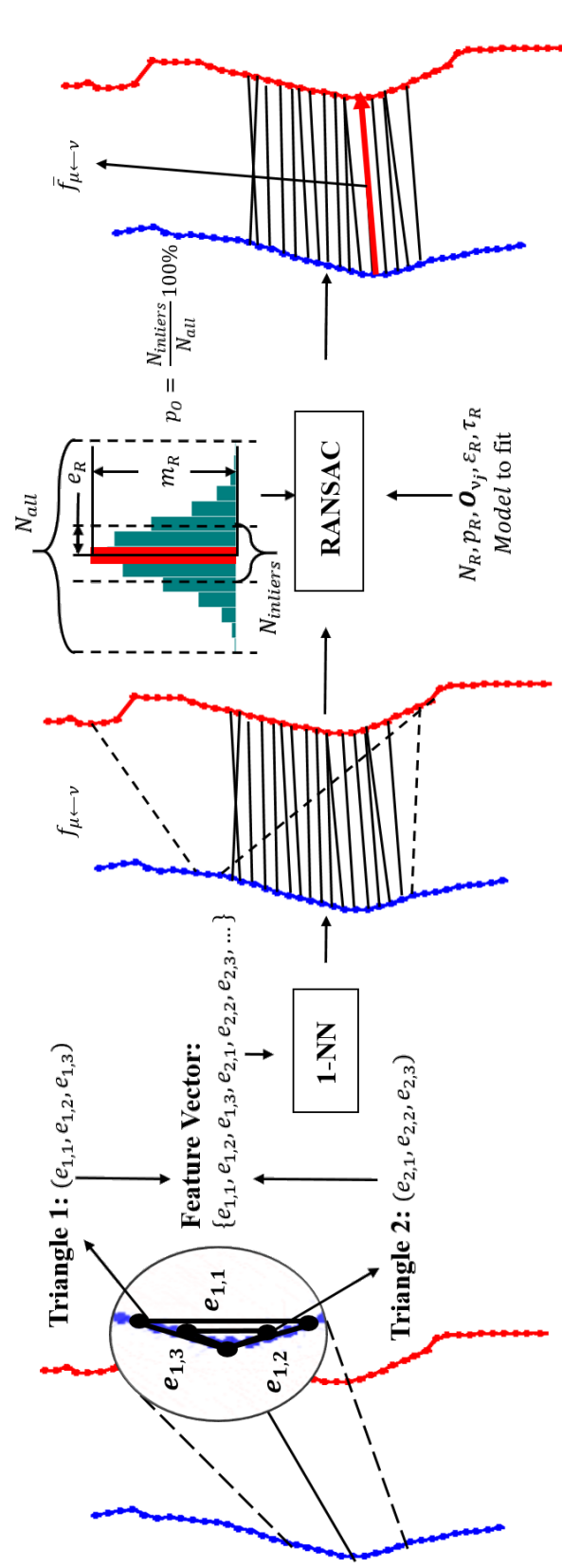


Figure 3.9: Calculating correspondence between 2D ROI centres using the triangulation topology feature: within a large neighbourhood of a point, the edges of a few predefined triangles were used to form the feature vector; the correspondence between the 2D ROI centres can be found by searching for the nearest neighbours; the correspondence between slices are calculated first with a RANSAC-least-square scheme to exclude the outliers shown as dash lines; if the statistic error of this correspondence is bigger than 1, the correspondence is recalculated using the ICP method.

3.3 Registration Methodology

After the correspondence of slices is calculated, the data can be initially aligned with a transformation calculated by the least square method. Let \mathbf{R}_{ini} and \mathbf{t}_{ini} be the 3×3 rotation matrix and 3×1 translation vector of this initial transformation respectively, \mathbf{R}_{ini} and \mathbf{t}_{ini} then are obtained by minimizing the sum of squared difference function [182]:

$$(\mathbf{R}_{ini}, \mathbf{t}_{ini}) = \arg \min_{\mathbf{R}_{ini}, \mathbf{t}_{ini}} \sum_{j=1}^{N_v} w_j \left\| \left(\mathbf{R}_{ini} \mathbf{o}_{\mu_j} + \mathbf{t}_{ini} \right) - \mathbf{o}_{\nu_{j+\delta}} \right\|^2, \quad (3.14)$$

where N_v is the number of slices, as well as number of 2D ROI centres, in ν , and w_j is a pre-defined weight assigned to each point. Because in this work the initial alignment doesn't require sub-voxel accuracy, for all ROI centres, the weight is simply $\frac{1}{N_v}$. Note that each element from \mathbf{O}_{μ} and \mathbf{O}_{ν} is a column vector that stores the 3D coordinate of a 2D ROI centre.

First, the centre vectors of \mathbf{O}_{μ} and \mathbf{O}_{ν} were calculated as [182]:

$$\bar{\mathbf{o}}_{\mu} = \frac{\sum_{j=1}^{N_{\mu}} w_j \mathbf{o}_{\mu_j}}{\sum_{j=1}^{N_{\mu}} w_j}, \quad (3.15)$$

and

$$\bar{\mathbf{o}}_{\nu} = \frac{\sum_{j=1}^{N_{\nu}} w_j \mathbf{o}_{\nu_j}}{\sum_{j=1}^{N_{\nu}} w_j}, \quad (3.16)$$

where N_{μ} is the number of slices in μ . Then the centre vectors were subtracted from each elements of \mathbf{O}_{μ} and \mathbf{O}_{ν} , and the resulted matrices were denoted as \mathbf{X}_{μ} and \mathbf{X}_{ν} [182]:

$$\mathbf{x}_{\mu_j} = \mathbf{o}_{\mu_j} - \bar{\mathbf{o}}_{\mu}, \quad (3.17)$$

$$\mathbf{x}_{\nu_j} = \mathbf{o}_{\nu_j} - \bar{\mathbf{o}}_{\nu}, \quad (3.18)$$

where \mathbf{x}_{μ_j} and \mathbf{x}_{ν_j} are respectively the j th element of \mathbf{X}_{μ} and \mathbf{X}_{ν} . A covariance matrix

\mathbf{C} then can be calculated as [182]:

$$\mathbf{C} = \mathbf{X}_v \mathbf{W} \mathbf{X}_\mu^T, \quad (3.19)$$

where \mathbf{W} is a diagonal matrix and $W_{jj} = w_j$. Thus in this work, $\mathbf{W} = \mathbf{I}$. \mathbf{C} can be singular vector decomposed in the following form:

$$\mathbf{C} = \mathbf{U} \mathbf{\Sigma} \mathbf{V}^T. \quad (3.20)$$

Then the rotation \mathbf{R}_{ini} of the initial alignment can be calculated by:

$$\mathbf{R}_{ini} = \mathbf{V} \begin{pmatrix} 1 & & & \\ & 1 & & \\ & & \ddots & \\ & & & \det(\mathbf{V} \mathbf{U}^T) \end{pmatrix} \mathbf{U}^T \quad (3.21)$$

and the translation of vector can be obtained by:

$$\mathbf{t}_{ini} = \bar{\mathbf{o}}_\mu - \mathbf{R}_{ini} \bar{\mathbf{o}}_\nu. \quad (3.22)$$

The transformation matrix of the initial alignment was then built up as:

$$\mathcal{T}_{ini} = \left(\begin{array}{ccc|c} & & & \\ & \mathbf{R}_{ini} & & \mathbf{t}_{ini} \\ & & & \\ \hline 0 & 0 & 0 & 1 \end{array} \right). \quad (3.23)$$

Then ν is transformed by \mathcal{T}_{ini} to achieve the initial alignment. Figure 3.10 shows an example of two initially aligned T2*-weighted (T2*W) images.

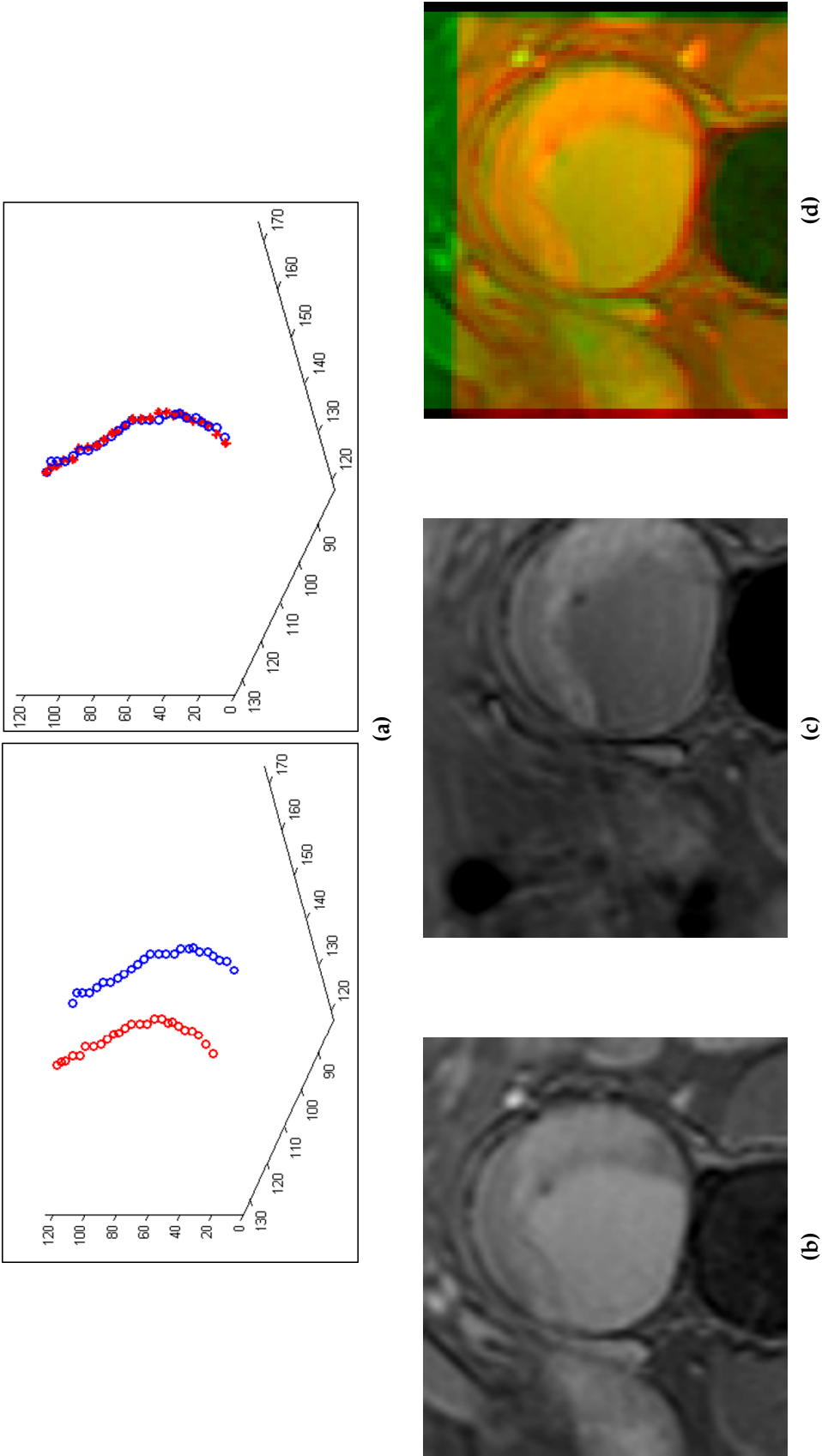


Figure 3.10: Example of initial alignment process using the automatically tracked region of interest (ROI) centres; (b) the ROI selected on a slice of the pre-contrast T2*W image; (c) the ROI selected on a slice of the post-contrast T2*W image; (d) the initially aligned ROIs of the post- and pre-contrast T2*W data visualized in red and green colour channels.

3.3.4 Voxel Intensity Based Registration

Once the data are initially aligned, the floating data should have been transformed to a position relatively close to reference image. Further alignment then can be achieved by a voxel intensity based registration process. Simple measures based on intensity differences, such as SSD which is used in the ROI tracking process, are sufficient to measure the similarity or difference between intra-modality data. However, excepting simultaneous analysis of the reproducibility and the baseline assessments, the data to be aligned in this work were acquired with multiple contrasts, different parametric settings, or from different modalities. Thus mutual information (MI) was used as the similarity measure due to its robustness to the non-linear correlation of the intensity values in reference and floating data.

As discussed in the literature review, mutual information is a combination of individual and joint entropy values of two images [148]. Denoting $\mathcal{H}(\cdot)$ the Shannon entropy of an image, and $\mathcal{H}(\cdot, \cdot)$ joint entropy of two images, the mutual information S_{MI} was calculated as:

$$S_{MI}(\mu, \nu) = \mathcal{H}(\mu) + \mathcal{H}(\nu) - \mathcal{H}(\mu, \nu). \quad (3.24)$$

The entropy values of images can be computed using histograms, and joint histograms, which estimate marginal and joint probability distributions of the image intensities.

3.3.4.1 Asymmetric histogram binning

To build up image histograms, the number of bins, an interval of intensity is often defined arbitrarily; the intensity range often being divided into equidistant bins [188]. This equidistant binning process ignores the intensity distributions of different objects within an image. Thus voxels belonging to the same object may be assigned to different bins, and vice versa, which can bias the measure of image similarities. Knops

et al. proposed applying k -means binning to the joint histogram between two images, for a more natural clustering of intensities, providing adaptively variable bin sizes [189]. This method was applied to register CT, MR, and positron emission tomography (PET) images. Liu et al. [188] pointed out that applying k -means on *both* the reference and floating images may lead to loss of details, and thus attenuate the sensitivity of the similarity measure. Instead, they proposed a "top-to-down" k -means clustering to perform an *asymmetric cluster-to-image* CT-MR registration [188]. The "top-to-down" k -means binning was used to reduce the sensitivity of clustering to the initialization of the clusters [188].

In this work, the asymmetric cluster-to-image framework was modified to register multi-contrast and multi-parametric MR images, as well as multi-modal CT-MR images. Registering multi-contrast T2*W MR images, the post-contrast image was k -means clustered. When aligning T2W-T2*W MR image pairs, or CT-T2*W images, the k -means clustering was applied to the T2W image, or CT image, which provides better visibility of anatomical structures.

The k -means algorithm is used to find an arbitrary number of cluster centres $\mathbf{c}_k, k = 1, \dots, N_c$ for N_u observations of a random variable $\mathbf{u}_n, n = 1, \dots, N_u$, by minimizing the following cost function [190]:

$$J = \sum_{n=1}^{N_u} \sum_{k=1}^{N_c} \gamma_{nk} \|\mathbf{u}_n - \mathbf{c}_k\|^2, \quad (3.25)$$

where γ_{nk} is a binary indicator that denotes whether the observation \mathbf{u}_n is assigned to the cluster centre \mathbf{c}_k . The cluster centres \mathbf{c}_k and cluster membership of each observation \mathbf{u}_n are iteratively fixed using the Expectation and Maximization (EM) Algorithm [191]. In the Expectation step, or E step, the cluster membership is assigned by:

$$\gamma_{nk} = \begin{cases} 1, & \text{if } k = \arg \min_j \|\mathbf{u}_n - \mathbf{c}_j\| \\ 0, & \text{otherwise} \end{cases}. \quad (3.26)$$

Each cluster centre \mathbf{c}_k updates each iteration in the Maximization step using the average of its associated observations [191]:

$$\mathbf{c}_k = \frac{\sum_j \gamma_{jk} \mathbf{u}_j}{\sum_j \gamma_{jk}}. \quad (3.27)$$

To reduce the sensitivity of k -means to initialization, and for better interpretation of the anatomical structures displayed in the clustered image, the “top-to-down” k -means method initializes a large amount of cluster centres. Then in each iteration of the k -means, after the assignment of cluster centres refined by an EM step, two clusters were merged if the distance between their centres was less than a predefined threshold. In this work, this bottom-up structure of “top-to-down” k -means is slightly modified, as shown in Algorithm 2. Before the EM step, the range of image intensities was firstly calculated, and the cluster centres were initialized uniformly within this intensity range. The clusters close to each other are then merged in each iteration of the k -means, after the assignment of cluster centres refined by an expectation-maximization (EM) step, and the empty cluster centres removed. Note that in the “top-to-down” k -means this step is done each time the algorithm converged, then the EM step re-runs. This means it uses more iterations and thus longer time to merge the cluster centres.

In this work, the number of clusters were initialized as $K = 10$. An example of a clustered T2*W image is shown in figure 3.11. The threshold of the cluster distance is defined based on the range of intensity and K . Let μ_{max} and μ_{min} be the maximum and minimum values of image intensity, ξ is then fixed by:

$$\xi = \frac{|\mu_{max} - \mu_{min}|}{10}. \quad (3.28)$$

Algorithm 2 Bottom-up k -means

Input: μ : input image; K : number of clusters; ξ : predefined threshold of cluster distance.

Output: v : clustered image; c : cluster centres; K : number of clusters.

```

1: Initialization  $c = \{c_1, \dots, c_K\}$  {evenly distributed in the range of intensity};
2:  $u_j = \mu(x_j)$ ; {intensity value of  $\mu$  at position  $x_j$ }
3: while  $c$ ,  $\gamma_{nk}$  and  $K$  changes do
4:   for all  $x_j$  in the image  $u$  do
5:     Compute all  $\gamma_{nk}$  using equation 3.26; {E step: associate data to clusters;}
6:     Compute all  $c_k$  using equation 3.27; {M step: recalculate cluster centres;}
7:   end for
8:   for all  $\|u_i - u_j\| < \xi$  do {merge two cluster centres too close to each other}
9:      $c = c - \{c_i, c_j\}$ ;
10:     $c = c + \left\{ \frac{(c_i + c_j)}{2} \right\}$ ;
11:     $K = K - 1$ ;
12:   end for
13: end while
14: for all  $x_j$  in  $\mu$  do
15:   if  $\gamma_{jk} = 1$  then
16:      $v(x_j) = c_k$ ; {generate clustered image.}
17:   end if
18: end for

```

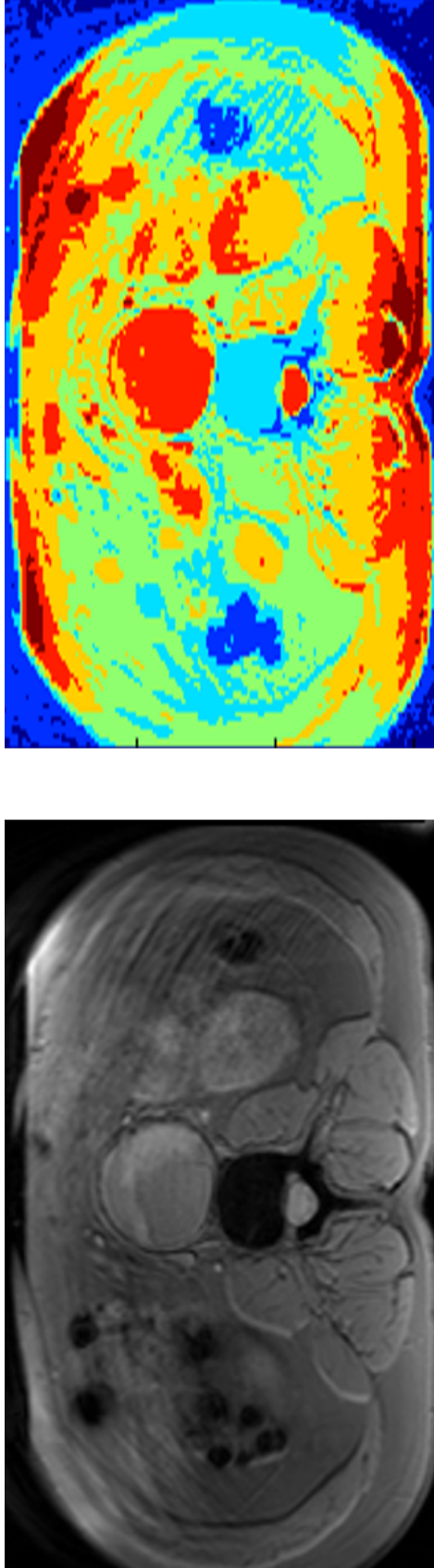


Figure 3.11: Example of a pre-contrast T2* weighted image clustered by the bottom-up k-means while K were initialized as 10 but converged to 6.

3.3 Registration Methodology

The clustered image is then used for cluster-to-image registration with MI calculated using a rectangular, but non-square, joint histogram. Optimal transformation of the floating image is calculated by searching for the global optimum of similarity measure within the searching space with predefined boundaries. To avoid the situation where alignment terminates at local optima of similarity measure, and to make a robust search for optimal transformation independent from gradient variation, we used the DIRECT algorithm [166] as the optimization strategy.

To boost the speed of the whole registration framework, a two-level multi-resolution scheme was used. A low resolution volume was first created for a coarse-level registration, by down-sampling the original data. In this cluster-to-image registration framework, the clustered image obtained through the bottom-up k -means algorithm was directly down-sampled. To reasonably maintain the information contained by the unclustered image, it was firstly clustered using the bottom-up k -means algorithm with a relatively large number of clusters, $K = 32$. Thus, the coarse-level registration is actually an asymmetric cluster-to-cluster registration. Figure 3.12 demonstrates the method used to create the lower resolution data for the non-clustered data.

The transformation calculated for the lower resolution volume can be converted to transform the original data by:

$$\mathcal{T}_{origin} = \left(\begin{array}{ccc|c} & & & \\ & \mathbf{R}_{low} & & \delta \mathbf{t}_{low} \\ & & & \\ \hline 0 & 0 & 0 & 1 \end{array} \right), \quad (3.29)$$

where \mathbf{R}_{low} and \mathbf{t}_{low} are the rotation and translation components of the coarse-level transformation, and $\delta = (\delta_x, \delta_y, \delta_z)$ is the down-sampling rate of each dimension.

This transformation calculated by the coarse-level registration then can be refined using the original data through a cluster-to-image registration, but within a much

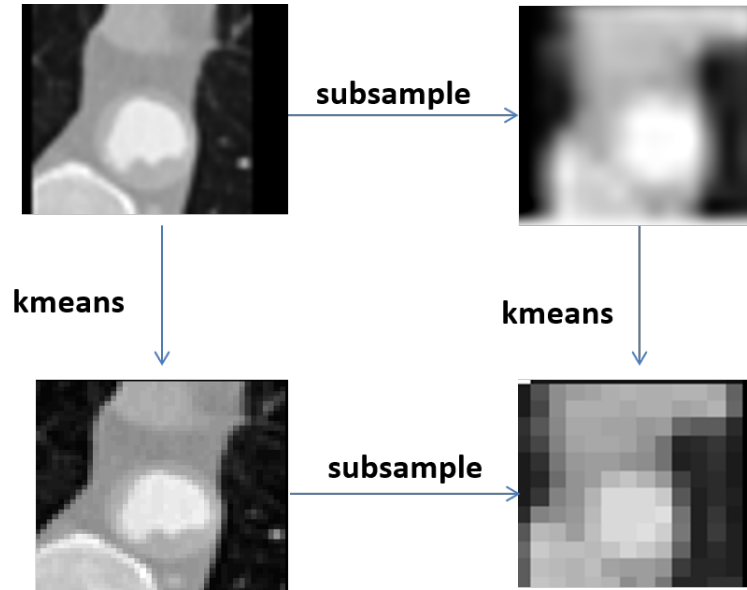


Figure 3.12: *Creation of low resolution data from an example CT volume.*

smaller search space. A $K \times 128$ joint histogram was used to calculate the MI in this fine-level registration. To obtain the same registration results, when $\delta = (3,3,3)$, this dual-level, multi-resolution approach can be up to 100 times quicker than directly using the original data.

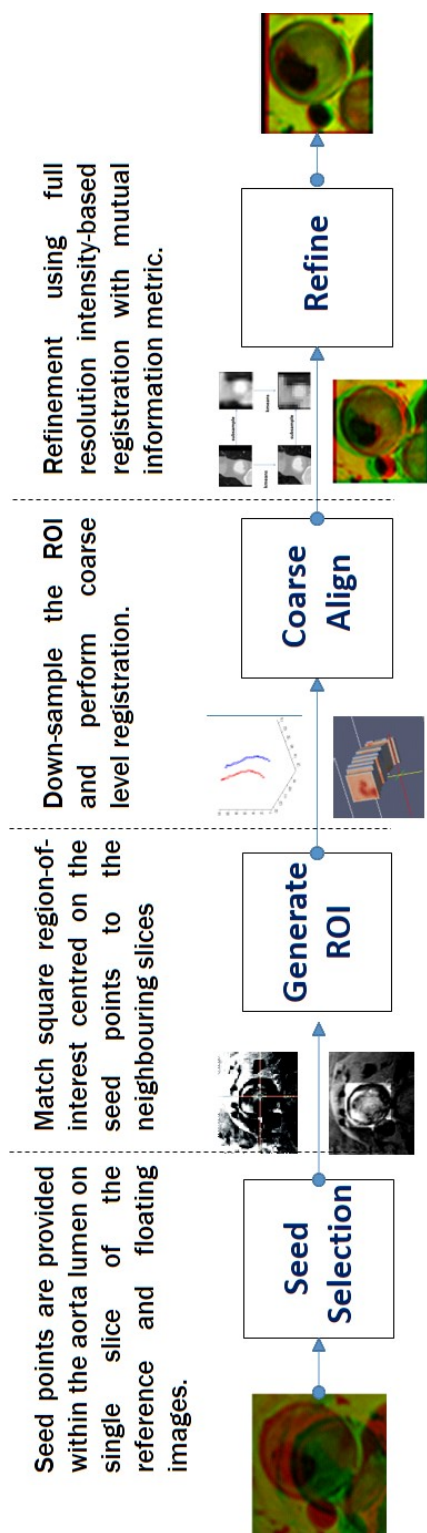


Figure 3.13: Registration Procedure

3.3.5 Registration Schedule

In summary, the registration framework starts with an interactive process where the user manually places two seeds on the reference and floating datasets. Each seed should locate the approximate centre of the aorta on one of the 2D axial slices. A 2D ROI is then generated around the seed. Then for each 3D volume, the manually generated 2D ROI is used to automatically track the seeds and 2D ROIs on other slices of the same volume. All the 2D ROI centres of the two volumes, considered as two point clouds, are then used to calculate an initial alignment of the reference and the floating datasets, using the triangulated topological features and the least squares SVD method. After the initial alignment, the data alignment is then refined by a voxel intensity based asymmetric cluster-to-image registration process, within a dual-level, multi-resolution framework. Figure 3.13 demonstrates the structure of this registration framework.

3.4 Graphical User Interface

The registration framework described above is designed to assist the clinicians and researchers analysing data acquired for the *MA³RS* study. Feedback and ground truth collected from these users is critical for validation and evaluation of the registration algorithm performance. Thus I developed a clinician-friendly graphical user interface (GUI) to allow users to register data and collect ground truth for the evaluation. The software featured two interfaces, as shown in figures 3.14 and figure 3.15.

Figure 3.14 shows the GUI used to load the data and perform registration. It reads multiple 2D slices from the different modalities saved in DICOM format, automatically building 3D volumes based on the DICOM header information. Users may easily adjust some pre-defined parameters, observe the data, and define ROIs. Using the default parameter settings, the only interaction between the user and the data is the two clicks required to place the seed points on the reference and floating images. The GUI also allows users to separately perform the initial alignment, coarse-level registration and fine-level registration following the real-time instructions displayed by a *HELP* module, and supervise the progress of the registration. The original data can also be preprocessed using simple contrast enhancement and noise removal methods for better visibility.

When the registration process is complete, users have a comprehensive visual assessment of the results using the second GUI, shown in figure 3.15. This GUI allows users to observe the result from different viewing angles, and using different intensity ratios between the reference and floating volumes. Importantly, there is a manual registration module that allows users to manually correct the automatic rigid transformation, or to directly perform a purely manual registration and save the errors or transformation. This module collected both the qualitative and quantitative evaluation results used in this project. Furthermore, the alignment results may be displayed with different visualization methods, for example overlapped colour

channels, or chessboard visualization with different colour maps. The user can dynamically switch the display between reference and floating datasets. Some buttons were provided for customized functions specifically to support the imaging and analysis protocol of the *MA³RS* project. For example, there are customized buttons that apply a saved transformation matrix to different floating datasets, or aortic wall manually segmented by clinicians, and buttons that align all the images using all the available transformation matrices. Figure 3.16, 3.17 and 3.18 show examples of a pair of aligned pre- and post-contrast T2*W datasets displayed with different visualization methods. Figure 3.19 shows a registration example of the R2* map dataset, which were aligned by applying the transformation matrix obtained from the registration performed between T2*W datasets. This GUI also allows the user to visualize three volumes at the same time using red, green and blue colour channels. Figure 3.20 shows an example of the manually segmented aortic structures overlapped with pre- and post-contrast R2* map dataset.

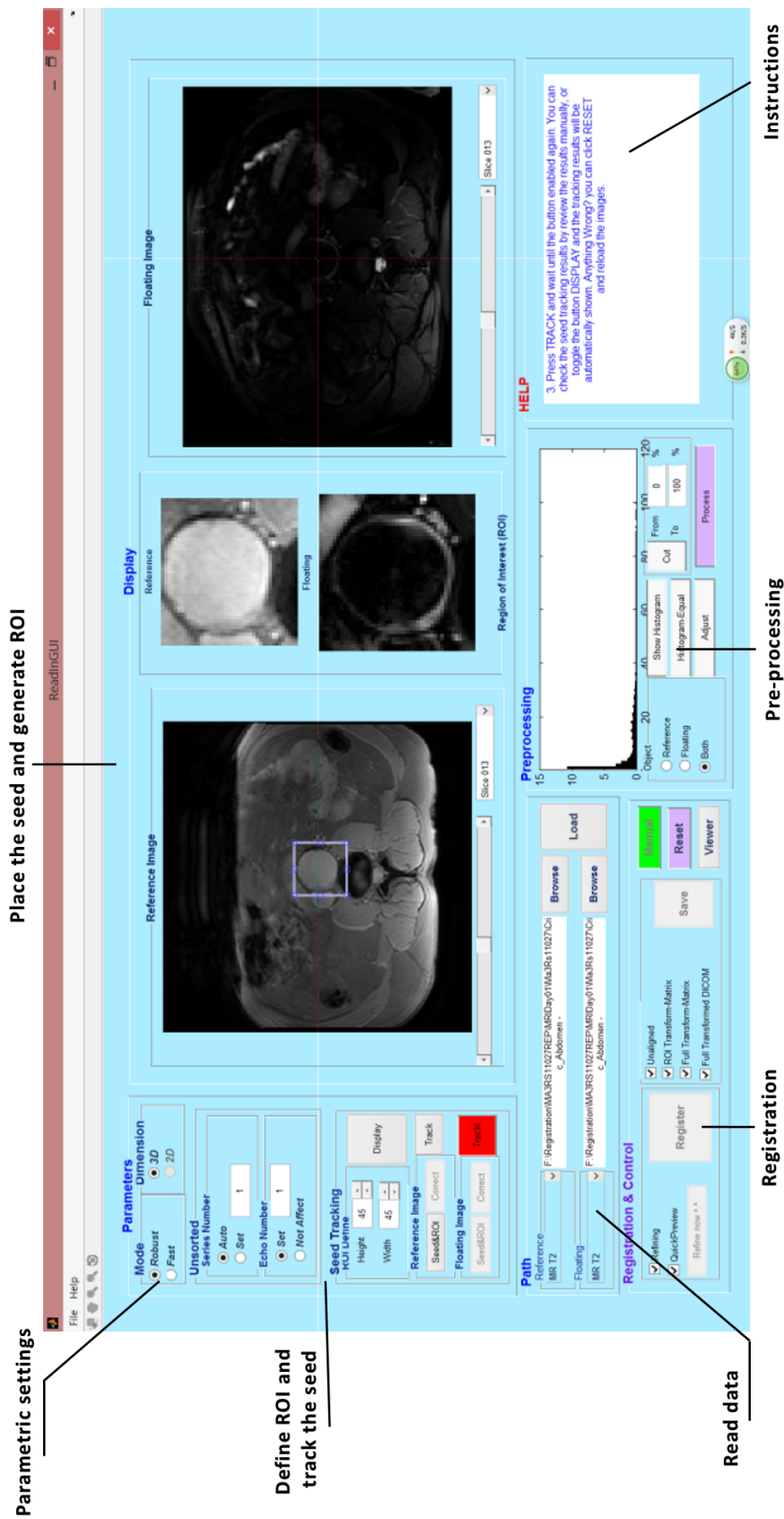


Figure 3.14: The GUI used for semi-automatic registration

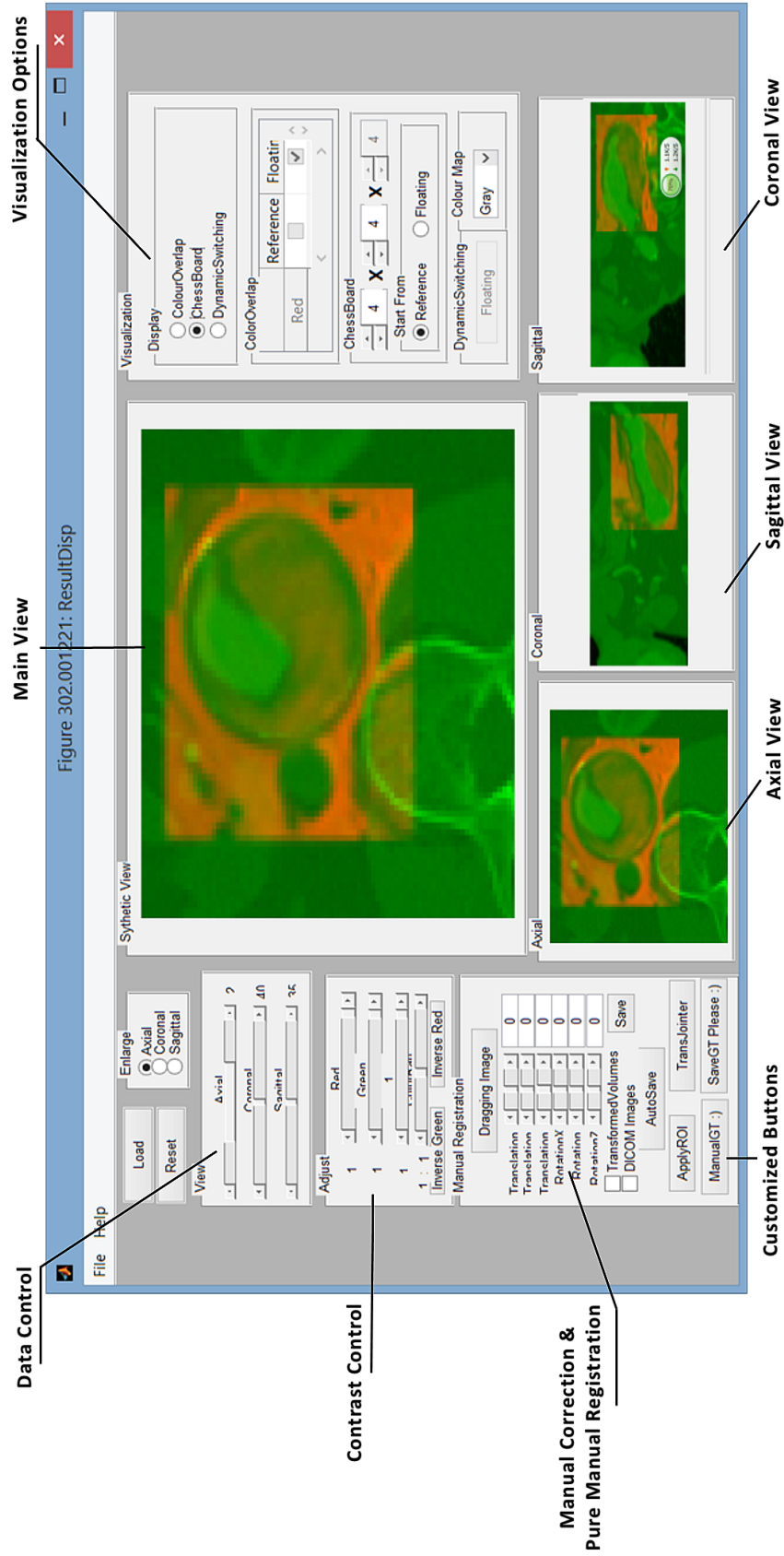


Figure 3.15: The GUI used for observing results and manual registration

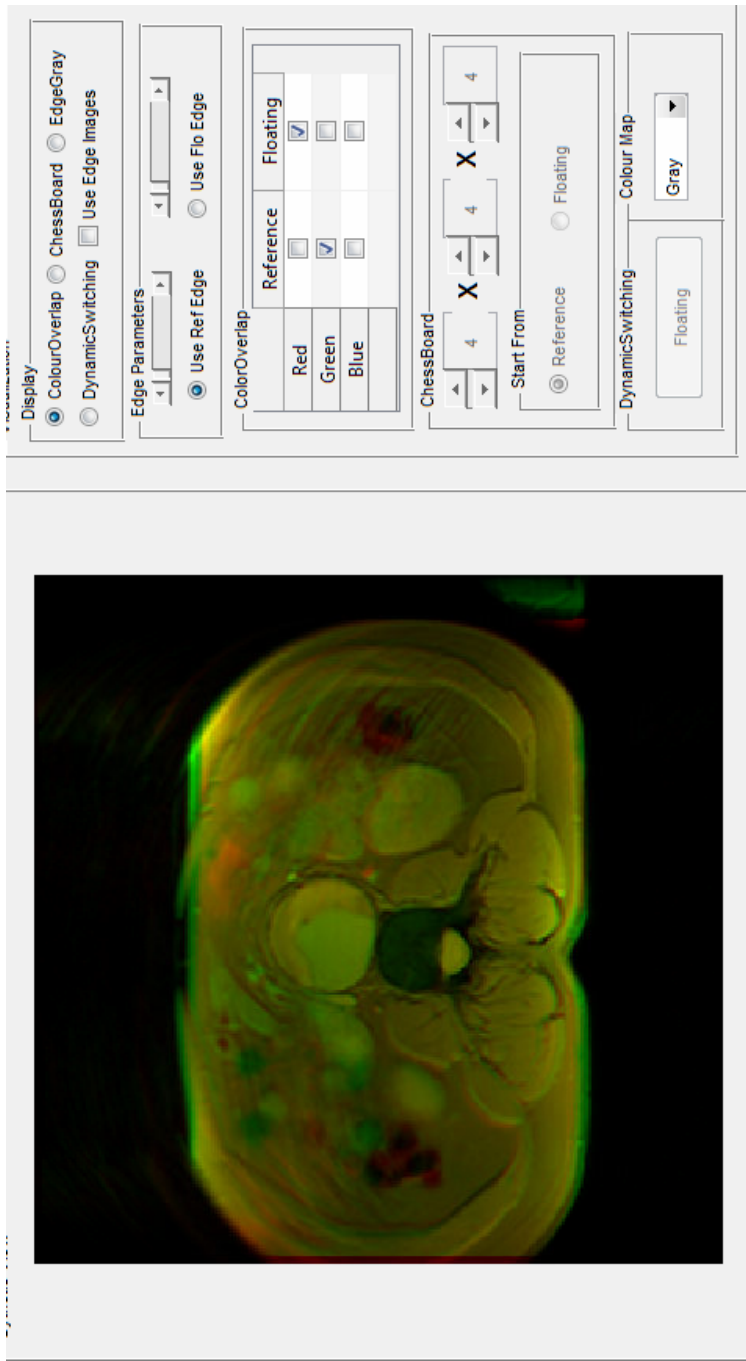


Figure 3.16: An example of aligned multi-contrast T2* weighted data visualized by overlapped red-green colour channels.

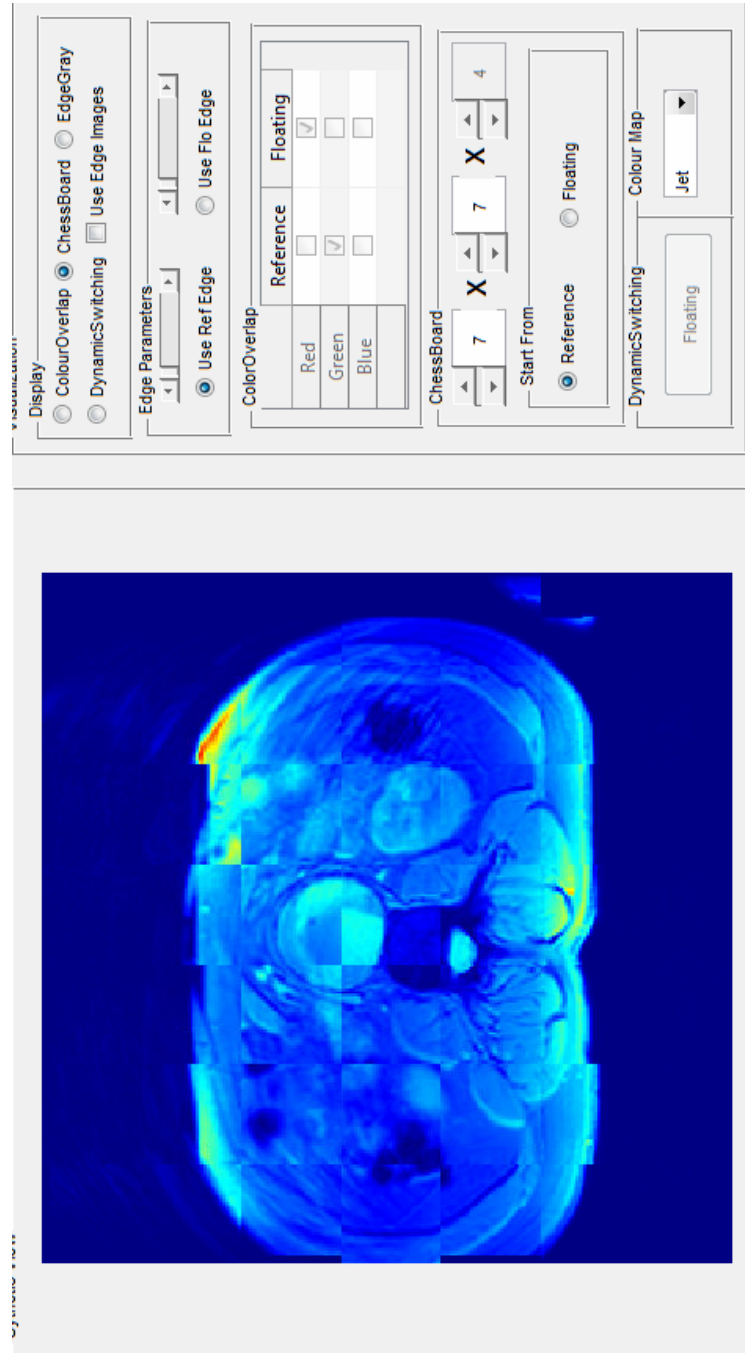


Figure 3.17: An example of chessboard visualization of aligned multi-contrast T2* weighted data.



Figure 3.18: An example of aligned multi-contrast T2* weighted data visualized by overlapping the edge image of the floating data with the reference data.

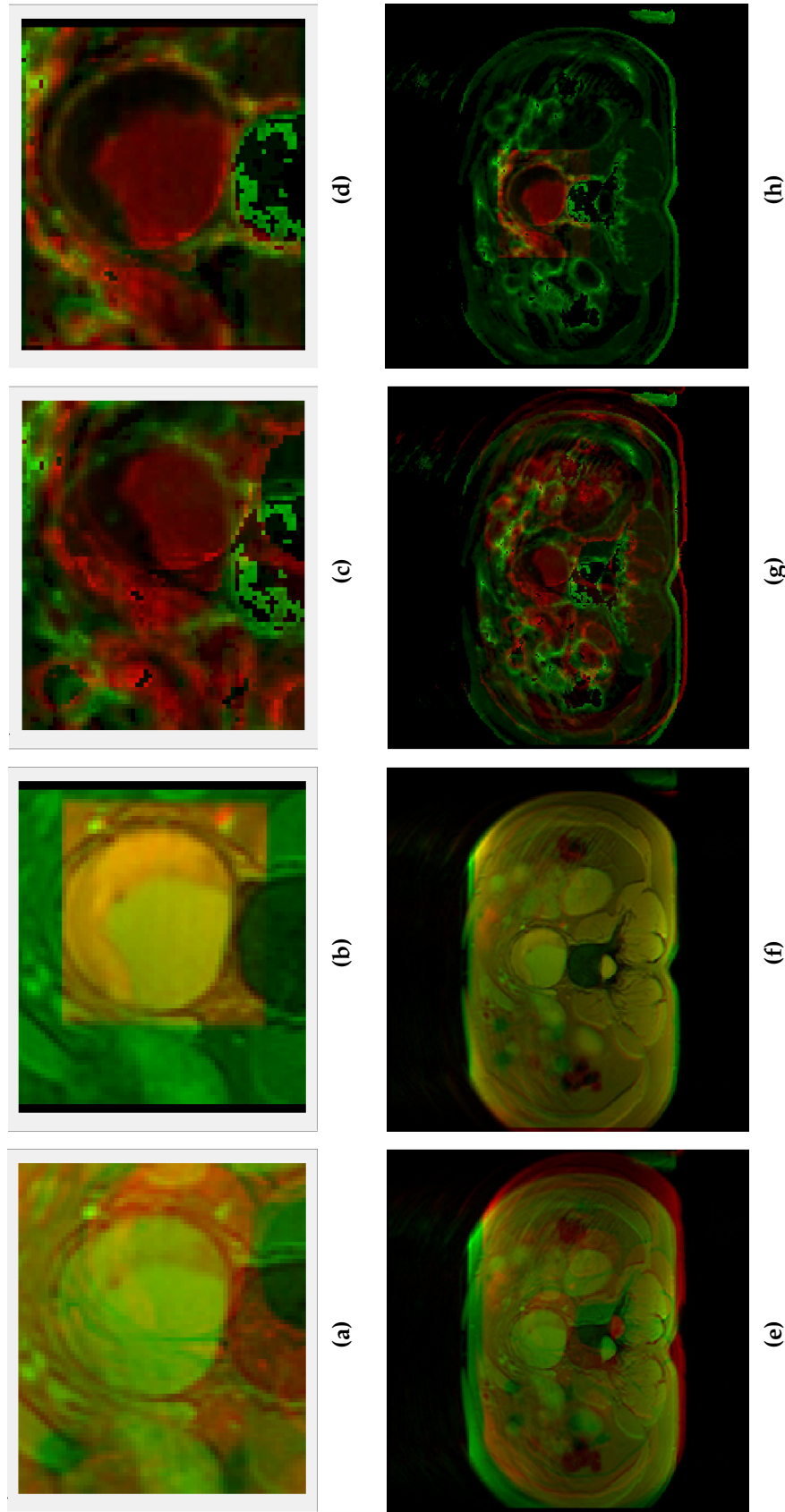


Figure 3.19: Example of aligning R2* weighted data using the transformation matrix obtained by registering the T2* weighted data: (a), (b), (e), (f) show the ROI and full image of T2*W data before and after registration; (c), (d), (g), (h) show the R2*Map data before and after applying the transformation. Data is visualized using overlapped red-green colour channels, overlapped parts tend to be yellow.

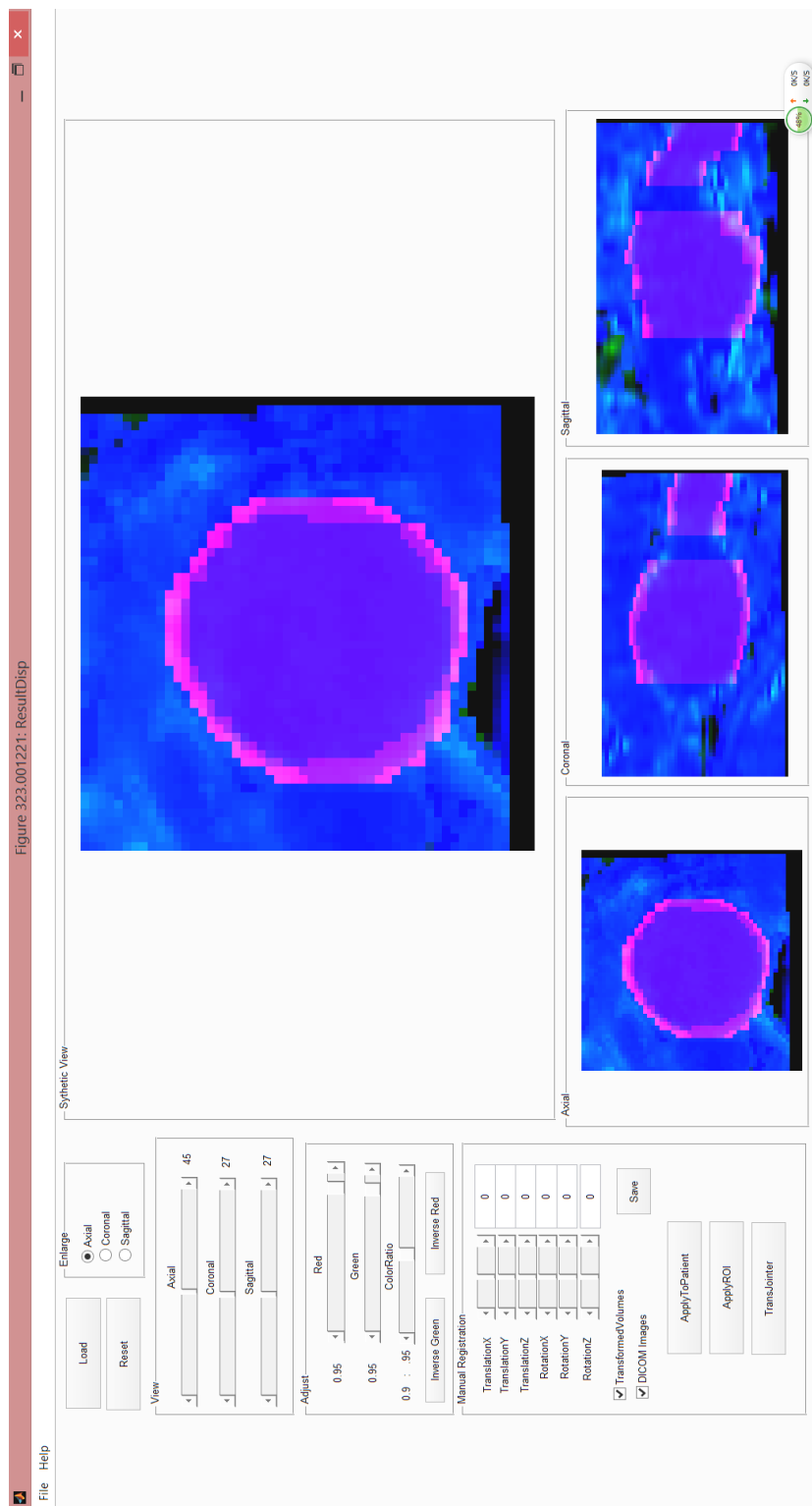


Figure 3.20: Alignment results of Day1 and Day2 R2*Map volumes with the manual segmented aortic wall. Red channel is the aortic wall, while green and blue channels show Day1 and Day2 axial data respectively.

3.5 Evaluation criteria of Registration Results

Based on the *MA³RS* imaging and analysis protocol, in each two-day clinical assessment, the purpose of co-registration is to align the pre- and post-contrast T2*W data acquired before and after administration of USPIO, and to align T2*W data with T2W data, with or without fat suppression, on which the anatomical structures (aortic wall, thrombus, blood pool, etc.) of aneurysm were manually segmented. CT data is also available for analysis of anatomical information. Thus for each assessment, at least one registration is performed for post- to pre-contrast T2*W data, and one is performed to align the pre-contrast T2*W data to T2W data. All the images of a patient can be aligned using transformation matrices obtained from these two registrations, except the CT data, which generates all the clinical analysis required by the *MA³RS* protocol. Data from 344 patients were registered. 22 of them went through one-month reproducibility assessments, and 59 went through one-year reproducibility assessment and 20 through two-year reproducibility assessment. Thus transformations from $344 + 22 + 59 + 20 = 445$ post- to pre-contrast T2*W registrations, and the same number of pre-contrast T2*W to T2W registrations were performed.

These data provide an abundant resource to perform and develop quality measures of evaluation of the proposed registration framework. Various qualitative and quantitative evaluation standards have been proposed in the past decades [106, 192]. With sufficient corresponding landmarks, which unfortunately was not the case for the *MA³RS* project, then the registration performance may be evaluated based on the target registration errors (TRE). In practice, the limited accessibility to gold standard ground truth has meant a variety of lesser rigid registration validation methods have been employed in various applications [193]. Many validation methods compare the results gained by the proposed work with a few well-known schemes, and use different types of similarity measures as quantitative references of

3.5 Evaluation criteria of Registration Results

success. Most quantitative validations require extra work, such as segmentation or identification of particular landmarks and features [30].

In this work, the registration results were evaluated both qualitatively and quantitatively. Both the qualitative and quantitative assessments relied on visual inspection. The users observed the result of each registration, visualized by the different options in the GUI shown in Figure 3.15. They then manually corrected the transformation, including translations and rotations in each dimension, until they felt the alignment could not be improved any further. The corrected translations and rotations were automatically recorded by the software as they can be considered as a type of quantitative means of the automatic registration accuracy. This evaluation method has the advantage that it allowed us to collect large numbers of results, with minimal additional effort on the part of the users. However, the disadvantage of this method was that it is possible the users' judgements of the registration could be biased by the automatic result they saw first. Thus, pure manual registrations were also performed to try and avoid this potential bias. The differences between these pure manual registration and the automatic registration results were used as the errors. Although the quality measures based on visual inspection are less objective than TRE calculated using fiducial markers or landmarks, it has been accepted that human vision system can be relied on detecting a TRE greater 2mm for CT and MR images [194]. Figure 3.21 shows a diagrammatic sketch of the methods used to evaluate the registration framework.

3.5.1 Evaluation using manual corrections

For the qualitative evaluation, users directly manipulated the automatic registration results of ROIs, as this is faster and more accurate than manually correcting the full volumes. Thus, the transformation matrices for the full images are unknown in these cases, and translational and rotational errors were measured independently. Besides analysis along each dimension, the performance of a registration should be evaluated

by a single translational error and a single rotational error. The translational error can be measured comprehensively by the Euclidean distance. For rotational errors, Euler's rotation theorem states that any rotation of a rigid body in a three-dimensional space can be represented by a single Euler angle and a Euler axis, which is also known as the axis-angle representation [195]. The Euler angle can be calculated from the rotation matrix by [195]:

$$\Theta_e = \cos^{-1} \left(\frac{\text{Tr}(\mathbf{R}_e) - 1}{2} \right) \in [0, \pi], \quad (3.30)$$

where Θ_e is the rotational error represented by a Euler angle measured in radians, \mathbf{R}_e is the rotational error represented by a rotation matrix, and $\text{Tr}(\cdot)$ is the trace of a matrix. For the qualitative evaluation, the rotational matrices are just the sub-matrices of the ROI transformation matrices representing the manual corrections. For the *MA³RS* project, results from all the 445 clinical assessments were used for qualitative assessments. All the data used for registration were re-sampled uniformly to a resolution of $1.5625 \times 1.5625 \times 5$ mm. The translational errors were measured in millimetres, and the rotational errors in degrees. To attenuate the inter-personal variances, the automatic registration results were evenly and randomly distributed to 4 users (2 clinical researchers and 2 registration experts).

3.5.2 Evaluation using pure manual registrations

For the quantitative evaluation, because the manual registration and the automatic registration results were obtained independently, transformation matrices of the full data can be easily calculated for both. When considering the manual registrations as golden standard, the TRE can be estimated using 8 quasi-landmarks located at the centres of the 8 corner voxels for the full volume data as discussed in the *Retrospective Image Registration Evaluation (RIRE)* project [193] conducted by Vanderbilt University. *RIRE* is designed to compare retrospective CT-MR and PET-MR registration techniques. Due to the intensive interactions required by the users to quantitatively evaluate this registration framework, data of 78 patients were manually

3.5 Evaluation criteria of Registration Results

registered by three users with different academic backgrounds. For each patient, this involved a post- to pre-contrast T2*W registration, a T2*W to T2W registration, as well as a CT to T2W registration. The TRE was estimated in millimetres.

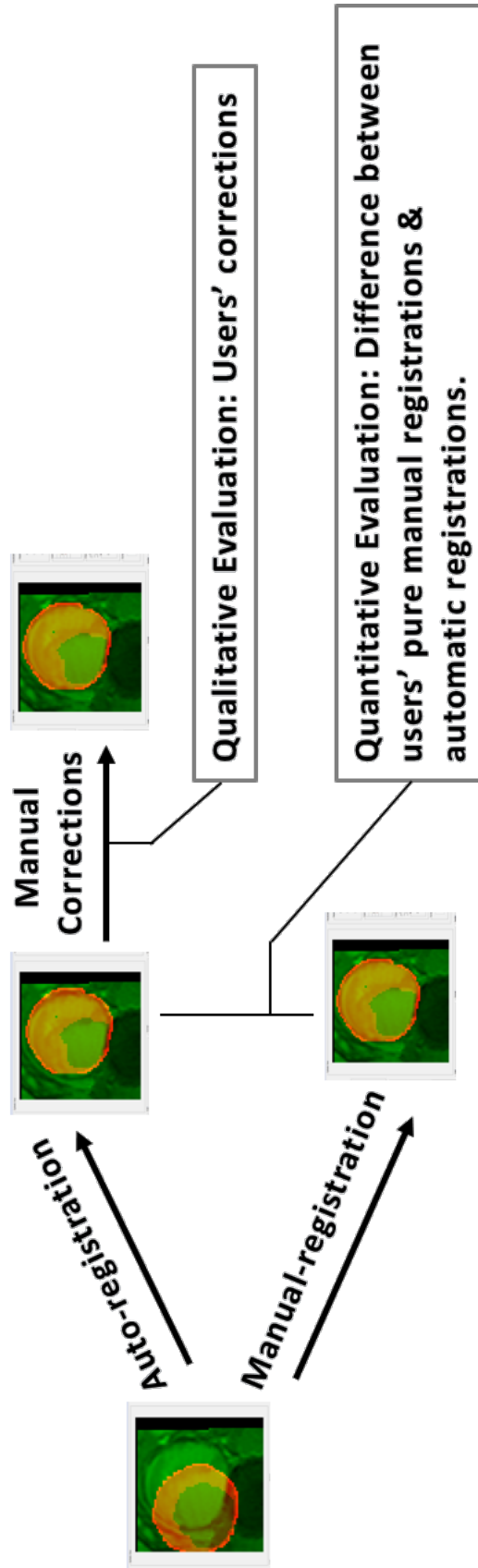


Figure 3.21: *Evaluation of registration*

3.6 Results

3.6.1 Visualization

Figures 3.22, 3.23 and 3.24 show an example of the pre-contrast T2*W data overlapped with the aneurysm anatomical structures manually segmented on the T2W data acquired on the same day, including the ROIs and full data before and after automatic registration and manual corrections. It can be clearly seen that manipulating the ROI images was easier than directly transforming the full volume data. These visualized data were used for qualitative evaluations based on the users' visual assessments. Figures 3.25, 3.26 and 3.27 show an example of the edge image of a post-contrast T2*W data generated with Canny edge detector [196] overlapped with pre-contrast data, before and after automatic and manual registration. Figures 3.28, 3.29 and 3.30 show an example of overlapped CT and pre-contrast T2*W data, before and after automatic and manual registration, visualized using the red and green colour channels.

3.6.2 Qualitative Evaluation Results

Table 3.1 shows the mean translational and rotational errors along each dimension, as well as errors measured by Euclidean distance and single Euler angle, for post-to pre-contrast T2*W registration, and T2W to T2*W registration. Figure 3.31 shows the histograms of the translational and rotational errors for all registrations. For the T2*W–T2*W registrations, the translational errors for 215/445 subjects were less than the voxel size, i.e. less than 1.5625 mm. For 284/445 subjects there was no rotational error. For the T2W–T2*W registration, the proposed method achieved sub-voxel translational accuracy for 190/445 patients, and 378 out of 445 subjects had no measurable rotational error. Since the T2W data provided more anatomical information than the T2*W images, the T2W–T2*W registrations resulted in comparable mean translational error, but smaller rotational error than the T2*W–

T2*W registrations. As a result of the proposed initial alignment method based on the triangulation topological features, the out-of-plane translational errors along the z direction tend to be smaller than those in the other two directions.

3.6.3 Quantitative Evaluation Results

Statistics of quantitative evaluation results, measured as TRE, are shown in Table 3.2. Of the data from 78 subjects included in the quantitative evaluation, the following percentages achieved sub-voxel accuracy: 29.5% of T2*W–T2*W registrations, 43.6% of T2W–T2*W registrations, and 26.9% of CT–T2*W registrations achieved sub-voxel accuracy. The T2W–T2*W volume pairs tend to be aligned better based on the mean, median, and standard deviation of the registration results. The proposed method can achieve CT–T2*W registration accuracy that is comparable to multi-contrast T2*W–T2*W registration.

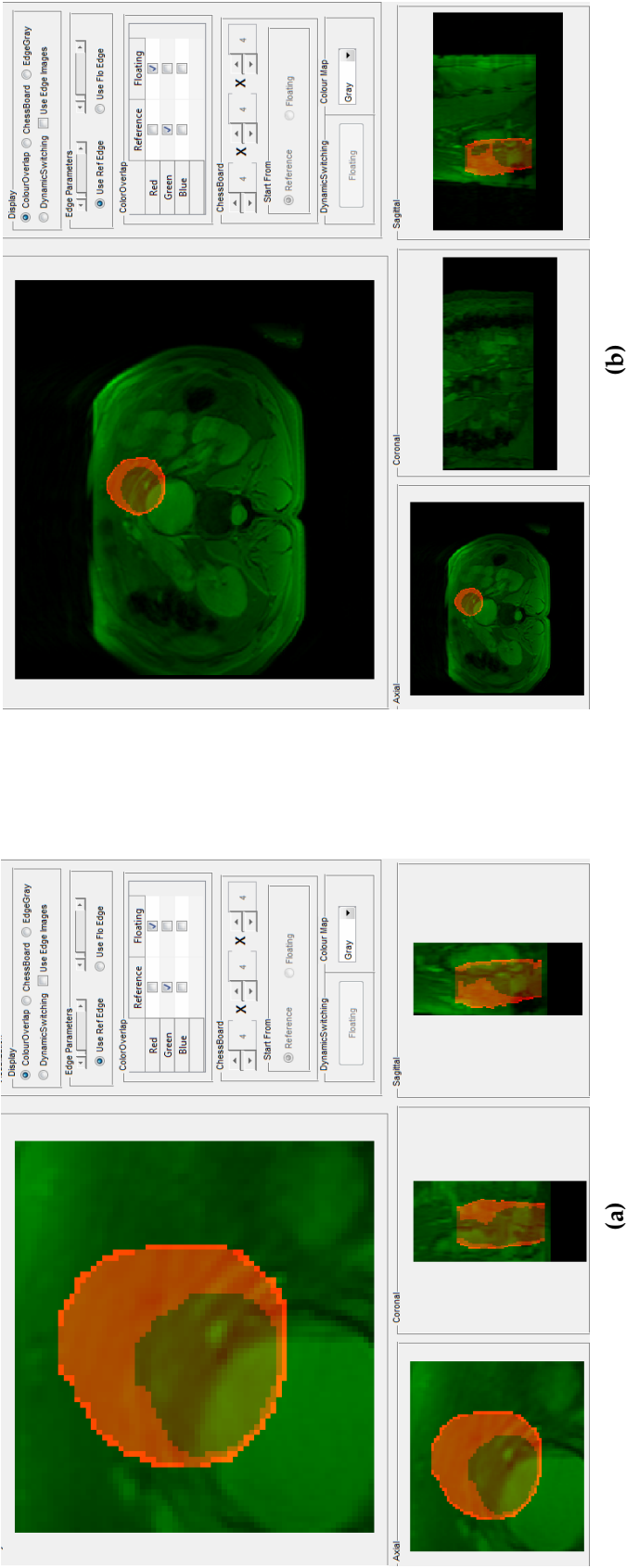


Figure 3.22: A pre-contrast T2* weighted volume overlapped with anatomical structures manually segmented from a T2 weighted data before registration visualized in green and red colour channels: (a) ROIs; (b) full volumes.

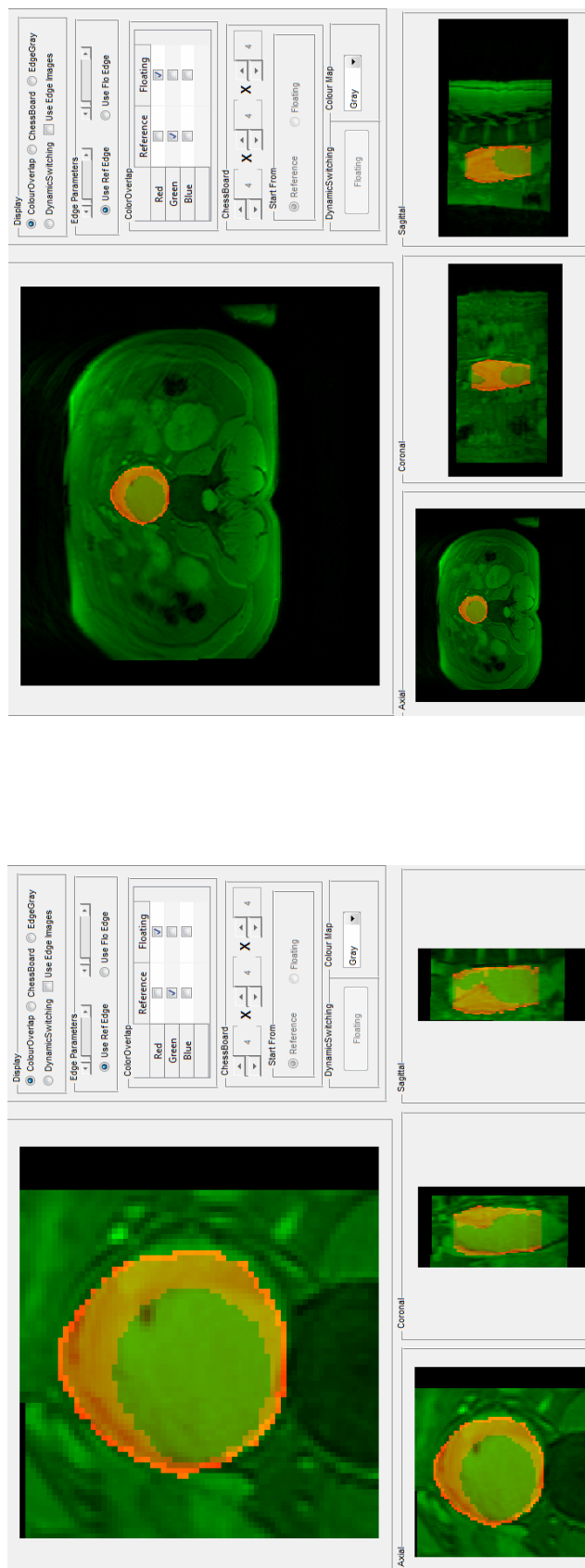


Figure 3.23: A pre-contrast T2* weighted volume overlapped with anatomical structures manually segmented from a T2 weighted data after automatically registered using the proposed method visualized in green and red colour channels: (a) ROIs; (b) full volumes.

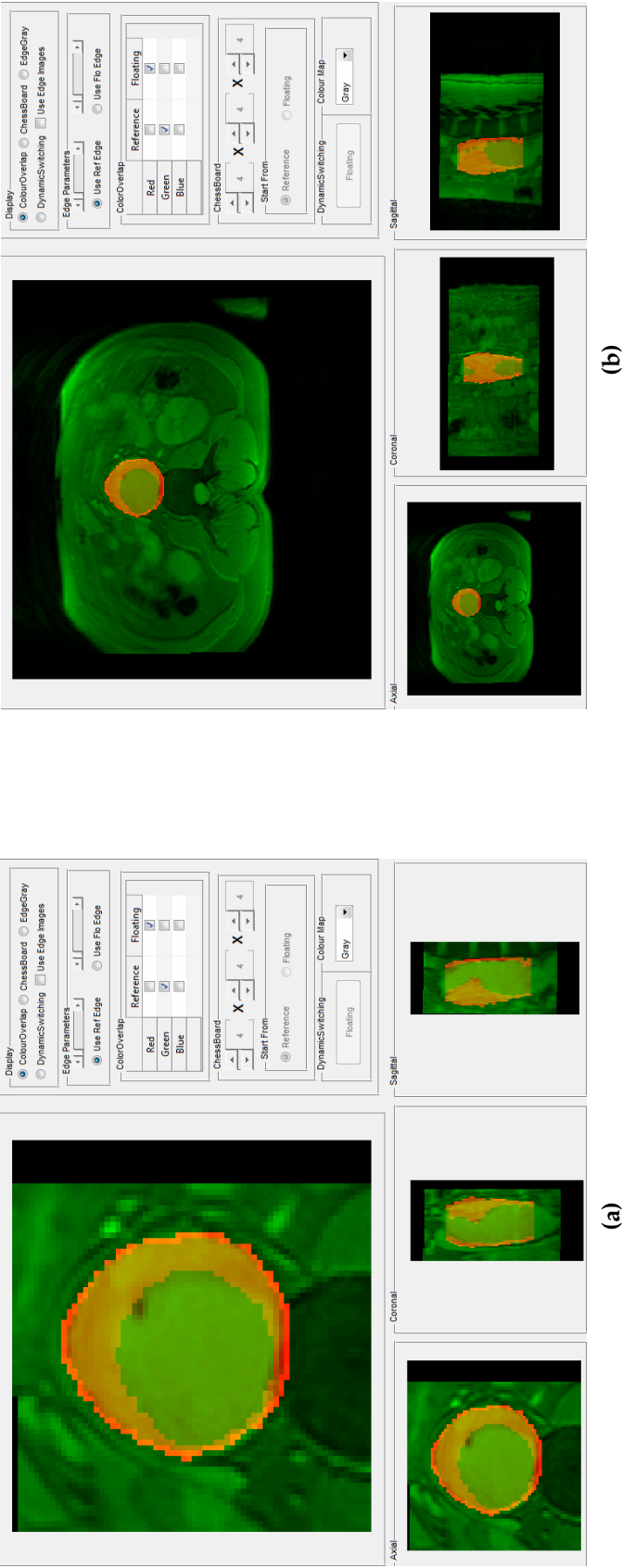


Figure 3.24: A pre-contrast T2* weighted volume overlapped with anatomical structures manually segmented from a T2 weighted data after manually registered visualized in green and red colour channels: (a) ROIs; (b) full volumes.

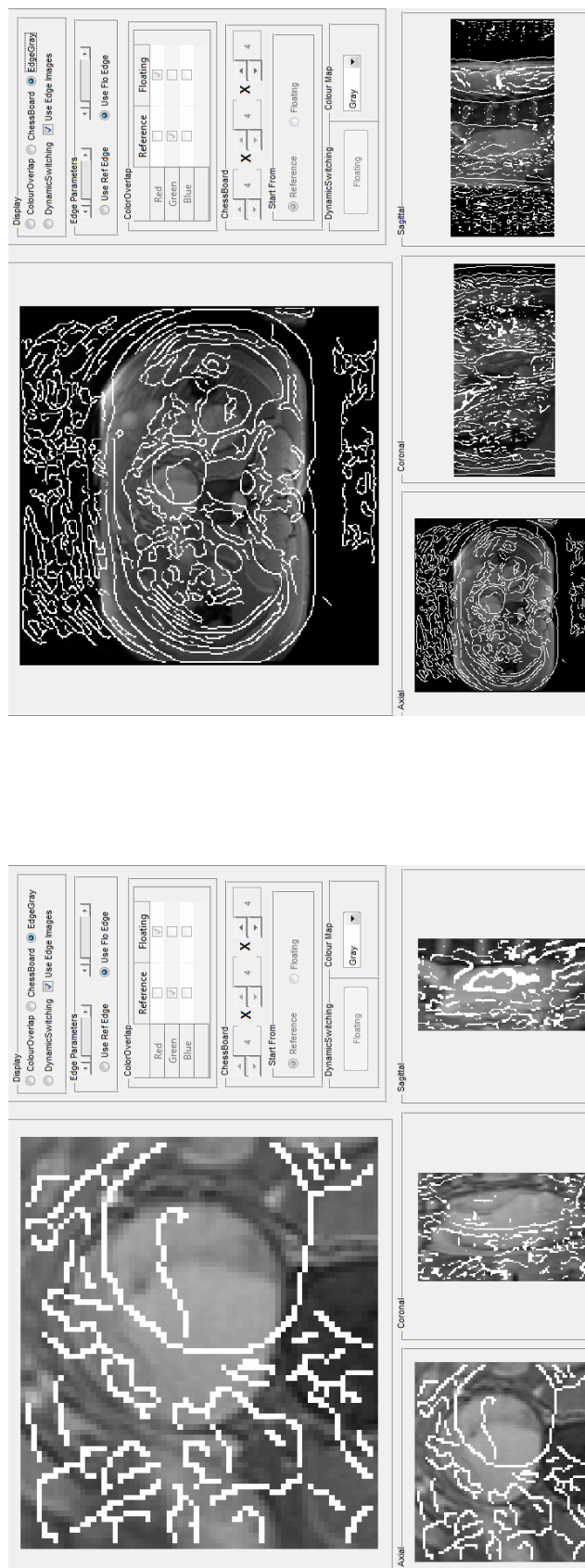


Figure 3.25: Visualization of the edge image of post-contrast T2* weighted (T2*W) data overlapped with pre-contrast T2*W data before registration: (a) ROIs; (b) full volumes.

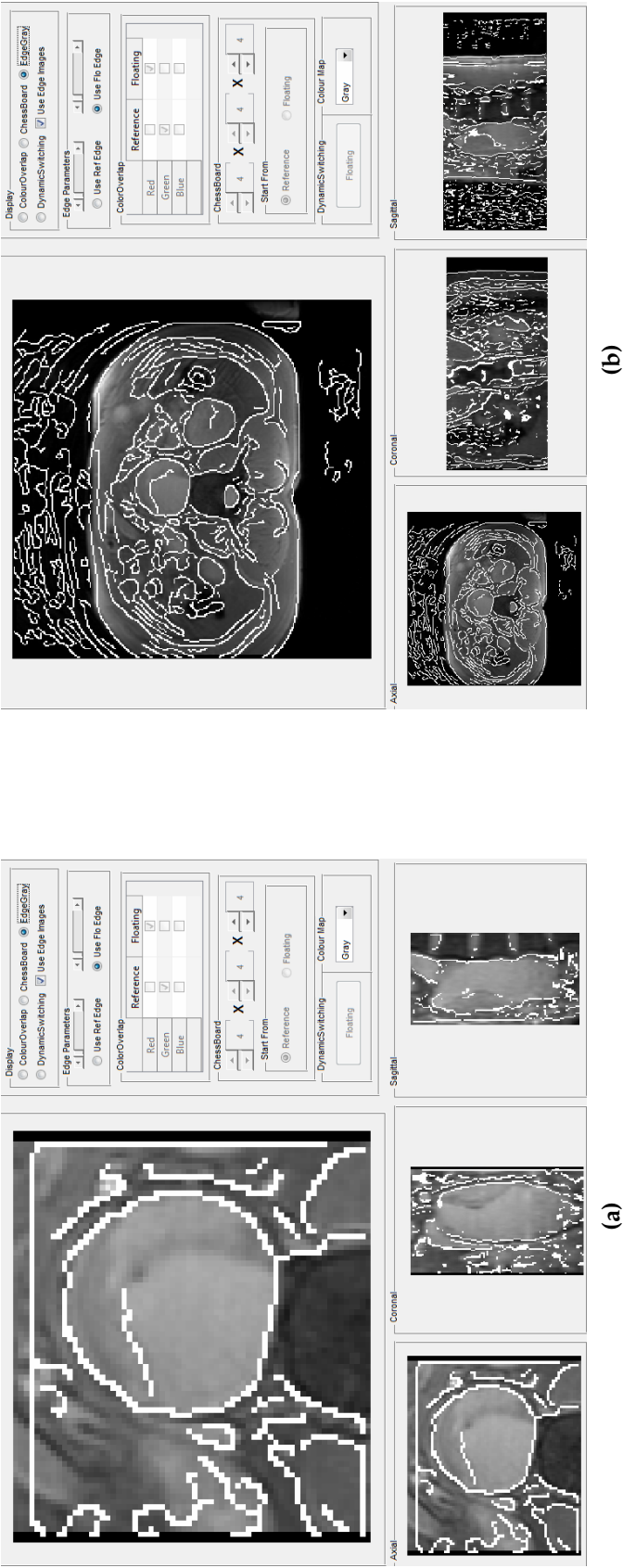


Figure 3.26: Visualization of the edge image of post-contrast T2* weighted (T2*W) data overlapped with pre-contrast T2*W data after automatically registered by the proposed method: (a) ROIs; (b) full volumes.

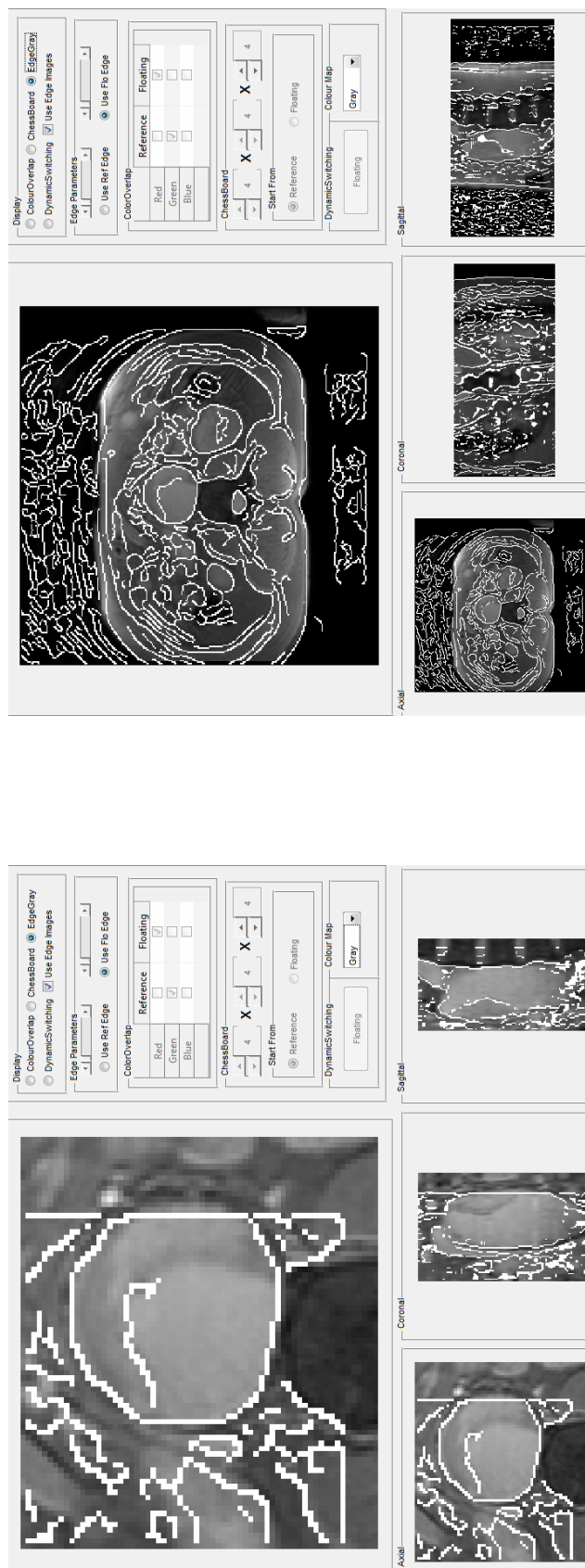


Figure 3.27: Visualization of the edge image of post-contrast T2* weighted (T2*W) data overlapped with pre-contrast T2*W data after manual registrations: (a) ROIs; (b) full volumes.

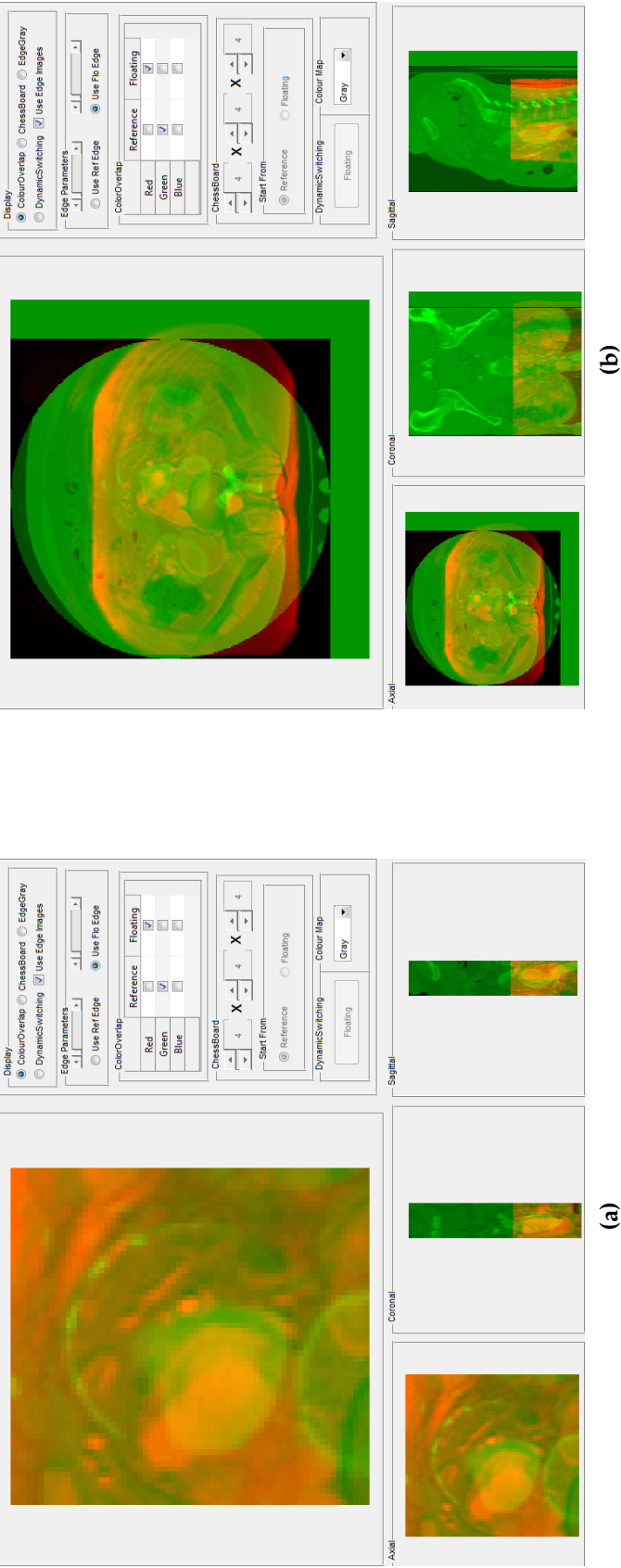


Figure 3.28: A pre-contrast T2* weighted volume overlapped with CT data before registration visualized in green and red colour channels: (a) ROIs; (b) full volumes.

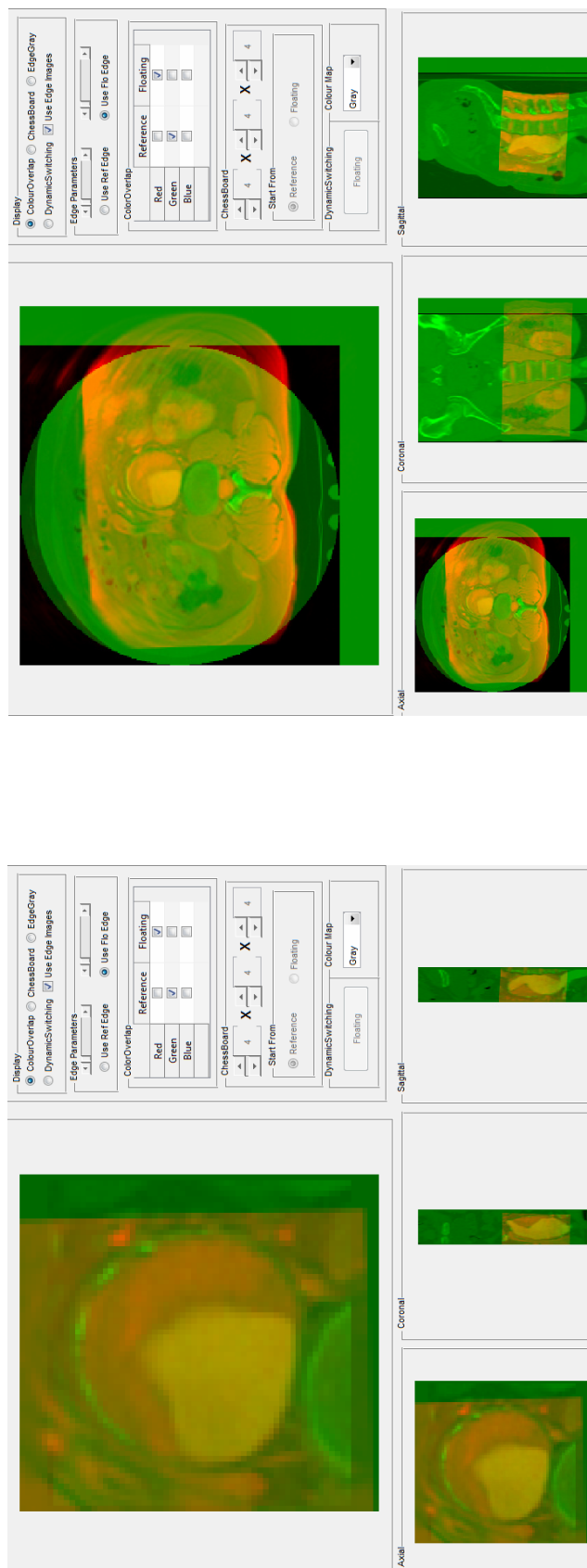


Figure 3.29: A pre-contrast T2* weighted volume overlapped with CT data after automatic registration by the proposed method visualized in green and red colour channels: (a) ROIs; (b) full volumes.

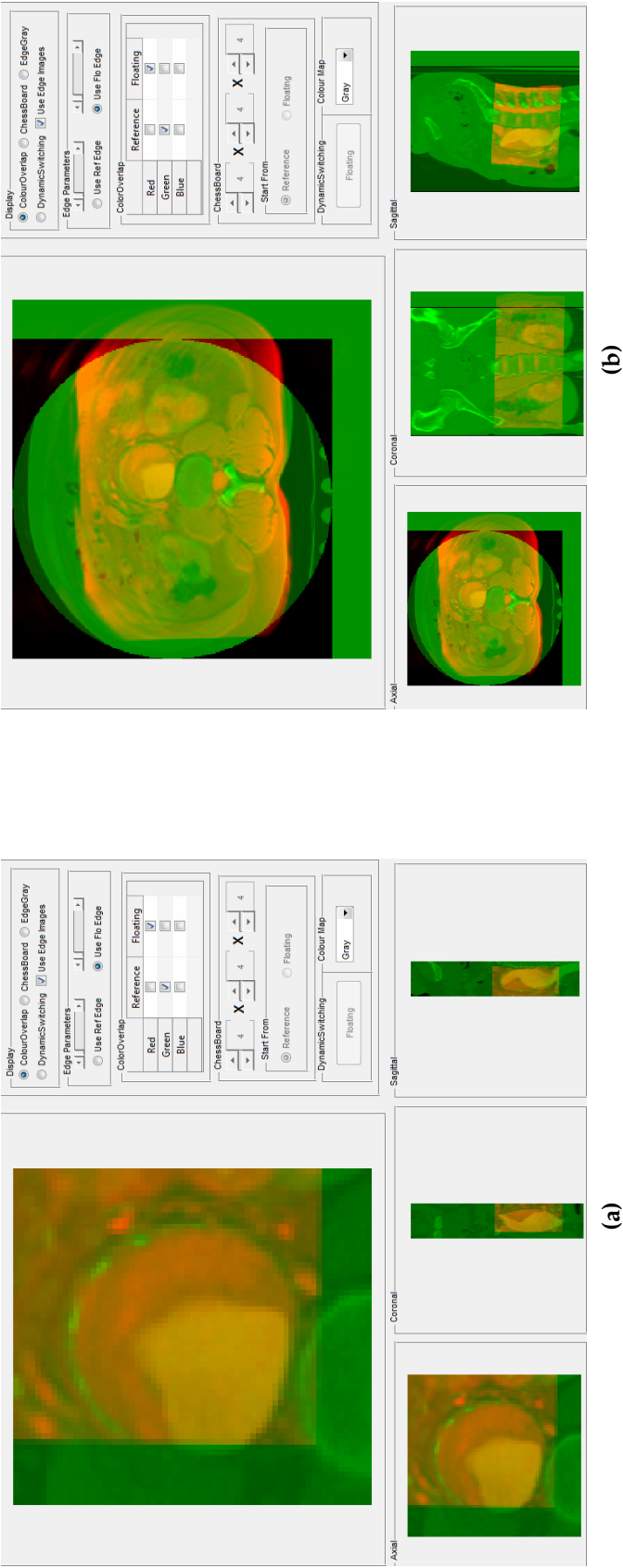


Figure 3.30: A pre-contrast T2*-weighted volume overlapped with CT data after manual registration visualized in green and red colour channels: (a) ROIs; (b) full volumes.

3.7 Conclusion and Discussion

This chapter described a new semi-automatic rigid registration framework integrated into a novel graphical user interface, customized for the on-going MA³RS clinical trial. The method requires only two user interactions, to place two seed points on the reference and floating images. The full 3D ROI is then automatically generated by tracking the centre of the aorta on each axial slice. The novel contributions in this chapter include an automatic ROI tracking method that is applicable to axial images of tubular objects, a new initial alignment step using a triangulation feature and a simplified implementation of RANSAC method, a new multi-resolution, cluster-to-image registration framework based on the “bottom-up” implementation of k -means algorithm, and a set of GUIs that allow manual improvements and evaluation of the registration results. The performance of rigid registration methods is qualitatively evaluated based on the “angle-axis” representation of user manual corrections, as well as the differences between the automatic registrations and the pure manual registrations. Over half of the registrations were seen to achieve sub-voxel accuracy. This framework can easily be extended to non-rigid registration, by using transformation models with more degrees of freedom, and adopting local optimization methods, after the data is rigidly registered. It can also be applied to register short-axis cardiac data, since the left ventricle also displays an approximately circular cross-section, and thus can be tracked by the same ROI generation process.

A serious problem encountered when dealing with MR data is *intensity inhomogeneity*, the so-called bias field, which can significantly degrade the registration results. In the past two decades, many intensity inhomogeneity correction methods have been proposed as a pre-processing step to reduce the effect of this artefact on further image analysis results. In the next chapter, a comparison is made of popular correction methods in preparation of my own pre-processing procedure, before a novel registration algorithm is applied.

3.7 Conclusion and Discussion

Table 3.1: MR image registration errors, including translational and rotational errors in x , y , z directions, and the mean Euclidean errors and rotational errors calculated as the equivalent single rotation by the rotational errors. Translational error presented as millimetres and number of pixels (shown within brackets), and rotational error in degrees where all images were down sampled to 1.5625mm per voxels.

axis	T2*W–T2*W			
	Translation	Rotation	Euclidean Translation	Rotation Angle
x	1.5532(0.99)	0.3600	2.8440(2.30)	0.8396
y	1.9559(1.25)	0.0965		
z	1.3603(0.87)	0.4918		
axis	T2W–T2*W			
	Translation	Rotation	Euclidean Translation	Rotation Angle
x	2.1617(1.38)	0.0659	3.1583(2.61)	0.2169
y	2.0019(1.28)	0.0353		
z	1.1378(0.73)	0.1600		

Table 3.2: Statistics of target registration errors measured in mm

	Mean	Median	STD	Sub-voxel accuracy
T2*W-T2*W	6.5466	3.1466	7.6571	23/78
T2W-T2*W	4.0582	2.1155	5.5251	34/78
CT-T2*W	6.4416	3.0800	6.6606	21/78

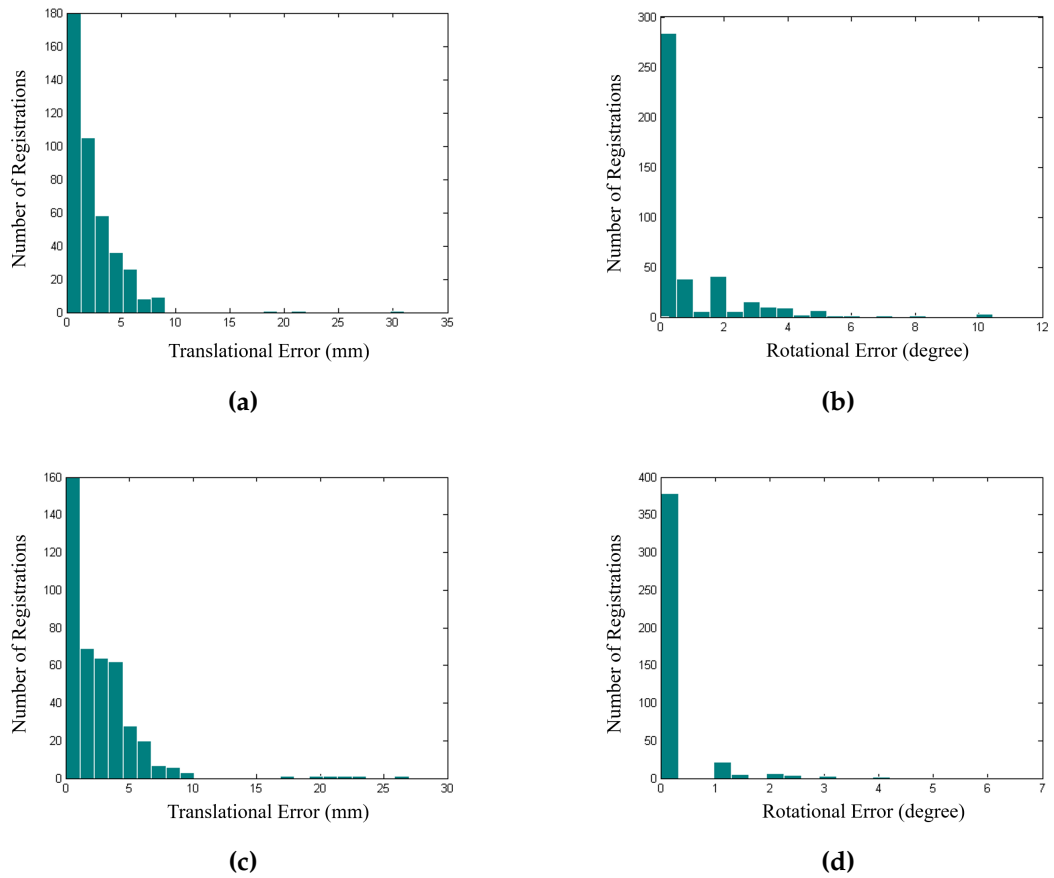


Figure 3.31: Histograms of number of registrations verses translational and rotational errors of the post- to pre-contrast T2* weighted (T2*W) registration and T2 weighted (T2W) to T2*W registration: the results of T2*W-T2*W registration are shown at the top, results of T2W-T2*W registration at the bottom; the translational errors measured in mm are shown on the left, rotational errors measured in degree on the right.

Preprocessing: Intensity Inhomogeneity Correction for Effective Post-processing

ABSTRACT

The registration framework described in the last chapter successfully registered the majority of the data acquired for the *MA³RS* trial. However, when the framework was applied to cardiac data from another clinical trial, it failed for almost half of the registrations. The reason for the failure was the presence of severe intensity inhomogeneities in the MR cardiac data. Thus, an additional preprocessing step was necessary to correct the inhomogeneity before the registration was performed.

To gain an insight into state of the art intensity inhomogeneity correction methods, and to prepare for the development of a preprocessing step for the proposed registration framework, a comparison was made of inhomogeneity correction methods. Following a brief review of typical methods, four representative correction methods were selected for experiments, with a widely used benchmark MR data simulator. The conclusions were obtained from simulated data with different parametric settings about the performance of the difference methods under different levels of intensity inhomogeneity and additive noise.

4.1 Introduction

MR images may suffer from a number of artefacts that cause both intensity and spatial errors. One of the most common artefacts that affects the performances of image analysis algorithms is intensity inhomogeneity, often described as the “bias field”. This artefact can confound subsequent analysis of the images. The registration tool developed for the *MA³RS* project, as introduced in last chapter, can successfully process most data collected for this clinical trial. However, when the same method was much less successful when applied to align the multi-parametric and multi-contrast cardiac MR (CMR) data from another clinical trial (Iron nanoparticle enhanced MRI in the assessment of inflammation after myocardial infarction, or *IRNMAN*, The British Heart Foundation and Chief Scientist Office: CH/09/002, 2012-2016).

The *IRNMAN* study, led by the Clinical Research Imaging Centre (CRIC), University of Edinburgh, aims to assess inflammation in the myocardium post-infarction, through a combination of T2* weighted (T2*W) pre- and post-contrast ultra-small superparamagnetic particles of iron oxide (USPIO) data, in a similar application for targeted inflammation imaging like the *MA³RS* trial, along with standard clinical delayed enhancement assessment of myocardial infarction. Inclusion criteria for participants were that they must be aged 18 to 80 years, and had sustained a recent myocardial infarction with 12-hour plasma troponin I concentration ≤ 5000 ng/l. Exclusion criteria were known critical stenosis ($>95\%$) of left main stem, ongoing symptoms of angina, heart failure (Killip class ≤ 2), renal failure (estimated glomerular filtration rate <30 ml/min, and contraindication to MRI or ferumoxytol infusion. Multi-parametric MR data of 30 patients were acquired contiguously in the short-axis plane, and were ECG-gated to be acquired during diastole and expired breath-holding, which enabled rigid-body registration. The short-axis images are acquired to show the cross-sections of left and right ventricles along the perpendicular direction of long-axis of left ventricle as shown in Figure 4.1 [4]. Each subject had one T1 weighted

(T1W) delayed enhancement volume to assess myocardial infarction, one pre-contrast T2*W volume, and at least three post-contrast T2*W volumes to visualize the uptake of USPIO, all having a resolution of $1.56 \times 1.56 \times 10$ mm.

Similar to the co-registration protocol of the *MA³RS* project as introduced in chapter 3, for this *IRNMAN* trial, pre- and 24 hrs post-USPIO T2*W data is co-registered to assess localisation of the USPIO (macrophage uptake) throughout the myocardium. To assess the co-localisation of USPIO uptake with presence of infarct, the T2*W and delayed enhancement (acquired to visualize infarct) datasets are also registered. However, this cardiac T2*W data suffers from a more severe intensity inhomogeneity than *MA³RS* data, which is caused by patient loading and coil proximity effects. Figure 4.2 shows an example of T2*W images from the two clinical trials. This makes the asymmetric k-means cluster-to-image registration framework fail to register over half of the *IRNMAN* data. Figure 4.3 shows an example of a failed registration performed for aligning a pre-contrast T2*W image to a T1W delayed enhancement image of the *IRNMAN* project. Thus an intensity inhomogeneity correction method needs to be used to pre-process the data before applying the registration algorithm. This chapter presents a comparison study of different inhomogeneity correction methods to prepare for development of the preprocessing technique of my registration framework. In the next chapter, the detailed mechanism of the intensity inhomogeneity causing registration failures is introduced to derive a new preprocessing technique specifically applicable to *IRNMAN* data.

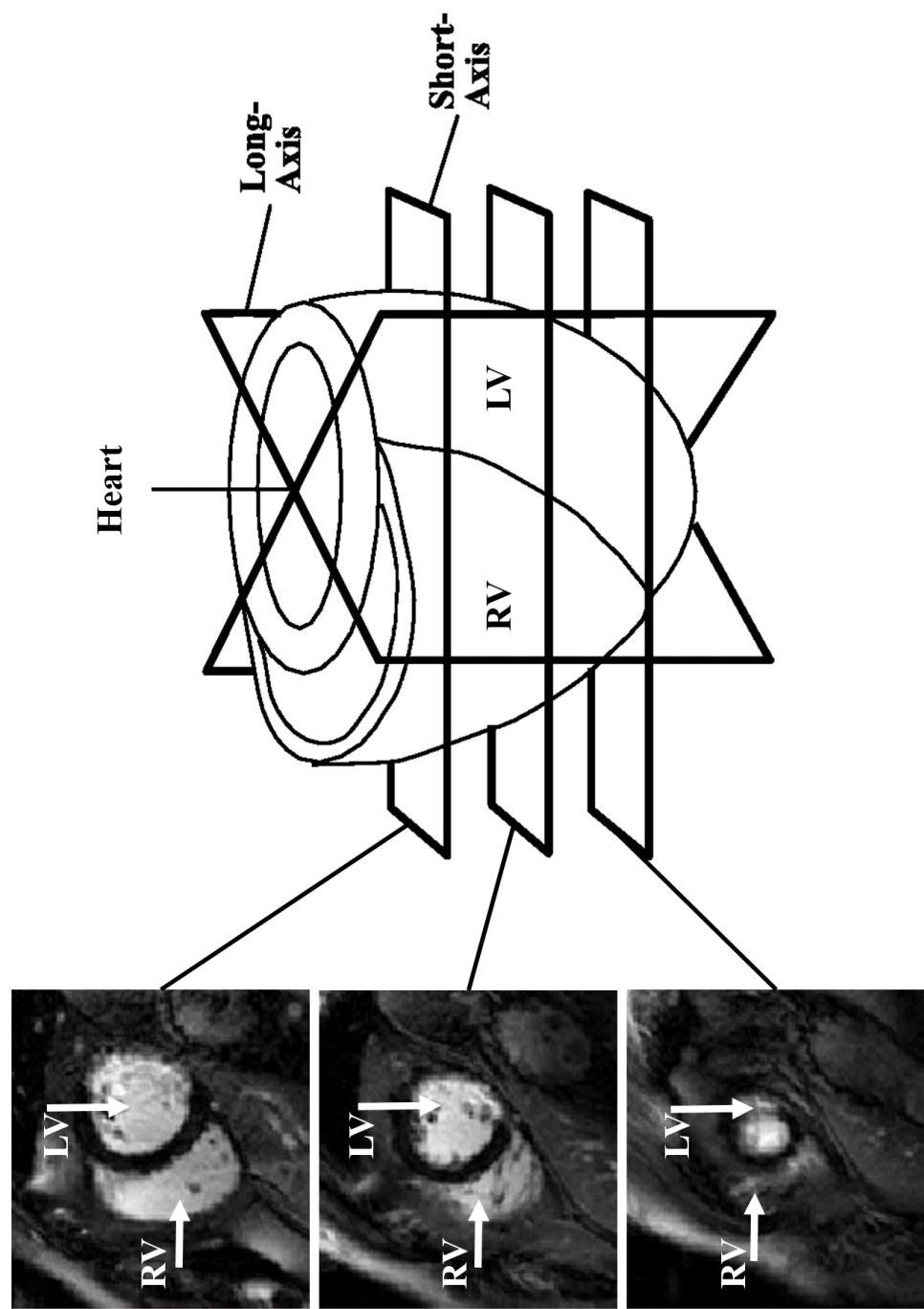


Figure 4.1: Demonstration of short-axis imaging planes of the heart and examples of short-axis T1 weighted delayed enhancement images that are used to visualize the interested structures (left and right ventricles) [4].

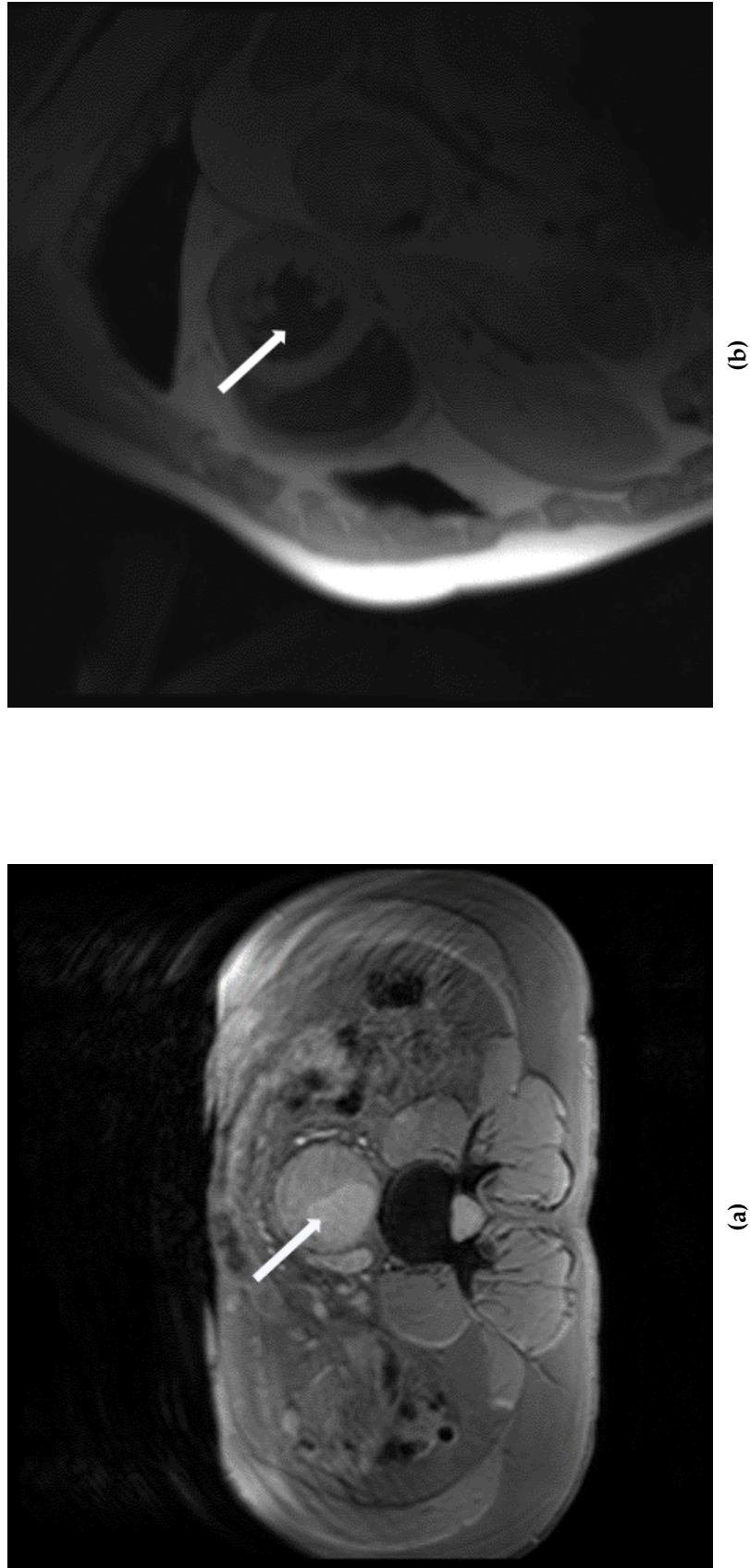


Figure 4.2: Example T2*W data from MA³RS and IRNMAN clinical trials: (a) MA³RS data, with the white arrow pointing to the aorta; (b) IRNMAN data, with the white arrow pointing to the left ventricle.

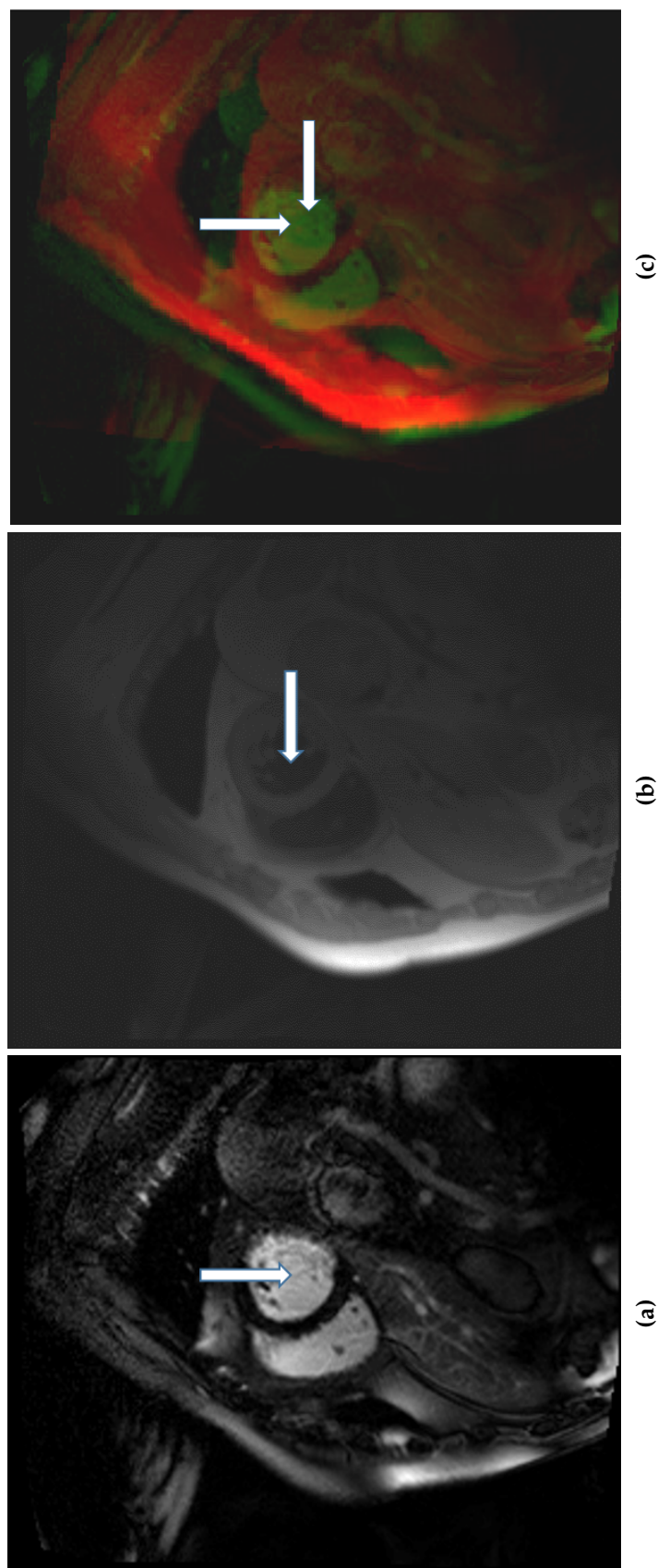


Figure 4.3: An example of a failed registration caused by intensity inhomogeneity: (a) T1 weighted delayed enhancement data; (b) pre-contrast T2* weighted data with severe intensity inhomogeneity; (c) alignment of the T2* weighted data and T1 weighted delayed enhancement data after registration visualized in overlapped red and green colour channels. The horizontal and vertical white arrows separately point to the centre of the left ventricle in the T2* weighted and delayed enhancement data.

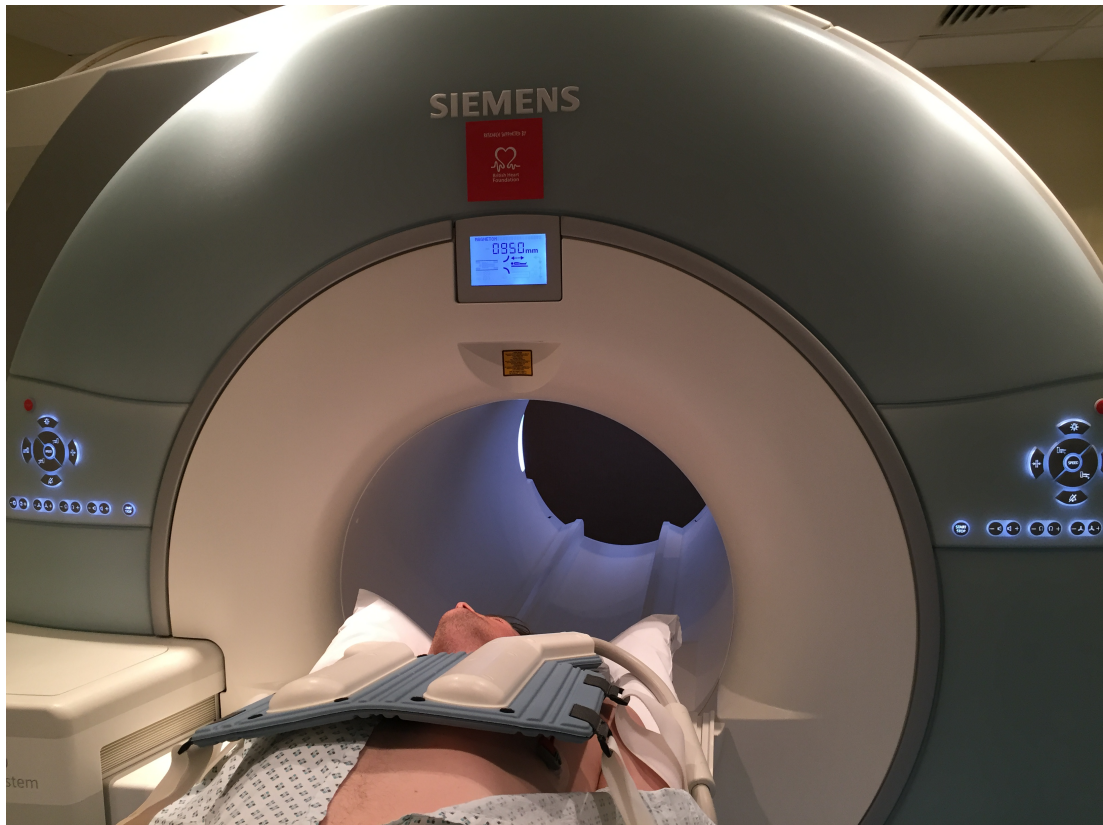


Figure 4.4: *Devices and patient setup for acquiring cardiac T1 weighted delayed enhancement and T2* weighted data.*

4.1.1 Sources of MR intensity inhomogeneity

There are many sources of intensity inhomogeneity in MR images, including non-uniform B_0 field, radiofrequency (RF) coil inhomogeneity, the shape of the imaged object (which can have a significant influence on the RF penetration and RF standing wave effects)[5, 197]. The appearance of intensity inhomogeneity is usually a slow and smooth intensity variation across the image[198]. Several comprehensive surveys and evaluations of correction methods have been published [5, 199, 200]. With only a few exceptions [201, 202, 203, 204, 205], most literature reviews of inhomogeneity correction methods concentrate on brain images.

However, the sources of inhomogeneity of neuro, body and cardiac imaging can be different, as well as the imaging techniques used to avoid intensity inhomogeneity. The inhomogeneity is generally caused by the sensitivity of the distance between the imaged object and the electromagnetic receivers in the MR RF coils of different sizes. The inhomogeneity can be attenuated by a birdcage combination of the head coil elements when acquiring brain images. For body imaging, for example, in the CRIC MA^3RS project, I selected a couple of the receivers roughly in line with the spine that detect signals from the posterior parts of the body. The anterior part was imaged by coils wrapped around the body which were designed for a 'standard' sized person, and different sizes and shapes of patients lead to different levels of inhomogeneity. The intensity inhomogeneity through the body can be reduced by combining signals detected by these coils with the spine coils. For the *IRNMAN* project, the spine coil was replaced by a dedicated posterior cardiac array of coils sitting behind the heart, combined with an anterior array sitting over the chest, as shown in figure 4.4. This dedicated cardiac coil is physically smaller than the body coils used for the abdomen imaging. This leads to optimal signal responses from the heart, but less homogeneous coverage of the rest of the thorax. Furthermore, at the interface between two tissues of significantly difference magnetic susceptibilities, there can be a distortion of the main magnetic field, which introduces additional artefacts. Therefore, *IRNMAN* images

suffers more intensity inhomogeneity and other artefacts than MA^3RS data. The use of surface coil is also a common reason for larger intensity inhomogeneity in cardiac imaging. Different intensity inhomogeneity correction methods may focus on different “bias fields” that are specific to different types of MR data, different imaged objects, or even different imaging devices. This means an inhomogeneity correction method that was tested on a brain image is possibly not applicable to the *IRNMAN* data. Thus the methods selected for comparison in this chapter should be applicable to data acquired with different imaging techniques from different patients.

In most intensity inhomogeneity correction methods, the image corruption is usually modelled by a multiplicative model with additive noise [5]:

$$v(\mathbf{x}) = u(\mathbf{x})f(\mathbf{x}) + n(\mathbf{x}) \quad (4.1)$$

where, at location \mathbf{x} , v is the measured signal, u is the true signal, f is the smoothly varying intensity inhomogeneity, and n is white noise that is assumed to be independent of u . The goal is to estimate f based on the observed values, v . However, this problem is ill-posed, as neither f nor u are known[5].

Intensity inhomogeneity correction methods can be classified as *prospective methods*, based on prior knowledge about the acquisition parameters and scanner, and *retrospective methods*, based solely on the image data[5]. Because the variability of inhomogeneity, especially in cardiac and abdominal MR data are patient- and acquisition-specific, prospective methods have limited applicability, and here I concentrate on the more general-purpose retrospective methods which are applicable to data from different imaged objects. A widely accepted classification of retrospective methods was proposed by Belaroussi et al. and is shown in figure 4.5[5].

This chapter reviews state-of-the-art retrospective correction methods, and the evaluation criteria I apply to them. Four methods are examined in more detail in a comparison study. Section 4.2 briefly summarizes the related studies, based on the classification of methods proposed by Belaroussi et al.[5]. Section 4.3 introduces

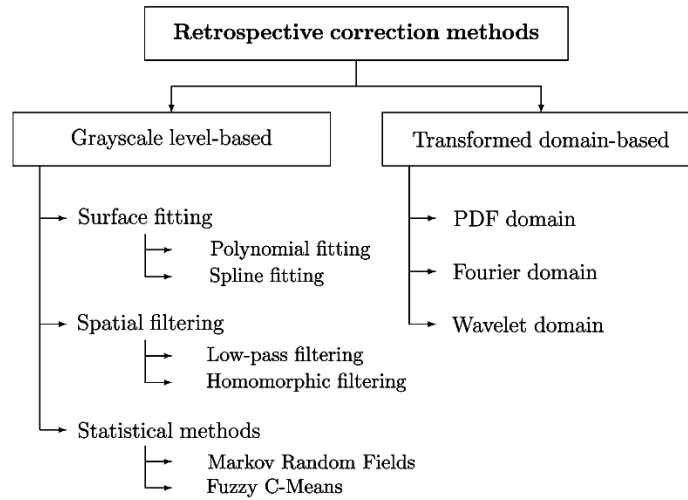


Figure 4.5: *Classification of existing correction methods [5].*

the four inhomogeneity correction methods selected from each class. The assessment criteria used in this study are described in section 4.4, and the evaluation results are shown in section 4.5. The conclusions of this study and discussions about future work can be found in section 4.6.

4.2 Related Works

4.2.1 Correction Methods

The retrospective intensity inhomogeneity correction methods can be further classified as grayscale spatial distribution-based methods and transformed domain-based methods [5], based on the domains of analysis. These solutions can either estimate the artefacts that should be removed, or the true signal that should be kept [5]. Grayscale methods assume that the intensity non-uniformity is piecewise constant, spatially smooth, and varies slowly across the spatial domain image. The purposes of grayscale level-based methods, such as fitting the smoothly varied background data, or filtering out low frequency signals, can also be achieved in some transformed domains, for example, Fourier, wavelet or probability density function (PDF) domains. The data is then transformed back to spatial domain after the analysis.

Surface fitting aims to fit a specified function to approximate the inhomogeneity. Spline and polynomial functions are often chosen as the basis functions, due to their smooth property. Spline basis fitting can either be single pass fitting, based on a set of control points, or multiple pass fitting, based on minimizing an energy function. For single pass fitting, Dawant et al. proposed an automatic control point selection method using a classifier [206]. Multiple pass fitting is often combined with segmentation to determine the spline parameters[207]. Similar to spline basis methods, parameters of the polynomial basis function of single pass fitting can be computed using a physical phantom [208] or a segmented dataset[209]. Multiple pass fitting computes Legendre polynomial coefficients by minimizing the energy functions[210].

Using a low-pass filter to estimate the intensity inhomogeneity relies on the assumption that the inhomogeneity consists of a low spatial frequency intensity variation. The inhomogeneous field is extracted from the original data and used to divide the original data voxel-by-voxel. Filters used to extract the inhomogeneity

4.2 Related Works

can be low-pass or homomorphic filters. The median filter is a popular strategy for extracting the inhomogeneity in single step methods, e.g. [211], [212] and [213]. Besides the filtering step, multiple processing step methods also extract the small intensity variations using either an average or median filter [214, 215]. Vokurka et al. proposed a method that estimates the bias field by removing the edges using low-pass filtering applied to a gradient image [205]. Homomorphic filtering simultaneously increases contrast and normalizes brightness which can be performed with median or average kernels. Brinkmann et al. proved that the latter kernel is more efficient for intensity non-uniformity correction[216].

Filtering may be performed in the Fourier domain. Low-pass gaussian filters have been applied to correct bias fields[217]. Wavelet-based methods may also be used to decompose the original image into a cascade of approximation and detail subspaces for different spatial resolutions. The approximation subspaces may then be used to estimate and correct the bias field. Relevant subspaces can be computed either based on the subspace coefficients or the reconstructed image[218].

Statistical methods aim to segment datasets whilst taking the bias field into account. Segmentation can be achieved by means of maximum likelihood (ML) or maximum a posteriori (MAP) based methods or by Fuzzy-C-Means (FCM). FCM has been successfully used for segmenting MR datasets. Ahmed et al. modified the original FCM methods by adding a constraint term to compensate the intensity inhomogeneity [219].

In the probability density function (PDF) domain, the bias field is often considered as a convolution term that smooths the real intensity distribution and thus increases entropy[5]. The data are considered as corrected once there are no more significant variations between two consecutive iterations. The N3 algorithm is a typical method of this category[220]. The same histogram assumptions are used in a variety of methods with an entropy minimization framework [32, 221, 222, 223]. Vovk et al. [224] proposed a method using second derivatives to reduce cluster overlap.

4.2.2 Evaluation Criteria

The performance of intensity inhomogeneity correction methods can be evaluated qualitatively or quantitatively. The qualitative evaluation criteria are mainly based on subjective visual inspection of the corrected data, often involving a comparison between the original data corrupted by the inhomogeneity and the corrected data. The quantitative evaluations rely on the objective measures relevant to particular applications. These two types of evaluations provide complementary information about the performances of the correction methods [5].

For quantitative evaluation of correction methods, there are several widely used objective criteria that measure the correction — directly or indirectly — based on whether a ground truth of the inhomogeneity, i.e. the true signal, is available. Detailed reviews of different validation datasets and qualitative and quantitative measures of correction quality can be found in [5] and [200].

Coefficient of variation The coefficient of variation (CV) is a widely used indirect metric found in most bias field correction articles. It is the ratio between the standard deviation, σ , and the mean, μ , intensity for a given tissue,

$$CV = \frac{\sigma}{\mu}. \quad (4.2)$$

A modification of the CV, the coefficient of joint variance (CJV), was used in [32]. It measures the overlap between two tissue distributions:

$$CJV = \frac{\sigma_1 + \sigma_2}{\mu_1 - \mu_2}. \quad (4.3)$$

The reduction of CV in the corrected tissue, ΔCV , was used in [225] to compare the performance of N4 with the original N3 algorithm.

$$\Delta CV = \frac{\sigma_{initial}}{\mu_{initial}} - \frac{\sigma_{corrected}}{\mu_{corrected}} \quad (4.4)$$

4.2 Related Works

These metrics assume an accurate tissue segmentation is available, and that a low coefficient of variation necessarily implies a good correction of the bias field.

Based on the experiments performed by Chua et al. [200], these values were measured on slightly smoothed images which have been shown to have a higher correlation with direct measures. Instead of using a small mean filter, as in [200], a b-spline smoothing kernel can be used to keep better edges between different tissues.

Entropy-based Measures As the homogeneity within a particular tissue should be improved after bias field correction, entropy is considered another measure of the corrected data. Whatever measure is used, the correction process should reduce entropy. Thacker et al. [226] proposed a scale invariant information measure, L , based on the following entropy definition:

$$L = \sum_{a=1}^n \sqrt{\frac{P(g_a)}{g_a}} \quad (4.5)$$

where, given a set of N grayscale measurements g_a , $P(g_a)$ is the associated probabilities.

Segmentation-based Measures Accuracy of segmentation before and after correction can be a useful metric. Styner et al. used detection rates to measure the performance of their correction method [210], by computing the rates of correctly classified tissue and misclassified tissue. Correctly classified tissue leads to a true positive ratio, the corrected detected rate(CDR):

$$CDR = \frac{N_{TP}}{N_1} \quad (4.6)$$

where N_1 denotes the number of voxels in the given segmentation, and N_{TP} the number of true positive voxels. Similarly, the incorrect detection rate(IDR) is defined by:

$$IDR = \frac{N_{FP} + N_{FN}}{N_1} \quad (4.7)$$

where N_{FP} and N_{FN} are the number of false positive and false negative voxels [210].

Zijdenbos et al. proposed another statistical measure, the similarity index, which may be considered to be more sophisticated [5, 227]. With the set of voxels in a given tissue class A before and after correction, respectively A_b and A_a , the similarity index, S , is defined by:

$$S = 2 \frac{n(A_a \cap A_b)}{n(A_a) + n(A_b)} \quad (4.8)$$

where $n(A)$ is the number of voxels in class A .

Direct Measures The quantitative measures discussed above are considered to be *indirect* [200], as they were derived through tissue intensity variability or segmentation performance indirectly. Some review experiments [200] revealed that these evaluation metrics often lead to conflicting suggestions about performance of the correction methods. More reliable measures should compare the true and estimated bias fields, such as correlation [228], root mean square error [152, 216, 229], standard deviation error, mean square error, mean square distance [210, 230], etc.

Chua et al. used the normalized L_2 -norm of the difference between the true B_t and the estimated bias field B_e :

$$L_2 = \min_{\omega} \sqrt{\frac{\sum (\omega B_e - B_t)^2}{\sum B_t^2}} \quad (4.9)$$

where ω is the normalization coefficient which is calculated by:

$$\omega = \frac{\sum B_t B_e}{\sum B_e^2}. \quad (4.10)$$

However, the application of these metrics is often limited to simulated images because of the requirement for a known true bias field. An evaluation of reliability of different quantitative metrics can be found in [200].

4.3 Compared Methods

To comprehensively evaluate the suitability of different types of intensity inhomogeneity correction methods, four methods were selected for a comparison study: (1) the Nonparametric Nonuniform intensity Normalization (N3), and also its popular variant, called N4, (2) the pre-processing function from the Statistical Parametric Mapping (SPM) software package, (3) a polynomial surface fitting method, and (4) a low-pass filtering method based on the discrete wavelet transformation.

The four methods to be compared cover a wide range of categories of intensity inhomogeneity correction methods discussed. The polynomial method estimates the inhomogeneity of the image by fitting a surface in the spatial domain; N3, N4, and SPM are statistical methods: while N3 and N4 work in the PDF domain, SPM operates in the cosine domain (a subspace of the Fourier domain). The wavelet-decomposition method is a representative low-pass filtering method operating in the wavelet domain. Each of these four methods, except the wavelet method, involves an iterative optimization strategy, which searches for the optimal estimation of the “bias field”, or true signal, in the spatial, Fourier, Wavelet, or PDF domains. A brief description of the four methods, outlined by the classification, target of estimation, search space and optimization strategy, is shown in Table 4.1. The technical details of each algorithm are introduced in the following subsections.

4.3.1 N3 and N4

The N3 algorithm [6] is one of the most popular intensity inhomogeneity correction methods, due to its proven performance and free availability. It is derived from the logarithm of the noise free case of equation 4.1 where the noise n is ignored. Using the notation $\hat{u}(\mathbf{x}) = \log[u(\mathbf{x})]$ the degradation model becomes:

$$\hat{v}(\mathbf{x}) = \hat{u}(\mathbf{x}) + \hat{f}(\mathbf{x}), \quad (4.11)$$

Table 4.1: *Brief Information of the Methods to Compare*

Method	Category	Estimation Target	Searching Space	Optimization Strategy
Polynomial	Surface fitting	Space domain of real image	Polynomial coefficients of real image	Powell's method searching for minimum cost function
N3/N4	Statistical	Bias field	PDF domain of real image	Linearly maximizing posterior probability
SPM	Statistical	Real image	Fourier domain of real image	Find maximized log-likelihood using Gradient descent
Wavelet	Low-pass filtering	Bias field	Wavelet domain	

where \hat{v} and \hat{f} are logarithms of v and f in equation 4.1.

As a typical PDF based method, the PDF of the original data $V(\hat{v})$ is modelled as the convolution of the true signal and the bias field:

$$V(\hat{v}) = F(\hat{v}) * U(\hat{v}) = \int F(\hat{v} - \hat{f})U(\hat{f})d\hat{f} \quad (4.12)$$

where F and U are the PDFs of the nonuniformity and the true intensity distribution, respectively. Further details of equation 4.12 can be found in [231].

Given the distribution V , for a measure \hat{v} at location \mathbf{x} , \hat{u} is estimated using U and F as follows:

$$E[\hat{u}|\hat{v}] = \int_{-\infty}^{\infty} \hat{u}p(\hat{u}|\hat{v})d\hat{u}. \quad (4.13)$$

4.3 Compared Methods

Writing $p(\hat{u}|\hat{v})$ as $\frac{p(\hat{u},\hat{v})}{V(\hat{v})}$, \hat{u} can be estimated as:

$$E[\hat{u}|\hat{v}] = \frac{\int_{-\infty}^{\infty} \hat{u} F(\hat{u} - \hat{v}) U(\hat{u}) d\hat{u}}{\int_{-\infty}^{\infty} F(\hat{u} - \hat{v}) U(\hat{u}) d\hat{u}}. \quad (4.14)$$

The estimation of \hat{f} can then be calculated by:

$$\hat{f}_e(\hat{v}) = E[\hat{f}|\hat{v}] = \hat{v} - E[\hat{u}|\hat{v}] \quad (4.15)$$

where \hat{f}_e is an estimation of \hat{f} at location \mathbf{x} based on the single measurement of \hat{v} . The estimated bias field is then smoothed by a B-spline operator S :

$$\hat{f}_s(\hat{v}) = S\{\hat{f}_e(\hat{v})\} = S\{\hat{v} - E[\hat{u}|\hat{v}]\} \quad (4.16)$$

Given the distribution of the bias field, F , and the distribution of the original data, V , then U can be calculated using:

$$\tilde{G} = \frac{\tilde{F}^*}{|\tilde{F}|^2 + Z^2} \quad (4.17)$$

$$\tilde{U} = \tilde{G}\tilde{V} \quad (4.18)$$

where, \tilde{F} and \tilde{F}^* denote the Fourier transform of F and its complex conjugate, respectively, and Z is a constant term used to limit the magnitude of \tilde{G} . Thus U can be obtained by deconvolution. The N3 method uses this estimation of U to estimate the bias field \hat{f} [6].

In the N3 algorithm, F is assumed to be a Gaussian distribution defined by its full-width-half-maximum (FWHM). U is then computed as described above. F can be optimized using the iterative optimization frame work shown in figure 4.6 [6]. The optimization will be terminated based on the coefficient of variation given by:

$$e = \frac{\sigma\{r_n\}}{\mu\{r_n\}}, n = 1 \dots N \quad (4.19)$$

where r_n is the ratio between the bias field estimations generated at the n th and $(n - 1)$ th iterations, and σ and μ denote the standard deviation and mean value, respectively.

Tustison and Gee [232] proposed a variant implementation of N3, named “N4”. The main differences in their implementation are: (a) a hierarchical modification of the optimization and, (b) a fast and robust generalized $n - DC^k$ B-spline smoothing method. Denoting the smoothing operator as S^* , the true data distribution, U , is estimated hierarchically using:

$$\hat{u}^n = \hat{u}^{n-1} - \hat{f}_r^n = \hat{u}^{n-1} - S^* \{ \hat{u}^{n-1} - E [\hat{u} | \hat{u}^{n-1}] \} \quad (4.20)$$

where \hat{f}_r^n is the estimated residual bias field.

The N3 and N4 algorithms often work on down-sampled data, to focus on the low-frequency spectrum of the data. Thus, a down-sampling rate, or “shrink factor” is specified before they are applied. Based on Sled et al.’s experiments [6], I investigated shrink factors set to 2 and 4.

4.3.2 SPM

SPM usually refers to the statistical method used to measure differences of brain activities during the functional neural imaging experiments [7]. This includes techniques such as segmentation and registration. In this work, only the inhomogeneity correction step of the SPM framework was needed.

SPM uses a similar degradation model as N3/N4. It directly maximizes the logarithm of likelihood $p(u|v)$. The intensity distribution of the true signal is calculated by inverse discrete cosine transformation (DCT). The choice of DCT bases is decided by the dimension of the data, and a pre-defined number of histogram bins. The DCT coefficients, as well as the corresponding log-likelihood, are updated iteratively based on the derivatives of likelihood with respect to the coefficients and

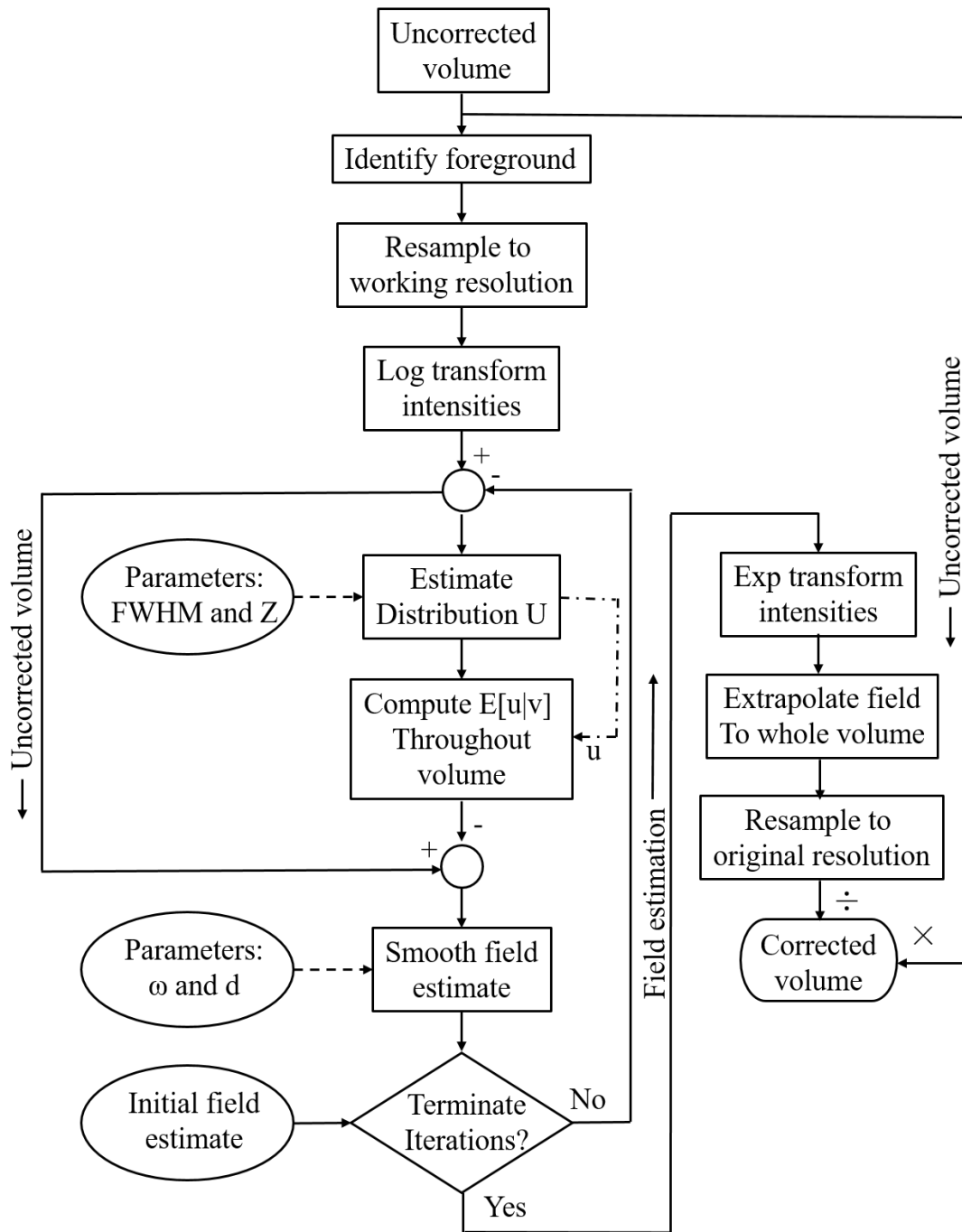


Figure 4.6: N3 Bias Field Correction Framework from [6]

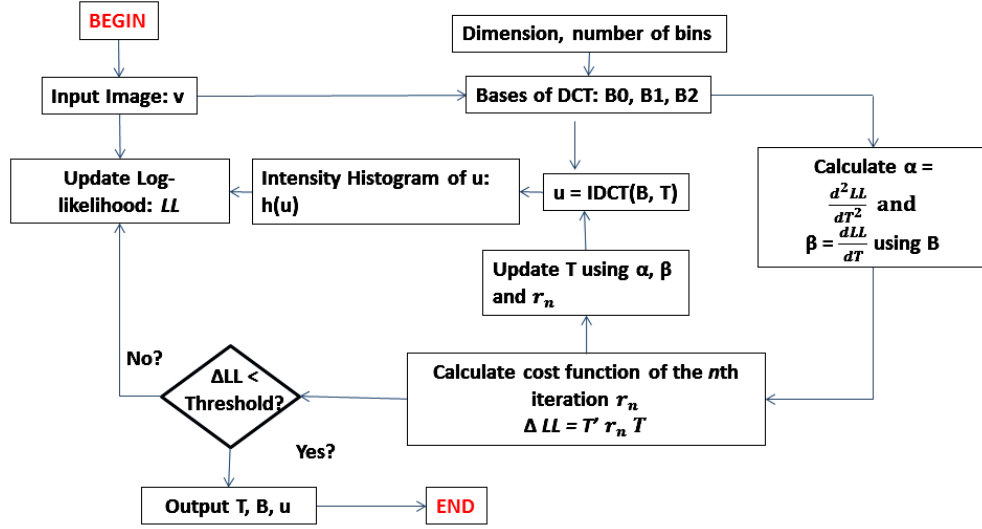


Figure 4.7: SPM Bias Field Correction Procedure [7].

a cost function defined for these derivatives. This optimization process terminates when the change in log-likelihood is smaller than a pre-defined threshold. Figure 4.7 shows a block diagram of the SPM inhomogeneity correction procedure.

4.3.3 Wavelet-based method

Wavelets are a powerful tool for spatial-frequency analysis. The discrete wavelet transformation (DWT) transforms the signal to wavelet space using a set of short-term finite discrete-time filterbanks. The DWT can decompose the data into detailed and approximation subspaces. As the bias-field inhomogeneity is assumed to vary smoothly, the approximation subspaces can be used as a rough estimation of the bias field. In this comparison work, a simple wavelet-decomposition based low-pass filtering method was used to estimate the bias field as combination of the approximation subspaces using a similar iterative optimization framework to that of N3[232]. The wavelet approximation subspaces are obtained using a DWT decomposition, $\tilde{W}\{\}$, of the original data, V . The decomposition coefficients are given by:

$$W_v = \tilde{W}\{\hat{v}\} \quad (4.21)$$

4.3 Compared Methods

where W_v denotes the decomposition coefficients. The coefficients of the bias field, W_f , are obtained by keeping the first N coefficients and setting the remainder to 0:

$$W_f(i) = \begin{cases} W_v(i), i = 1 \cdots N \\ 0, i > N \end{cases}. \quad (4.22)$$

The threshold of the measure e in equation 4.19 is set to 0.0001 as default. According to the N3 algorithm, a thresholding algorithm based on histogram analysis is first applied to the original data to obtain the mask M for the object to measure [233]. The final estimation of bias field is calculated by:

$$F = \exp \left(\frac{\tilde{W}^{-1}\{W_f\} \cdot M}{wlf(M)} \right) \quad (4.23)$$

where \tilde{W}^{-1} denotes the inverse DWT and wlf is the processed mask filtered using equation 4.22.

To eliminate the down-sampling effects of the DWT, the stationary wavelet transformation (SWT) can be applied to the inhomogeneity corrupted data. The decomposition level of the SWT is limited by the data dimensions. Each level of decomposition reduces the data resolution to half of the previous level. Because the data were sampled to 256×256 for the sake of simplicity, the decomposition level can be up to 7 due to the down-sampling effect of wavelet decomposition.

4.3.4 Polynomial surface fitting

A set of preselected Legendre polynomial basis functions are used to directly fit a multiplicative correction factor surface which is correlated to the intensity non-homogeneity of the image. The estimated true signal is obtained by pixel-by-pixel multiplication of the sampled observed data with this correction factor surface. Legendre polynomial coefficients are computed by minimizing an energy function using the Powell optimization algorithm. The general form of a Legendre polynomial

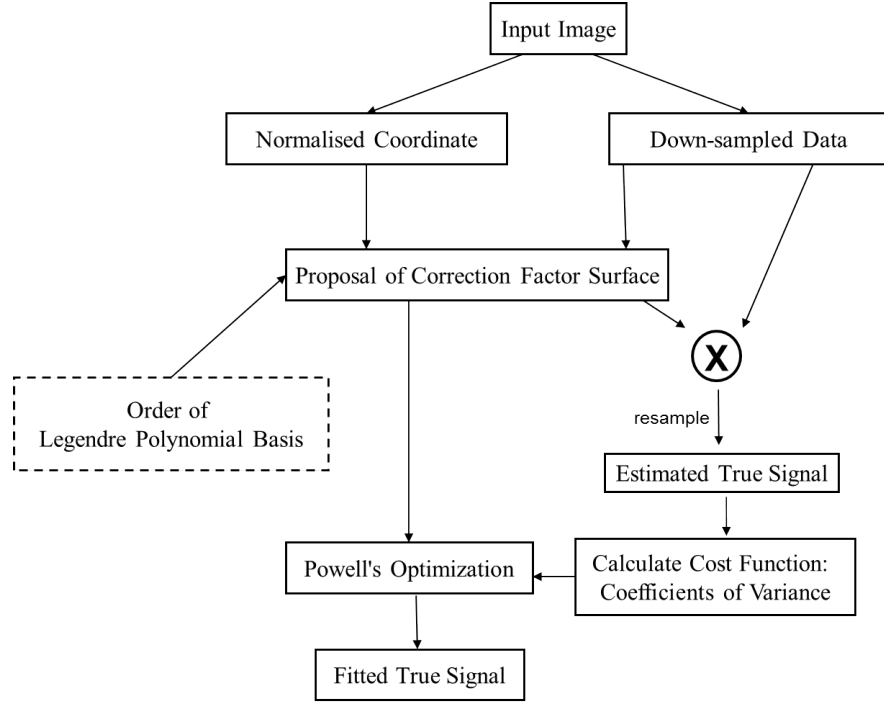


Figure 4.8: Polynomial surface fitting bias field correction procedure

P_n of order n is given by:

$$P_n(x) = \sum_{m=0}^M (-1)^m \frac{(2n-2m)!}{2^n m! (n-m)! (n-2m)!} x^{n-2m} \quad (4.24)$$

where $M = n/2$ or $(n-1)/2$, which ever is an integer.

The cost function is defined as the change of CV of the estimated true signal. The order of the polynomial model is adjustable from 1 to 5, and the default setting is 3. A diagram of this correction algorithm is shown in figure 4.8.

4.4 Assessment Methodology

In this work, the *Advanced Normalization Tools (ANTs)*¹ software package is used for the N3 and N4 implementation. For SPM method, the SPM8 package is used [234]. The wavelet-based method is implemented in Matlab, and the polynomial surface fitting method is coded in C++.

4.4.1 Evaluation datasets

Using “real data” to evaluate intensity inhomogeneity is difficult, as the absolute ground truth is not known, and the analysis must rely on less powerful, indirect measures. Even using a phantom, which can be scanned to a very high quality with low noise and without motion artefacts, may still include some intensity inhomogeneity. An alternative strategy is to synthesize test data, where the ground truth inhomogeneity is known. The synthesized data need not have any anatomical resemblance, though there are clearly advantages to realistic test data. *BrainWeb*² is an example of this type of dataset [235]. The current BrainWeb databases contain simulated brain MRI data based on two anatomical models, normal and multiple sclerosis. Full 3-dimensional data volumes have been simulated using three sequences (T1-, T2-, and proton-density-weighted) and a variety of slice thicknesses, noise levels, and strength of intensity non-uniformity. The strengths of the bias field are measured using a percent ratio of the full width at half maximum (FWHM) of the PDF of the intensity inhomogeneity (f in the Equation 4.1) versus the range of image intensity values. The noise levels are measured by the percent ratio of the standard deviation of the white Gaussian noise versus the signal for a reference tissue. In BrainWeb simulator, the These data are available for viewing in three orthogonal views.

In this study, I chose the simulated T1-weighted axial data of normal brain with

¹<http://stnava.github.io/ANTs/>

²<http://brainweb.bic.mni.mcgill.ca/brainweb/>

different bias fields (inhomogeneity strength = 0%, 20%, 40%, and 80% of intensity range), and additive Rayleigh noise (noise percentage = 0%, 3%, and 5% of quantity of pixels). The pixel size was set to $1 \times 1 \times 3$ mm. An example of different simulated data is shown in figure 4.9.

The differences between data simulated with different parametric settings are difficult to observe visually. Figure 4.10 shows an example of the bias field generated by the BrainWeb simulator.

Bromiley pointed out several problems of BrainWeb simulated data when used to evaluate segmentation algorithms, e.g., confusion between effects of partial volume effects and image noise, generation of histogram artefacts, lack of relevance to performance on genuine MR data, etc [236]. Because this study only focuses on the relation between true signal and bias field corrected data without assessing the change of performances of segmentation algorithms, the problems revealed by [236] are not considered an issue.

4.4.2 Assessment metrics

Both qualitative and quantitative evaluations were performed in this study. Qualitative evaluation is based solely on the visual impression of the corrected result, whereas quantitative methods are more objective. Quantitative methods can be divided into *direct* and *indirect* methods. Direct methods assume that the true image is known, such that a direct comparison of the corrected image and the true image is possible. Sum of squared differences and correlation coefficients are common direct measures.

For the simulated datasets, masks of two regions were created for each dataset. The indirect measures, such as CV and CJV, should be calculated within these two regions. The masks were generated either by manual segmentation or using a simple region growing algorithm performed on k-means clustered images. The masks were used as ground truth of the segmentation accuracy tests. For the BrainWeb datasets,

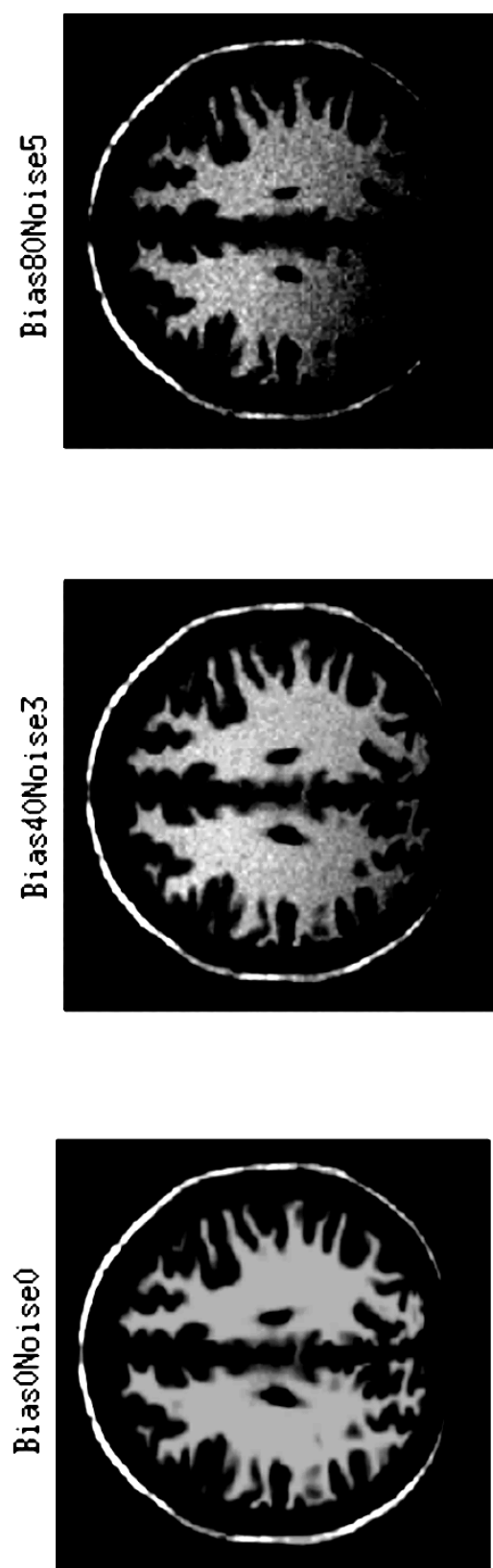


Figure 4.9: Example of simulated data: on the left is the original image without intensity nonuniformity and additive noise; in the middle is the image affected by 40% bias field and 3% noise; the image with bias field FWHM = 80% and 5% noise is on the right.

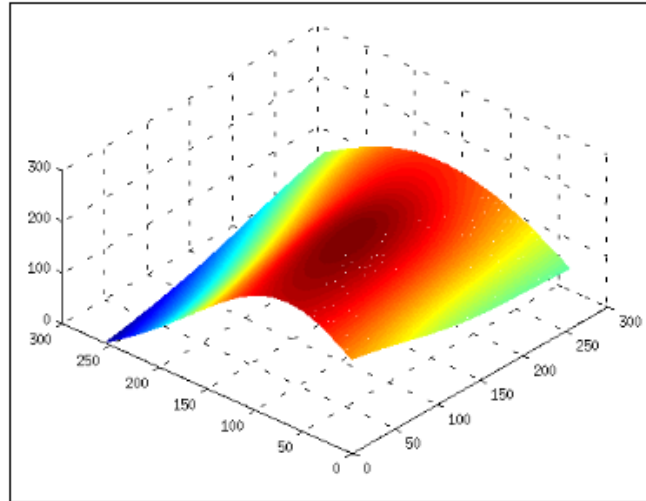


Figure 4.10: Example of intensity inhomogeneity generated using the BrainWeb simulator: the spatial domain of the image represented in number of pixels is placed in the horizontal plane, and the height of a point on the surface represents the strength of the inhomogeneity that affect a pixel of the image.

the grey and white matter masks were used as the segmentation ground truth.

In this study, because the bias-free true data are available from the BrainWeb simulator, more attention was paid to direct measures, in case particular algorithms may introduce linear or non-linear mapping of intensity distribution. Correlation coefficients (CC) were also calculated. Many existing publications remind that the CV and CJV can mislead the assessment results in particular cases [5, 200, 220]. Furthermore, the optimization step in the polynomial surface fitting, N3 and N4 methods actually minimizes the CV within the process [6], which may further mislead the assessments. Thus in the following section, only visualised results of direct measures were calculated and displayed.

In practice, using real data, the true image is not known and indirect measures are necessary. These are usually based on some form of (usually manual) segmentation of the dataset. For instance, the coefficient of variation within particular tissue types is an indirect measure based on the assumption that the variation within each tissue class should be small relative to its mean value [32]. However, great care must be taken when using indirect methods as they are dependent on a number of assumptions,

4.4 Assessment Methodology

including correct segmentation, which may not hold for a particular dataset[200]. Common indirect measures include entropy [210], correct detection rate, incorrect detection rate Thacker et al. [226] and similarity index [5, 227], etc. In this study, the following measures were used to compare the results.

Sum of squared differences The sum of squared differences (SSD) is a direct metric given by:

$$SSD = \sum_i (X_i - Y_i)^2 \quad (4.25)$$

where X_i and Y_i are the pixel values in the ground truth and corrected datasets. According to its definition, smaller SSD indicates a closer estimation of bias-free data, and vice versa.

Correlation coefficients It is possible that particular bias field correction methods may introduce linear intensity mapping of the true signal. Thus some corrected data may have large SSD between the ground truth however more homogeneous intensity distribution within each type of tissue. This make calculation of correlation coefficients (CC) necessary. For images X and Y , CC can be calculated by:

$$CC = \frac{E[(X - \mu_x)(Y - \mu_y)]}{\sigma_x \sigma_y} \quad (4.26)$$

where μ_x , μ_y , σ_x and σ_y are the average and standard deviation of X and Y , $E[.]$ represents the expectation.

For convenient visual assessments, I use $-1 \cdot CC$ here so that both the SSD and CC values are smaller for better inhomogeneity correction. To compare the performances of different corrections methods, the boxplots of SSD and CC are used for visualizing the results. A result is considered as a outlier if it is larger than $q3 + 1.5(q3 - q1)$ or smaller than $q1 - 1.5(q3 - q1)$ where $q1$ and $q3$ are the 25th and 75th percentiles of the results.

4.5 Results

The BrainWeb simulator uses bias field of a uniform shape while also adding non-ignorable noise to the simulated images. The choice of bias-field parameters was based on the limit of intensity inhomogeneity strength of the simulator. Most published literature only considers the bias fields whose strength are 20% and 40% of the intensity range while this current assessment includes wider range of intensity so that the results can be qualitatively compared to the manually created datasets.

4.5.1 Qualitative Evaluation

Figures 4.11 and 4.12 display examples of data before and after correction of a range of different simulated bias fields and noises. Based on visual inspection, differences between data with different parametric settings processed by the same method are not obvious. For the same “Corrupted” data, only the wavelet decomposition and polynomial surface methods show non-linear mappings of intensity. Results from the other methods did not show visible differences. For a larger strength of bias field, the polynomial method shows a larger non-linear intensity variance.

4.5.2 Quantitative Evaluation

Based on the discussion above, the SSD and CC between the corrected data and the “Corrupted” data were calculated, as shown in Figure 4.13 and Figure 4.14. For convenient evaluation of performances of different correction methods, I calculated negative correlation coefficients. The corrected data is closer to true signal without any bias field and noise leading to smaller SSD and CC. As shown in Figure 4.13 and 4.14, identical data with true signal will have 0 SSD and -1 CC. From the calculated SSD and CC, the wavelet decomposition method introduced extensive additional variation to the data. This is because the approximation subspaces also contained significant amounts of the true signal. Generally speaking, output data from N4 gave the closest

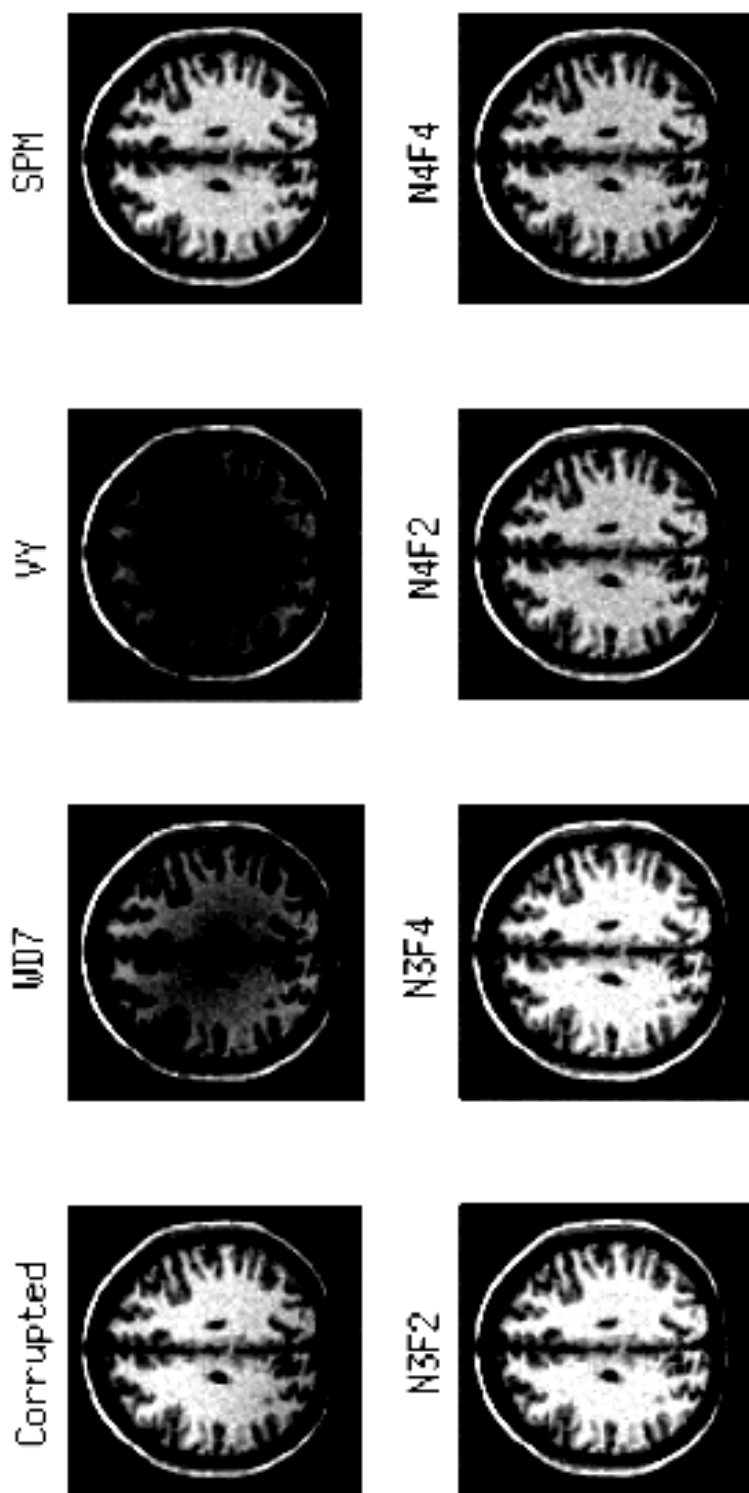


Figure 4.11: Example of simulated data before after correction: strength of bias field is 40% with no noise. The bias-corrupted data was labelled as "Corrupted"; "WD7" is the result from wavelet decomposition correction; "VY" represents the result using the polynomial surface method. N3 and N4 methods, with shrink factor set as 2 and 4, are labelled as "N3F2" "N3F4" "N4F2" "N4F4".

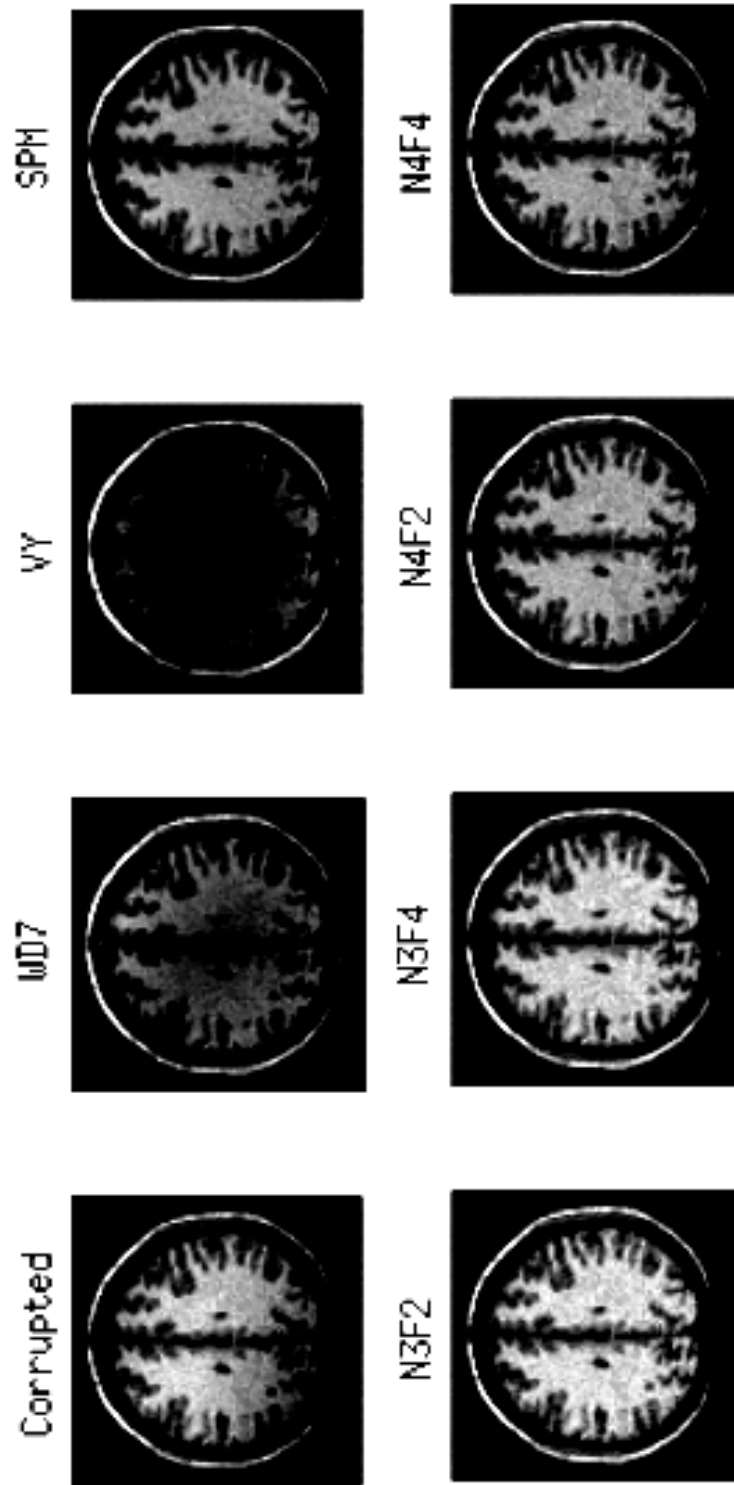


Figure 4.12: Example of simulated data before after correction: strength of bias field is 80 with 5 % noise. The bias-corrupted data was labelled as "Corrupted"; "WD7" is the result from wavelet decomposition correction; "VY" represents the result using the polynomial surface method. N3 and N4 methods, with shrink factor setted as 2 and 4, are labelled as "N3F2" "N3F4" "N4F2" "N4F4".

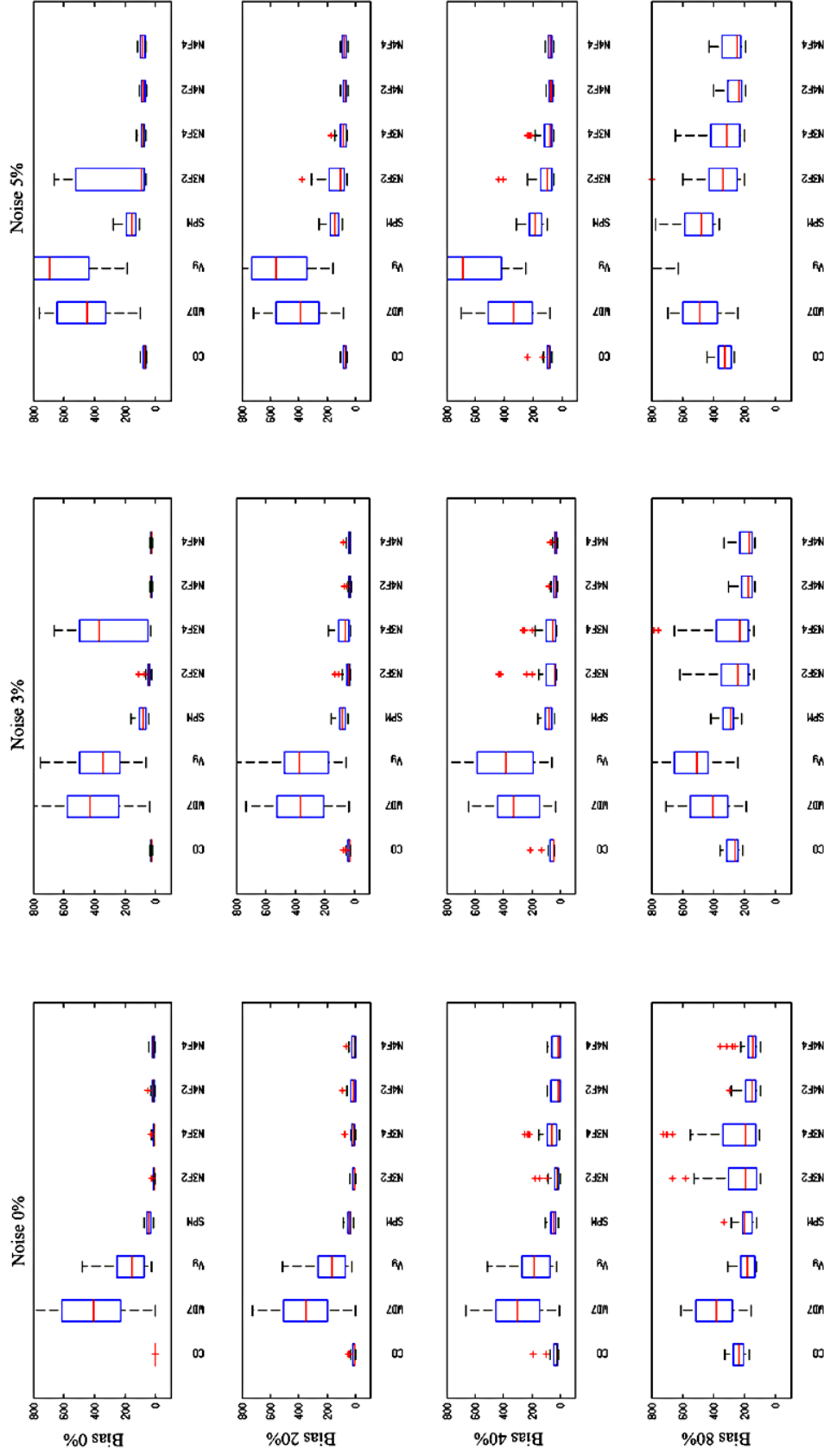


Figure 4.13: SSD between the corrected data from all 7 methods and the data corrupted by the simulated bias field and noises: Noise from left to right is 0%, 3% and 5%; the strength of the bias field from top to bottom is 0%, 20%, 40% and 80%. The true signal without bias field and noise is shown on the left in the upper left subplot.

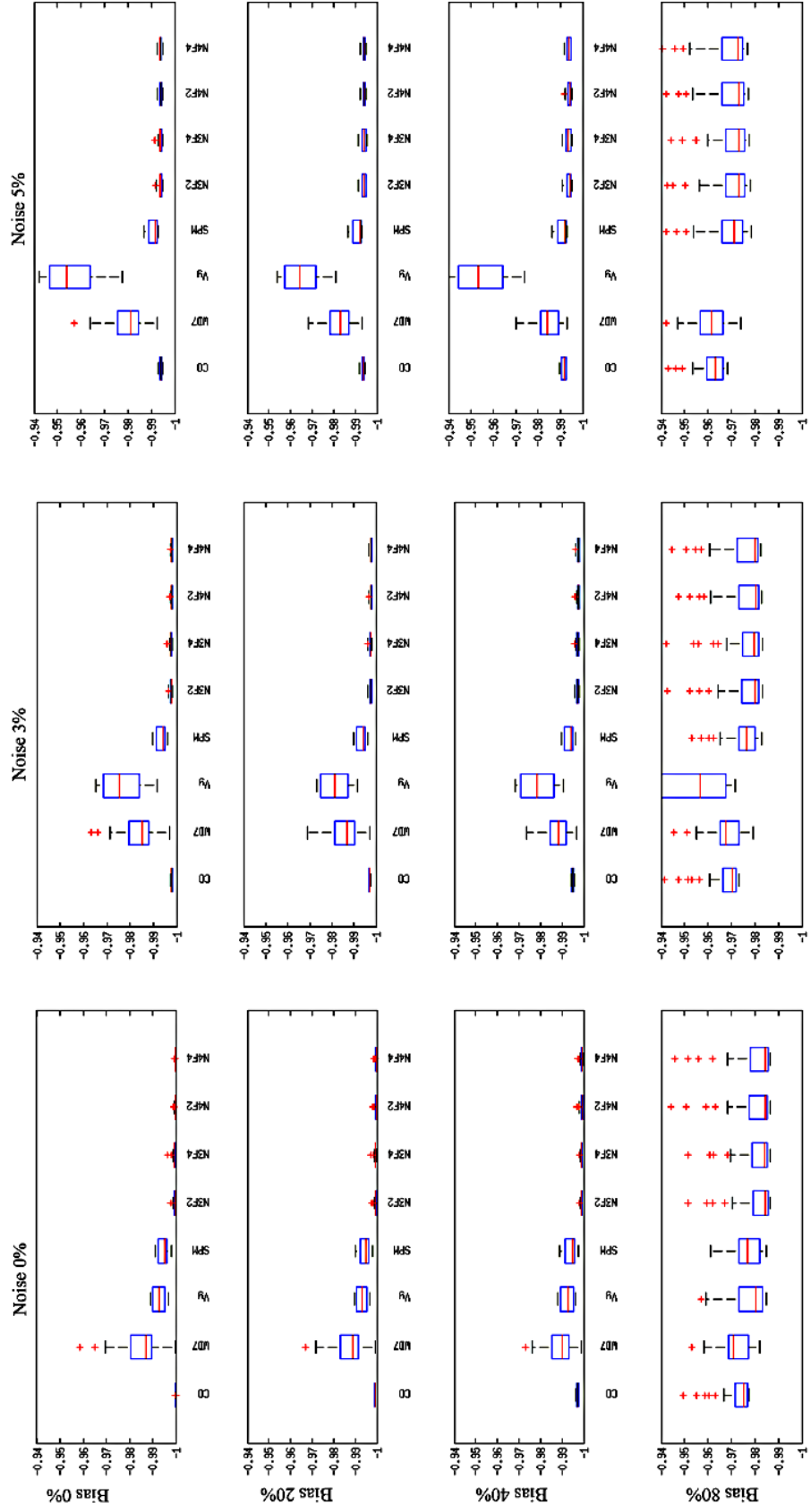


Figure 4.14: Correlation coefficients between the corrected data from all 7 methods and the data corrupted by the simulated bias field and noises: Noise from left to right is 0%, 3% and 5%; the strength of the from top to bottom is 0%, 20%, 40% and 80%. The true signal without bias field and noise is shown on the left in the upper left subplot.

4.5 Results

estimation to the true signal. In most cases, N3 provides a better estimation than SPM and the polynomial method, whilst with the shrink factor set to 4 the performance is more stable. In the case of less additive noise, the N3 methods become more unstable when the strength of the bias field is larger. A similar situation happened with SPM methods.

All the methods, with the exception of the polynomial surface and wavelet decomposition methods, reduce the variation in the data. The polynomial method produced slightly better estimations than SPM when the strength of bias field is 80% and there is no additive noise. However, it is very sensitive to noise. As both the strength of the bias field and the percentage of noise increase, the performance of the polynomial method rapidly becomes worse than the wavelet decomposition method.

4.5.3 Quantitative Analysis of the polynomial method

To obtain more insight into the polynomial method, the effect of the order of the polynomial model was investigated. In these experiments the order ranged from 1 to 5, as shown in Figure 4.15 and 4.16. Clearly, smaller polynomial orders make this method less sensitive to additive noise, but also less powerful to correct stronger bias fields. When the order is 1, the polynomial simply models the input data — no correction is actually performed (the slight difference between the output and input is just a result of the limits placed on the polynomial coefficients). Thus the optimal parametric setting is based on the bias field distribution in real cases.

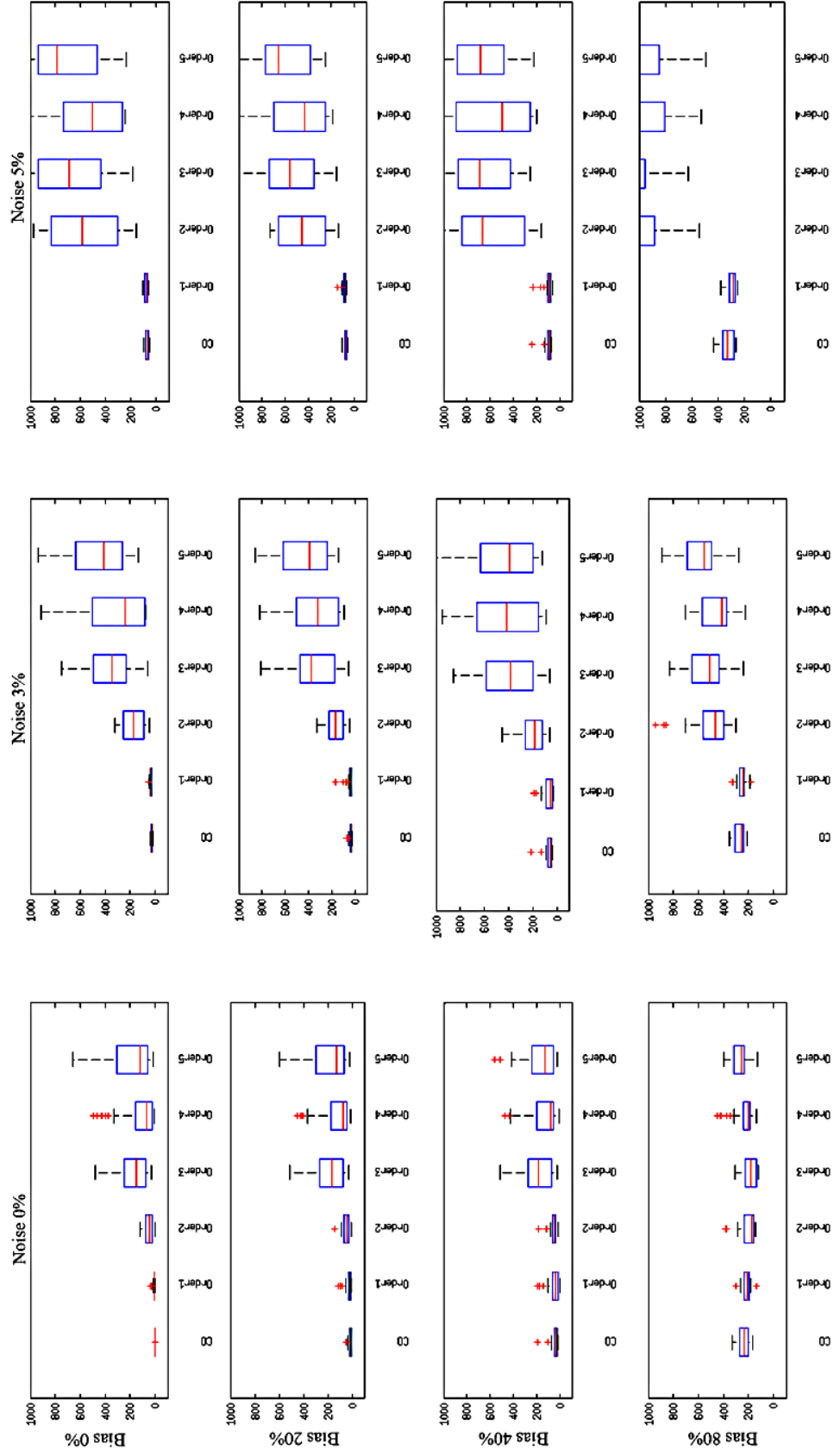


Figure 4.15: SSD between the data corrected by the polynomial method, when changing the order of polynomial model from 1 to 5 and the data corrupted by the simulated bias field and noises: Noise from left to right is 0%, 3% and 5%; the strength of the bias field from top to bottom is 0%, 20%, 40% and 80%. The true signal without bias field and noise is shown on the left in the upper left subplot.

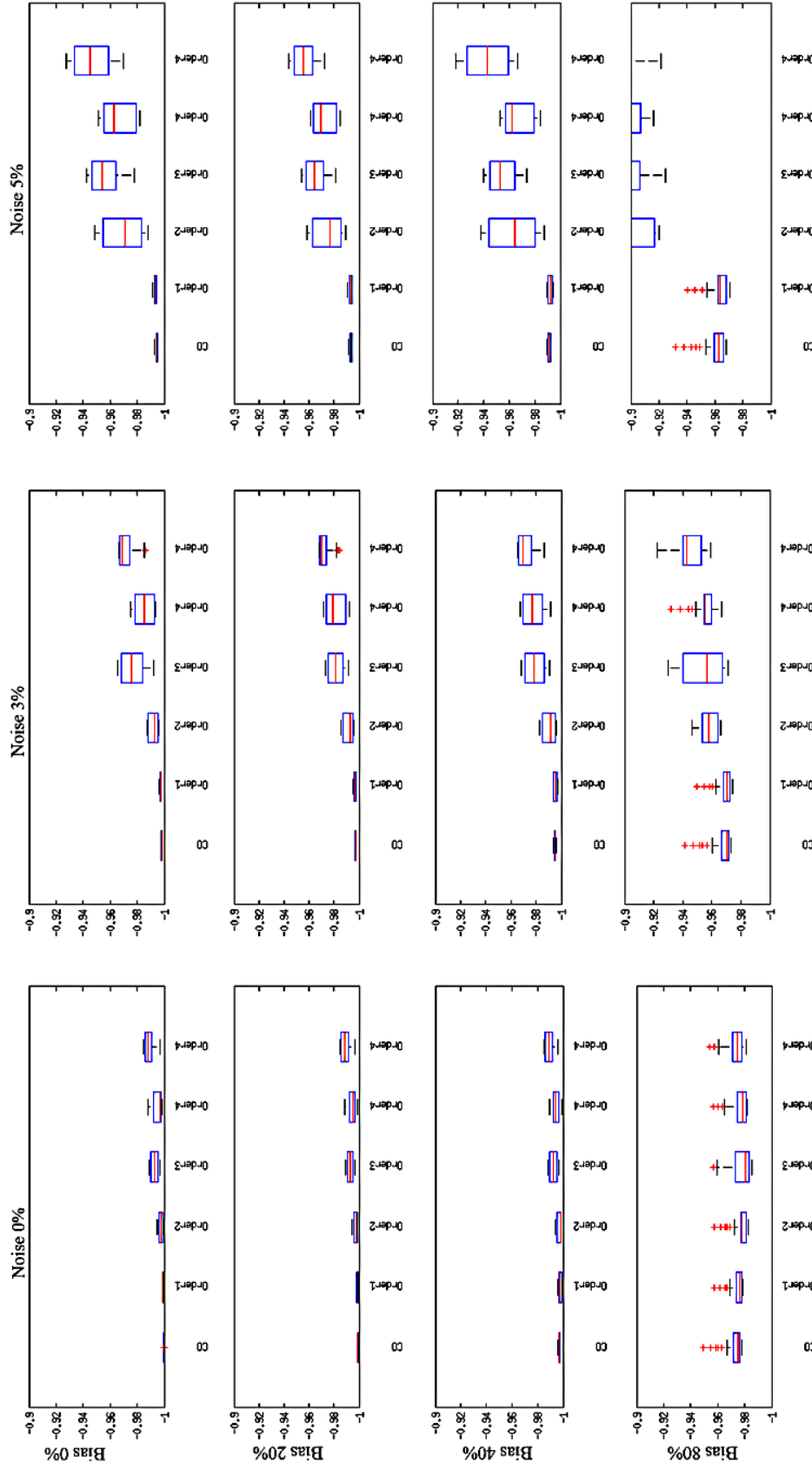


Figure 4.16: Correlation coefficients between the data corrected by the polynomial method when changing the order of the polynomial model from 1 to 5 and the data corrupted by the simulated bias field and noises: Noise from left to right is 0%, 3% and 5%; the strength of the bias field from top to bottom is 0%, 20%, 40% and 80%. The true signal without bias field and noise is shown on the left in the upper left subplot.

4.6 Discussion and Conclusion

This report compares the performances of four bias-field correction methods. The bias-field corrupted data were generated using the BrainWeb simulator, with different combinations of bias-field and additive noise. The corrected datasets were qualitatively and quantitatively compared. N4 is consistently the most reliable correction method, followed by N3 and SPM. N3 and N4 are more robust to noise at higher shrink factors (presumably due to signal averaging). This is consistent with the results reported by Arnold et al. [228]. The correction method used should not increase the intensity distortion and would ideally be idempotent. However, inspection of the results shows that both the wavelet and polynomial methods introduce significant distortion to the bias free and noise free image. The polynomial method is very sensitive to noise. Despite being comparable to the best methods without added noise, its performance rapidly deteriorates as more noise is added. The correlation coefficient metric is insensitive to linear relationships between the corrected data and ground truth. The polynomial result with no inhomogeneity or noise added appears much better when assessed using the correlation coefficient rather than SSD.

There are also some limitations with this study that could be addressed in future. The study only investigated correction of brain data. The ranking of performances may have been different if a wider range of body regions were included. The study only used simulated data, primarily to provide high quality ground truth to enable a quantitative comparison. These results should therefore be confirmed on real scanner acquisitions, which would address some concerns regarding simulated data [236]. The downside would be that indirect quality metrics would have to replace the SSD and CC, since the true signal is unknown. A common approach in this situation is to use manual segmentations to calculate the coefficient of variation within tissue types. This assessment was not performed in this comparison study due to lack of appropriately landmarked data.

4.6 Discussion and Conclusion

This comparison study was performed in order to gain an overview of different intensity inhomogeneity correction methods, and to prepare for developing the preprocessing step for the image registration framework described in the next chapter. Generally speaking, N3/N4 can be the candidate method to add to the proposed registration framework. However, the publicly available implementations have strict requirements about data format and therefore limited applicability to a narrow range of data. Furthermore, the four methods compared in this chapter are all general-purpose algorithms, which means no prior knowledge about the specific applications were integrated. Thus, although the compared methods are applicable to the data acquired in our clinical trials, a customized inhomogeneity correction method will be proposed. The effect of this pre-processing on the performance of our registration framework will be studied in the next chapter.

Automatic Multi-parametric MR Registration Method Using Mutual Information Based On Adaptive Asymmetric K-means Binning

ABSTRACT

Multi-modal or multi-parametric MR registration often requires preprocessing for intensity inhomogeneity. In the previous chapter different inhomogeneity correction methods were compared. In this chapter, a new preprocessing method, based on the homogeneous dynamic intensity ratio and re-arranged histogram specification, is developed. Besides this preprocessing step, the registration framework was further improved by a new multi-resolution optimization strategy. The new framework was validated using both cardiac and neonatal datasets, and has shown superior performances in these applications than the previous algorithm developed for use in abdominal aortic MRI data (see chapter 3).

Results from this chapter were published at The Institute of Electrical and Electronics Engineers (IEEE) International Symposium on Biomedical Imaging (ISBI) 2015, New York, USA. The application of this registration framework to cardiac and

neonatal MR data was presented separately at the European Society for Magnetic Resonance in Medicine and Biology (ESMRMB) annual meeting 2015, Edinburgh, UK.

5.1 Introduction

For multi-modal and multi-parametric registration, entropy-based voxel similarity measures, such as mutual information (MI), were perhaps the most widely applied techniques in the past two decades, [55], as they require less user-interactions than feature-based methods, and demonstrate better robustness than other similarity measures. However, for those registration applications that involve MR data, intensity inhomogeneity can bias the intensity correspondences between the reference and floating images, since unfortunately the inhomogeneities in both images can have very different appearances.

In chapter 3, a registration framework was proposed and successfully applied to the CT and MR images acquired in the *MA³RS* clinical trial. However, as discussed in chapter 4, dealing with cardiac MR data from the *IRNMAN* project, it failed to register a considerable amount of data due to severe intensity inhomogeneity, or “bias field”, appearing in the images. This means that a preprocessing step was required to minimize the effect of this artefact that may bias the later registration. To prepare for this preprocessing step, a comparison study of different “bias field” correction methods was performed as discussed in the last chapter. Among the four compared methods, the Nonparametric Nonuniform intensity Normalization (N3), as well as its popular variant, N4, showed the most promise on the simulated datasets. N3 and N4 can both be classified as *statistical methods*, working in the probability distribution function (PDF) domain. However, all four of the inhomogeneity correction methods are general-purpose algorithms. Hence application specific prior knowledge, that is commonly available in registration problems, was not used. Furthermore, when processing the “real” data, it is often impossible to precisely remove the intensity inhomogeneity. Thus, for registration applications, it is more realizable to reduce the negative effects from the intensity inhomogeneity on the similarity measure than to attempt to directly remove the inhomogeneity itself.

5.1 Introduction

In this chapter, instead of directly applying any general-purpose correction method, a new preprocessing step was developed for use with the asymmetric cluster-to-image registration framework. A new parameter is calculated from the reference and floating datasets, called the *homogeneous dynamic intensity ratio* (HDIR). It allows for optimal selection of target of k -means binning. Following this, a rearranged histogram specification (RHS) technique is used to improve the intensity distribution of the non-clustered data. Preprocessing is applied in the PDF domain, by manipulating the datasets' histograms, in a similar fashion to the N3 and N4 techniques. Besides this preprocessing step, the registration framework was improved using a new multi-resolution and optimization strategies. The performance of the new registration framework is evaluated using two quite different sets of data from ongoing clinical studies at the University of Edinburgh: cardiac data from the *IRNMAN* study, and neonatal brain data, details of which are introduced in section 5.4. Experiments were performed to show how the different stages of the proposed framework are important to the accuracy and robustness of the results. The theory and details of this histogram based preprocessing method are introduced in section 5.2. Other improvements applied to the registration framework can be found in section 5.3. Section 5.4 describes the data and experiments used to validate the new registration framework, and the results are shown in section 5.5. Finally, some discussions and conclusions are made in section 5.6.

5.2 Re-arranged Histogram based Intensity Distribution Correction

In the registration framework introduced in the previous chapter, the asymmetric k -means clustering method was used to calculate MI. The motivation of this is to overcome the histogram dispersion problem in the data without breaking the ability of distinguishing detailed structures [237]. However, when the data suffers from intensity inhomogeneity, especially when the appearances of the inhomogeneity in the reference and floating data are different, histogram dispersion problems can still be caused. This can cause failure of the registration process as discussed in previous chapters. Figure 5.1 shows a example of two types of short axis cardiac MR data (T1-weighted (T1W) inversion recovery delayed enhancement and T2* weighted (T2*W) as introduced in chapter 4), with different intensity inhomogeneity artefacts, processed by different binning strategies, either linear binning or k -means binning. It can be easily seen that the T2*W data which has more severe inhomogeneity also displays more obvious histogram dispersion, no matter whether processed by linear or k -means binning methods. Figure 5.2 shows, with two visualization methods, an example of the failed registration. This failure can be caused by the histogram dispersion effects, which can be proved in a simulated experiment demonstrated below.

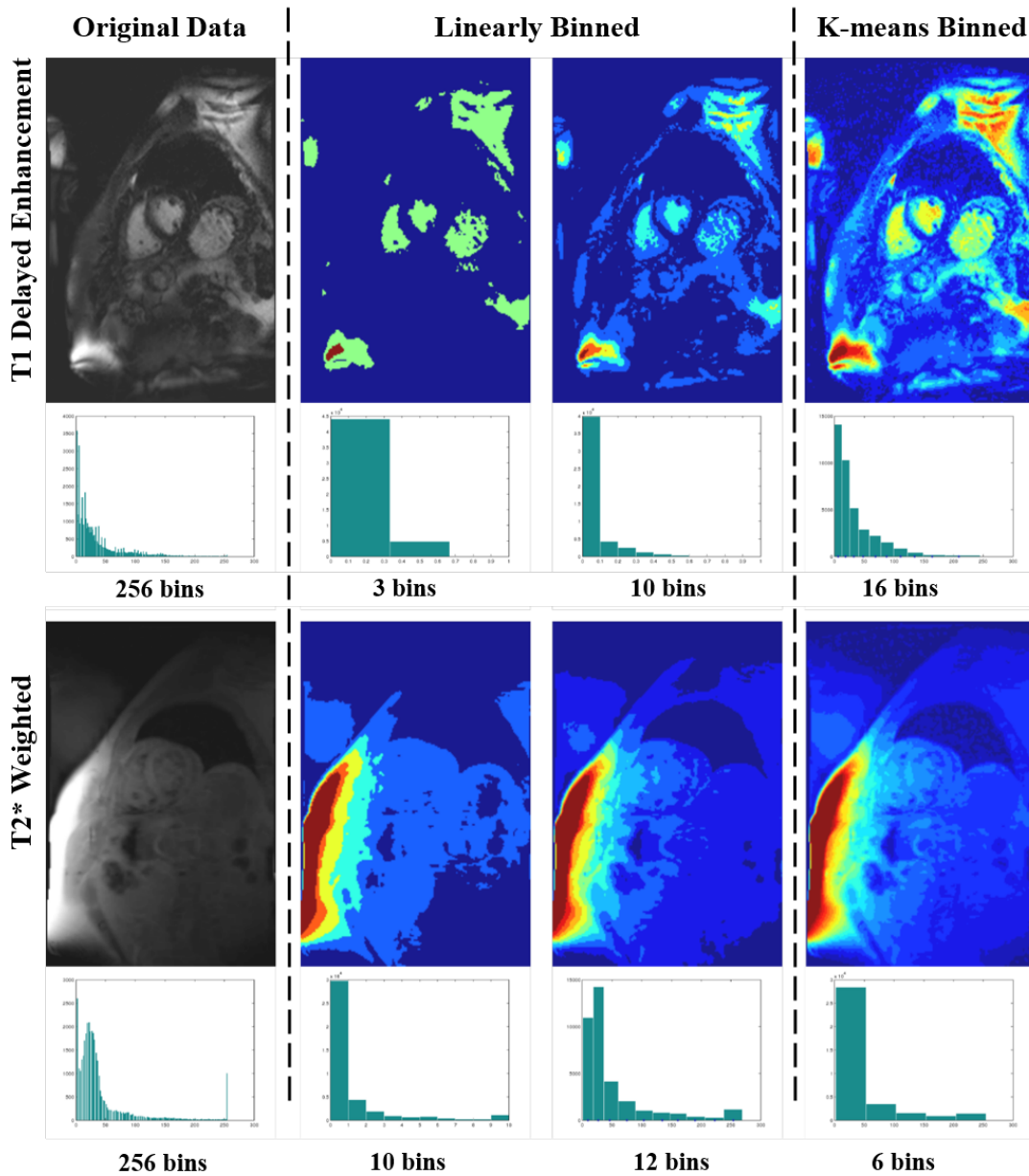
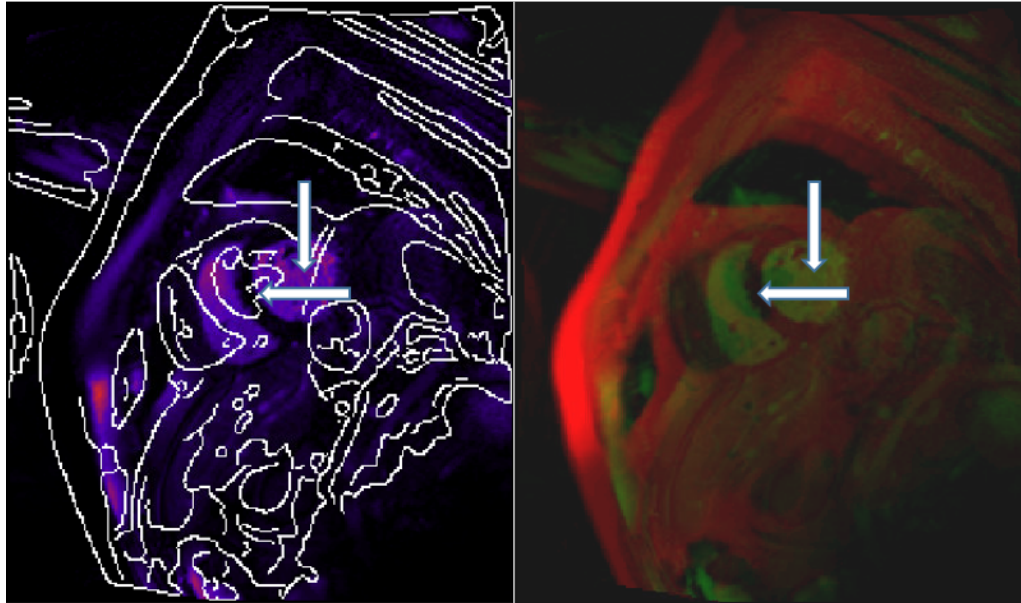


Figure 5.1: Examples of short axis cardiac images with different intensity inhomogeneity artefacts processed by different binning methods: at the top is the T1 weighted delayed enhancement data, at the bottom is the T2* weighted data which suffered more severe intensity inhomogeneity.

Before registration



After registration

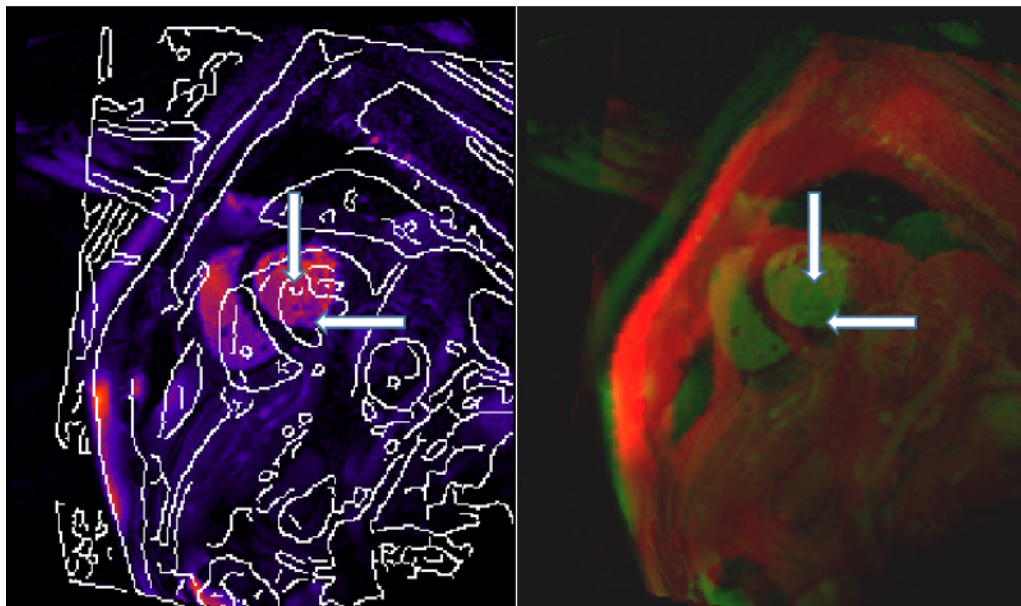


Figure 5.2: Visualizations of the failed registration caused by histogram dispersion: the edge image of the transformed T2*W data overlapped with the original T1W delayed enhancement data are shown on the left; the overlapped red-green visualizations are shown on the right, where the T2*W data is shown in red and T1W delayed enhancement data shown in green. The left ventricle, as the object of interest in our study, is shown by the vertical arrows in T1W delayed enhancement data, and by the horizontal arrows in the T2*W data.

5.2 Re-arranged Histogram based Intensity Distribution Correction

As discussed in chapter 3, to apply the asymmetric cluster-to-image registration method, one of the images — either the reference or floating image — has to be chosen for k -means binning. It was found that the best results were obtained when the clustering was applied to the image with the largest dynamic range, and fewest artefacts. This is because clustering the image with less dynamic range and/or severe inhomogeneities emphasizes the dispersion effects on both histograms. Such dispersion reduces registration accuracy.

The effects of histogram dispersion and different choices of clustering on registration is demonstrated by the simple simulation shown in Figure 5.3. The synthesized images show four rectangles of different sizes. Figure 5.3(a) and 5.3(b) show the synthesized reference and floating images with different numbers of dynamic grayscale levels, with their corresponding intensity histograms shown in Figure 5.3(d) and 5.3(e). The intensities used to represent the same object in the reference and floating images have a non-linear correspondence. Figure 5.3(c) and 5.3(f) show the floating image, and its histograms, after corruption by a simulated intensity inhomogeneity. It is easily observed that, on the histograms of the data without intensity inhomogeneity, the imaged objects are clearly represented by separated groups of intensities. However, this is not true in the data corrupted by the “bias field”, due to the histogram dispersion caused by the intensity inhomogeneity. As shown in Figure 5.4, when applying the k -means algorithm introduced in chapter 3 to the data corrupted by the intensity inhomogeneity, a large proportion of the pixels belong to different objects are grouped into the same cluster, while pixels belonging to different objects are well separated by the clustering process. As a result, the selected clustered image plays an important role in the registration process. As shown in Figure 5.5, when the reference image is selected for k -means clustering, all the four rectangles in the uncorrupted floating image are well aligned to the reference image. When registering the floating image corrupted by the intensity inhomogeneity, the rectangles located at the top-left and bottom-right corners are misaligned by a few

pixels. No rectangle is aligned when the corrupted floating image is chosen for clustering.

When dealing with the MA^3RS data, for CT-MR registration, the k -means binning was applied to the CT data, and to the T2W data for T2*W-T2W registration. Compared to the T2*W data, both the T2W and CT data show the anatomical structures with more dynamic range, while suffering less inhomogeneity. However, when registering similar MR sequences, for example such as in the *IRNMAN* project, a measure is required to help inform which image should undergo k -means binning to give the best result. In this new registration framework, a histogram-based measure, *homogeneous dynamic intensity ratio* (HDIR), was used to measure dynamic intensity ranges and inhomogeneity levels.

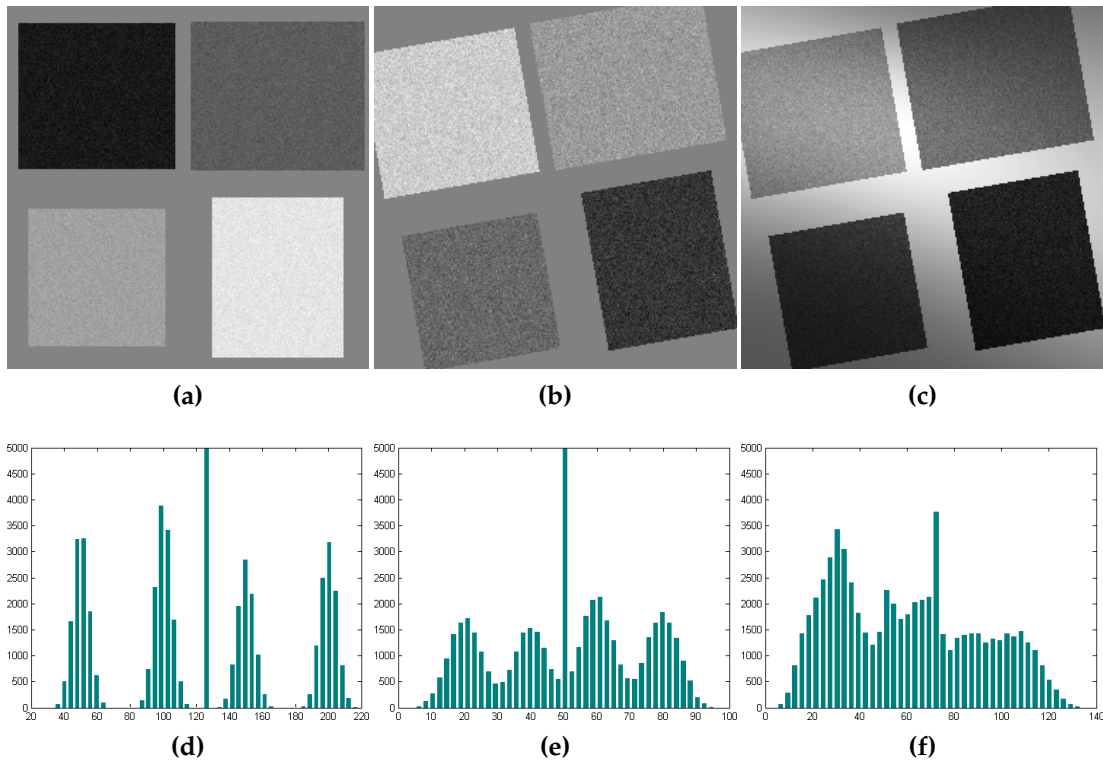


Figure 5.3: Synthesized data contain four rectangles of different sizes and represented by different ranges of intensity used to observe the histogram dispersion effects on the performance of registration: (a) and (d) the reference image, and its histogram, that has a 255-level dynamic grayscale; (b) and (e) the floating image, and its histogram, that has a 100-level dynamic grayscale; (c) and (f) the floating image, and its histogram, corrupted by an intensity inhomogeneity with a strength equal to 40% of the intensity range.

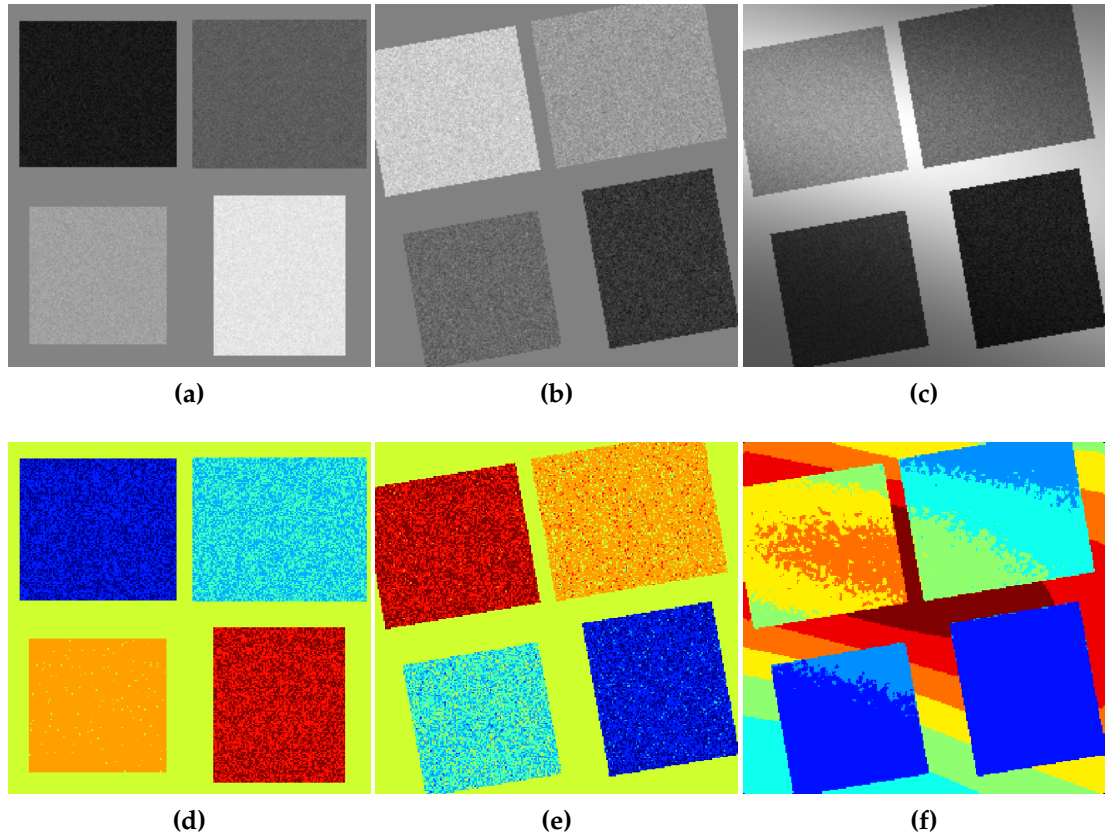


Figure 5.4: Clustered images obtained by applying the k -means method to the synthesized data: (a) and (d) the original and clustered reference image; (b) and (e) the original and clustered floating image without intensity inhomogeneity; (c) and (f) the original and clustered floating image corrupted by the intensity inhomogeneity.

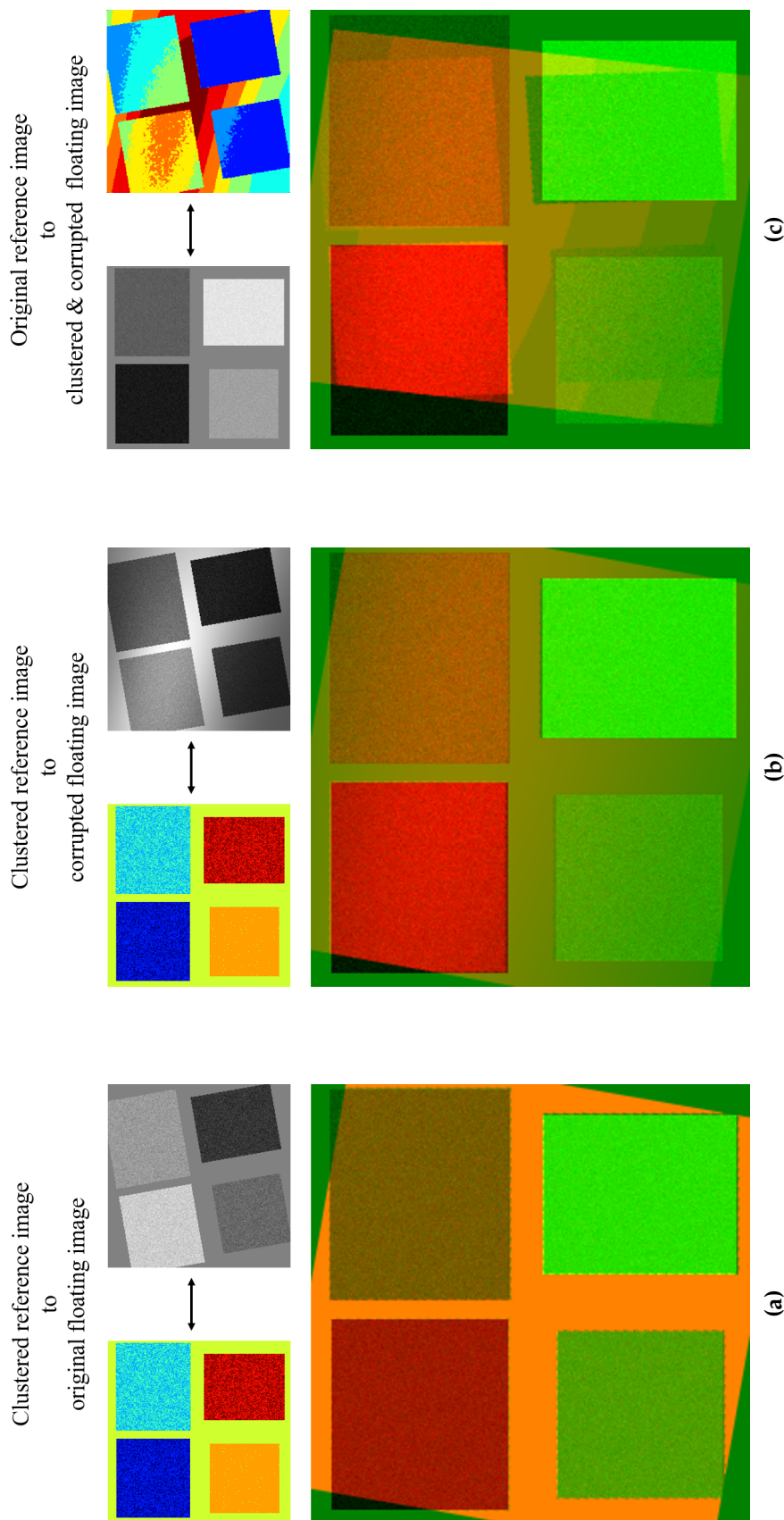


Figure 5.5: Results of affine registration obtained from the synthesized data visualized by overlapped red and green colour channels: (a) the results of registering the original floating image without intensity inhomogeneity to the clustered reference image; (b) the results of registering the floating image corrupted by inhomogeneity to the clustered reference image; (c) the results of registering the clustered floating image corrupted by the inhomogeneity to the original reference image.

The experiment shown in Figure 5.3, 5.4 and 5.5 provides a clue to derive a quantitative measure which can be used to choose the clustered image for asymmetric cluster-to-image registration. The empirical standard used in chapter 3 is that the image chosen to be clustered should suffer from less intensity inhomogeneity and additive noise. Ignoring background intensity value which is represented by the highest bin in Figure 5.3(d), 5.3(e) and 5.3(f), the rest intensity values are considered as “dynamic” intensity values which are used to represent the imaged objects. In the ideal case shown in this simulation experiment, the numbers of “dynamic” voxels should be the same in both reference and floating images. However, in real medical images the voxels belong to the imaged objects may have the same intensity values with the background due to the imaging property of different modality. These voxels are useless when calculating joint-histogram-based similarity measures, such as MI, as they will drop in the same cluster, thus the same row and column in the joint histogram, with the background voxels. So intensities of these voxels are not considered as “dynamic” voxel intensities. In the *IRNMAN* and *MA³RS* data, the background voxels tend to have the lowest intensity value of the image. In other words, the background voxels are smaller than and out of the range of “dynamic” intensity values. Furthermore, as a result of the “bias field” and the additive noise, some voxels have higher intensity values than their true values. Some of them can be moved out of the “dynamic” range, and introduce biases in the joint histogram. So when all the images are sampled to the same resolution and cropped to the same size, more voxels should be included in the “dynamic” range on the image influenced by less intensity inhomogeneity and additive noise.

Figure 5.6 shows the images used in this simulation experiments with the “dynamic” ranges marked on their histograms. Note that the background is normalized so that its intensity value is 0, and that a considerable amount of voxels are moved out of the “dynamic” range as a result of intensity inhomogeneity. For the image shown by Figure 5.6(d) and 5.6(e), there is 66.68% voxels dropped in the

5.2 Re-arranged Histogram based Intensity Distribution Correction

“dynamic” range. When it is corrupted by the “bias field” as shown in Figure 5.6(c) and 5.6(f), only 52.72% remains. The percentage of voxels drop in the “dynamic” range can be measured using the probability densities function (PDF) of the voxel intensity.

Beside the number of voxels in the “dynamic” range, the choice of the clustered image is related to the distribution of bins on the image histogram within the “dynamic” range. For the image which has better visibility of anatomical structure, the variation of histogram bin heights within the “dynamic” range should be higher as the bins of its histogram are better separated for different imaged objects. The variation of histogram bin heights can be measured by the variance value. For example, for the image shown in Figure 5.6(a) whose histogram is shown in Figure 5.6(d), this variance is 1.793×10^6 . For Figure 5.6(b) and 5.6(e), this variance is 3.671×10^5 . Furthermore, after the histogram dispersed by the intensity inhomogeneity tend to merge the gaps between different groups of bins that represent different imaged objects, thus reduces the variation of image intensity within the “dynamic” range. In this case, the variance of the histogram bin heights within the “dynamic” range tend to decrease. For example, this variance for the image shown by Figure 5.6c and 5.6(f) is 1.968×10^5 .

To sum up, degrading the image quality leads to two effects on image histograms: a) the voxels “leaking” out of the “dynamic” range (or the “voxel leaking” effect); and b) reduce the variation intensity values within the “dynamic” range (or the “variation decreasing” effect). However, when dealing with real images, it is difficult to find this “dynamic” range due to the fact that the ground truth of the intensity inhomogeneity and the additive noise is unavailable. Alternatively, a pair of fixed thresholds, a higher and a lower bounds, can be used with the normalized images where the intensity values are within the range $[0, 1]$. As shown in Figure 5.7, the intensity inhomogeneity and the additive noise lead to similar “voxel leaking” and “variation decreasing” effects in this range. The HDIR is defined based on the quantity of voxels and variance of voxel intensities within this range.

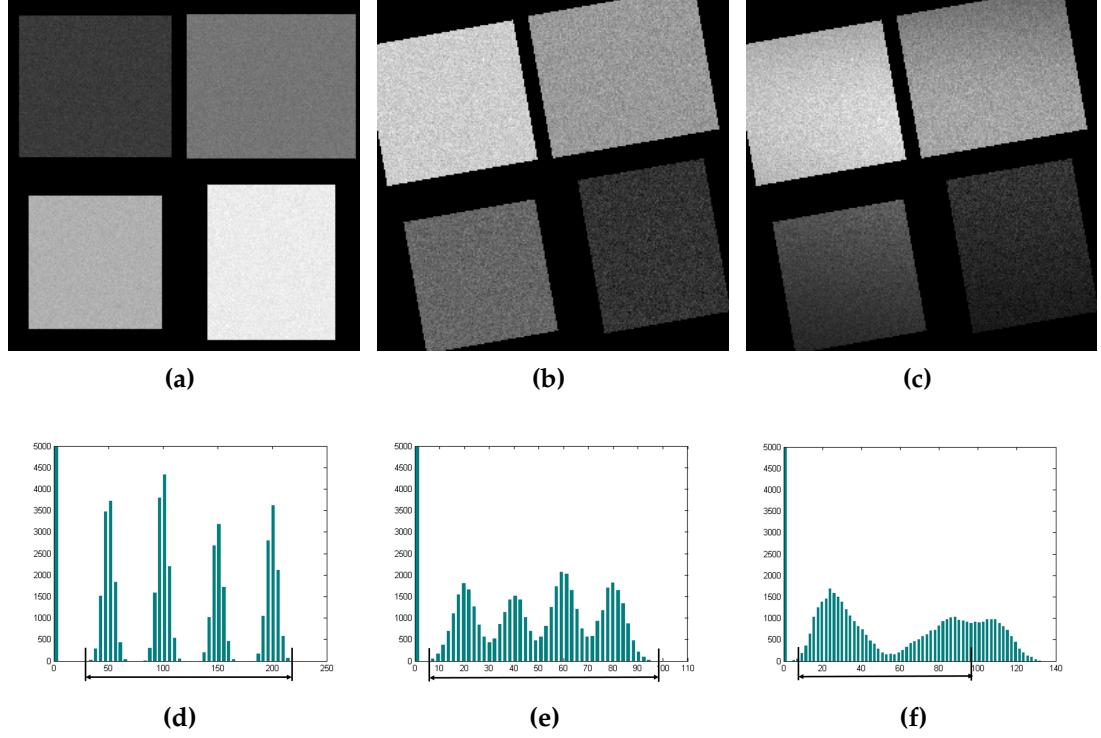


Figure 5.6: The images used in the simulation experiment and their histograms shown with the “dynamic” ranges: the reference image which is chosen to be clustered and its histogram are shown in (a) and (d); the floating image without intensity inhomogeneity and its histogram are shown in (b) and (e); the floating image with intensity inhomogeneity and its histogram are shown in (c) and (f). The “dynamic” ranges of these images are marked by the black arrows, and the range define on (f) is the same with (e).

5.2 Re-arranged Histogram based Intensity Distribution Correction

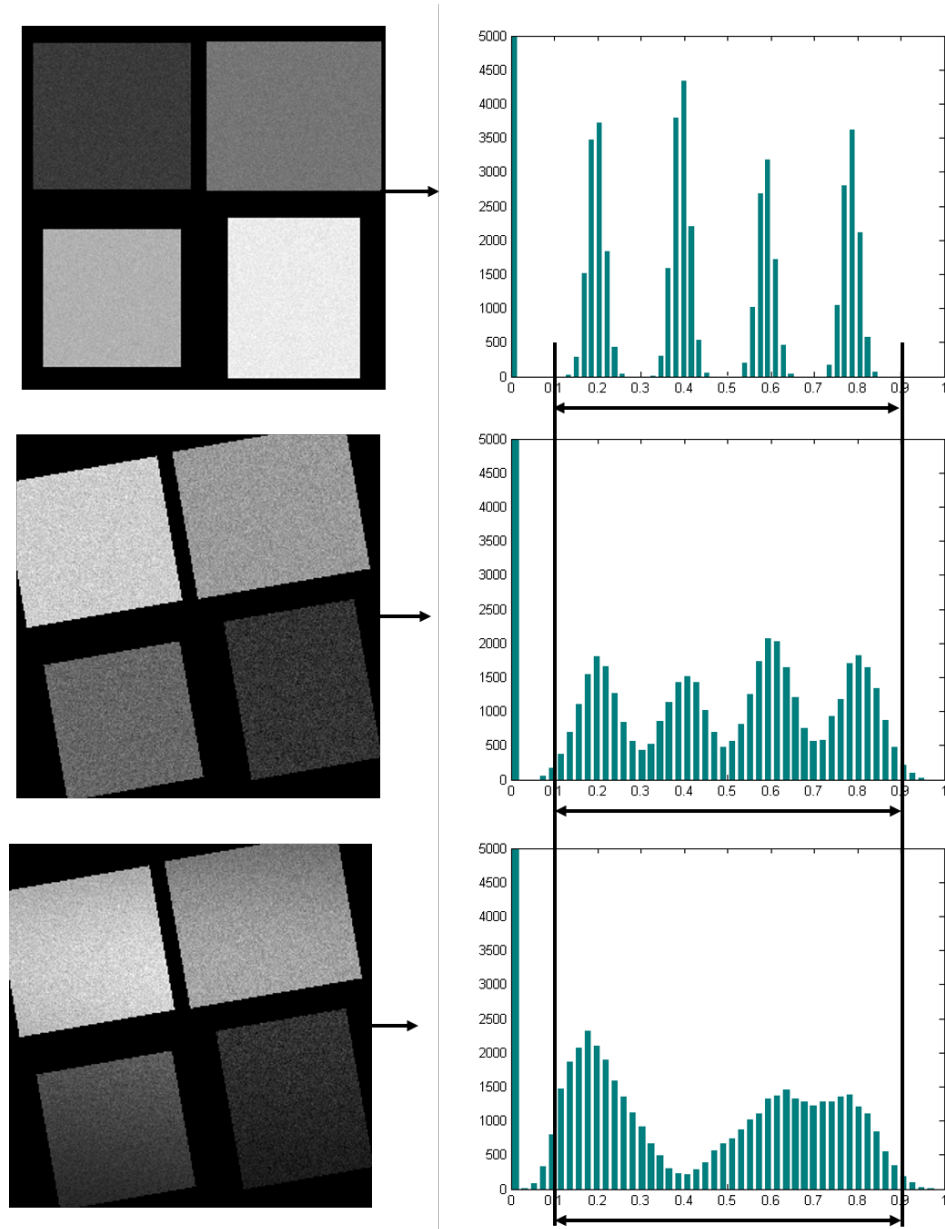


Figure 5.7: The range of normalized intensity values decided by two thresholds define on the histograms of each image in the simulated experiment. From top to bottom: the reference image (selected to be clustered), the floating image without intensity inhomogeneity, and the floating image corrupted by intensity inhomogeneity.

First, both the reference and floating images are normalized so that the same higher and lower bounds of the “dynamic” intensity range can be defined for both

images. For an image I' , its normalized image I is given by:

$$I = \frac{I'_{max} - I'}{I'_{max} - I'_{min}}, \quad (5.1)$$

where I'_{max} and I'_{min} are the maximum and minimum intensity values of I' .

Let $\rho_I(\bullet)$ be the PDF of the normalized voxel intensity, $i \in [0,1]$, of image I . A probability \mathcal{P}_I is defined as:

$$\mathcal{P}_I = \int_{i \in [b_L, b_U]} \rho_I(i), \quad (5.2)$$

where b_L and b_U are two thresholds defined on image intensity. Practically, the normalized histogram can be used as a discrete estimation of the PDF ρ_I , which is calculated by:

$$\hat{\rho}_I = \frac{\hat{\mathcal{H}}_I}{\sum \hat{\mathcal{H}}_I}, \quad (5.3)$$

where $\hat{\mathcal{H}}$ is the intensity histogram for a image I , and $\hat{\rho}_I$ is the estimated PDF. Then the estimation of the probability \mathcal{P}_i is calculated by:

$$\hat{\mathcal{P}}_I = \sum_{i \in [b_L, b_U]} \hat{\rho}_I(i). \quad (5.4)$$

Given the reference image μ and the floating image ν , the HDIR is:

$$\text{HDIR} = \frac{\text{var}(\hat{\mathcal{H}}_\mu) \hat{\mathcal{P}}_\mu}{\text{var}(\hat{\mathcal{H}}_\nu) \hat{\mathcal{P}}_\nu}, \quad (5.5)$$

where $\hat{\mathcal{H}}_\mu$ is the intensity histogram for image μ , excluding the intensity values larger than b_U or smaller than b_L , and similarly $\hat{\mathcal{H}}_\nu$ is the truncated histogram for ν . $\text{var}(\bullet)$ represents the variance of the histogram. $\hat{\mathcal{P}}_\mu$ and $\hat{\mathcal{P}}_\nu$ are the probabilities calculated using equation 5.4 for μ and ν . Here $b_L = 0.05$ and $b_U = 0.95$ were used empirically.

Essentially, the HDIR compares the product $\text{var}(\hat{\mathcal{H}}_I) \cdot \hat{\mathcal{P}}_I$ of the two images μ and ν . Based on the definition of variance, it is a measure of the average variation of each voxel. Thus the product can be explained as the amount of variation within

5.2 Re-arranged Histogram based Intensity Distribution Correction

the range defined by b_L and b_U . If the $\text{HDIR} \geq 1$, it means the reference image μ has better visibility of the anatomical structures while suffering less inhomogeneity, then the k -means binning is applied to image μ , otherwise it will be applied to image ν . For the three images shown in figure 5.7, the values of $\text{var}(\hat{\mathcal{H}}_I) \cdot \hat{\mathcal{P}}_I$ are 8.273×10^{10} , 7.534×10^{10} and 7.360×10^{10} . Thus to perform asymmetric K-means binning, the reference image shown at the top of Figure 5.7 should be chosen to be clustered for better registration result. This is consistent with the results shown in Figure 5.5. Furthermore, the HDIR is also validated using MA^3RS data from 50 randomly selected patients. The results show the CT and T2W images should be clustered when being registered with T2*W images, which is consistent with the results of Chapter 3.

The HDIR helps choosing the clustered image when perform the asymmetric cluster-to-image registration. At the same time, the RHS is applied to the other image to correct its intensity distribution. In case of registering the T2*W images to T1W delayed enhancement images of the *IRNMAN* project, $\text{HDIR} \geq 1$ indicates that μ is the T1W delayed enhancement image, and ν is the T2*W data.

The conventional histogram specification method is based on the histogram equalization technique which transforms the intensity distribution of an image μ using its cumulative density function (CDF), $\phi_\mu(i)$:

$$\hat{i} = \phi_\mu(i) = \sum_{j=0}^i \rho_\mu(j), \quad (5.6)$$

where i and \hat{i} are the intensity level before and after equalization.

Let ϕ_μ and ϕ_ν present the CDF of the two images μ and ν . The conventional histogram specification [238] then maps the intensity distribution of ν by a transformation function $\psi_{\nu \rightarrow \mu} = \phi_\mu^{-1}(\phi_\nu(\bullet))$. To perform RHS, here I introduce transformation functions $f_\mu(\bullet)$ and $f_\nu(\bullet)$ which rearrange the histograms of image μ and ν in descending order by ρ_μ and ρ_ν . Then I calculate the CDFs of both re-arranged histograms, denoted as $\phi_{f_\mu}(\bullet)$ and $\phi_{f_\nu}(\bullet)$. The transformation function of this

re-arranged histogram specification then becomes $\psi_{\nu \rightarrow \mu} = f_{\nu}^{-1}(\phi_{f_{\mu}}^{-1}(\phi_{f_{\nu}}(f_{\nu}(\bullet))))$. Figure 5.8 shows an example of a pre-contrast cardiac T2*W image before and after its intensity distribution is corrected by the histogram of a delayed enhancement image using RHS. It can be easily observed that the intensity inhomogeneity of the T2*W was attenuated while many details of some anatomical structures were enhanced.

Just as with the previous registration method that was successfully applied to the MA³RS project, the “Bottom-up” k -means method was applied for asymmetric cluster-to-image registration. The HDIR described above can be used to select the optimal candidate for k -means binning between the reference and the floating data, as well as the target image to perform RHS for better visibility of anatomical structures and intensity homogeneity. The “Bottom-up” k -means clustering method uniformly initializes a large number of cluster centres at the beginning of the clustering process. Then at the end of each iteration of expectation maximization (EM), neighbouring clusters with distances smaller than a threshold are merged. This framework performs k -means clustering and intensity distribution correction simultaneously, as shown in Figure 5.9. Finally, the clustered and corrected non-clustered images are used to calculate a MI-based similarity measure.

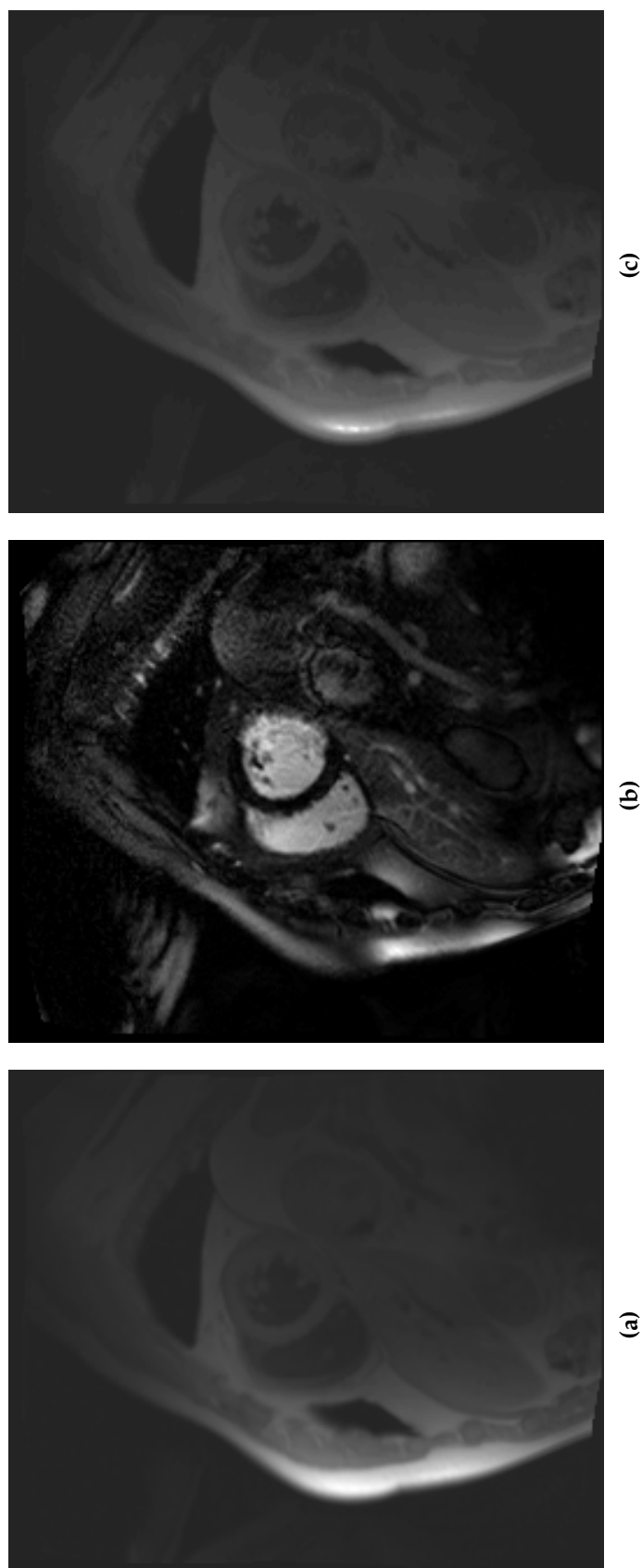


Figure 5.8: An example of cardiac MR data before and after being processed by ranked histogram specification: (a) the T2*W image before being processed using RHS; (b) the delayed enhancement image used to correct intensity distribution of the T2*W image; (c) the T2*W image after being processed using RHS.

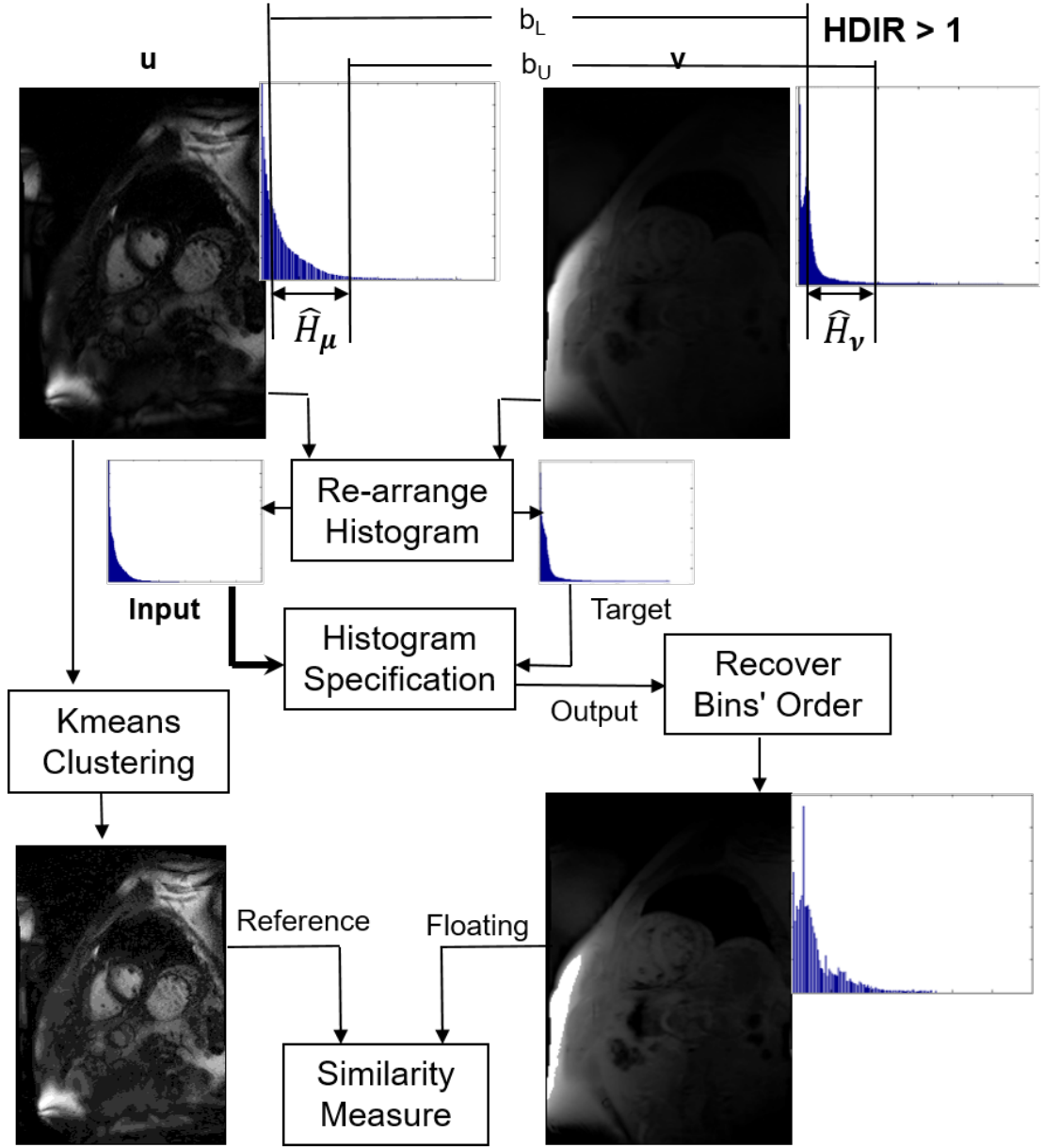


Figure 5.9: The intensity distribution correction based on rearranged histogram specification and k-means binning process: μ and v are the reference and floating images, \hat{H}_μ and \hat{H}_v is the intensity histograms between two thresholds b_L and b_U . In the case of registering T2* weighted data to T1 weighted delayed enhancement data, $\text{HDIR} > 1$ indicates that the T1 weighted delayed enhancement data has better visibility of the anatomical structures while suffering less inhomogeneity. Thus the intensity of the T2* weighted data is corrected using the rearranged histogram specification method.

5.3 Registration Framework Implementation

As introduced in chapter 3, the registration pipeline starts with the selection of a region of interest (ROI) on each of the reference and floating datasets. The ROI is defined so as to include the left and right ventricles, as shown in Figure 5.10. Since the cardiac datasets are stacks of multiple 2D slices, a ROI needs to be manually selected first by placing a seed on a single slice which shows good visibility of the left and right ventricles. Then the ROIs on other slices are generated through a similar bi-direction tracking method as for the aortic image registration in chapter 3. Because the ROI correction step using Hough transformation is designed only for objects with a circular shape, it is not used here. In this work new slices were created so that the distance between the neighbouring slices is less than 1.5 mm, which is the empirical threshold to allow adequate tracking of centres of ROIs that include the interested anatomical structures. Once the ROI centres on all the slices are generated, the data can be initially aligned by registering the ROI centres: first using the iterative closest points (ICP) algorithm [180], before performing the voxel intensity based registration as shown in chapter 3. Alternatively, if the correspondences between slices are known, the least squares method [181] can be applied to solve this non-iteratively, using singular vector decomposition (SVD). Figure 5.11 shows an example of the initial alignment achieved between a T2*W cardiac image and a delayed enhancement image.

To improve speed and robustness, a multi-resolution approach, based on the discrete wavelet transformation, was used. Registration starts from the lowest resolution and progresses to the highest resolution. Figure 5.12 shows an example of down-sampled data obtained using the Gaussian pyramid and wavelet pyramid approaches. It can be seen that the wavelet pyramid has advantages with regard to compactness, orthogonality, and retaining both the spatial and frequency information, compared with the Gaussian pyramid used to register MA^3RS data. When performing k -means clustering, with a L -level wavelet pyramid, the largest number of cluster

centres, \mathcal{N}_k , on the k th layer of the pyramid is limited to $\max(48, 8 * k), k = 1, 2, \dots, L$.

For robust registration and efficient searching, global, gradient-independent, optimizers were used. In the previous work for MA^3RS registration [239], the DIRECT optimization algorithm [240] was used. Although this algorithm has been subsequently been improved in various ways, it still has limited efficiency dealing with functions with local optima. This is because the DIRECT algorithm is deterministic, and the searching complexity tends to increase along with the size of searching space and number of local optima. In this method, I used the particle swarm optimizer (PSO) [28] to search for the optimal transformation. A detailed introduction of PSO methods can be found in chapter 6. Experiments performed by Eberhart and Kennedy [28] showed that it is sufficient to solve an optimization with 10 initialized particles for each dimension. Thus for this rigid-body registration problem, I used 60 initialized particles.

The preprocessing step, as well as other similar intensity inhomogeneity correction methods, may allow more effective alignments. However, it also inevitably changed the quantitative information in the data. Thus, for reliable clinical assessments and calculation of quantitative values from the data for the clinical trials, the optimal transformation, which was calculated by the registration framework with the preprocessed data, was finally applied to the unprocessed original data.

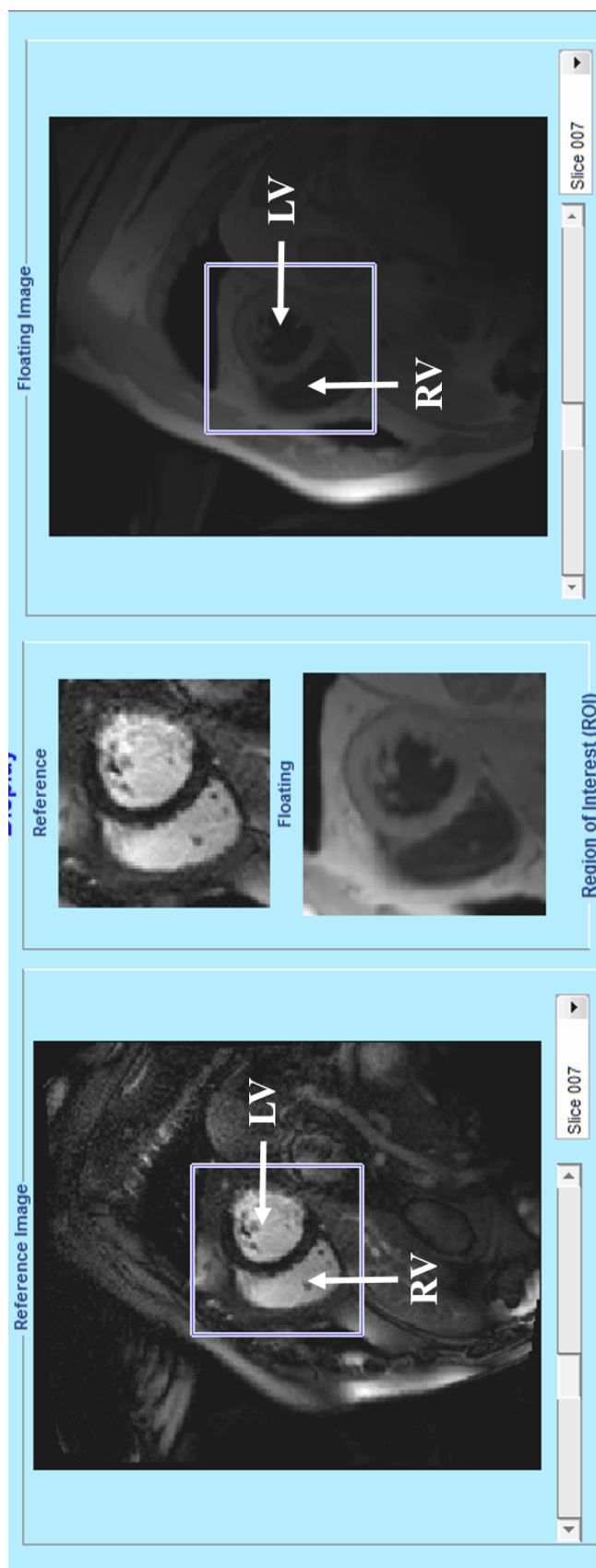


Figure 5.10: Examples of ROIs selected on the T1 weighted delayed enhancement data (left) and pre-contrast T2* weighted image (right). The blue boxes show the regions of interest in both reference and floating images. A region of interest includes the left ventricle (LV) shown by the horizontal arrows, and the right ventricle (RV) shown by the vertical arrows.

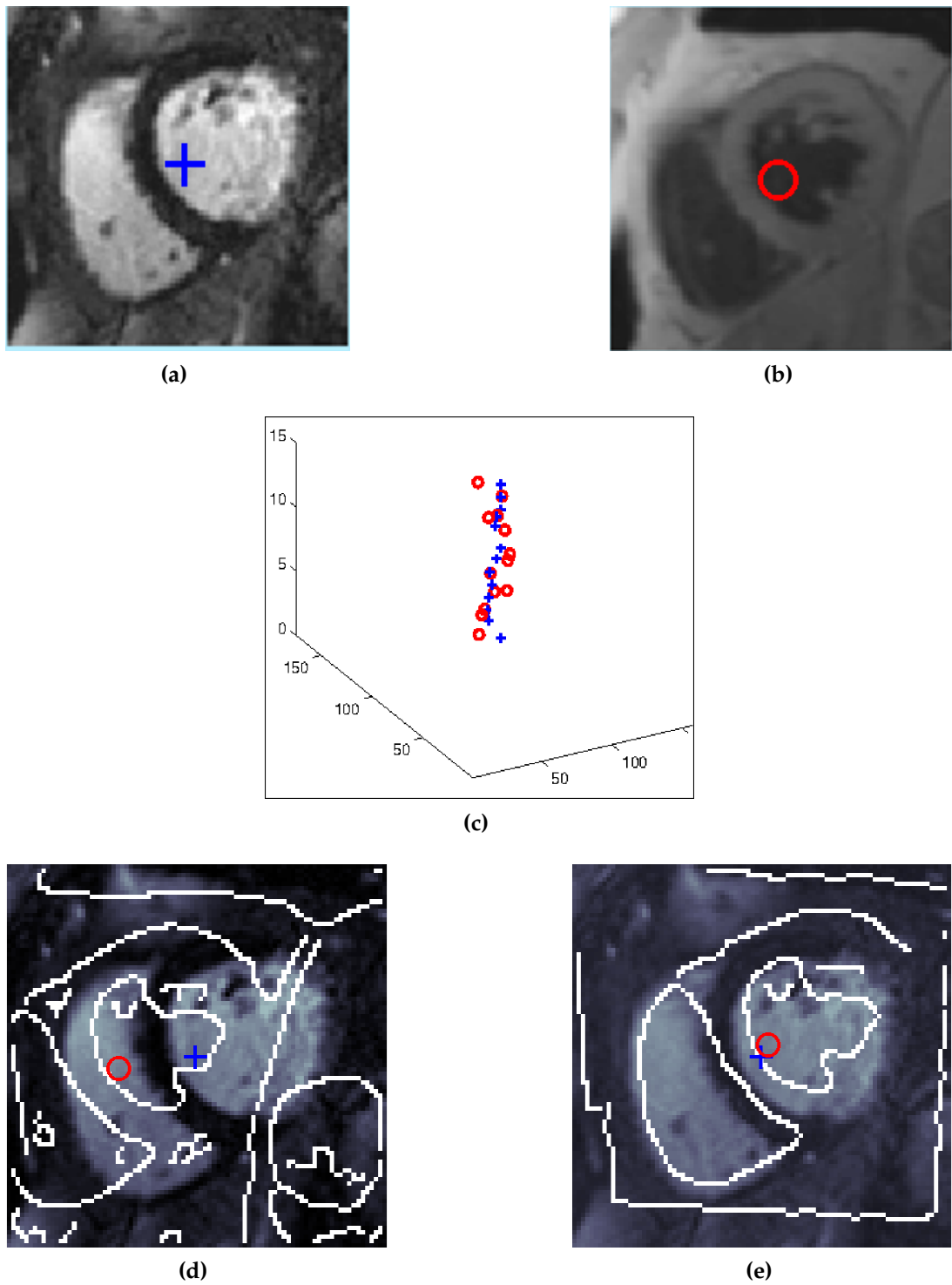


Figure 5.11: An example of a T2* weighted cardiac data initially aligned to a delayed enhancement data achieved using automatically tracked ROI centres: (a) and (b) ROI centres on the reference and floating data (c) Alignment of 2D ROI centres (b) and (e) Visualization of overlapping the edge image of the delayed enhancement data over the T2* weighted data before and after the initial alignment.

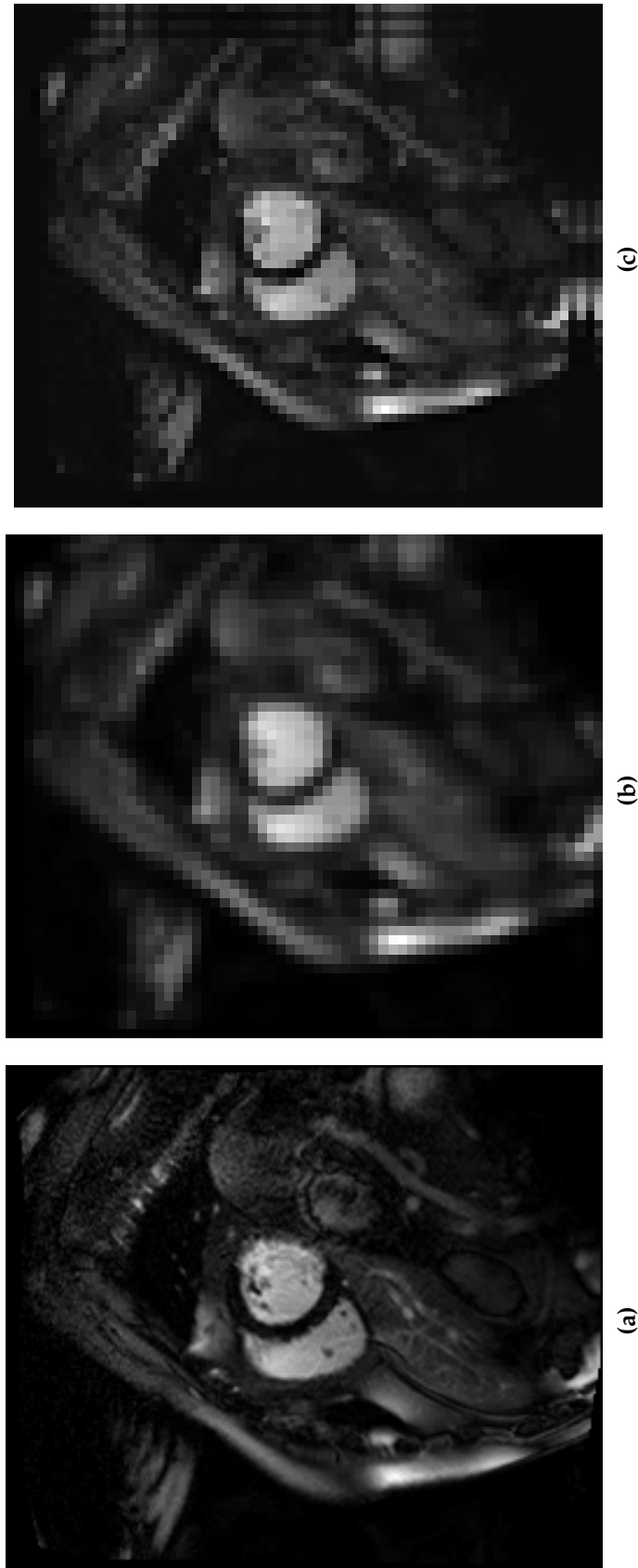


Figure 5.12: Example of data down-sampled to 0.25 of the original resolution obtained from Gaussian pyramid and wavelet pyramid: (a) the original delayed enhancement data; (b) the down-sampled data from Gaussian pyramid; (c) the down-sampled data from wavelet pyramid.

5.4 Experiments and Validation

The registration method was validated using two diverse sets of data, both acquired as part of on-going clinical trials. Both sets of data were registered using the three-level multi-resolution framework described above. This new registration framework was integrated in the GUI tools introduced in chapter 3.

5.4.1 Cardiac Data

The registration framework is first applied to register the cardiac MR data of the *IRNMAN* project which has been introduced in chapter 4. Examples of data used in this study have been shown in Figure 5.8(a) and 5.8(b). The registration ROI was defined to cover the whole left ventricle and main structures of heart as shown in Figure 5.10.

As discussed in chapter 3, for the *MA³RS* project, the performance of registration was evaluated using the differences between pure manual registrations performed by the users and the automatic registration results produced by the registration software. However, it is difficult to perform pure manual registrations for our cardiac data as the reference and floating data are far from each other in the searching space, and have different imaging qualities. So the performance of the registration was evaluated by purely manual corrections performed by experienced clinicians on the automatic registration results. Errors were calculated in the form of Euclidean distances, and Euler angles [195] used in the axis-angle rotation representation. Although the automatic registration results may have incentive effects on manual corrections, compared to the previously proposed framework which failed most registrations of these datasets as shown in Figure 5.2, sometimes even manually uncorrectable, useful conclusions can be drawn about the performance of the proposed registration method. Figure 5.13 displays an example of the ROI on the pre-contrast T2*W data aligned to the ROI on T1W delayed enhancement data after registration by the proposed

5.4 Experiments and Validation

method, and after the registration result being manually corrected. Data of 30 patients were collected, and 45 Post- to Pre-contrast T2*W image registrations and 53 T2*W to Delayed enhancement image registrations were evaluated.

5.4.2 Neonatal Data

For a more reliable validation of the new registration framework, I also used a dataset of 31 neonatal volumes, and calculated target registration error (TRE) from 1908 pairs of corresponding landmarks (18 on each volume). The data were from a clinical research project aiming to analyse premature brain functions. Ethical approval was obtained from the National Research Ethics Service, and informed written parental consent was obtained. Infants were scanned at 38-44 weeks' postmenstrual age in natural sleep with pulse oximetry, temperature and electrocardiography data monitoring. Exclusion criteria include infants with congenital infection, major chromosomal abnormalities, and evidence of central nervous system malformation or injury on MRI. All the data were acquired using a Siemens Magnetom Verio 3T MRI clinical scanner (Siemens AG, Healthcare Sector, Erlangen, Germany) and 12-channel phased-array head coil. Figure 5.14 shows the imaging devices (12-channel Siemens head matrix coil) and patient setup to acquire these data. Data with different contrasts, for example, T1-weighted (T1W) rapid three-dimensional gradient-echo (MPRAGE), T2-weighted (T2W) SPACE data were obtained. Examples of neonatal data used in this study are shown in Figure 5.15. As shown in Figure 5.14, because an adult coil was used to image the neonates, some neonatal motions between scans and repositioning of waking neonates between acquisitions, were experienced throughout the population. The landmarks were manually selected by an experienced clinical researcher of Toshiba Medical Visualization System - Europe (TMVSE). To ensure the coverage and distribution of the landmarks, they were selected from 20 proposed critical points, as listed in Table 5.1. Figure 5.16 illustrates some the landmarks selected on the neonatal data. The data were aligned using a rigid-body transform, calculated

within a $51 \times 51 \times 41$ mm ROI selected around the corpus callosum and thalamus.

Table 5.1: *Critical points proposed for landmark selection.*

Location of critical point(s)	Number
Superior aspect of eye globe	2
Centre eye globe	2
Attachment point of optic nerve to eye	2
Base of pituitary gland	1
Frontal horn of lateral ventricle	2
Pineal gland	1
Anterior aspect of the pons	1
Inferior point of vermis	1
Occipital pole	2
Temporal pole	2
Lateral aspect of postero.superior cerebellar lobe	2
Superior aspect of lateral ventricle	2

Furthermore, to test the importance of each step in the overall registration framework, several components were either omitted completely or exchanged with alternative methods. The changes were: (a) Gaussian pyramid down-sampling instead of the wavelet pyramid; (b) omitting the k -means step; (c) omitting the histogram specification step; (d) replacing PSO with the DIRECT optimizer; and (e) reversing the decision of selection of the clustered and non-clustered image. Finally, the results were also compared with our previous algorithm [239]. Registrations that have TREs bigger than 8mm are easily detected by visual inspection, and are thus considered as failures.

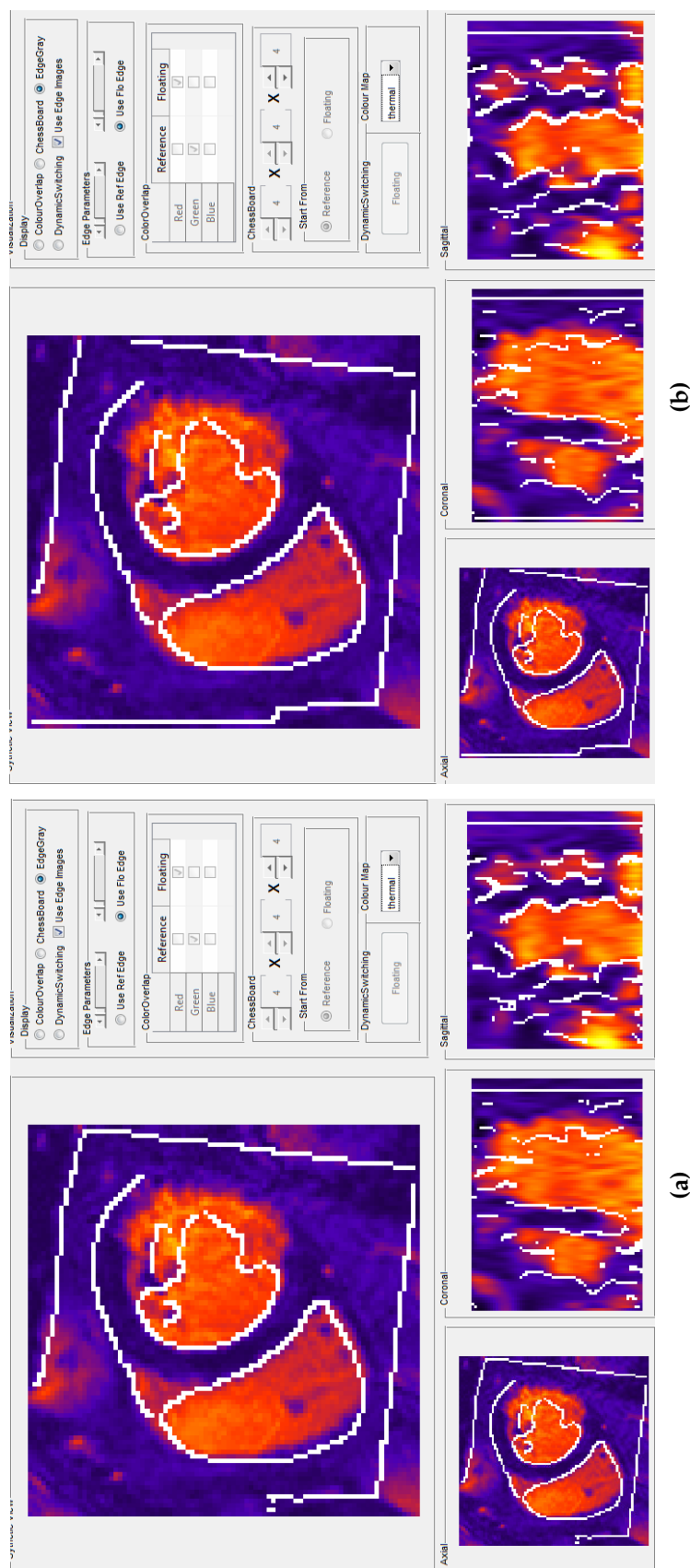


Figure 5.13: Example of the pre-contrast T2* weighted image aligned to the T1 weighted delayed enhancement data, visualized by overlapping the edge image of the T2* weighted data to the T1 weighted data using the proposed method, and after the registration result being manually corrected: (a) data registered by the proposed method; (b) the manually corrected registration result.



Figure 5.14: Imaging devices (12-channel Siemens head matrix coil) and patient location for acquiring the neonatal MR data used to evaluate the performance of the proposed registration framework.

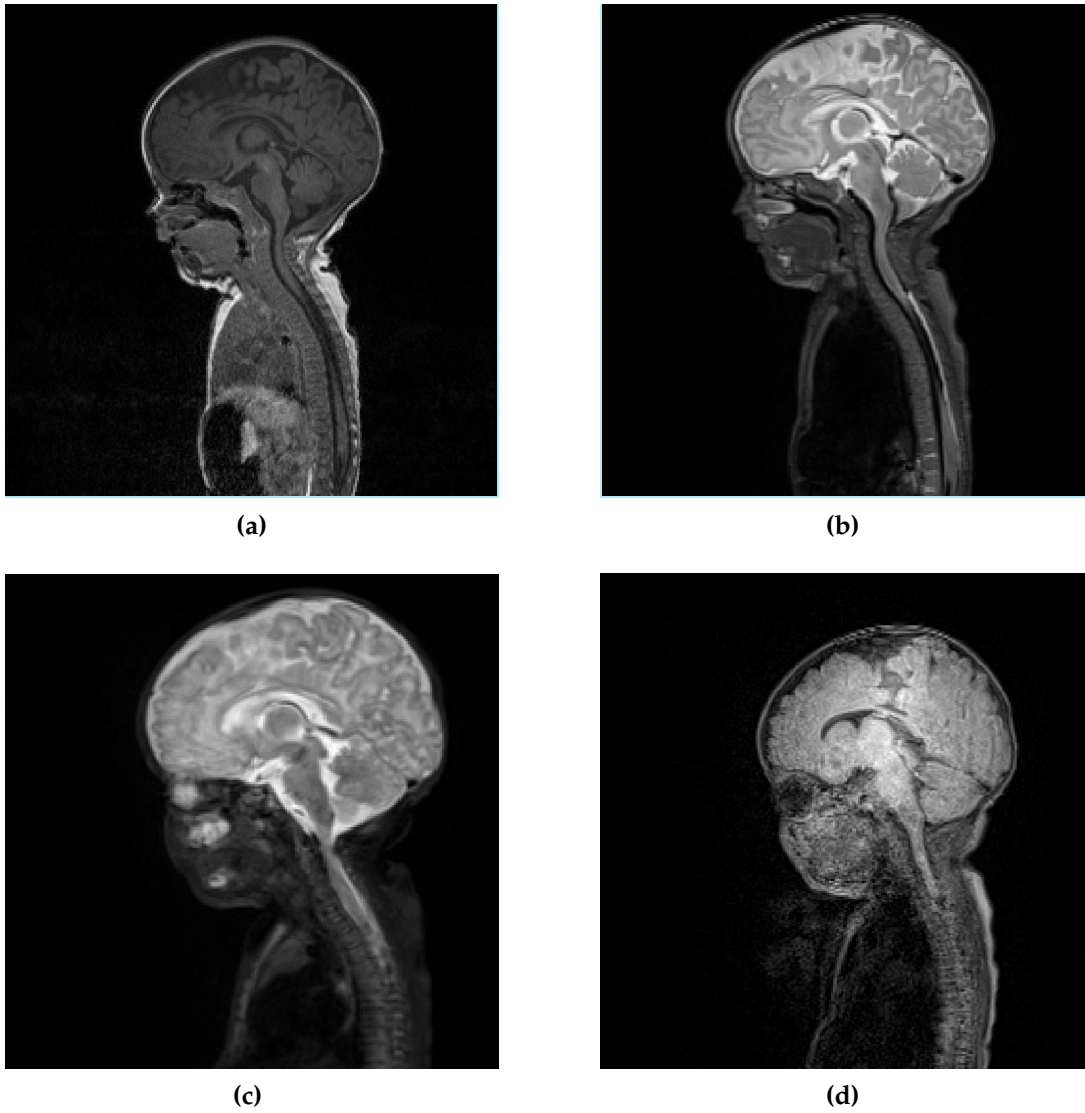
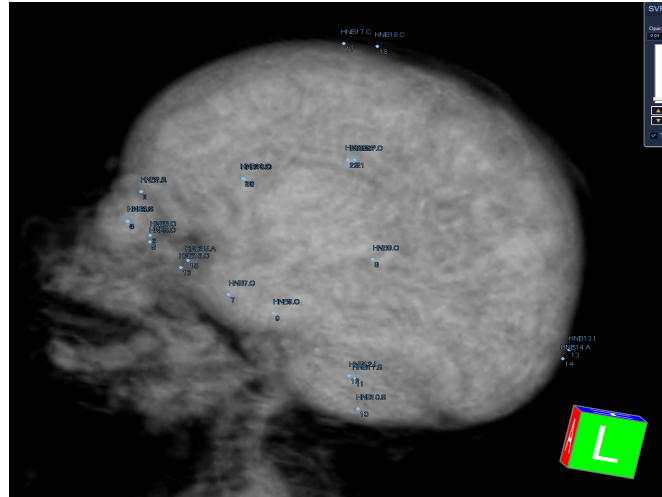
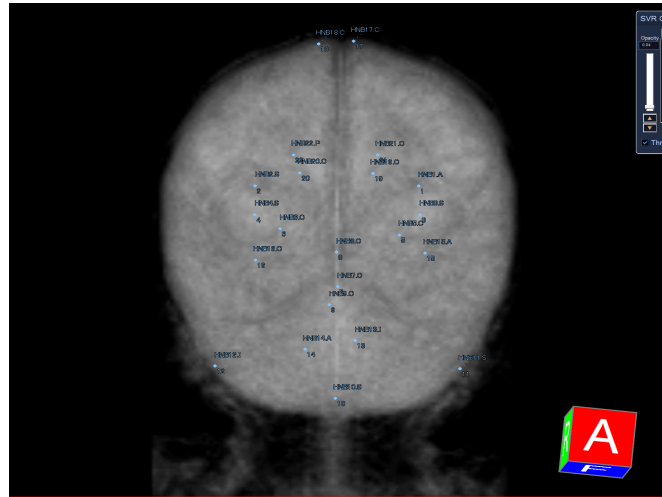


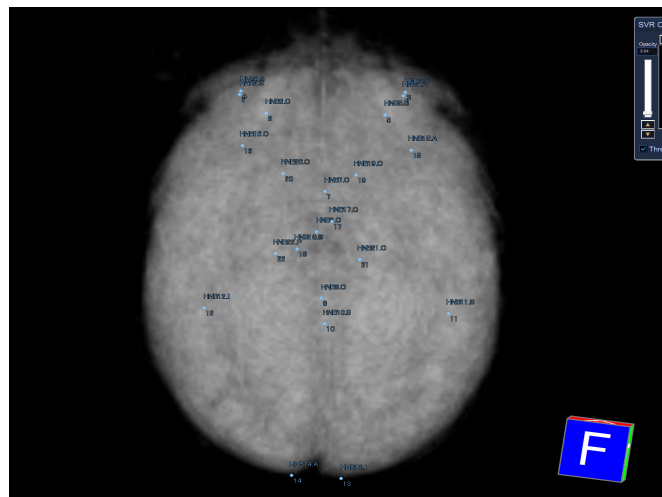
Figure 5.15: Examples of neonatal data used for validation of registration: (a) T1 weighted MPRAGE; (b) T2 weighted; (c) T2 weighted STIR; (d) T2 weighted Dark-fluid.



(a)



(b)



(c)

Figure 5.16: Illustration of landmarks picked on the 3D neonatal data: (a) sagittal view; (b) coronal view; (c) axial view.

5.5 Results

5.5.1 Cardiac Data

An example of the results of registering the pre-contrast T2*W data to the T1W delayed enhancement data shown in Figure 5.2 obtained by the method proposed in chapter 3, as well as the new method introduced in this chapter, is displayed in Figure 5.17 and Figure 5.18 using different visualization methods. The average rotational and translational errors across the 98 registrations are shown in Table 5.2. The mean of translational and rotational errors are 1.61 voxel (about $2.66mm$) and 0.68 degrees, respectively. 55% of the registrations achieved translational errors less than 1 voxel while rotational errors less than 0.1 degree, and 40% could not be improved further by manual adjustment.

5.5.2 Neonatal Data

An example of a neonatal registration result is shown in Figure 5.19. Table 5.3 and Figure 5.20 illustrate the results of 31 T2W-T1W MR registrations. When tested on rigid, but “moved” neonatal neuro datasets, the new algorithm gave smaller TREs than our previous methodology, and produced less failed registrations. Omitting or exchanging any of the important steps listed above lead to worse registration results with higher TREs or more failed alignments. All the compared methods failed when registering the T2W Dark-fluid data to the T1W MPRAGE data of one patient (No. 2956) as shown in Figure 5.21 and 5.22.

Table 5.2: *Average Translational and Rotational Errors of Cardiac Registration: voxels and degrees of manual correction. The standard deviation of the errors are shown within the brackets.*

	Translation	Rotation
T2*W to T2*W	1.76(2.107)	0.81(0.021)
T2*W to DE	1.55(1.737)	0.04(0.007)

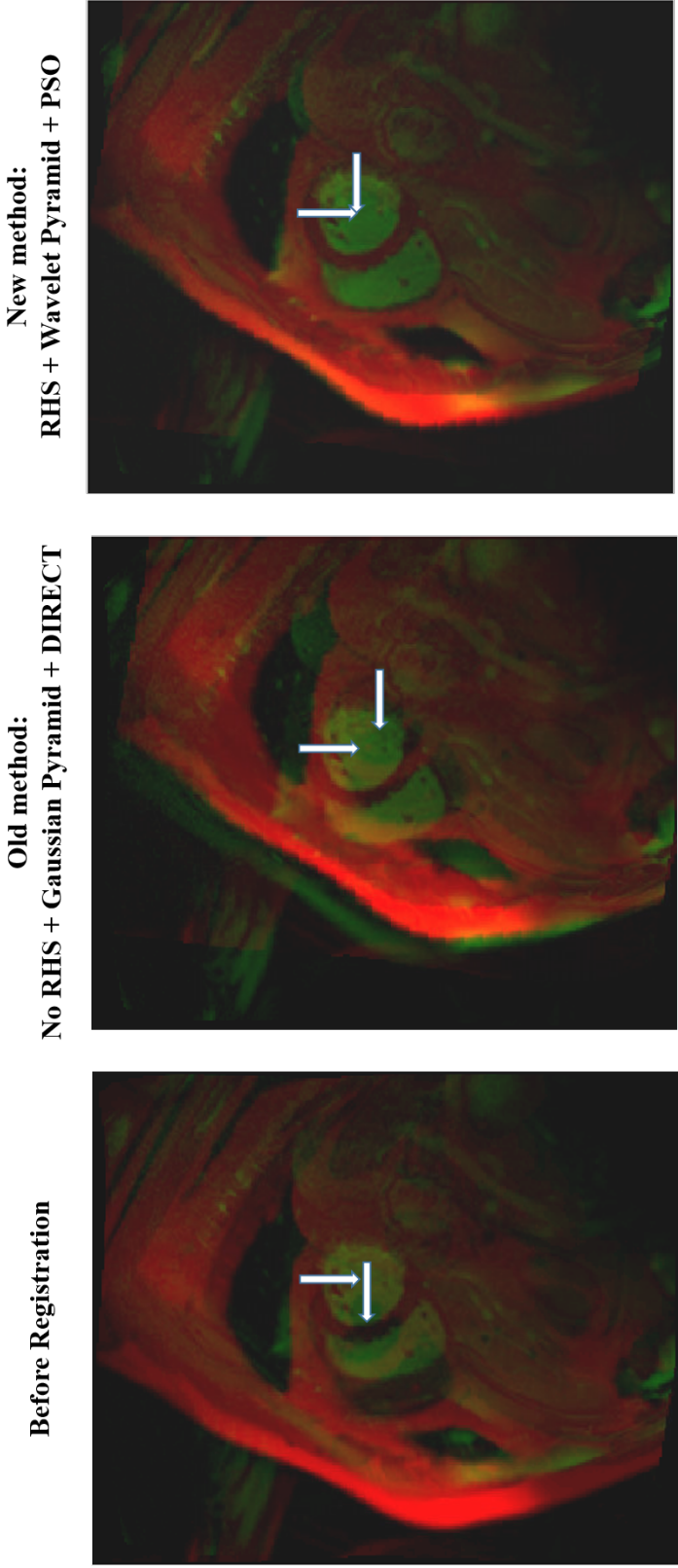


Figure 5.17: An example of the results of registering the pre-contrast T2* weighted data to the T1 weighted delayed enhancement data, visualized using overlapped red and green colour channels. White arrows pointed to the left ventricle.

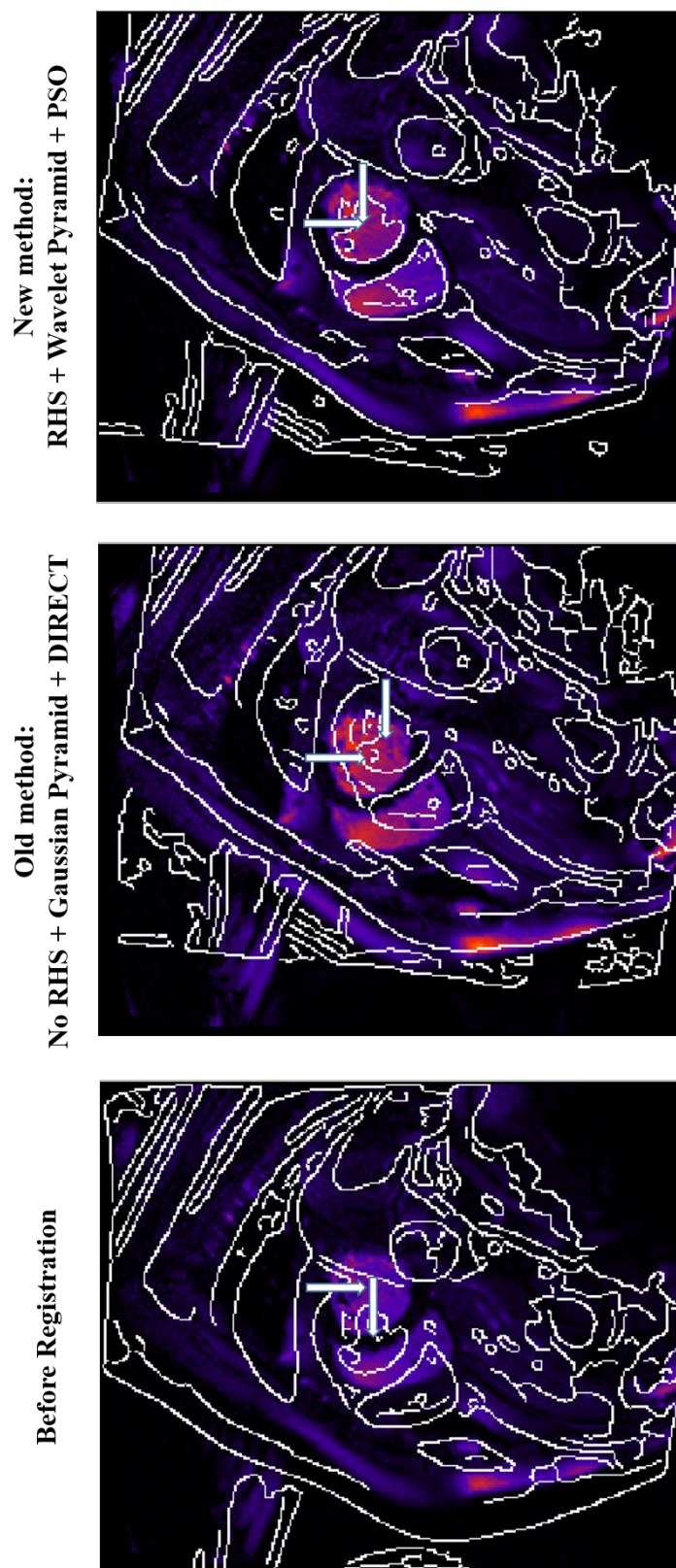


Figure 5.18: An example of the results of registering the pre-contrast T2* weighted data to the T1 weighted delayed enhancement data, visualized by edge image of the T2* weighted data to the T1 weighted data.

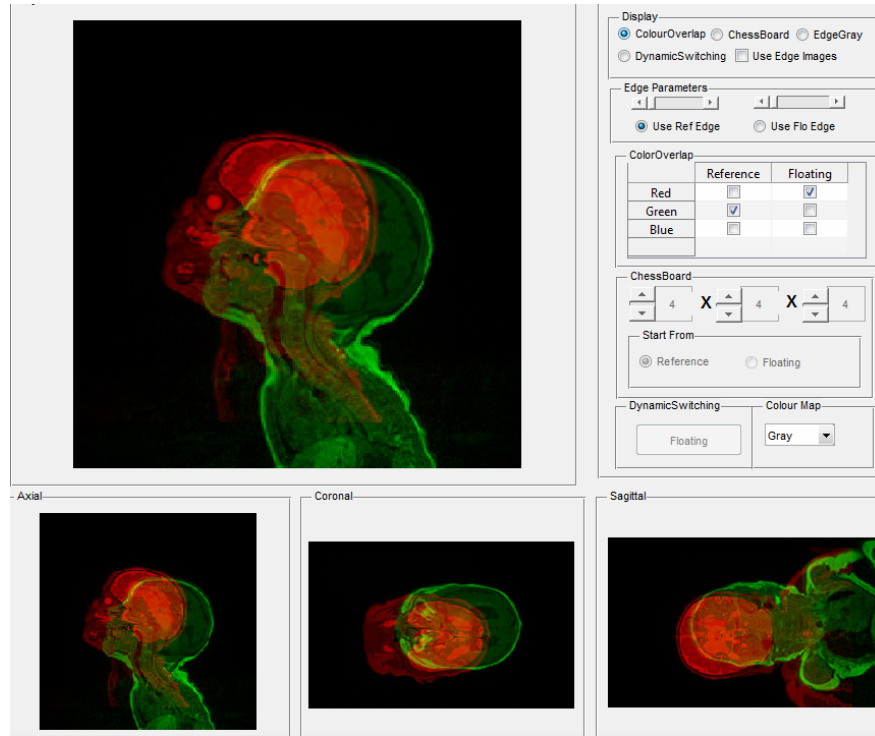
5.6 Discussion and Conclusion

A multi-parametric MR data registration framework with a new preprocessing step is proposed in this chapter. The new framework is more robust to data that exhibits significant intensity inhomogeneities and non-stationary artefacts than the previous registration method used in chapter 3. Performance of registration has been evaluated using multi-modal and multi-parametric cardiac and neonatal data obtained from clinical research trials. The design of this framework has been “tuned” to an optimal status whereby omitting or exchanging any of the important components leads to larger registration errors. The clustering and intensity correction steps, as well as optimization using PSO used in this framework, can be easily parallelized to allow the processing time to be significantly reduced. Furthermore, we noticed that the ROI tracking step is also robust to common noise and artefacts appearing in the experimental cardiac data, which will allow us to potentially develop efficient fully automatic cardiac MR registration algorithms in the future.

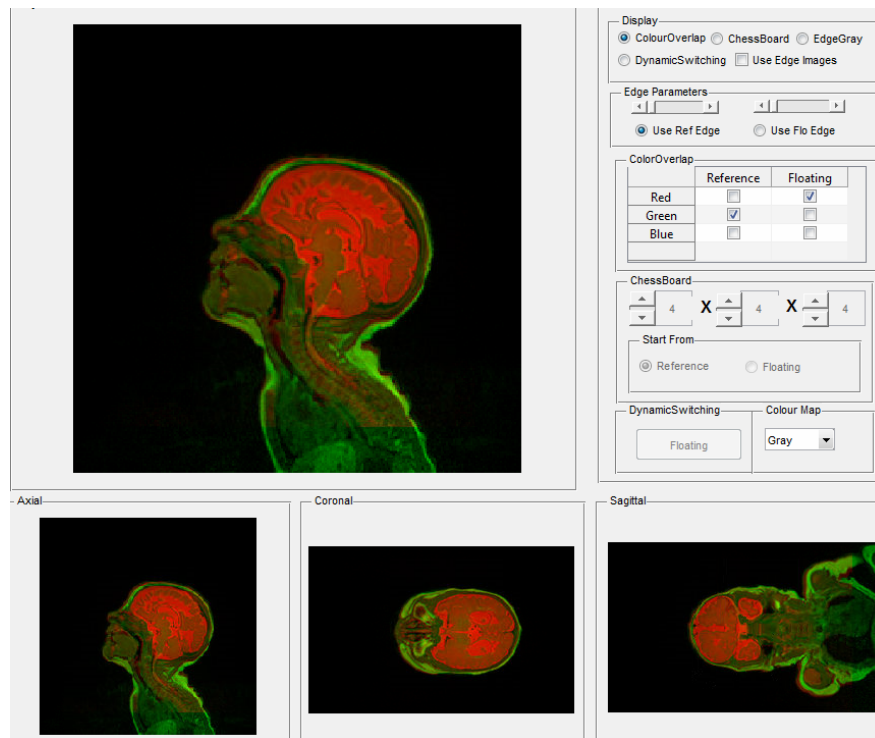
An important improvement of this new registration framework is using PSO to search for the optimal transformation. PSO has been shown to be more robust to local optima and image noise in this work, but premature convergence is still a problem of the original PSO method. As shown in the registration results of the neonatal data, this new registration framework still failed to register the T2W Dark-fluid data to the T1W MPRAGE image of one patient. The data which caused this failed registration is shown in Figure 5.21. Severe motion artefacts and noise can be observed from the T2W Dark-fluid image, which could be the cause of the failed registration, as shown in Figure 5.22. In the past few decades, various modified versions of PSO have been proposed. Thus further improvement of this registration framework could be an optimization strategy that is more robust to local optima in the searching space caused by imaging artefacts and noise. A literature review of existing PSO methods that have been applied to different image registration problems is introduced in the

5.6 Discussion and Conclusion

next chapter. Based on this reviewing study, a specifically registration-oriented novel PSO method will be introduced.



(a)



(b)

Figure 5.19: Example results of registering T2W-T2W neonatal data visualized by overlapped red and green colour channels: (a) before registration; (b) after registration.

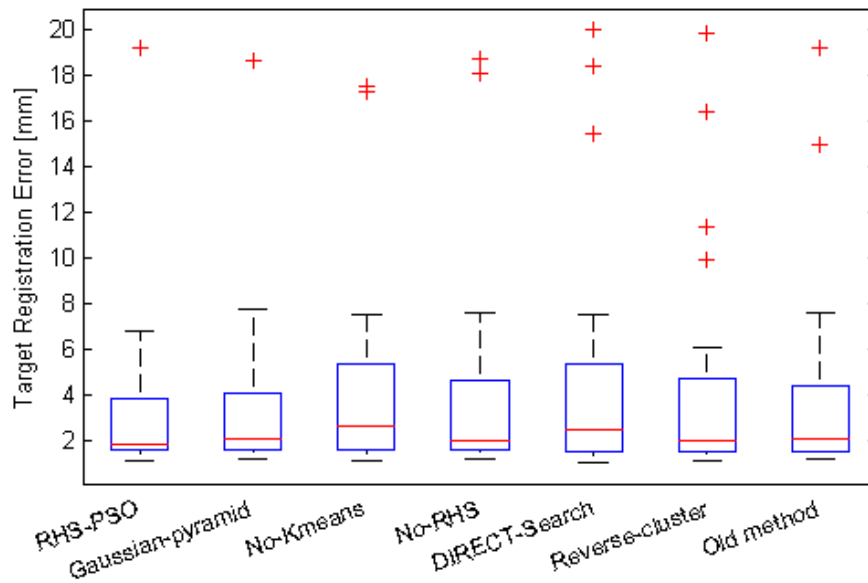


Figure 5.20: Boxplots of registration results obtained from neonatal data.

Table 5.3: Registration accuracy evaluated by median and standard deviation (STD) of target registration error (TRE) calculated with the neonatal data: The method proposed in this work is underlined. Gaussian-pyramid method replaces wavelet image pyramid with Gaussian pyramid. No-Kmeans method simply uses linear binning when calculating mutual information. No-RHS method does not perform rearranged histogram specification (RHS). I also tried to use DIRECT to replace the particle swarm optimization (PSO) searching. Finally, the previous framework was also evaluated. The PSO method is applied with parametric setup recommended by Eberhart and Kennedy [28]: 10 particles are used for each dimension; both the social and self acceleration coefficients are initialized as 2.0; the inertia weight is initialized as 1.1, and vary between 0.1 and 1.1; when the change of the optimal value similarity measure is less than 10^{-6} , the optimization converges; the maximum number of iterations is 300. For the DIRECT search, the same standard is used to detect convergence, and the maximum number of iterations is also 300.

Method	<u>RHS-PSO</u>	Gaussian-pyramid	No-kmeans	No-RHS	DIRECT Search	Reverse cluster	Old method
Median	1.88	2.11	2.61	1.97	2.45	1.99	2.06
STD	1.65	1.82	1.96	1.84	1.91	1.53	1.78
Failures	1	1	2	2	3	4	2

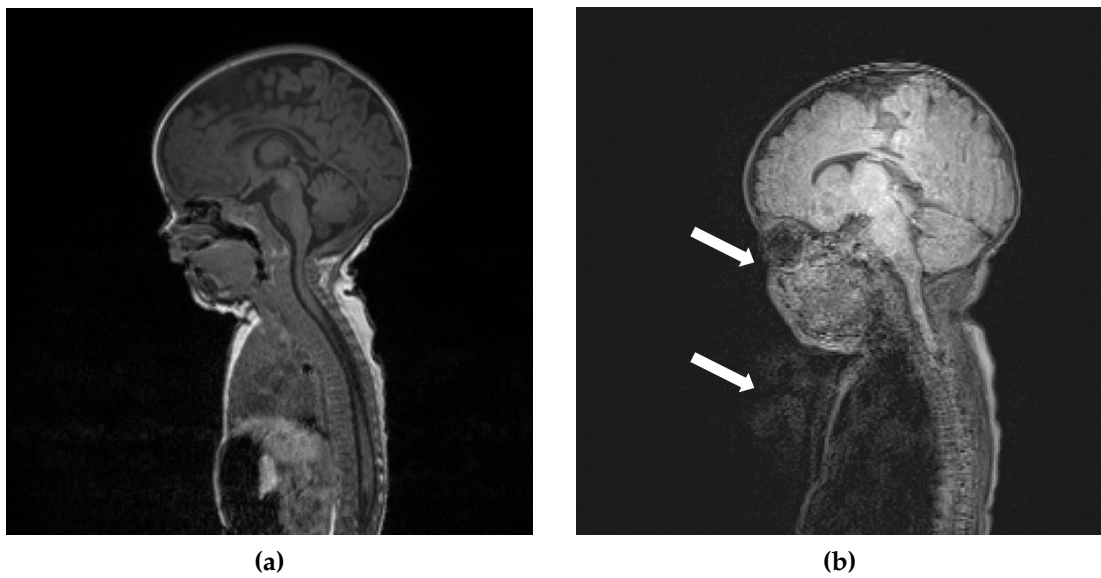
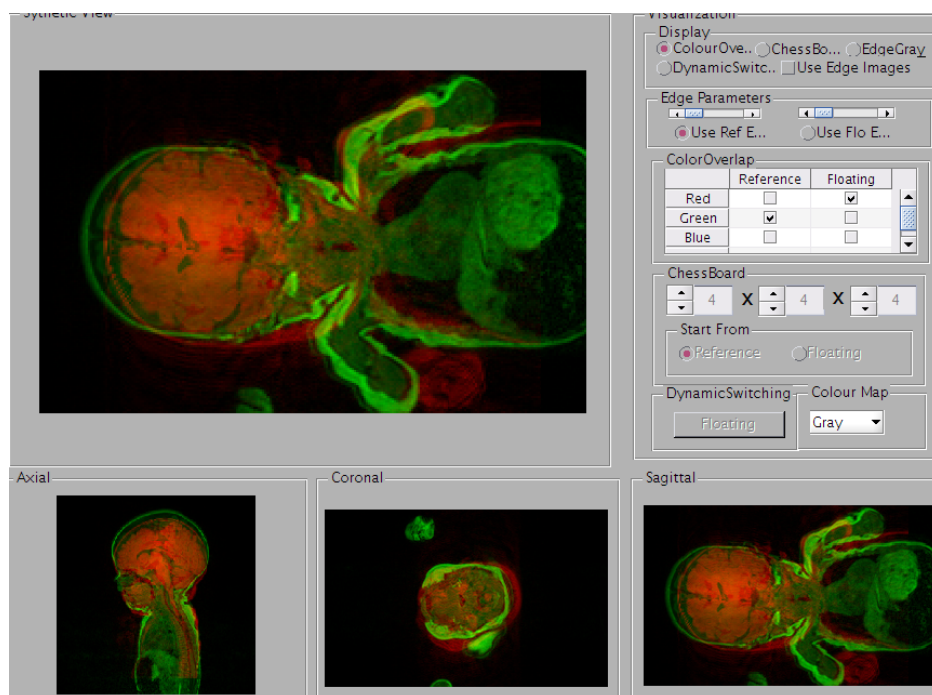
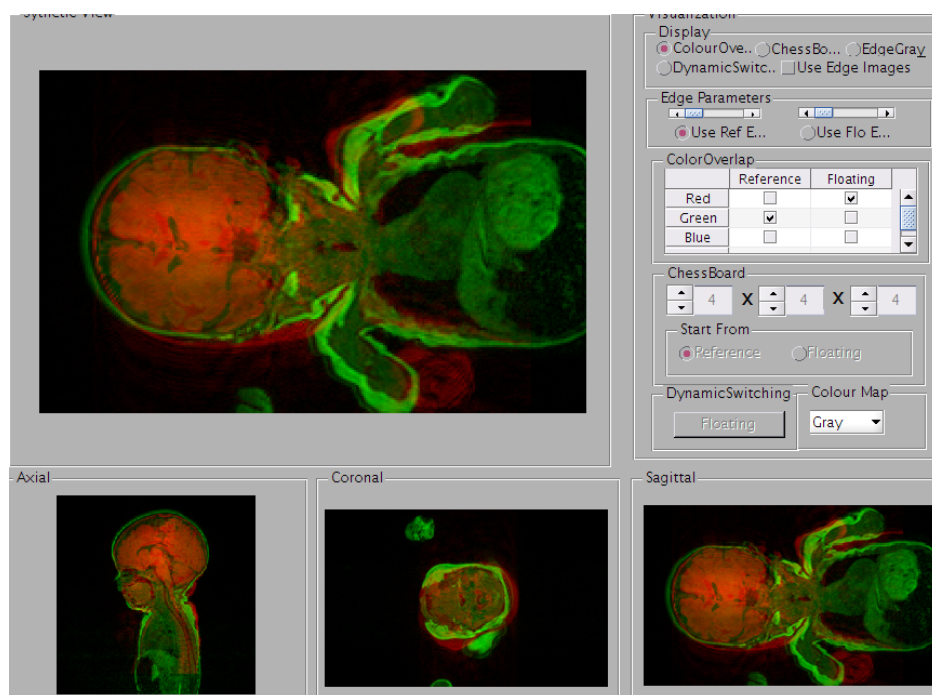


Figure 5.21: Data from the failed registration (patient No.2956): (a) a slice of T1 MRPAGE data; (b) a slice of T2 Dark-fluid data which suffers from severe motion artefact as shown by white arrows and noise.



(a)



(b)

Figure 5.22: The T2 weighted Dark-fluid image aligned with the T1 weighted MRPAGE data of patient No.2956, visualized by overlapped red and green colour channels, before and after registered using the proposed method: (a) before registration; (b) failed registration.

Particle Swarm Optimizers Applied to Medical Image Registration

ABSTRACT

Besides adequate image features and similarity measures, robust optimization of the algorithm used is another important factor that can affect final alignment results. In the registration framework proposed in the last chapter, I have used PSO to search for the global optimum in the problem space built up by MI or other similarity measures. However, premature convergence is still a major drawback of the original PSO method in presence of multiple local optima. Many modified PSO methods have been proposed and applied to image registration algorithms in the past few decades. In this chapter, a comprehensive literature review of various PSO models that have been applied to image registration problems is presented. This review was performed for possible improvements that can be applied to the optimization module of my registration framework. However, most of them are still classified as general purpose optimization processes, and none of the reviewed methods were specialized for registration applications. Thus in the next chapter, novel registration-oriented PSO methods will be introduced. A few widely used PSO models reviewed in this chapter will be selected for comparison purposes.

6.1 Introduction

Optimization is a significant component in most medical image registration processes, being used to search for the optimum in similarity measure by exploring the solution space [27]. For volumetric registration techniques, although optimization has not been studied as intensively as other important elements of registration, such as feature selection, transformation, and similarity measure, the image alignment process has mostly been treated as a cost function minimization problem, often being solved iteratively [241]. The optimal solution is obtained when the global optimum similarity measure is obtained. The local optimization algorithms search for the optimal solution within a neighbourhood around the first evaluated position in the explored parametric space. Unfortunately, in realistic registration applications, the similarity function is not smooth, containing many local optima [151]. This makes the quality of the registration results very sensitive to the initialization of the searching process. For example, in the last chapter, all of the compared methods failed to register the data of one patient when aligning T2-weighted (T2W) dark fluid data to the T1-weighted (T1W) MRPAGE data. Figure 6.1(a) and 6.1(b) show an example slice from each type of data which caused the failed registration as discussed in chapter 5, and Figure 6.1(c) displays the plot of the similarity measure values while transforming the T2 dark fluid data along one dimension of the problem space. Multiple local optima can be clearly observed. When the local optimization methods are initialized in a place far from the true global optimum, they can easily converge to the local optima.

Robustness of local optimization methods can be improved by using multi-resolution image pyramids or using global optimization schemes. Optimization methods boosted by multi-resolution frameworks have been reviewed and compared by many previous studies [27, 30, 46, 55, 151, 242]. Some groups warn that because the real global optimum can be absent from the searching space when registering down-sampled data, the local optimization methods may easily become trapped

in local optima [30, 243, 244]. Thus global optimization is specifically required. Among existing global optimization methods, evolutionary computation, which uses computational models of evolutionary processes, plays an important role [25]. Since the first evolutionary programming methods proposed in the 1960s [245][246], many advanced global searching methods, such as genetic algorithms (GA) [247], simulated annealing (SA) [248], ant colony optimization (ACO) [249], etc., have been applied to various image registration applications [30, 250, 251, 252, 253]. However, besides some common limits of these heuristic searching methods [30], they often lack fine tuning abilities and can be very slow to calculate, especially when the evaluation of similarity measures are computationally costly [244, 254]. Inspired by social and cooperative behaviour, such as bird flocking and fish schooling, Kennedy and Eberhart [28] proposed a simple and robust heuristic search strategy called particle swarm optimization (PSO) in the mid 1990s[246]. Because of the promising results it returned, both the original searching schedule and various modified versions of PSO have been applied to different image registration applications [244, 254, 255, 256, 257, 258, 259, 260, 261, 262, 263]. Meanwhile, many efforts have been made to improve the convergence speed and robustness of PSO when dealing with huge problem spaces which exhibit local optima. Intensive comparison works and reviews of different variants of PSO can be found in [246][264] and [265].

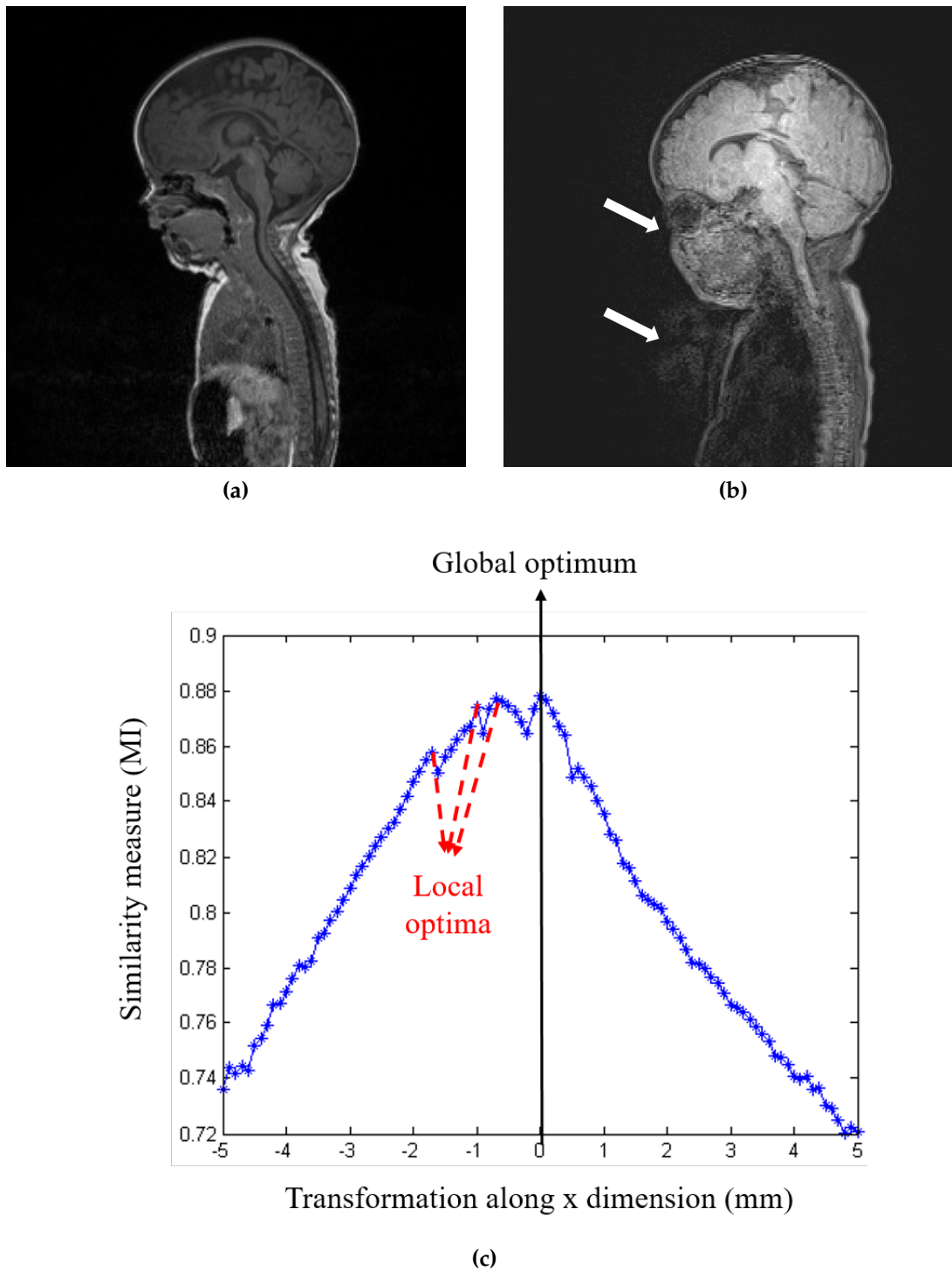


Figure 6.1: Example of data from a failed registration: (a) a slice of T1 MRPAGE data; (b) a slice of T2 dark fluid data which suffers from severe motion artefact and shown by white arrows and noise; (c) a plot of mutual information values when transforming the T2W data along one dimension of the searching space.

The original form of PSO method was used in the registration framework introduced in the last chapter. To further improve this framework, to process the data shown above which failed the registration described in the last chapter, more advanced versions of PSO need to be adopted. It is also necessary to modify these methods based on some unique characteristics of registration. Although the existing PSO methods are still general-purpose optimization strategies, many of them have inspiring mechanisms to encode prior knowledge into the PSO formulae. This chapter presents a comprehensive literature review of existing PSO methods that have been applied to image registration problems, and explores a possible way to add registration-oriented prior knowledge to the optimization algorithms. The original form of PSO method and its common extended formulae are introduced in section 6.2. Section 6.3 describes the methods that use new particle speed and position updating mechanisms. Section 6.4 reviews the applications of these PSO models to real registration problems. In section 6.5, the PSO methods based on Bayesian theory, which allow us to encode some prior knowledge in the form of probability distribution, are summarized. Conclusions and discussions can be found in section 6.6.

6.2 Original PSO Algorithm and Common Improvements

6.2.1 The Original Formulae

As a heuristic optimization method, PSO simulates the social and cooperative behaviour of a swarm of potential solutions, called particles [246]. Each potential solution corresponds to one position in the solution space. Each particle explores the solution space in an individual random speed that is partially affected by combined knowledge about the up-to-date global optima and local optima within its local neighbourhood [264]. In the example of searching for global optima in a D -dimension solution space with K particles, at the t th iteration of the PSO, a solution represented by the position of the i th particle is a D -element vector, $\mathbf{x}_i(t) = \{x_{i1}(t), x_{i2}(t), \dots, x_{iD}(t)\}$, $i \in \{1, 2, \dots, K\}$, the speeds of the particles, $\mathbf{v}_i(t+1)$, are given by [28, 246, 264]:

$$\mathbf{v}_i(t+1) = \mathbf{v}_i(t) + c_p r_p (\mathbf{x}_i^p - \mathbf{x}_i(t)) + c_g r_g (\mathbf{x}^g - \mathbf{x}_i(t)), \quad (6.1)$$

where \mathbf{x}_i^p and \mathbf{x}^g are the locally best solution found by the i th particle and the best up-to-date global optimum, respectively. c_p and c_g are the acceleration constants that weight the attraction of local and global optima to each particle, and r_p and r_g are random generated numbers drawn from the uniform distribution over the range of $(0, 1)$ [246]. The particle positions in the next iteration are updated using [28, 246, 264]:

$$\mathbf{x}_i(t+1) = \mathbf{x}_i(t) + \mathbf{v}_i(t+1). \quad (6.2)$$

Equation 6.1 consists of three components: the previous velocity $\mathbf{v}_i(t)$, the cognition component $c_p r_p (\mathbf{x}_i^p - \mathbf{x}_i(t))$, and the social component $c_g r_g (\mathbf{x}^g - \mathbf{x}_i(t))$. The effect

of these three parts is a compound velocity that moves the particles toward the local and global optima, while preventing any drastic changes from the particles' previous directions [246]. With this mechanism, the convergence of the algorithm is stepwise improved, until all the particles move into a small constrained area, or the global best position remains unchanged for certain number of iterations. Other than the coefficients which appear in the PSO formulae, the most common modifiable parameters include the swarm size (i.e. the number of particles), the searching range, and the maximum number of iterations.

6.2.2 Common Extensions

Although the PSO is proposed as a global optimization algorithm, it still may suffer from premature convergence, and its performance strongly depends on the initial orientation, for example because of high selection pressure, or high gene flow[266]. Thus different 'optimization' versions were developed to avoid local optima while dealing with complicated optimization problems. Based on the original PSO formulae, Shi and Eberhart [267] introduced a widely used inertia weight parameter, ω , to control the influence of the previous velocity, $\mathbf{v}_i(t)$, so as to balance the local and global searching ability of each particle [246]. In this scheme the velocity is updated using

$$\mathbf{v}_i(t+1) = \omega \mathbf{v}_i(t) + c_p r_p (\mathbf{x}_i^p - \mathbf{x}_i(t)) + c_g r_g (\mathbf{x}^g - \mathbf{x}_i(t)). \quad (6.3)$$

This parameter can be generalized from a positive constant to a positive function of time, $\omega(t)$, called dynamic inertia weight, to further improve the robustness and speed of convergence. A common way to update $\omega(t)$ is given by [244, 268]:

$$\omega(t+1) = \omega(t) + d\omega, \quad (6.4)$$

6.2 Original PSO Algorithm and Common Improvements

where $d\omega$ is a fixed step length that reduce the inertia weight in each iteration. This step length is defined by:

$$d\omega = \frac{\omega_{min} - \omega_{max}}{T}, \quad (6.5)$$

where ω_{min} and ω_{max} are the minimum and maximum of the dynamic inertia weight, and T is the maximum number of iterations.

Another common modification of the PSO, introduced by Clerc and Kennedy [266, 269], is to multiply equation 6.1 (or equation 6.3) by a constriction parameter, χ , such that the velocity updating equation becomes [246, 264]:

$$\mathbf{v}_i(t+1) = \chi(\mathbf{v}_i(t) + c_p r_p (\mathbf{x}_i^p - \mathbf{x}_i(t)) + c_g r_g (\mathbf{x}^g - \mathbf{x}_i(t))), \quad (6.6)$$

or

$$\mathbf{v}_i(t+1) = \chi(\omega \mathbf{v}_i(t) + c_p r_p (\mathbf{x}_i^p - \mathbf{x}_i(t)) + c_g r_g (\mathbf{x}^g - \mathbf{x}_i(t))), \quad (6.7)$$

where

$$\chi = \frac{2}{|2 - (c_p + c_g) - \sqrt{(c_p + c_g)^2 - 4(c_p + c_g)}|}, \quad (6.8)$$

when $c_p + c_g > 4$.

It has been verified that when the maximum particle velocity is constrained, using the parameter χ can significantly improve the searching performance. Empirically, optimal parametric settings of c_p , c_g , χ , ω , alternative distributions used to generate r_p and r_g , as well as the number of initialized particles, were also investigated by different studies [246, 270, 271].

Riget et al. proposed an attractive and repulsive PSO (ARPSO) [272], to overcome premature convergence by controlling the diversity of particles. The diversity, $d(t)$, of a group of K particles at the t th iteration is defined by [272]:

$$d(t) = \frac{1}{KL_{max}} \sum_{i=1}^K \sqrt{\sum_{j=1}^D (x_{ij}(t) - \bar{x}_j(t))^2}, \quad (6.9)$$

where $x_{ij}(t)$ is the solution value of the i th particle on the j th dimension, and $\bar{x}_j(t)$ the mean value for the j th dimension. L_{max} is the largest range of searching space among all dimensions. Then the modified velocity update equation becomes:

$$\mathbf{v}_i(t+1) = \mathbf{v}_i(t) + S_{dir}(c_p r_p(\mathbf{x}_i^p - \mathbf{x}_i(t)) + c_g r_g(\mathbf{x}^g - \mathbf{x}_i(t))), \quad (6.10)$$

where S_{dir} is a direction indicator, which is decided by two thresholds, T_{low} and T_{up} . The algorithm starts in attractive mode, with $S_{dir} = 1$, and the particles are attracted to each other. If $d(t)$ is lower than T_{low} , which means the particles are too similar to each other and possibly trapped in local optima, S_{dir} is assigned the value -1 [272]. The algorithm then begins to work in repulsive mode and tries to expand the group of particles, until $d(t)$ becomes higher than T_{up} .

6.3 Modified Speed and Position Update Mechanisms

6.3.1 Neighbourhood and Population Information

Besides directly modifying the PSO formula, neighbourhood topology structures are also widely studied [29]. Kennedy and Mendes proposed a PSO with a local ring structure neighbourhood, and the von Neumann topological structure PSO to deal with the problem of multiple local optima [273, 274]. PSO methods with changing neighbourhood structures have also been proposed to dynamically adjust inefficient fixed neighbourhood topology [275, 276, 277]. Rather than only using a single local optimum, a fully informed particle swarm was developed to formulate the cognition components of the velocity update equation using the whole neighbourhood [278]. Similarly, Liang et al. proposed a comprehensive learning PSO (CLPSO) method, which uses historical local optima of other particles to update the speed of each particle [279].

These methods, focusing on neighbourhood structure, can effectively avoid local optima, although often with extra computational cost [29]. Zhan et al. proposed an adaptive PSO (APSO) method to achieve both better optimization results and better convergence speed [29]. APSO uses evolutionary state estimation (ESE) to check the particle population distribution, and adaptively adjust the inertia and acceleration parameters. To capture the population distribution information, the average of the Euclidean distances from each particle to all other particles is calculated first by [29]:

$$d_i = \frac{1}{K-1} \sum_{j=1, j \neq i}^K \sqrt{\sum_{m=1}^D (x_{im} - x_{jm})^2}, \quad (6.11)$$

where d_i is the average distance calculated for the i th particle. Among the average distances of all particles, there is a maximum, d_{max} , a minimum, d_{min} , and one for the

Table 6.1: *The Rule of Changing Acceleration Coefficients [29]*

State	c_p	c_g
Exploration: S_1	Increase	Decrease
Exploitation: S_2	Slightly Increase	Slightly Decrease
Converge: S_3	Slightly Increase	Slightly Increase
Jumping-Out: S_4	Decrease	Increase

global best particle, d_g . Using these distances as evolutionary factors, f , is defined by [29]:

$$f = \frac{d_g - d_{min}}{d_{max} - d_{min}} \in [0, 1], \quad (6.12)$$

then the inertia weight is calculated as a function of f [29]:

$$\omega(f) = \frac{1}{1 + 1.5e^{-2.6f}} \in [0.4, 0.9], \forall f \in [0, 1]. \quad (6.13)$$

At the beginning of the searching process, $\omega(f)$ is initialized as 0.9.

The evolutionary factor, f , not only controls the inertia weight, but also decides the evolutionary state. In Zhan et al.'s work [29], this was achieved using a fuzzy logic scheme. First, a quarter-state fuzzy set is defined on f to represent four states in the evolution process [29]: Exploration, S_1 , Exploitation, S_2 , Convergence, S_3 , and Jumping-out, S_4 . In the searching process of the PSO, the evolutionary state changes from S_1 to S_4 , then back to S_1 . This sequence repeats until ended at S_3 [29]. Secondly, a simple if-then fuzzy operator is defined on the four-state fuzzy set, to dynamically control the acceleration coefficients c_p and c_g using different strategies at different stages of the PSO. A brief description of this fuzzy logic operator is shown in Table 6.1 [29]. The algorithm starts with $c_p = c_g = 2.0$. As c_p and c_g have profound effects on optimization results and now are changing with time, their increments are limited by a threshold to prevent over-interruptive behaviour [29]. Once $c_p + c_g > 4.0$, they will be re-normalized so that $c_p + c_g \leq 4.0$.

The APSO also uses an elitist learning strategy (ELS), to adaptively avoid local

6.3 Modified Speed and Position Update Mechanisms

optima during the converging process. Let x_{gi} be the i th dimension of the best historical global optimum within the searching range $[X_{iMin}, X_{iMax}]$. The ELS is defined as a zero-mean Gaussian perturbation course [29]:

$$x_{gi} = x_{gi} + (X_{iMax}, X_{iMin}) \cdot \mathcal{N}(0, \sigma^2(t)). \quad (6.14)$$

The standard deviation of the random learning rate $\mathcal{N}(0, \sigma^2(t))$ at the t th iteration is given by [29]:

$$\sigma(t) = \sigma_{max} - (\sigma_{max} - \sigma_{min}) \frac{t}{t_{max}}, \quad (6.15)$$

where σ_{max} , σ_{min} , and t_{max} are predefined thresholds set for $\sigma(t)$ and t .

The reported evaluation for both uni-modal and multi-modal benchmark functions demonstrate improved accuracy and robustness [29]. A detailed mathematical derivation, and suggested parameter settings, for the APSO may be found in [29].

6.3.2 Quantum Behaved PSO

Although the original PSO modelled bird flocking behaviour, its linear form is insufficient to depict a far more complex social system [280]. Inspired by quantum system analysis in [266], Sun et al. developed a new algorithm, that uses mean best position and a delta potential 'well' model, called quantum behaved particle swarm optimization (QPSO) [281]. According to wave-particle duality in quantum mechanics, the state of each particle can be depicted by its wavefunction, $\Psi(x, t)$. Based on the uncertainty principle, rather than deciding the speed and position simultaneously, only the probability of a particle appearing in a position can be learned. This possibility can be calculated from the probability density function (PDF), $|\Psi(x, t)|^2$, that depends on the potential field the particle lies in [280].

Sun et al. employed the Delta potential well that is described by a potential centre, \mathbf{p} and a parameter \mathbf{L} which specifies the search scope [280]. In [280], \mathbf{L} of each particle

is given by [280]:

$$\mathbf{L}_i(t+1) = 2 \cdot \alpha \cdot |\mathbf{p}_m(t) - \mathbf{x}_i(t)|, \quad (6.16)$$

where α is the only tunable parameter in QPSO, called “Creativity Coefficient” [280], and \mathbf{p}_m is the “Mean Best” of the particle population which is the average of “personal bests” of all particles, calculated by [280]:

$$\mathbf{p}_m(t+1) = \frac{1}{K} \sum_{i=1}^K \mathbf{x}_i^p(t). \quad (6.17)$$

Then, using the Monte Carlo method, the position of a particle can be predicted by the following equation [280]:

$$\mathbf{x}_i(t+1) = \mathbf{p}_i(t) \pm 0.5\mathbf{L}_i(t+1)\ln(1/\mathbf{u}), \quad (6.18)$$

where each dimension \mathbf{u} is a random number drawn from a uniform distribution between 0 and 1. \mathbf{p}_i is the local attractor extracted based on the analysis in [266]. It is calculated using the acceleration constants by:

$$\mathbf{p}_i(t) = \frac{c_p \mathbf{x}_i^p(t) + c_g \mathbf{x}^g(t)}{c_p + c_g}. \quad (6.19)$$

The specific form of the dual-term equation 6.18 is decided by another independent random sampled number drawn from a uniform probability distribution. If a number less than 0.5 is obtained, the new particle is generated by the sum of the two terms, otherwise from the difference [280].

The two main innovative ideas introduced by QPSO are the Delta potential well and the use of the mean best position [281]. The Delta potential well widens the search space using an exponential distribution of positions. The early version of QPSO before introducing the concept of the mean best value, which is called Quantum Delta-Potential-Well-based PSO (QDPSO), uses \mathbf{p}_i , rather than \mathbf{p}_m , in equation 6.16 [282]. Further study shows that the use of the mean best value enhances cooperation of the

particles [280]. Fang et al. [281] conducted a comparison of QPSO with a few other probabilistic methods, and pointed out that QPSO displays better ability to escape local optima. However, dealing with complex multimodel problems, it still suffers from premature and slow convergence. Thus different strategies have been developed for improving the original QPSO method.

Sun et al. analysed the relation between parameter selections and the convergence of the QPSO, and proposed two parameter controlling methods based on a stochastic simulation experiment [283, 284]. The diversity-guided mechanism has subsequently been introduced to QPSO for adaptive parameter selection [282], and has been demonstrated to play an increasingly important role using the ARPSO diversity measurement, as shown in equation 6.9 [285]. Besides monitoring diversity, some research shows that the global searching ability can be improved by using multi-swarm cooperative models [286], or some probability distribution models [287]. QPSO has been intensively studied and used in wide range of applications. A comprehensive review and comparison of this work can be found in [281].

6.3.3 Hybridizations

Another popular direction to improve the PSO methods, is hybridizing other optimization algorithms, usually population based ones [246]. For example, the GA-PSO and PSO-GA methods proposed in [288], or the hybrid simplex-PSO method [289]. One typical hybridization is to add the GA operators, mutation and crossover [268][244], to the PSO framework. In each iteration, a proportion of the particles are selected in pairs with possibility, p_c . Each pair of selected particles, \mathbf{x}_i and \mathbf{x}_j , $i \neq j$, are updated by crossover with a possibility p drawn from a uniform distribution over $(0,1)$ [244, 290]:

$$\begin{aligned}\mathbf{x}_i(t+1) &= p\mathbf{x}_i(t) + (1-p)\mathbf{x}_j(t), \\ \mathbf{x}_j(t+1) &= p\mathbf{x}_j(t) + (1-p)\mathbf{x}_i(t).\end{aligned}\tag{6.20}$$

The speed of the particles then can be updated by [244, 290]:

$$\begin{aligned} \mathbf{v}_i(t+1) &= \mathbf{v}_i(t) \frac{\mathbf{v}_i(t) + \mathbf{v}_j(t)}{\|\mathbf{v}_i(t) + \mathbf{v}_j(t)\|} \\ \mathbf{v}_j(t+1) &= \mathbf{v}_j(t) \frac{\mathbf{v}_i(t) + \mathbf{v}_j(t)}{\|\mathbf{v}_i(t) + \mathbf{v}_j(t)\|} \end{aligned} \quad (6.21)$$

This hybrid method can be further improved by dividing the particles into subpopulations, using any suitable clustering method, and perform crossover operations between the subpopulations [244, 290]. A more in depth survey of hybrid PSO methods is out of the scope of this chapter, as we shall concentrate on methods applicable to registration. A comprehensive comparison study about hybrid PSO methods can be found in [246].

Similar to the hybridization of the original PSO method, or PSO methods with linear forms of velocity update equations, hybrid QPSO methods were also proposed [281], for example, hybridization of QPSO with SA [291], immune system [292], differential evolution [293], or GA mutation operations [294]. A widely used hybridization of QPSO is combining it with chaotic search [261, 281, 295, 296]. Chaos is a bounded unstable situation sensitively dependent on initial conditions [261], a commonly observed phenomenon in natural nonlinear systems. Combined with PSO, it can effectively increase diversity of particles in the later searching stage [295]. The chaotic behaviour is modelled using a simple and well-known logistic equation. For a time variant function $f(t)$, its evolution is formulated by [297]:

$$f(t+1) = \mu f(t)(1 - f(t)) \quad (6.22)$$

when $\mu = 4$ and $f(1) \neq 0.25, 0.5, 0.75$, $f(t)$ will finally, with best periodicity, visit every neighborhood in a subinterval over $[0, 1]$. As small differences in the initial values cause largely different long-term behaviour, chaotic values are used to initialize particles and the creativity coefficient, α , in QPSO. Ceolho introduced [294] a time-variant mutation function $p_m(t)$ to chaotic search hybridized QPSO to allow mutation

6.3 Modified Speed and Position Update Mechanisms

operation when a random sampled number is larger than $p_m(t)$. The reported results show that these modifications can further improve convergence and accuracy of QPSO performances on common benchmark functions [261, 294, 295, 296].

6.4 Applications to Registration

The convergence and accuracy of various PSO methods are usually evaluated using a series of benchmark functions in most publications discussed above. However, verification of their suitability for application to image registration problems relies on post-registration alignment errors. Although the PSO has been widely used in various image analysis applications [265], there are few publications on registration using it, and even fewer involving intra or inter-modality medical images [244, 254, 255, 256, 258, 259, 261, 262, 263, 296, 298, 299, 300, 301, 302, 303, 304]. There are a few methods which align images using novel pre-processing, feature extraction, or multi-resolution strategies with slightly modified PSO methods and specially chosen parameters [254, 258, 259, 301, 303]. A representative modification [258] is to generate r_p and r_g using different probability distributions based, on the directions of cognition and social components in the PSO speed update equation.

Instead of directly applying, or slightly modifying, the original PSO methods to registration applications, those sophisticated versions of the PSO have also been used. For example, to register multi-modality brain data, Xuan et al. [305] directly applied the ARPSO and Wang et al. [306] uses the APSO. Furthermore, some modifications, or even innovative PSO methods were also especially derived for different registration tasks. Li and Sato [307] added a third term, $c_3 r_3 (\mathbf{x}_i^g \mathbf{x}_i^p)$, to the original velocity update equation. Wei et al. [263] combined the PSO with SA in optimization procedure. Senthilnath et al. [308] introduced a new definition for the velocity vector in the multi-objective discrete PSO (DPSO) method for feature based alignment of multi-sensor images.

Wachowiak and Smolíková first introduced a PSO to medical image registration in the early 2000s [244]. They compared eight different PSO methods with Powell's method, and seven evolutionary strategies [244]. Note that the "original" form of PSO in [244] has an inertia weight function, $\omega(t)$, updated by equation 6.4 and 6.5. It

6.4 Applications to Registration

was also pointed out that for image registration applications, the initial orientation of particles contain important prior knowledge as the initial transformation is often manually picked [244]. In this case, the speed of particles previously controlled by equation 6.3 can then be updated by [244]:

$$\begin{aligned} \mathbf{v}_i(t+1) = & \omega(t)\mathbf{v}_i(t) + c_p r_p (\mathbf{x}_i^p - \mathbf{x}_i(t)) + c_g r_g (\mathbf{x}^g - \mathbf{x}_i(t)) \\ & + c_{init} r_{init} (\mathbf{x}_{init} - \mathbf{x}_i(t)), \end{aligned} \quad (6.23)$$

where \mathbf{x}_{init} is the initialized solution of PSO, the force that moves the particles toward the initial position is controlled by the acceleration constant, c_{init} , and the random number, r_{init} , drawn from a uniform probabilistic distribution over (0,1). The same extension can be applied to all the speed updating functions discussed above. The hybrid PSO methods extended by crossover and/or subpopulations in [244] also utilize this speed update strategy.

Another early PSO-based registration method was proposed in [262]. This work also used a hybrid PSO method with differential evolution crossover operation, but with a different particle selection mechanism and a different inertia weight function [262]:

$$\omega = \frac{(\omega_{max} - 0.4)(t_{max} - t)}{t_{max}} + 0.4, \quad (6.24)$$

where ω_{max} was set to 0.4 and t_{max} is the pre-defined maximum number of iterations.

Both the results reported by Wachowiak et al. [244], and Talbi and Batouche [262], confirmed that the performance of PSO is enhanced by hybridization. Lin et al. [256] and Chen et al. [255] developed a similar hybrid PSO method in which the global optima of each subpopulation were used to update the particle speeds, and the crossover operation was only performed between particles rather than subpopulations [255, 256]. There are also hybridizations of other evolutionary methods with original PSO. There is a registration method which attempts to hybridize PSO with a steepest

gradient algorithm [298], or with an integrated tree-shape hierarchy [309] that controls the comparison frequency of each particle, although without enough information about the datasets and metrics used for validation.

For ultrasound image registration, Jin et al. [300] proposed a variable neighbourhood selection PSO (VNS-PSO) method which sets a threshold T_g for improved value of similarity measure between two successive iterations. When the improvement is below the threshold, a proportion of the particles will be reselected within an expanding neighbourhood around the currently found global optima [300]. This mechanism increases the ability of jumping out of local optima for PSO.

QPSO and its derivations are presently the most widely used of all the reviewed methods mentioned above [260, 261, 296, 304, 310] because of its fast convergence [310]. Li et al. [260] uses Niche chaotic mutation QPSO (NCQPSO) [311] which hybridizes QPSO with subpopulation based mutation, chaotic search, and Niche evolution strategies. A method developed from other applications, but applicable to medical image registration, is the chaotic quantum-behaved PSO based on Lateral Inhibition (LI-CQPSO) proposed in [296]. Another simple hybridization model of chaotic search QPSO for registration can be found in [261]. Meshoul and Batouche [261] use a time variant threshold to detect stagnation of the search process. When stagnation happens, the position update function becomes:

$$\mathbf{x}_i(t+1) = \mathbf{x}_i(t) + \mathbf{x}_i(2f(t) - 1) \quad (6.25)$$

where $f(t)$ is calculated using equation 6.22. When stagnation doesn't occur, positions of particles are updated by equation 6.16 and 6.18.

Zhou et al. [304] modified the original QDPSO with hybrid probability distribution by introducing a new term to the QDPSO position update equation which becomes[304]:

$$\begin{aligned} \mathbf{x}_i(t+1) = & \mathbf{p}_i(t) \pm \alpha |\mathbf{p}_i(t) - \mathbf{x}_i(t)| \ln(1/\mathbf{u}) \\ & + \beta |\mathbf{p}_m(t) - \mathbf{x}_i(t)| \mathbf{r} \end{aligned} \quad (6.26)$$

where β is another creativity coefficient, and \mathbf{r} is sampled with standard normal distribution, while \mathbf{u} is the uniform distribution. This method is called revised QPSO (RQPSO). Furthermore, the diversity controlled RQPSO (DRQPSO) was developed in [304] by introducing the diversity equation 6.9 into RQPSO. Both methods were tested using both benchmark functions and registration of multi-modality brain data [304].

6.5 Inspiring Methods

The purpose of this review is to explore the mechanism to encode registration based prior knowledge to a PSO method. Although some of the methods mentioned above were proposed and tested in registration applications, most of them still concentrate on improving the PSO method itself. Other than in Wachowiak et al.'s work [244], there is no prior knowledge about registration integrated in the optimization process, where it may be very useful. However, there are still a few modified PSO methods which gave theoretical inspirations. These methods either provide a probabilistic perspective for updating the velocities or positions of the particles, or provide an adaptive mechanism to integrate prior knowledge to the current evolution process.

6.5.1 Gaussian Extensions and Bare Bones PSO

In the original PSO velocity update equation the random numbers r_p and r_g are drawn from uniform distribution. From a probabilistic point of view, this means that the possibility of each particle's speed is equally distributed within an area decided by personal and global optima, and current speed. However, it is also reasonable to argue that this probability distribution can be non-uniform, as the directions toward global optimum of the whole searching space and personal optima associated to each particle, as well as current speed direction, should be assigned higher probability. This can be modelled as a compound Gaussian distribution, which leads to new forms of velocity updating equations, for example [269, 312]:

$$\begin{aligned} \mathbf{v}_i(t+1) = & \chi(\mathbf{v}_i(t) + \\ & \mathcal{N}(\mathbf{x}_i^p - \mathbf{x}_i(t), \frac{|\mathbf{x}_i^p - \mathbf{x}_i(t)|}{2} \cdot \mathbf{I}) \cdot (\mathbf{x}_i^p - \mathbf{x}_i(t)) + \\ & \mathcal{N}(\mathbf{x}^g - \mathbf{x}_i(t), \frac{|\mathbf{x}^g - \mathbf{x}_i(t)|}{2} \cdot \mathbf{I}) \cdot (\mathbf{x}^g - \mathbf{x}_i(t))), \end{aligned} \quad (6.27)$$

where \mathbf{I} is the identity matrix.

From the model above, if we ignore the constraints of speeds and allow free movement in a probabilistic sense, the bare bones PSO model can be obtained [270]. The bare bones PSO directly updates particle positions using a Gaussian distribution obtained from \mathbf{x}_i^p and \mathbf{x}^g by [270, 312]:

$$\mathbf{x}_i(t+1) = \mathcal{N}\left(\frac{\mathbf{x}_i^p(t) + \mathbf{x}^g(t)}{2}, |\mathbf{x}_i^p(t) - \mathbf{x}^g(t)| \cdot \mathbf{I}\right). \quad (6.28)$$

Further modifications on bare bones PSO include different choices of covariance matrix [270, 313], replacing the Gaussian possibility distribution with Cauchy [271] or Levy [312] distribution based on the nature of the problem.

6.5.2 Kalman Filter PSO

Also based on the assumption of Gaussian distribution, Monson and Seppi [8, 314] analysed the iterative optimization scheme of PSO using a hidden Markov model (HMM), and proposed use of a Kalman filter to calculate the probability distribution in the next iteration [264]. Kalman filter is an algorithm that estimate a state of a process with an effective computational means calculated by minimizing the mean of square error [315]. It has been widely used to solve navigation problems in robotics. Here it is used to guide the movements of particles in PSO. The general idea is to predict the hidden true optimal solution with the observed local and global optimal positions. For application of the Kalman filter, the state of each particle, $\mathbf{y}_i(t)$, is defined as its position and speed, $(\mathbf{x}_i(t), \mathbf{v}_i(t))^T$. The initial prediction of the Kalman filter, $\bar{\mathbf{y}}_i(0)$ is equal to the initial position and speed of a particle, $\mathbf{y}_i(0)$. Based on the filtering process [315], with the covariance matrices of prediction, observation and system uncertainty defined as Σ_y , Σ_z , and $\Sigma(t)$, the Kalman gain at the t th iteration can calculated by [314]:

$$\mathbf{K}(t) = \frac{(\mathbf{F}\Sigma(t-1)\mathbf{F}^T + \Sigma_y)\mathbf{H}^T}{\mathbf{H}(\mathbf{F}\Sigma(t-1)\mathbf{F}^T + \Sigma_y)\mathbf{H}^T + \Sigma_z}, \quad (6.29)$$

where \mathbf{F} and \mathbf{H} are the state transition matrix and observation matrix of Kalman filter. Then with an observation \mathbf{z}_i , the filtered state estimation can be obtained by [314]:

$$\bar{\mathbf{y}}_i(t) = \mathbf{F}\bar{\mathbf{y}}_i(t-1) + \mathbf{K}(t)(\mathbf{z}_i(t) - \mathbf{H}\mathbf{F}\bar{\mathbf{y}}_i(t-1)), \quad (6.30)$$

$$\Sigma(t) = (\mathbf{I} - \mathbf{K}(t)\mathbf{H})(\mathbf{F}\Sigma(t-1)\mathbf{F}^T + \Sigma_y). \quad (6.31)$$

The observation, \mathbf{z}_i , is defined by:

$$\mathbf{z}_i(t) = \begin{pmatrix} \mathbf{x}_i(t) + \phi(\mathbf{x}^g - \mathbf{x}_i(t)) \\ \phi(\mathbf{x}^g - \mathbf{x}_i(t)) \end{pmatrix}, \quad (6.32)$$

where ϕ is a random number drawn over $[0,2)$. In the original PSO formulae, because of the random number r_g and r_p , the true position and speed of particles in the t th iteration can not be precisely predicted in the $t-1$ th iteration, thus have to be “observed” after the states of the particles updated. The coefficient ϕ plays an similar role here.

Finally, the prediction of next state will be sampled from a Gaussian distribution $\mathcal{N}(\mathbf{F}\bar{\mathbf{y}}_i(t), \Sigma(t))$. A weighted combination of personal and global optima was subsequently introduced to equation 6.30 as a new way to obtain the observation [8] instead of only using global optima as in equation 6.32. Then, the state evolution process becomes [8]:

$$\begin{aligned} \bar{\mathbf{y}}_i(t) = & (\mathbf{I} - \mathbf{K}(t)\mathbf{H})\mathbf{F}\bar{\mathbf{y}}_i(t-1) \\ & + \mathbf{K}(t)(\mathbf{I} - \mathbf{W})\mathbf{y}_i^p + \mathbf{K}(t)\mathbf{W}\mathbf{y}^g, \end{aligned} \quad (6.33)$$

where \mathbf{y}_i^p and \mathbf{y}^g are state vectors of local and global optima of a particle, and \mathbf{W} is a matrix that balances the influence of global and local optima. Using the particle motion model introduced by Monson and Seppi, Monson and Seppi, and assuming

$\mathbf{F} = \mathbf{I}$ and $\mathbf{H} = \mathbf{I}$, the Kalman filter PSO (KPSO) velocity update equation becomes [8]:

$$\begin{aligned}\bar{\mathbf{v}}_i(t) = & (\mathbf{I} - \mathbf{K}_v(t))\bar{\mathbf{v}}_i(t-1) \\ & + \mathbf{K}_v(t)(\mathbf{I} - \mathbf{W}_v)(\mathbf{x}_i^p - \mathbf{x}_i(t-1)) \\ & + \mathbf{K}_v(t)\mathbf{W}_v(\mathbf{x}^g - \mathbf{x}_i(t-1)),\end{aligned}\tag{6.34}$$

where \mathbf{K}_v and \mathbf{W}_v are the sub-matrices of \mathbf{K} and \mathbf{W} that influence particle velocity only. Furthermore, K and W can be further simplified to be constant scalars a and b , which results in the “ **p** Approximate Kalman Swarm ” (PAKS) algorithm, with velocity update equation:

$$\begin{aligned}\bar{\mathbf{v}}_i(t+1) = & (1-a)\mathbf{v}_i(t) + ab(\mathbf{x}_i^p - \mathbf{x}_i(t)) + \\ & a(1-b)(\mathbf{x}^g - \mathbf{x}_i(t)).\end{aligned}\tag{6.35}$$

Then $\mathbf{v}_i(t+1)$ is estimated using Gaussian distribution:

$$\mathbf{v}_i(t+1) \sim \mathcal{N}(\bar{\mathbf{v}}_i(t), \psi \frac{\|\bar{\mathbf{v}}_i(t)\|^2}{D} \mathbf{I}),\tag{6.36}$$

where ψ is a small constant number.

The KPSO model treats optimization problems solved by PSO as a dynamic Bayesian network (DBN), and proposes the idea to estimate the new position using a convex-like combination of current position, and local and global optima.

6.5.3 Bayesian Interpretation

Andras [264] proposed a new Bayesian interpretation of PSO process based on a review of original PSO, KPSO, and bare bones PSO with extensions of different probability distributions. Instead of directly manipulating the particle, this Bayesian interpretation focuses on the likelihood of each point in the problem space being the optimal solution. It allows the possibility that the evaluated fitness value, $\hat{f}(\mathbf{x})$, is

noisy and given true values of the fitness function, $f(\mathbf{x})$:

$$\hat{f}(\mathbf{x}) = f(\mathbf{x}) + \xi, \quad (6.37)$$

where ξ is the additive noise following a noise distribution, typically zero-mean Gaussian distribution. When applying PSO to image registration problem, the estimated fitness function $\hat{f}(\mathbf{x})$ is the similarity measure calculated when applying different transformations to the floating image. The transformation applied to the floating image corresponds to a position \mathbf{x} in the problem space. The fitness function $f(\mathbf{x})$ is the ground the truth of the similarity between the reference image and the transformed floating image.

The knowledge of the particle states is given in the form of a prior probability density function (PDF), $\mathcal{P}(\mathbf{x})$, defined over the searching range. Based on the Bayes theorem, given all $\hat{f}(\mathbf{x}_i(0))$, the posterior PDF is then calculated by:

$$\begin{aligned} \mathcal{P}(\mathbf{x}|\hat{f}(\mathbf{x}_i(0)), i=1, \dots, K) \\ = \frac{\mathcal{P}(\hat{f}(\mathbf{x}_i(0)), i=1, \dots, K|\mathbf{x}) \cdot \mathcal{P}(\mathbf{x})}{\mathcal{P}(\hat{f}(\mathbf{x}_i(0)), i=1, \dots, K)}, \end{aligned} \quad (6.38)$$

where $\mathcal{P}(\hat{f}(\mathbf{x}_i(0)), i=1, \dots, K|\mathbf{x})$ is the likelihood of finding the fitness value $\hat{f}(\mathbf{x}_i(0))$ given the optimal solution \mathbf{x} . It is assumed that the likelihood is proportional to $\hat{f}(\mathbf{x})$. If we assume fitness evaluation values of the particles are dependent on each other, the PDF can be given using a kernel density estimation method:

$$\begin{aligned} \mathcal{P}(\hat{f}(\mathbf{x}_i(0)), i=1, \dots, K|\mathbf{x}) = \\ \frac{1}{\sum_{i=1}^K \hat{f}(\mathbf{x}_i(0))} \sum_{n=1}^K \hat{f}(\mathbf{x}_i(0)) \cdot G(\mathbf{x}; \mathbf{x}_i(0)), \end{aligned} \quad (6.39)$$

where the basis function, $G(\mathbf{x}; \mathbf{x}_i(0))$, is limited by $\int G(\mathbf{x}; \mathbf{x}_i(0)) d\mathbf{x} = 1$. If we assume the fitness evaluation values of the particles are independent to each other, the PDF is instead given by:

$$\mathcal{P}(\hat{f}(\mathbf{x}_i(0)), i = 1, \dots, K | \mathbf{x}) = \left(\prod_{n=1}^K G(\mathbf{x}; \mathbf{x}_i(0))^{f(\mathbf{x}_i(0))} \right)^{\frac{1}{\sum_{n=1}^K f(\mathbf{x}_i(0))}}. \quad (6.40)$$

During the progression of PSO, the prior probability, $\mathcal{P}(\mathbf{x})$, changes every iteration. Thus it is redefined as $\mathcal{P}_t(\cdot)$. The evolution of $\mathcal{P}_t(\cdot)$ can be modelled as:

$$\begin{aligned} \mathcal{P}_{t+1}(\mathbf{x}) &= \frac{\mathcal{P}(\hat{f}(\mathbf{x}_i(t)), i = 1, \dots, K | \mathbf{x}) \cdot \mathcal{P}_t(\mathbf{x})}{\mathcal{P}(\hat{f}(\mathbf{x}_i(t)), i = 1, \dots, K)} \\ &= a_t \mathcal{P}(\hat{f}(\mathbf{x}_i(t)), i = 1, \dots, K | \mathbf{x}) \cdot \mathcal{P}_t(\mathbf{x}), \end{aligned} \quad (6.41)$$

where a_t is a normalization constant to make the sum of $\mathcal{P}_{t+1}(\mathbf{x})$ over the definition domain equal to one. Analysing this Bayesian interpretation using gradient ascent optimization for maximization problem, or gradient descent for minimization, with a learning rate γ the position update of PSO is then given by:

$$\mathbf{x}_i(t+1) = \mathbf{x}_i(t) + \gamma \cdot \left. \frac{\partial}{\partial \mathbf{x}} \ln \mathcal{P}_{t+1}(\mathbf{x}) \right|_{\mathbf{x}=\mathbf{x}_i(t)}. \quad (6.42)$$

Andras suggested a Gaussian PSO method, that is different from Clerc's model, by setting $G(\cdot)$ as a Gaussian distribution:

$$G(\mathbf{x}; \mathbf{x}_n(h)) = \sigma_n^h \cdot \exp \left(-\frac{\beta}{2} \|\mathbf{x} - \mathbf{x}_n(h)\|^2 \right), \quad (6.43)$$

where σ_n^h is the normalization constant for the integral requirement of the distribution, and to clearly differentiate the particles used to estimate the likelihood probability and the new particles generated in each iteration, let $\mathbf{x}_n(h)$ denote the old particle positions in the former iteration. In this situation, the initial probability can be a zero-mean Gaussian or a uniform distribution. Based on equation 6.41, to calculate the second term in equation 6.42, the history of fitness evaluations need to be recorded. Then under mutual dependence conditions, the particles are re-sampled at each iteration by:

$$\begin{aligned}
 \mathbf{x}_i(t+1) = & \\
 & (1 - \gamma)\mathbf{x}_i(t) + \\
 & \gamma \cdot \frac{1}{\sum_{n=1}^K \hat{f}(\mathbf{x}_n(h)) \cdot G(\mathbf{x}_i(t); \mathbf{x}_n(h))} \\
 & \cdot \left(\sum_{n=1}^K \hat{f}(\mathbf{x}_n(h)) \cdot G(\mathbf{x}_i(t); \mathbf{x}_n(h)) \cdot \beta(\mathbf{x}_i(t) - \mathbf{x}_n(h)) \right).
 \end{aligned} \tag{6.44}$$

Under independence assumptions, the positions are updated by:

$$\begin{aligned}
 \mathbf{x}_i(t+1) = & (1 - \gamma)\mathbf{x}_i(t) + \\
 & \gamma \cdot \frac{1}{\sum_{n=1}^K \hat{f}(\mathbf{x}_n(h))} \left(\sum_{n=1}^K \hat{f}(\mathbf{x}_n(h)) \cdot \beta(\mathbf{x}_i(t) - \mathbf{x}_n(h)) \right).
 \end{aligned} \tag{6.45}$$

The Bayesian PSO model allows incorporation of prior knowledge of the problem space which can be considered as regularization constraints [264]. This model can then be extended to a kernel based PSO method assuming the prior knowledge implies that the combination of $G(\mathbf{x}; \mathbf{x}_n(h))$ in a transformed space can validly indicate the likelihood of an optimal solution. The transformation, $\Phi(\mathbf{x})$, corresponds to a Mercer kernel[264] \mathbf{K} :

$$\mathbf{K}(\mathbf{x}, \mathbf{y}) = \langle \Phi(\mathbf{x}), \Phi(\mathbf{y}) \rangle. \tag{6.46}$$

In this case, the basis function can be rewritten as:

$$\begin{aligned}
 G(\mathbf{x}; \mathbf{x}_n) = & \\
 & \sigma_n^h \cdot \exp \left(-\frac{\beta}{2} (\mathbf{K}(\mathbf{x}, \mathbf{x}) + \mathbf{K}(\mathbf{x}_n, \mathbf{x}_n) - 2\mathbf{K}(\mathbf{x}, \mathbf{x}_n)) \right),
 \end{aligned} \tag{6.47}$$

where $\mathbf{K}(\mathbf{x}, \mathbf{y})$ has a form of $\mathbf{H}(\|\mathbf{x} - \mathbf{y}\|)$.

The original PSO, bare bones PSO and Kalman filter PSO can also be validly expressed in the Bayesian and kernel form. This Bayesian interpretation gives

6.5 Inspiring Methods

a principled basis for better analysis and for understanding the mechanisms and performances of different PSO methods.

6.6 Conclusion and Discussion

This chapter comprehensively reviewed the present developments of PSO methods, as well as their applications to image registration problems. The purpose of this survey is to look for a PSO-based optimization strategy that is more suitable to solve rigid body image co-registration problem, and to find a mechanism that can encode prior knowledge of registration into the optimization framework. Since the first PSO method was proposed, the original form of the formulae has been improved and modified from different aspects.

Most of the reviewed methods that have been applied to registration problems are still general-purpose optimization algorithms, except Wachowiak et al.'s method which includes the initial manually picked particle position in the formulae. But for most registration solutions, the transformation represented in the searching space is usually randomly initialized, in which case the initial state of particles provide little useful information for optimization. Those methods derived from probabilistic theory, especially the Bayesian interpretation of PSO [264], provide a convenient way to encode prior knowledge in the form of a probabilistic distribution. At the same time, the Kalman filter PSO [8, 314] presents a HMM to represent the evolution of the probabilistic distribution. These methods inspired the theoretical derivation of a new type of registration-oriented PSO methods.

Based on this study, my own registration-oriented PSO method guided by unscented Kalman filter (UKF) is proposed. In the next chapter, the UKF-based PSO methods will be introduced to further improve the registration framework. Several methods reviewed in this chapter will be selected, and their performances in registration applications will be evaluated against my new UKF-based PSO methods using both benchmark and real data.

A Registration Oriented Single Point Kalman Filter Particle Swarm Optimization Method for Automatic Medical Image Alignment

ABSTRACT

As introduced in the last chapter, various improvements of the original PSO algorithm have been developed to overcome the premature convergence problem. Many of them have been applied to image registration. However, these modified PSO methods are mostly general purpose optimizations with no integrated prior knowledge focused on registration. In this chapter, I propose a novel type of registration-oriented PSO algorithm, guided by an unscented Kalman filter. The three newly implemented optimizers displayed better robustness to local optima in the searching space with less computational complexity in the comparison experiments performed using both benchmark and real data. This new PSO method provides a new efficient mechanism to integrate prior knowledge of a registration problem into the optimization process, which obviously enhanced the performance of the image registration algorithms.

7.1 Introduction

Particle swarm optimization (PSO) is a widely studied optimization method that has been applied in the field of image registration over the last two decades. As discussed in the previous chapter, various modifications have been made to improve its convergence and computation speed. However, when used in image registration frameworks, these modifications of PSO can still be considered as general purpose optimization methods. Furthermore, these optimizations are still considered as a separated step independent to other components of the registration algorithm, whereas in practical application, the nature of similarity measures can provide useful prior knowledge about the registration problem space. In this chapter, I introduce a novel type of registration-oriented PSO model, guided by an unscented Kalman filter (UKF), that can not only encode the prior knowledge extracted by analysis of the registration problem space, but also adaptively combine different similarity measures.

For most registration problems, the ground truth of image similarity/difference can be considered as the difference between the transformation under evaluation and the transformation that leads to the unique best alignment. To some extent, most similarity measurements previously proposed may be treated as a mapped function of this "ground truth" measure, which means that an appropriate noise-free similarity measurement should also be a function following a uni-modal distribution. Under this assumption, from the Bayesian perspective of PSO [264], I propose a UKF-PSO framework specially customized for image registration problems. Using an unscented Kalman filter [316], this new UKF-PSO algorithm iteratively estimates global optima with accumulated information about probability distribution of the similarity measurements. This leads to quick convergence, with improved robustness to local optima and a large searching space.

Another result of considering optimization as an independent step in registration is that the efforts made to achieve better registration results have often been made

solely on defining and mixing different features or similarity measurement functions. This leads to extra difficulties for assigning weights or significant factors for the selected features or similarity measures. Thus from the proposed registration oriented UKF-PSO optimizer, we derive a nested framework, named as nested UKF-PSO (N-UKF-PSO) that can solve this weighting issue adaptively during the convergence process of the Kalman filter.

This chapter is organised as follows. Section 7.2 describes theoretical backgrounds and the prior knowledge extracted from registration. The details of the proposed UKF-PSO method and its nested framework are introduced in section 7.3 and section 7.4. Some experiments performed using real CT and MR images are described in section 7.5, and the results of them shown in section 7.6. Final conclusions are made, with a discussion about possible extension of the proposed methods, in section 7.7.

7.2 Theory Derivation

Most of the reviewed methods in the previous chapter improve the convergence of the original PSO algorithm by combining the information obtained from each particle, and by enhancing the diversity of the population. Andras [264] proposed the Bayesian PSO method from a probabilistic point of view. This model assumes that the evaluation value of the fitness function is proportional to the probability of a point in the searching space being the optimal solution. Thus in a registration problem, a value computed from a similarity/difference measure can be considered as an unnormalized probability. This can be expressed using a set of factorized presentations of probabilistic distributions, or the probabilistic graphic model (PGM). The probability distribution over the whole searching range is interpolated using multiple Gaussian bases for the Bayesian Gaussian PSO, as is similar for the bare bones PSO method. Also from a perspective of probability theory, the Kalman filter PSO adopts a Bayesian optimization model (BOM) that frames the optimization problem in a dynamic Bayesian network (DBN). These works provide the possibility to integrate a type of prior knowledge into image registration, specifically, to the $\mathcal{P}(\mathbf{x})$ defined in Andras's work [264] as discussed in chapter 6. In this chapter, as a result of a simplified definition of $\mathcal{P}(\mathbf{x})$, there is no need to calculate the probability distribution under different dependence assumptions. It can be directly fitted using the evaluation values of all particles.

Target registration error (TRE) has been treated as the ground truth of registration problems in many publications. Ideally, the TRE of two perfectly aligned images is 0. We slightly generalize this concept. Let \mathbf{x} be a position in the problem space with represent a transformation. For example, when rigidly registering 3D data, \mathbf{x} can be a 6D vector which stores the translation and rotation along the three axes of a 3D orthogonal coordinate system. As discussed in Chapter 7, the ground truth of similarity or difference between the reference and the transformed floating image can

be considered as a fitness function $f(\mathbf{x})$. Let \mathbf{x}^o be the optimal transformation which leads to a TRE closest to 0. Then for a transformation \mathbf{x}_i , $f(\mathbf{x}_i)$ can be simply defined as the distance between \mathbf{x}_i and \mathbf{x}^o in the problem space, $\|\mathbf{x}_i - \mathbf{x}^o\|$. Here $f(\mathbf{x}_i)$ is a difference measure because its value decrease when \mathbf{x}_i moving closer to the optimal solution \mathbf{x}^o . Furthermore, any monotonic mapping of this distance, $\mathbf{K}^o(\|\mathbf{x}_i - \mathbf{x}^o\|)$, can be also considered as $f(\mathbf{x}_i)$. In this case, a similarity measure can be obtained by using monotonically increasing \mathbf{K}^o function so that $f(\mathbf{x}_i)$ increases when \mathbf{x}_i moving towards \mathbf{x}^o . For example, $\mathbf{K}^o(\cdot)$ can be a Gaussian function:

$$f(\mathbf{x}_i) = \exp\left(-\frac{\beta}{2}\|\mathbf{x}_i - \mathbf{x}^o\|^2\right). \quad (7.1)$$

This means the prior knowledge indicates that $\mathcal{P}(\mathbf{x})$ follows a Gaussian-like distribution with unknown expectation \mathbf{x}^o . Furthermore, we can also consider that the ground truth of any similarity measure, for example, mutual information (MI), can be modelled as:

$$f(\mathbf{x}_i) = \mathbf{K}\left(\exp\left(-\frac{\beta}{2}\|\mathbf{x}_i - \mathbf{x}^o\|^2\right)\right), \quad (7.2)$$

where \mathbf{K} is a monotonically increasing function.

The objective of a registration problem is to find the unknown unique true global optimum \mathbf{x}^o . Using PSO, this \mathbf{x}^o is directly estimated and predicted by the value of \mathbf{x}^g . The advantage of using this Gaussian-form similarity/difference measure is that \mathbf{x}^o is exactly the mathematical expectation, $\int \mathbf{x}\mathcal{P}(\mathbf{x})d\mathbf{x}$, over the whole problem space. Thus in each iteration of PSO, the global optimum $\mathbf{x}^g(t)$ can be estimated by the average of all $\mathbf{x}_i(t)$ weighted by normalized $f(\mathbf{x}_i(t))$, rather than directly selecting the maximum of all samples. Generally speaking, this weighted average over $\mathbf{x}_i(t)$ can find the global optima of uni-modal functions, but may not be able to handle multi-modal problems. However, a well-chosen similarity measure should be able to be converted to a uni-modal function after appropriately smoothed within the problem space, otherwise the registration problem is unsolvable with most optimization algorithms. Using multi-

7.2 Theory Derivation

resolution framework is a typical strategy to smooth the similarity function in the searching range includes.

In reality, the similarity/difference measure, $\hat{f}(\mathbf{x}_i(t))$, is noisy, which is modeled by equation 6.37. So a real similarity/difference measure can be expressed as,

$$\hat{f}(\mathbf{x}_i) = \mathbf{K}(\exp(-\frac{\beta}{2}\|\mathbf{x}_i - \mathbf{x}^o\|^2)) + \xi_o, \quad (7.3)$$

where ξ_o is a zero-mean Gaussian noise with unknown standard distribution. Then with a normalization coefficient, σ_o , a reasonable estimation of $\mathcal{P}(\mathbf{x}_i)$ is,

$$\mathcal{P}(\mathbf{x}_i) = \sigma_o(\cdot \mathbf{K}(\exp(-\frac{\beta}{2}\|\mathbf{x}_i - \mathbf{x}^o\|^2)) + \xi_o). \quad (7.4)$$

In this chapter, we assume that the mapping $\mathbf{K}(\cdot)$ is a linear function. So the above equation can be rewritten as:

$$\mathcal{P}(\mathbf{x}_i) = \sigma \cdot (\exp(-\frac{\beta}{2}\|\mathbf{x}_i - \mathbf{x}^o\|^2)) + \xi, \quad (7.5)$$

where σ is a rescale constant that stretches the Gaussian kernel while satisfying the integral requirement of the distribution. Then in the t th iteration of PSO the global optimum can be estimated by solving,

$$\frac{\partial}{\partial \mathbf{x}} \mathcal{P}_t(\mathbf{x}) = 0. \quad (7.6)$$

where $\mathcal{P}_t(\mathbf{x})$ the probability that a position \mathbf{x} is the global optimum in the problem space at the t th iteration. It is difficult to solve this equation as there is not enough prior knowledge of the additive noise ξ . However, in each iteration of PSO, $\mathcal{P}_t(\mathbf{x})$ can be estimated by fitting a Gaussian function using $\hat{f}(\mathbf{x})$ values obtained by all particles:

$$\hat{\mathcal{P}}_t(\mathbf{x}) = \sigma \cdot \exp(-\frac{\|\mathbf{x}_i(t) - \hat{\mathbf{x}}^g(t)\|^2}{2\hat{\delta}^2}), \quad (7.7)$$

where $\hat{\mathcal{P}}_t(\mathbf{x})$ is the estimation of $\mathcal{P}_t(\mathbf{x})$ which is obtained by fitting a Gaussian function using all $f\mathbf{x}_i(t)$. The mean of this fitted Gaussian function is $\hat{\mathbf{x}}^g(t)$ and variance δ^2 . The mean $\hat{\mathbf{x}}^g(t)$ is the estimated position of the global optimum at iteration t by solving,

$$\frac{\partial}{\partial \mathbf{x}} \hat{\mathcal{P}}_t(\mathbf{x}) = 0. \quad (7.8)$$

Although for a large searching range, the assumed Gaussian form of $\hat{\mathcal{P}}_t(\mathbf{x})$ can not accurately capture the shape of the similarity measure, it gives a reasonable estimation of global optima and will be improved as the searching range shrinks, as shown in Figure 7.1.

Andras formulated the PSO evolutionary process using a gradient ascent algorithm to solve Equation 7.6. In this work, using $\hat{\mathcal{P}}_t(\mathbf{x})$, Equation 7.8 can be solved by fitting $\ln \hat{\mathcal{P}}_t(\mathbf{x})$ using a quadratic least squares method. But this will introduce much higher extra computational complexity [317]. Furthermore, the purpose of fitting the Gaussian function is to obtain an estimated global optimum $\hat{\mathbf{x}}^g(t)$, and the variance δ^2 is not used in further optimization process. Thus I use the weighted mean of all particles obtained in each iteration to roughly estimate the initial global optimum,

$$\hat{\mathbf{x}}^g(t) = \frac{\sum_{i=1}^K \mathbf{x}_i(t) \hat{f}(\mathbf{x}_i(t))}{\sum_{i=1}^K \hat{f}(\mathbf{x}_i(t))}, t \in [0, N_t], \quad (7.9)$$

where N_t is the maximum of number of iterations. The estimation of the global optimum with different searching ranges is shown in Figure 7.2. As shown in Figure 7.2, this estimation moves towards the global optimum of similarity measure as the searching range shrinks during the optimization process.

One important assumption of equation 7.9 is that $\hat{f}(\mathbf{x}) \geq 0$ which is easy to achieve by normalization. In this work, this is achieved by applying a similarity measure to the images to be aligned. When solving the registration problem using

a difference measure, denoted as $\hat{f}^d(\mathbf{x})$, we can convert it to a similarity measure by,

$$\hat{f}(\mathbf{x}) = \exp(-\mathcal{E}(\hat{f}^d(\mathbf{x}))), \quad (7.10)$$

where $\mathcal{E}(\cdot)$ is a function of $\hat{f}^d(\mathbf{x})$ in the searching range.

To sum up, in each iteration of PSO method, a noisy estimation of the global optimum $\hat{\mathbf{x}}^g(t)$ can be obtained using Equation 7.9. This $\hat{\mathbf{x}}^g(t)$ then can be improved during evolutionary process of PSO by combining information from all particles and all the passed iterations.

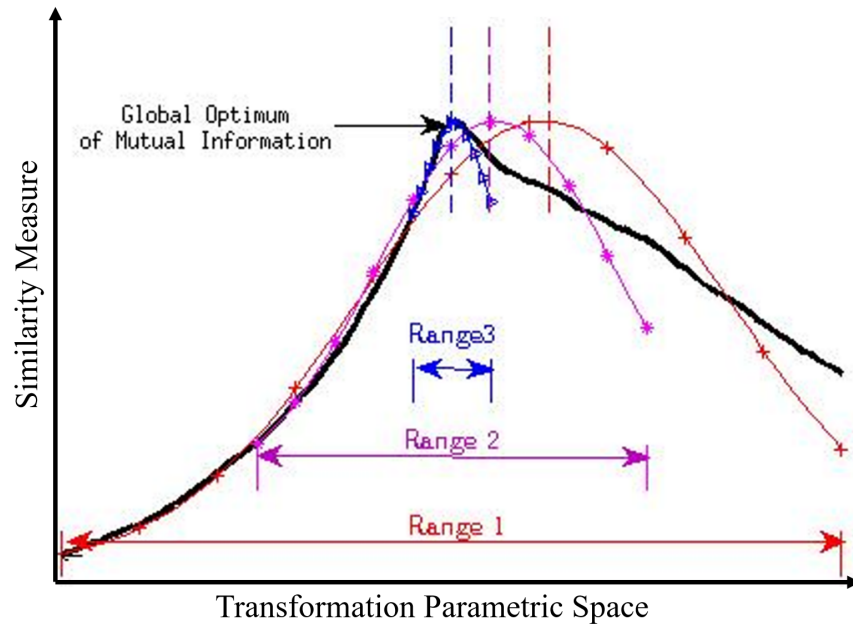


Figure 7.1: Fitting Gaussian function to distribution of mutual information within three different searching ranges. The fitted Gaussian function tends to give a more accurate estimation of the distribution within a smaller searching range.

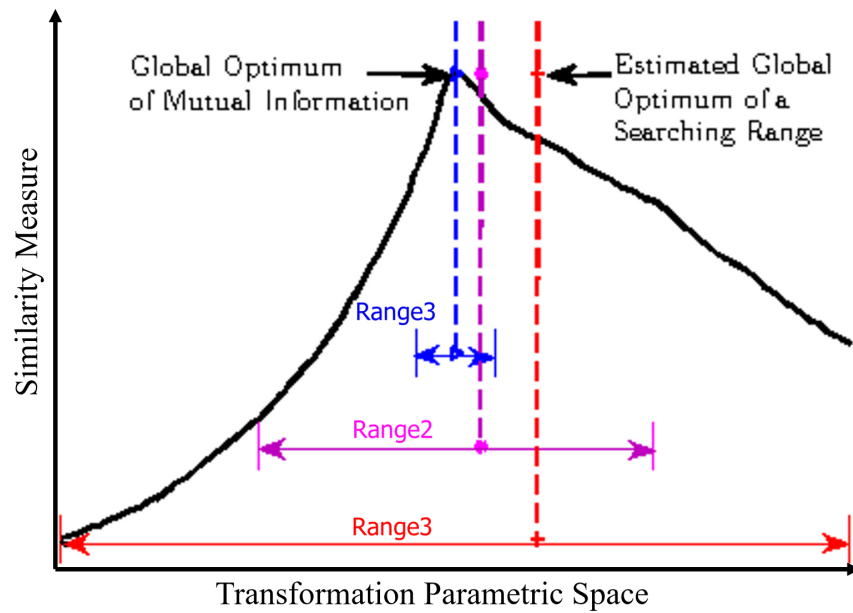


Figure 7.2: Estimation of the global optimum using the weighted mean of all particles within different searching ranges. The estimation of the global optimum tends to be closer to the real global optimum within a smaller searching range.

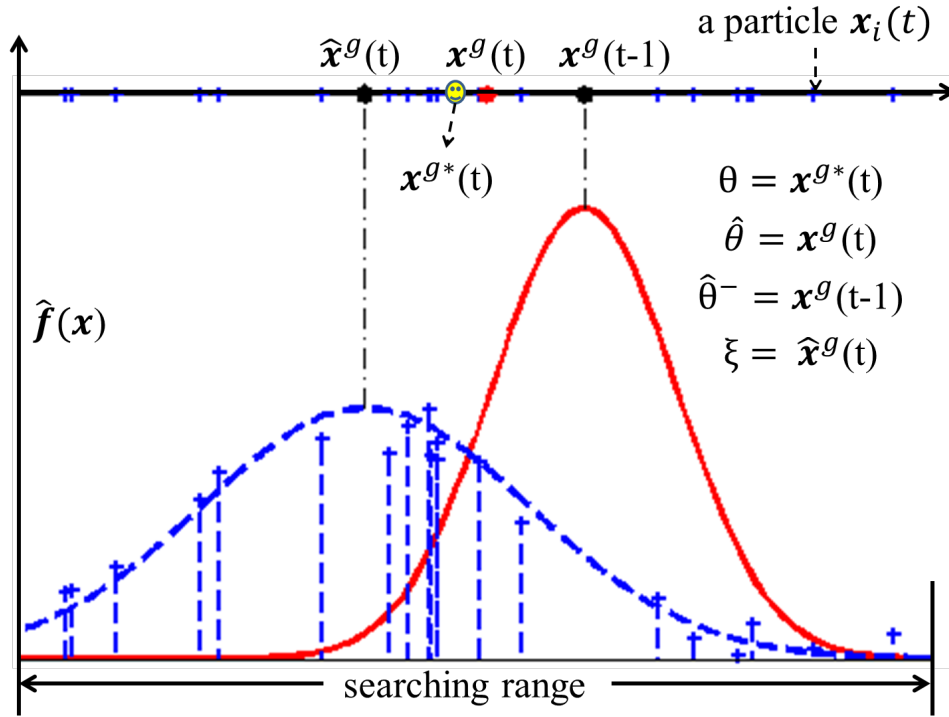


Figure 7.3: Information available at the t th iteration of PSO: in a dynamic Bayesian network, the hidden state θ represents an optimal estimation \mathbf{x}^{g*} of the true global optimum; the observed state ξ is defined as the average position of all particles $\hat{\mathbf{x}}^g$ weighted by the measured fitness function \hat{f} of each particle. An estimation of the hidden state \mathbf{x}^g is produced by fitting \hat{f} to a Gaussian function in each iteration of the optimization process. For the t -th iteration, $\mathbf{x}^g(t)$ can be obtained by combining $\mathbf{x}^g(t-1)$ and $\hat{\mathbf{x}}^g(t)$. When solving the optimization problem using a linear Kalman filter as reviewed in chapter 6, $\mathbf{x}^g(t-1)$ is treated as the output of time – update stage, $\hat{\theta}^-$, and $\mathbf{x}^g(t)$ is the output of the measurement – update stage, $\hat{\theta}$.

7.3 The UKF-PSO Method

The $\hat{\mathbf{x}}^g$ calculated using equation 7.9 can be directly used to replace \mathbf{x}^g in the PSO formulae as it moves closer to the optimum of $\hat{f}(\mathbf{x})$. However, with integrated prior knowledge, the estimation of PDF of \mathbf{x}^0 in the searching range can be improved by accumulating the historical information obtained in previous iterations. This can be achieved through the DBN built up in Monson and Seppi's work [8] which is used to characterize the time-sensitive relationship between observable and hidden states. For image registration problems using swarm optimization, the global and local optima obtained in each iteration can be encoded as the observed state ξ . Based on the theory in [8], the hidden state θ represents a particle position \mathbf{x}^{g*} that lead to a better fitness. The position \mathbf{x}^{g*} can be defined as the position that lead to the best $f(\mathbf{x})$ value within the range covered by the population of particles $\mathbf{x}_i(t)$. In this case, \mathbf{x}^{g*} changes over time as the searching range covered by the particles is changing over time. Alternatively, we can directly define $\mathbf{x}^{g*} = \mathbf{x}^0$. In this case \mathbf{x}^{g*} as the average of \mathbf{x}_i weighted by the noise-free fitness function $f(\mathbf{x}_i)$. An estimation $\hat{\theta}$ of the hidden state is given for each iteration.

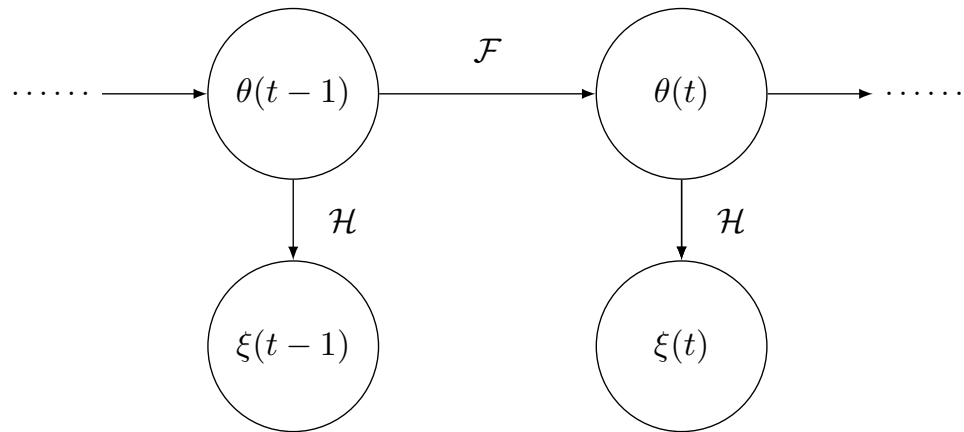


Figure 7.4: Hidden Markov model [8]: θ and ξ are the hidden and observed states.

However, because the prior knowledge of registration problems is integrated and $\hat{\mathbf{x}}^g$ is calculated using equation 7.9, a much simpler DBN can be adopted here using

7.3 The UKF-PSO Method

the raw information demonstrated in Figure 7.3. After $t - 1$ iterations, the hidden state is the ideal position $\mathbf{x}^{g*}(t)$ that is closer to \mathbf{x}^o , or equals \mathbf{x}^o . The observation ζ can be directly defined as $\hat{\mathbf{x}}^g(t)$. Each iteration has a current estimation of the hidden state $\mathbf{x}^{g*}(t)$ based on the observation. To obtain this estimation, the relationship between θ and ζ is depicted as an instance of hidden Markov model (HMM), as shown in Figure 7.4 [8]. The hidden state θ evolves over time based on some state transition model \mathcal{F} , and influences the observable state through a known observation model \mathcal{H} . The transition model F reflects how an estimated global optimum moves closer to locations of better fitness and the observation model may then be described as a model of the influence of $\mathbf{x}^{g*}(t)$ upon $\hat{\mathbf{x}}^g(t)$. When defining \mathbf{x}^{g*} as the average of \mathbf{x}_i weighted by $f(\mathbf{x}_i)$, as shown in Figure 7.5, \mathcal{F} can be specified such that the evolution of \mathbf{x}^{g*} depends on the movements of every particle. This assumes a highly non-linear state transition process, or we use \mathbf{x}^o as hidden state that assumes an identical state transition. In both cases, the observation model is an identical mapping.

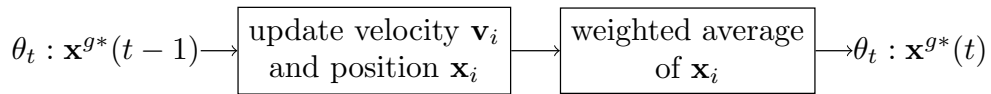


Figure 7.5: The non-linear state transition model \mathcal{F} used to evolve the optimal estimation \mathbf{x}^{g*} of the true global optimum

This influence of \mathbf{x}^{g*} on $\hat{\mathbf{x}}^g$ is inherently noisy, and the noise is used as a subjective uncertainty model of the accuracy of an observation [8]. Based on the prior knowledge being integrated, the current state is modeled by a Gaussian distribution with mean \mathbf{x}^g and a variance that models how strong the likelihood that \mathbf{x}^g reflects \mathbf{x}^{g*} . The goal of the registration process is then to reduce the uncertainty of this belief over \mathbf{x}^g to its lowest level and thus give the most accurate prediction. Because this prediction is produced by combining the information from all particles and all previous iterations, it is applicable to different PSO methods with different velocity and position updating mechanisms.

For the HMM described above, the Kalman filter [315] and its extensions

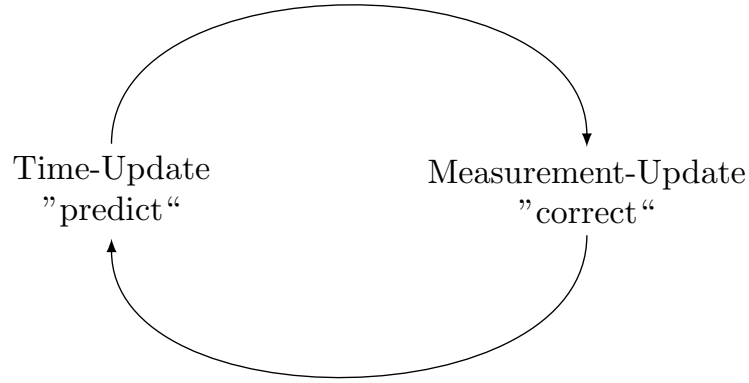


Figure 7.6: The predict – correct circle of Kalman filter and its extensions

[318][316] are useful solutions. When \mathcal{F} and \mathcal{H} are linear, and the HMM is therefore known as a linear dynamic system (LDS), the Kalman filter provides an efficient means to recursively estimate the state of a process while minimizing the mean of square error [319]. The Kalman filter models HMM as a *predictor – corrector* circle, as shown in Figure 7.6, where both the state-transition and observation are noisy processes with additive Gaussian noise. In our registration problem assuming a LDS, in the *prediction*, or *time – update*, stage, a prediction of $\mathbf{x}^{g*}(t)$ is given by,

$$\hat{\theta}^-(t) = \mathbf{F}\hat{\theta}(t-1), \quad (7.11)$$

$$\Sigma^-(t) = \mathbf{F}\Sigma(t-1)\mathbf{F}^T + \Sigma_{\theta}, \quad (7.12)$$

where \mathbf{F} is the matrix representation of the state transition function, $\theta^-(t)$ and $\Sigma^-(t)$ are the mean and variance of predicted $\mathbf{x}^g(t)$ respectively, and Σ_{θ} is the covariance of the state-transition noise. Assuming $\theta(t) = \mathbf{x}^{g*}(t) = \mathbf{x}^0$, \mathbf{F} is an identity matrix.

Then in the *correction*, or *measurement – update*, stage, the estimation of state is refined using the observation,

$$\mathbf{K}(t) = \frac{(\mathbf{F}\Sigma(t-1)\mathbf{F}^T + \Sigma_{\theta})\mathbf{H}^T}{\mathbf{H}(\mathbf{F}\Sigma(t-1)\mathbf{F}^T + \Sigma_{\theta})\mathbf{H}^T + \Sigma_{\xi}}, \quad (7.13)$$

$$\hat{\theta}(t) = \hat{\theta}^-(t) + \mathbf{K}(t)(\xi(t) - \mathbf{H}\hat{\theta}^-(t)), \quad (7.14)$$

$$\mathbf{\Sigma}(t) = (\mathbf{I} - \mathbf{K}(t)\mathbf{H})\mathbf{\Sigma}^-(t), \quad (7.15)$$

where the $\mathbf{K}(t)$ is the Kalman gain in the t th iteration that is used to balance the influence of prediction and observation, \mathbf{H} is the observation matrix which is identity, and $\hat{\theta}(t)$ and $\mathbf{\Sigma}(t)$ are the mean and variance of the estimation respectively, so that the estimate of global optimum can be given based on the following probability distribution [319],

$$\mathcal{P}(\theta(t)|\xi(t)) \sim N(\hat{\theta}(t), \mathbf{\Sigma}(t)). \quad (7.16)$$

When using the non-linear state transition model shown in Figure 7.5, the HMM is not a LDS. In this case the extensions of the Kalman filter should be applied to deal with the non-linear state transition process $\mathbf{x}^{g*}(t) = \mathcal{F}(\mathbf{x}^{g*}(t-1))$. The extended Kalman filter (EKF) requires calculation of a Jacobian matrix of $\mathcal{F}(\mathbf{x})$ [316] which is difficult for this complicated state transition function, thus we propose the novel use of an unscented Kalman filter (UKF) [316]. Rather than estimate an arbitrary transition function as the EKF, the UKF approximates a Gaussian probability distribution using standard vector and matrix operations of a set of weighted *sigmapoints*, $\mathbf{\varnothing}_j(t-1)$, $j = 1 \cdots 2D + 1$ [320]. For the t th iteration in a D -dimensional problem space, the sample mean and covariance of the set of sigma points are $\hat{\theta}(t-1)$ and $\mathbf{\Sigma}(t-1)$ [320]. Specifically, the sigma points and their associated weights are selected by,

$$\mathbf{\varnothing}_j(t-1) = \begin{cases} \hat{\theta}(t-1), & j=0, \\ \hat{\theta}(t-1) + (\sqrt{(D+\kappa)\mathbf{\Sigma}(t-1)}), & j=1 \cdots D, \\ \hat{\theta}(t-1) - (\sqrt{(D+\kappa)\mathbf{\Sigma}(t-1)}), & j=D+1 \cdots 2D+1; \end{cases} \quad (7.17)$$

$$\mathbf{W}_j = \begin{cases} \kappa / (D + \kappa), j = 0; \\ 1 / (2(D + \kappa)), j = 1 \cdots 2D + 1. \end{cases} \quad (7.18)$$

where \mathbf{W}_j is the weight associated with the j th sigma point. Details of selecting the weighting parameter κ can be found in [316] and [320]. In this chapter, we follow [320]'s recommendation that makes $\kappa + D = 3$. In the *time – update* stage, each sigma point is instantiated through the state transition function by [320],

$$\boldsymbol{\Theta}_j(t|t-1) = \mathcal{F}(\boldsymbol{\Theta}_j(t-1)), \quad (7.19)$$

then the mean of state prediction is calculated by [320]:

$$\theta^-(t) = \sum_{j=0}^{2D} \mathbf{W}_j \boldsymbol{\Theta}_j(t|t-1), \quad (7.20)$$

and the variance is given by [320],

$$\begin{aligned} \boldsymbol{\Sigma}^-(t) = & \sum_{j=0}^{2D} \mathbf{W}_j (\boldsymbol{\Theta}_j(t|t-1) - \theta^-(t)) \\ & \cdot (\boldsymbol{\Theta}_j(t|t-1) - \theta^-(t))^T. \end{aligned} \quad (7.21)$$

Because the observation model is an identical mapping function, we can still use the linear measurement update formulae of the original Kalman filter (equation 7.13-7.15) in the correct stage to obtain $\theta(t)$ and $\boldsymbol{\Sigma}(t)$.

Under this non-LDS assumption, because the uncertainty associated with the estimated global optimum is related to the distribution of particles, we can simply use either a sample, or all, of the particles, together with the estimated global optimum, as the sigma points of UKF. This allows the number of sigma points to be more than $2D + 1$, and makes integrating UKF into PSO more convenient. Additionally, besides the traditional stop criteria, $\boldsymbol{\Sigma}(t)$ can be an extra evidence about the convergence situation of PSO.

7.3 The UKF-PSO Method

To sum up, we combined the procedure of PSO which is briefly shown in Figure 7.7 into the *predict – correct* circle of the Kalman filter, as shown in Figure 7.6. For both LDS and non-LDS cases, our new UKF-PSO algorithm can be briefly presented as shown in Figure 7.8.

The estimated global optimum $\hat{\mathbf{x}}^g$ will be affected by the relative location of the global optimum in the searching range. Figure 7.9 shows how this estimation changes when using different searching ranges with the same size. The estimation is more accurate when the true global optimum is closer to the center of the searching range. Thus a slightly different observation can be used to improve the estimated global optimum: in each iteration, after the $\hat{\mathbf{x}}^g$ is calculated, all particles are resampled to be $\tilde{\mathbf{x}}_i$ so that the searching range is centered on $\hat{\mathbf{x}}^g$, then a new average $\tilde{\mathbf{x}}^g$ can be calculated, as the observation, weighted by new evaluations $\tilde{f}(\tilde{\mathbf{x}}_i)$. We name this model as the “shift particles observation” UKFPSO (SPO-UKFPSO). In this case, the HMM will be different from the one used in the above UKFPSO method, as shown in Figure 7.10, with different definition of θ , $\hat{\theta}$, Σ , \mathcal{F} and ζ . The workflow of the SPO-UKFPSO method is shown in Figure 7.11.

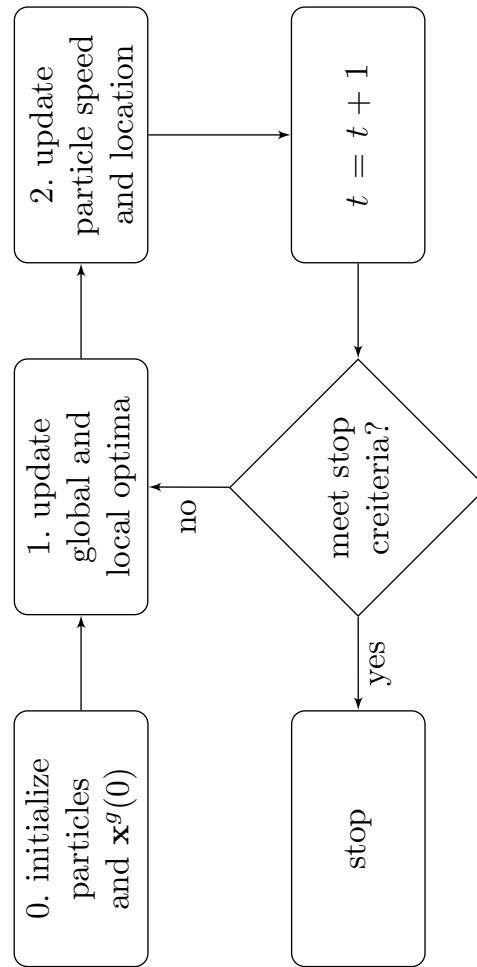


Figure 7.7: Brief workflow of the original particle swarm optimizer

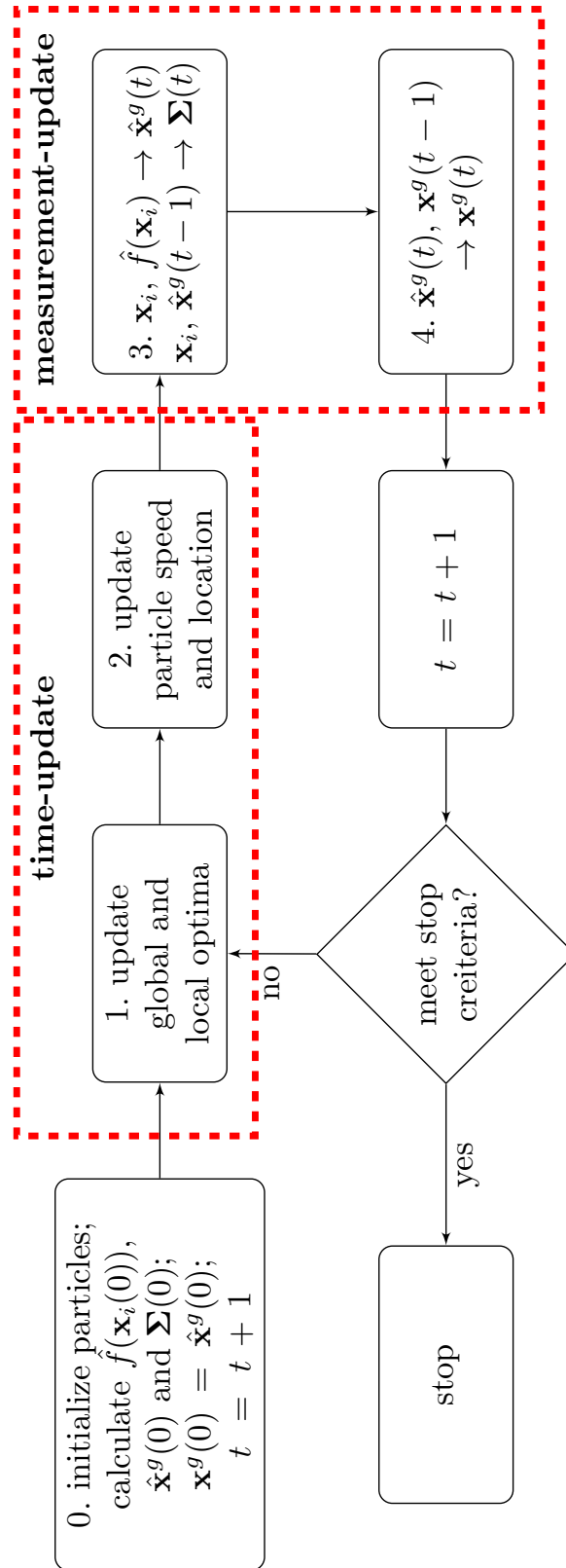


Figure 7.8: Brief workflow of the unscented Kalman filter particle swarm optimizer (UKF-PSO)

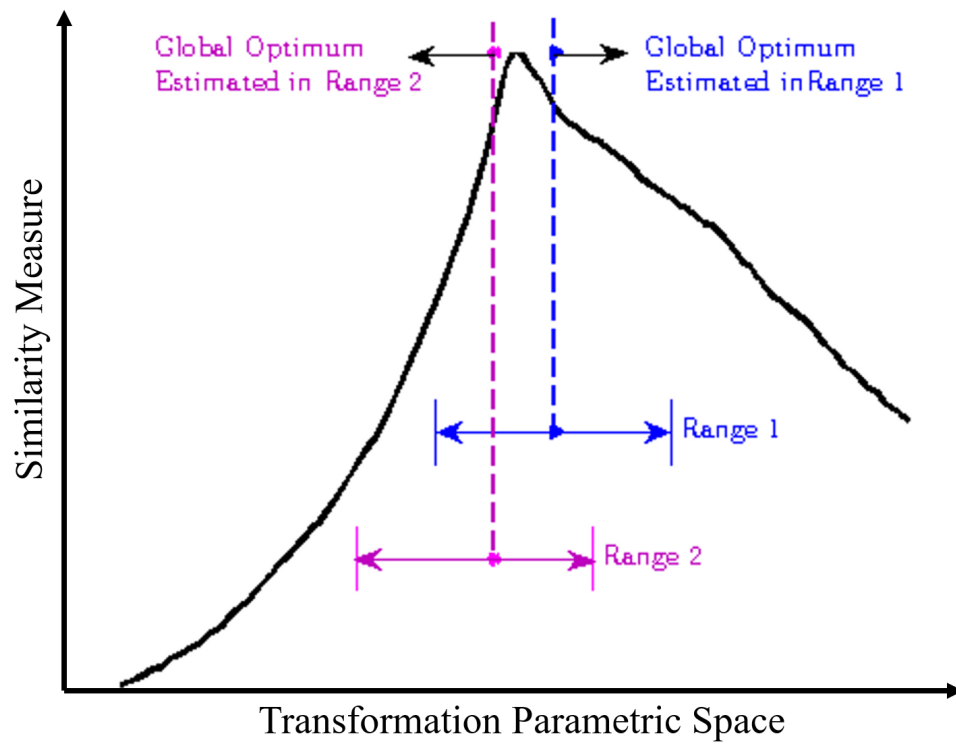


Figure 7.9: Estimations of global optimum when placing the searching range to different positions of the problem space

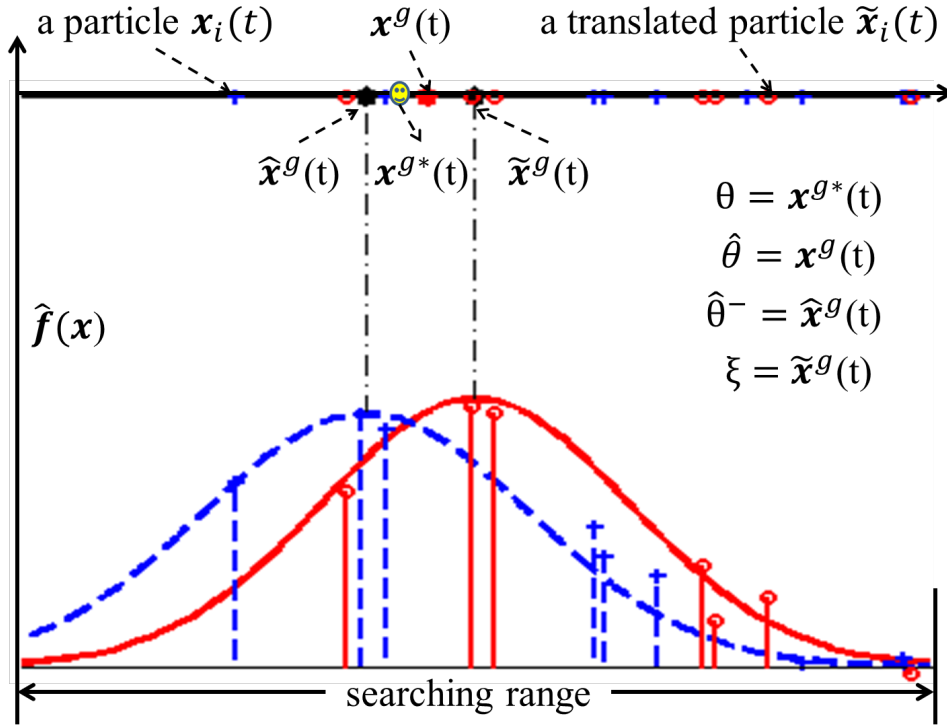


Figure 7.10: Information available at each iteration when solving the optimization process using a Kalman filter: the hidden state θ represents an optimal estimation x^{g*} of the true global optimum. An estimation of the hidden state x^g is produced by fitting the measured fitness function value \hat{f} to a Gaussian function in each iteration of the optimization process. The output of the time – update stage of the Kalman filter, $\hat{\theta}^-$, is defined as the mean value \hat{x}^g of all the particle positions weighted by \hat{f} . The population of particles is then moved to be centred on \hat{x}^g . The observed state ξ is then defined as the mean \tilde{x}^g of all the new particle positions. The up-to-date estimation of the global optimum, $x^g(t)$, is then provided by the output of the Kalman filter, $\hat{\theta}$, combining \hat{x}^g and \tilde{x}^g .

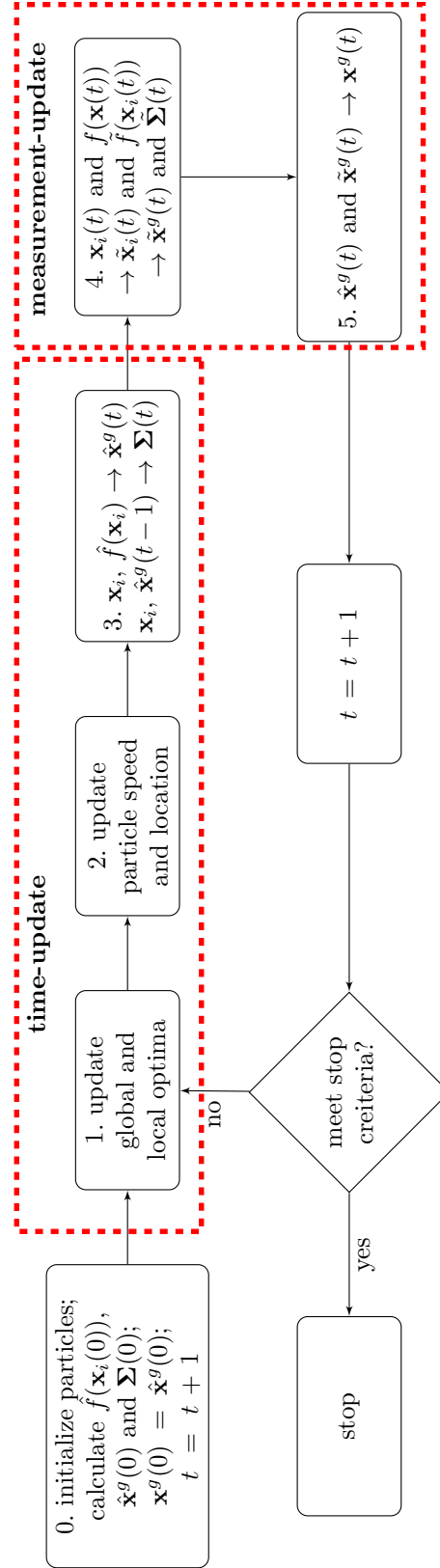


Figure 7.11: Workflow of the unscented Kalman filter particle swarm optimizer with “shift particles observation” (SPO-UKFPSO).

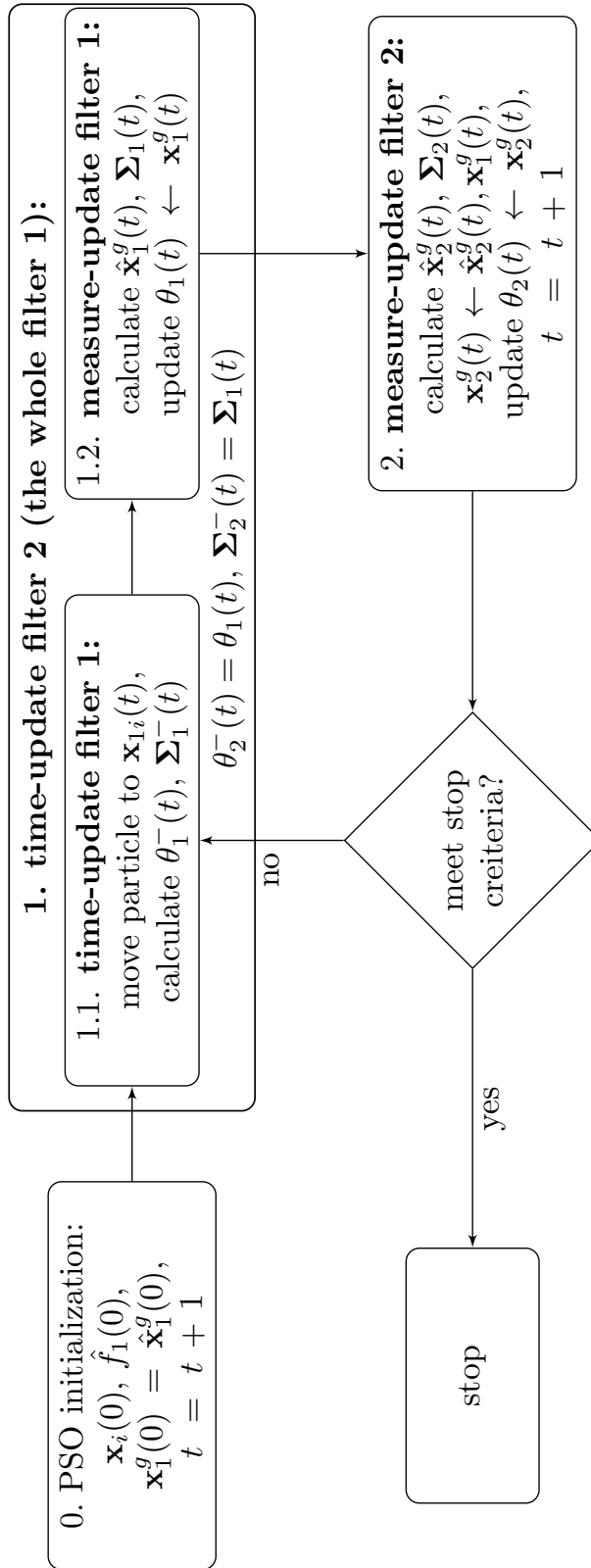


Figure 7.12: Workflow of nested unscented Kalman filter particle swarm optimizer (UKFPSO)

To apply the UKF guide PSO model to real image registration tasks, the choice of similarity/difference measure also has profound influence on the results. The chosen similarity/difference measure has to follow the prior knowledge modeled by equation 7.3, which allows the problem to be solved as shown in Figure 7.1. For example, for a multi-modality registration problem, the sum of squared difference (SSD) of intensity is an inadequate choice. Thus in this chapter, we choose the widely used standard mutual information (MI) as the tested measure. Briefly speaking, to register a reference image, μ , and a floating image ν , the MI is calculated using their joint entropy $H(\mu, \nu)$, and marginal entropies $H(\mu)$ and $H(\nu)$,

$$MI(\mu, \nu) = H(\mu) + H(\nu) - H(\mu, \nu). \quad (7.22)$$

MI is a similarity measure which makes registration a maximization problem.

7.4 The Nested UKF-PSO

Image registration can be performed using different types of similarity/difference measures, as well as different types of features. Combining these features and measures requires us to assign to them adequate weights, or importances, as well as to properly normalize them to comparable scales. These tasks introduce extra difficulties for registration as in many cases there is not enough information that indicates the importance of different measures or features. Furthermore, different measures and features may show different relativity with the registration results. However, no matter which features or measures are used, and no matter how they are weighted, they will finally influence the optimization algorithms in the image transformation space. As a result of the introduced model of prior knowledge, fitness values of any similarity/difference measure are automatically normalized so as to be samples of a probability distribution, which bring all the measures obtained from any features to a uniform scale.

Furthermore, the fundamental mechanism of the Kalman filter and its extensions in each iteration is to mix two Gaussian-shape probability distributions by multiplication. The distributions may be from two different, but relative, random variables. The final effect of the Kalman filter is to adaptively merge the two random variables to generate one single Gaussian probability distribution. The weights are only deterministic in a single iteration and decided by covariances of the two distributions. Based on these facts, we proposed a nested UKFPSO framework in this section that is used for multi-feature or multi-measure registration methods. Figure 7.12 illustrates the working procedure of this nested UKFPSO framework using the LDS-KFPSO model described above.

As shown in Figure 7.12, in the case where we have two similarity measures, $f_1(\mathbf{x})$ and $f_2(\mathbf{x})$, a UKF can be used to guide the registration with the measure $f_1(\mathbf{x})$. At the same time, the output of this UKF at each iteration of PSO can be considered as θ^-

of another UKF. The estimated global optimum obtained using $f_2(\mathbf{x})$ can be considered as the observation of the second UKF. As a result, the first UKF is nested into the *Time-Update* stage of the second UKF. The two UKFs share the same population of particles during the optimization process, which means that each particle obtains two fitness values in each iteration. This framework can be extended using multiple nested UKFs to allow an adaptive mixture of more features or measures.

7.5 Experiments

In this chapter, we evaluated the performance of the proposed PSO methods by solving both general optimization and image registration problems. A few representative PSO methods are also chosen for comparison purpose, having been previously used for registration. The chosen methods include: the original PSO method, QPSO, DRQPSO, chaotic QPSO, bare bones PSO, and the Kalman filter PSO.

All the tested PSO methods are initialized with $10D$ particles where D is the number of problem dimensions. The optimization process stop after 300 iterations if not converged. The common free parameters shared by different methods are set to the same values for a more reliable comparison. For the methods use the particle motion formulae shown by Equation 6.3, 6.4 and 6.5, such as the original PSO, bare bones PSO, LDS-KFPSO, SPO-UKFPSO, and the nested UKFPSO, the dynamic inertia bounds ω_{min} and ω_{max} are initialized as 0.1 and 1.1. The cognition acceleration constant c_p and social acceleration constant c_g are initialized as 2.0. For the methods based on the quantum behaviour model shown by Equation 6.16, such as QPSO, DRQPSO and chaotic QPSO, the creativity coefficient α is 0.55.

7.5.1 Benchmark Functions

The proposed UKFPSO models (LDS-KFPSO, and SPO-UKFPSO) were compared with other PSO methods through a series of comparison experiments. The general optimization power of the algorithms were compared using common benchmark functions which are widely used in the PSO literature [321], as shown in Table 7.1. Because the optimization methods proposed in this chapter are customized for image registration applications with the assumed prior knowledge described in section 7.3, we chose different types of benchmark functions, both single-objective and multi-objective, to comprehensively compare the power of different PSO methods. Because the nested UKFPSO method is designed especially for image registration applications,

requiring multiple types of features or different types of similarity measures, it isn't included in this benchmark function experiment.

Most of the publications reviewed in the previous chapter compare the optimization methods based on the optimal fitness function value returned by different algorithms. However, it is more important to find a position that is closer to the real global optima in the search space than to search for a better value of the fitness function. Thus in this chapter, the performances of the compared algorithms are measured by the norm of the differences between their returned vectors and the ground truths of the benchmark functions. Furthermore, because for seven of the eight chosen benchmark functions the ground truth optima locate in the center of the search space, a weak optimization algorithm that tends to converge to the center of searching space can obtain better results than others. To avoid this effect, in each run of this experiment, the searching range shown in Table 7.1 is randomly shifted. For example, for the Ackley function, the global optimum will be shifted from $(0,0)^D$ to $(10,10)^D$ when the searching range is shifted by -10 along each dimension. This shift is limited within 40% of the searching range so that the global optimum still locate in the searching space. For example, for Salomon function of which the searching range is $[-100,100]^D$ this shift should not be larger than 80.

Besides the random shift of the searching ranges, I tested the algorithms using a random problem dimension chosen between 2 to 30, and repeated each algorithm 100 times for each benchmark function. The mean and standard deviation (STD) of each algorithm were calculated. The stop condition of the algorithms was either reaching 300 iterations or reduction of the variability of the particle positions around the global optima to be less than 10^{-6} . For our proposed UKF based algorithms, an additional stop condition was that the uncertainty of UKF was less than 10^{-6} . All the algorithms were implemented in MATLAB with vectorized simulation of particle positions. Other than the particle position update mechanism, and some method specific parameters, all the implementations shared most of the code to ensure that the comparison was

7.5 Experiments

performed under similar circumstances.

Besides the accuracy, as all the tested methods were implemented on a uniform platform, convergence speeds and run times of each method were also measured. The speeds were evaluated using the average number of iterations and function evaluations of each run, as well as the raw convergence time. For a general view of the function performances, mean accuracies of each method over all benchmark functions in the experiment was also calculated.

7.5.2 Registering Benchmark Datasets

In order to evaluate the performances of the proposed PSO methods in real registration applications, we conducted a rigid registration experiment using the well-known multi-modality brain image datasets from *the Retrospective Image Registration Evaluation (RIRE) Project* [193]. Based on experiment results on the benchmark functions and the reviewed publications, we selected the original PSO, DRQPSO, bare bones PSO and the Kalman filter PSO for comparison with the proposed LDS-KFPSO, SPO-UKFPSO and the nested UKFPSO methods. For the nested UKFPSO, the measure $f_1(\mathbf{x})$ is MI, and the similarity measure based on the gradient features proposed by Pluim et al. [322] was used as $f_2(\mathbf{x})$.

Because of the data and the ground truths provided by RIRE project, we perform CT-MR_T2 registration for patient_001 to _007 and PET-MR_PD registration for patient_001, _002, and _005 to _009, as the CT volume is missing for patient_003 and _004. The voxel size is $0.65 \times 0.65 \times 4\text{mm}^3$ for CT data, $1.25 \times 1.25 \times 4\text{mm}^3$ for MR_T2 and MR_PD data, and $2.59 \times 2.59 \times 8\text{mm}^3$ for PET data. Data of the involved modalities chosen from patient_001 are shown in Figure 7.13.

As the purpose of this experiment is to compare the performances of different PSO methods in real image registration applications, rather than to obtain absolute highest registration accuracy, we integrated the PSO methods into a very simple registration framework. For the sake of simplicity and efficiency, each slice of both

the reference and floating volumes were down-sampled to 20% of the original in-plane resolution of the reference image along each dimension. The slice distance of the floating volume was also interpolated to the slice distance of the reference volume so that the optimization method can only deal with translation and rotation parameters. For further speed-up of the registration, we selected a cubic region of interest (ROI) in each volume by applying Otsu's histogram-based threshold selection method [233] to normalized data. The ROI only includes the data over the threshold.

The RIRE project measures the accuracy of registration using target registration error (TRE) calculated from multiple volumes of interest (VOIs). The transformation parameters calculated from the resampled data will be rescaled for transformation of the original volume. To test the robustness of each method, we did not use data rectified intensity inhomogeneity and scaling. For each patient, 10 trials of registration were completed, and in each run all methods use the same set of initialized particles that were generated by a MATLAB quasi-random number simulator.

7.5.3 Registering Data from A Real Clinical Trial

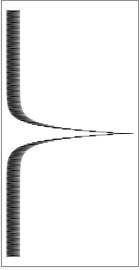
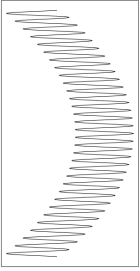
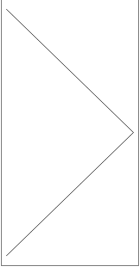
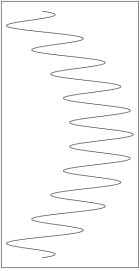



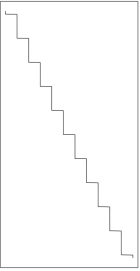
To further compare the performance of our methods with the original PSO, I also conducted an experiment using neonatal data collected from a real ongoing clinical trial in the clinical research imaging centre (CRIC), University of Edinburgh (UoE). This dataset has been introduced, and used to evaluate the performance of the registration framework based on rearranged histogram specification (RHS) in chapter 5. I used a subset of 31 images acquired at 38-44 weeks' postmenstrual age in natural sleep using a 3T Verio system (Siemens, Germany). Isotropic anatomical data were acquired with a range of contrasts as introduced in chapter 5. Images were assessed at point of acquisition for obvious motion artefacts. The range of contrast weightings were chosen to facilitate the development of volumetric brain segmentation algorithms for the main study.

In this experiment, I used our previous registration framework based on

7.5 Experiments

asymmetric K-means binning and re-ordered histogram specification from our previous work [303]. Based on the experiment results in [303], the original PSO always failed to register data of one patient (No. 2956) as a result of variant imaging quality. I replace the optimizer with the proposed models. Data from 10 patients were aligned using a rigid-body transform, calculated within a $51 \times 51 \times 41 \text{mm}^3$ user-positioned region of interest (ROI) on volumes with an isotropic voxel size of 1.56mm . Transformation matrices were obtained from data down-sampled to half of the original resolution. Performance was evaluated by TREs calculated using 1908 pairs of corresponding landmarks (18 on each volume). Examples of the data, and the manually selected landmarks can be found in Figure 5.15, Figure 5.16, and Table 5.1.

Table 7.1: Benchmark Functions

Ackley	Griewank	Modulus Sum	Rastrigin
$-20 \cdot e \left(-0.2 \sqrt{\frac{1}{D} \sum_{d=1}^D x_d^2} \right) - e \left(\frac{1}{D} \sum_{d=1}^D \cos(2\pi x_d) \right) + 20 + e$ <p>bounds: $[-30, 30]^D$ minimum: $(0, 0)^D$</p> 	$\frac{1}{4000} \sum_{d=1}^D x_d^2 - \prod_{d=1}^D \cos\left(\frac{x_d}{\sqrt{d}}\right) + 1$ <p>bounds: $[-600, 600]^D$ minimum: $(0, 0)^D$</p> 	$60 + \sum_{d=1}^D x_d $ <p>bounds: $[-5.12, 5.12]^D$ minimum: $(0, 0)^D$</p> 	$100 + \sum_{d=1}^D (x_d^2 - 10 \cdot \cos(2\pi x_d))$ <p>bounds: $[-5.12, 5.12]^D$ minimum: $(0, 0)^D$</p> 
Salomon	Schwefel	Rosenbrock	Step
$1 - \cos\left(2\pi \sqrt{\frac{1}{D} \sum_{d=1}^D x_d^2}\right) + 0.1 \sqrt{\sum_{d=1}^D x_d^2}$ <p>bounds: $[-100, 100]^D$ minimum: $(0, 0)^D$</p> 	$5000 + \sum_{d=1}^D -x_d \sin\left(\sqrt{ x_d }\right)$ <p>bounds: $[-500, 500]^D$ minimum: $(421.0, 421.0)^D$</p> 	$\sum_{d=1}^{D-1} (100 \cdot (x_{d+1} - x_d^2)^2 + (x_d - 1)^2)$ <p>bounds: $[-30, 30]^D$ minimum: $(1, 1)^D$</p> 	$60 + \sum_{d=1}^D \lfloor x_d \rfloor$ <p>bounds: $[-5.12, 5.12]^D$ minimum: $(-5.12, 5.12)^D$</p> 

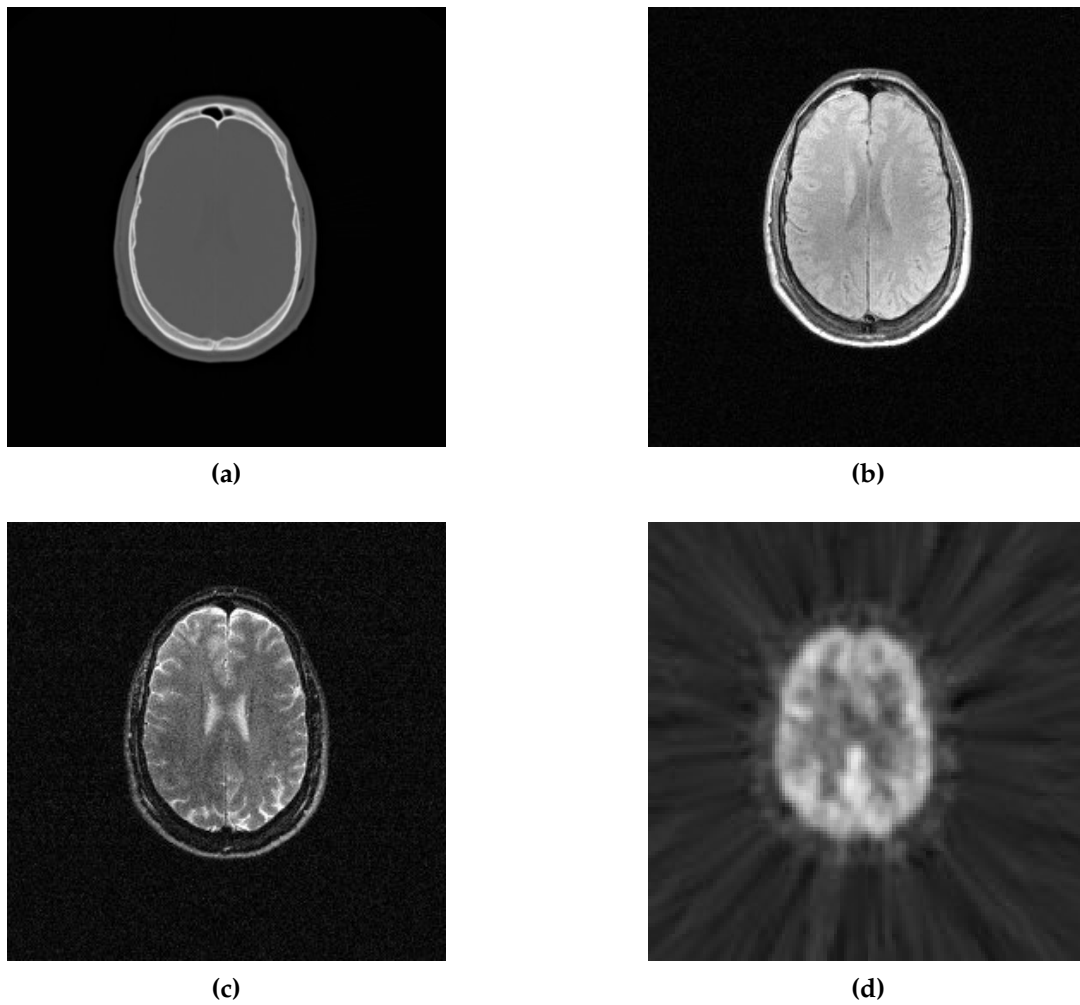


Figure 7.13: *Axial views of the data chosen from patient_001 of the Retrospective Image Registration Evaluation (RIRE) Project: (a) CT; (b) MR_PD; (c) MR_T2; (d) PET.*

7.6 Results

7.6.1 Benchmark Functions

Table 7.2 shows the average results of the compared algorithms working on the benchmark functions, the STD of each run is shown within the parenthesis. As shown in Table 7.2, the original PSO method gave the best result on the Step function. The bare bones PSO performed better on Griewank, Modulus Sum and Salomon functions. The proposed LDS-KFPSO method converged to positions that are closer to the true global optima dealing with Ackley, Schewefel and Rosenborck functions. It also gave better results than other tested methods although slightly worse than SPO-UKFPSO. For most of the benchmark functions, the proposed LDS-KFPSO and SPO-UKFPSO displayed best performances, or performances comparable to bare bones PSO. This is because these functions are either uni-modal function or can be smoothed to a uni-modal function, and the UKF in the proposed methods actually performed as a low-pass filter which smooths the functions within the searching ranges. In this case, the prior knowledge integrated in the proposed methods can make effective prediction of the global optimum in the whole searching range, but other methods can not make this prediction before the global optimum evaluated by the particles. The Step function is a special case among all the benchmark functions, as it is monotonically increasing and the global optimum is located around the upper bound of the search range. In registration applications, this may happen when the true global optima is not included in the search space. As expected, in this case, the LDS-UKFPSO and SPO-UKFPSO methods gave worse results.

Based on the results shown in Table 7.3, because of the simplicity of the position update model, our implementation of chaotic QPSO has the quickest convergence speed but also gave the worst optimization accuracy. Although in some cases it may take a slightly longer time to complete each iteration using the proposed LDS-KFPSO

7.6 Results

and SPO-UKFPSO, both used less numbers of iterations than other tested methods. The LDS-KFPSO model used the least number of function evaluations and shortest run time to achieve the best optimization results. The SPO-UKFPSO provided close accuracy compared to LDS-KFPSO and still converged quicker than most of the other tested methods.

7.6.2 RIRE Data

Figure 7.14 and Figure 7.15 show visualized examples of overlapped images before and after registration, as well as after being transformed by the ground truth of registration results. The statistics of the performed CT-MR_T2 and PET-MR_PD registrations are shown in Table 7.4. As shown in Table 7.4, all three proposed novel methods returned better results compared to other tested methods in terms of mean and median of TRE. For combined difference features and similarity measures, the nested-UKFPSO gave better results among the three proposed models. For the bare bones PSO and Kalman filter PSO, because these measures feature a more deterministic position update mechanism, these methods display better converge speed than the original PSO and DRQPSO. However, the searching positions of these two methods were highly dependent on the particle initialization, which gave very unstable performances in each run of the experiment.

7.6.3 Neonatal Data

Figure 7.16 displays the results of registering the T2 dark fluid and T1 MRPAGE images (from patient No. 2956) which failed registration using all the methods tested in chapter 5. The quantitative evaluation of registration results obtained using the real neonatal data are shown in Table 7.5. As shown in Table 7.5, the LDS-KFPSO and nested UKFPSO not only gave smaller TREs than the original PSO, but also successfully aligned the particular dataset that our previous method failed to register.

Table 7.2: Performances of the selected particle swarm optimizers applied to the chosen benchmark functions: the performances are measured by the average distances between the global optima they found to the ground truths obtained from 100 times of experiments with random initialization. The best result of each benchmark function is shown in bold font, and the standard deviations of results obtained from the 100 runs of this experiments are shown within parenthesis.

Function	original PSO	QPSO	DRQPSO	chaotic QPSO
Ackley	8.891(5.4)	6.859(4.1)	5.991(4.4)	10.23(5.8)
Griewank	3.042(1.2)	6.635(4.3)	1.696(0.7)	15.49(11.3)
Modulus Sum	0.013(0.03)	0.235(0.2)	0.002(0.005)	0.786(0.6)
Rastrigin	0.586(0.6)	0.614(0.5)	0.270(0.2)	1.046(0.7)
Salomon	0.536(0.5)	4.897(4.6)	0.932(1.2)	15.01(11.9)
Schwefel	331.4(218)	403.7(200)	280.1(112)	244.7(174)
Rosenbrock	0.795(0.8)	1.754(1.7)	0.857(0.5)	5.987(2.4)
Step	0.077(0.05)	0.079(0.05)	0.319(0.4)	1.184(1.2)
Function	bare bones PSO	Kalman filter PSO	LDS -KFPSO	SPO -UKFPSO
Ackley	9.070(5.5)	6.140(3.4)	0.665(0.3)	1.431(1.0)
Griewank	1.496(0.9)	4.652(2.3)	1.641(0.9)	1.616(0.8)
Modulus Sum	8e-7(1e-6)	0.062(0.1)	0.076(0.02)	0.067(0.02)
Rastrigin	0.334(0.3)	0.513(0.3)	0.239(0.03)	0.156(0.01)
Salomon	0.324(0.2)	2.160(2.6)	1.542(1.0)	1.560(0.9)
Schwefel	316.2(218)	367.3(214)	231.3(90)	233.4(90)
Rosenbrock	1.455(1.3)	1.190(0.4)	0.567(0.13)	0.590(0.2)
Step	0.078(0.05)	0.788(1.0)	2.294(1.08)	1.910(1.1)

Table 7.3: Comprehensive evaluation of the particle swarm optimizers applied to the chosen benchmark functions: the optimal results are shown in bold font.

Statistics	original PSO	QPSO	DRQPSO	chaotic QPSO
Error Per Function	1.9917	3.0105	1.4380	7.1051
Overall Error STD	3.2096	3.0312	2.0844	6.5266
Number of Iterations	148.85	88.29	138.01	46.31
Function Evaluation	10804	6074	10374	2994
Seconds Per Run	0.6523	0.3924	0.6813	0.1915
Statistics	bare bones PSO	Kalman filter PSO	LDS -KFPSO	SPO -UKFPSO
Error Per Function	1.8225	2.2148	1.0033	1.0466
Overall Error STD	3.2557	2.3081	0.8276	0.7569
Number of Iterations	144.96	93.02	39.65	39.92
Function Evaluation	10807	6575	2572	5054
Seconds Per Run	0.6654	0.4213	0.2905	0.3990

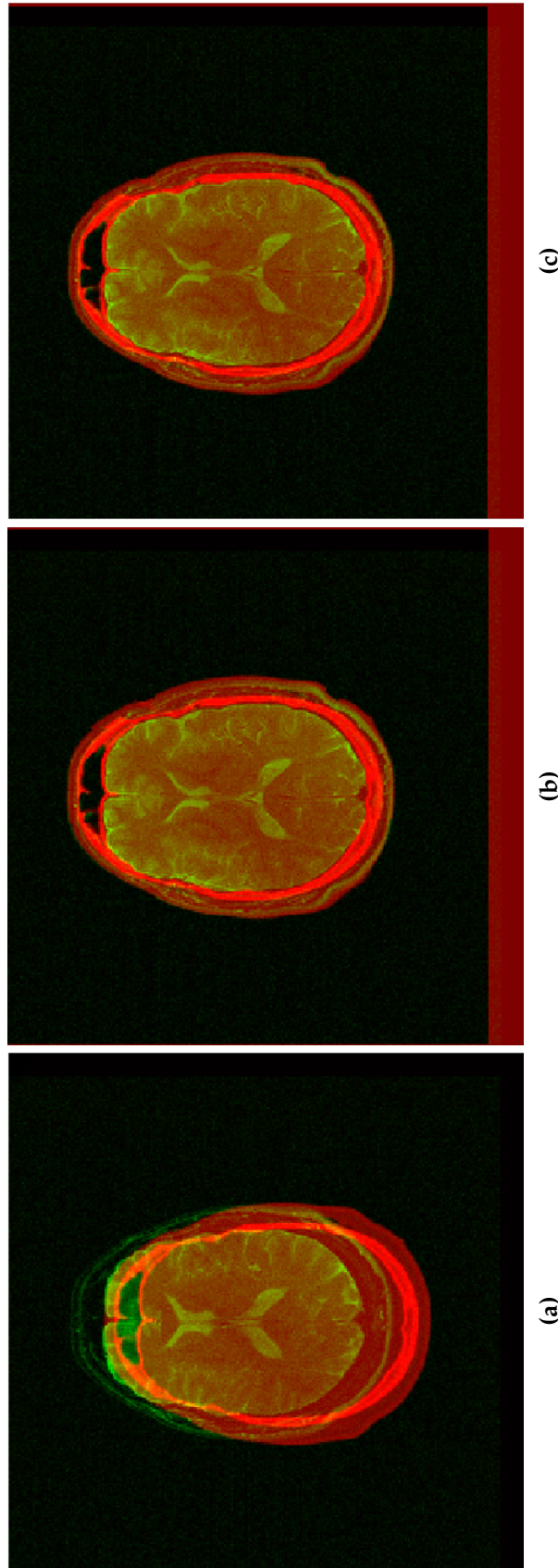


Figure 7.14: Example of the overlapped T2 weighted image and CT image from the Retrospective Image Registration Evaluation (RIRE) Project, visualized using overlapped red and green colour channels: (a) before registration; (b) after being registered; (c) after being registered using the ground truth.

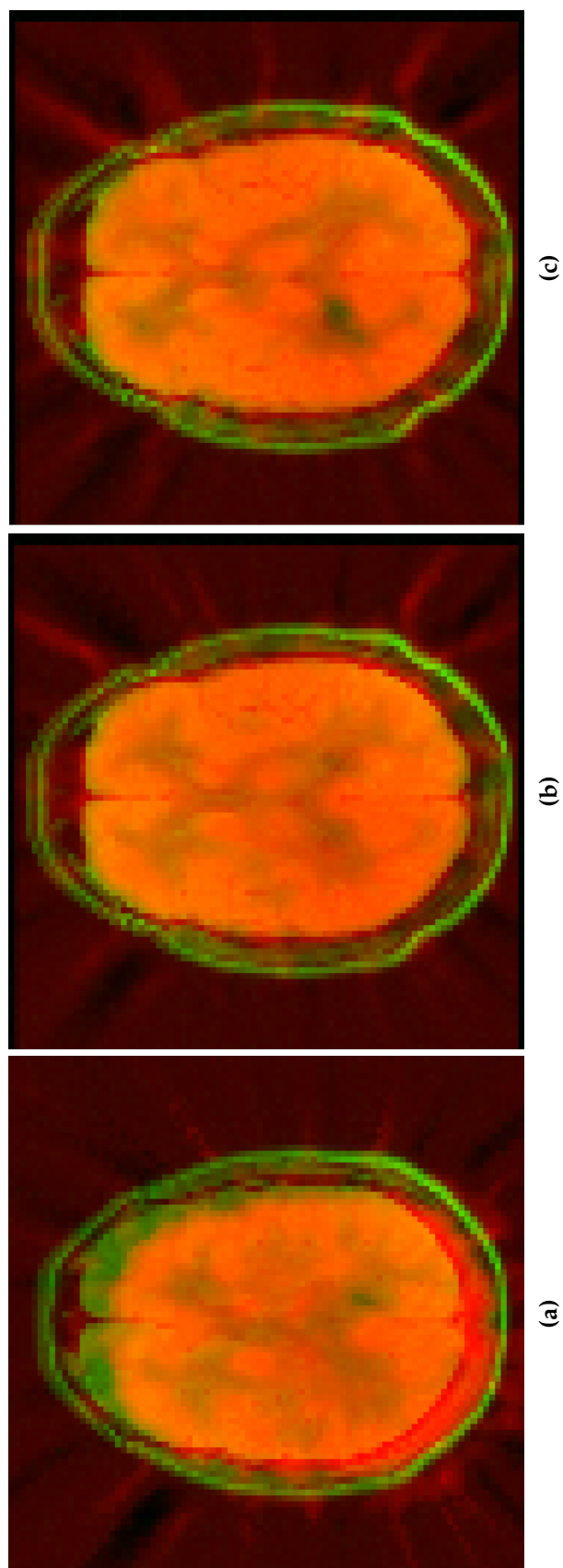


Figure 7.15: Example of the overlapped PET and MR_PD images from the Retrospective Image Registration Evaluation (RIRE) Project, visualized using overlapped red and green colour channels: (a) before registration; (b) after being registered; (c) after being registered using the ground truth.

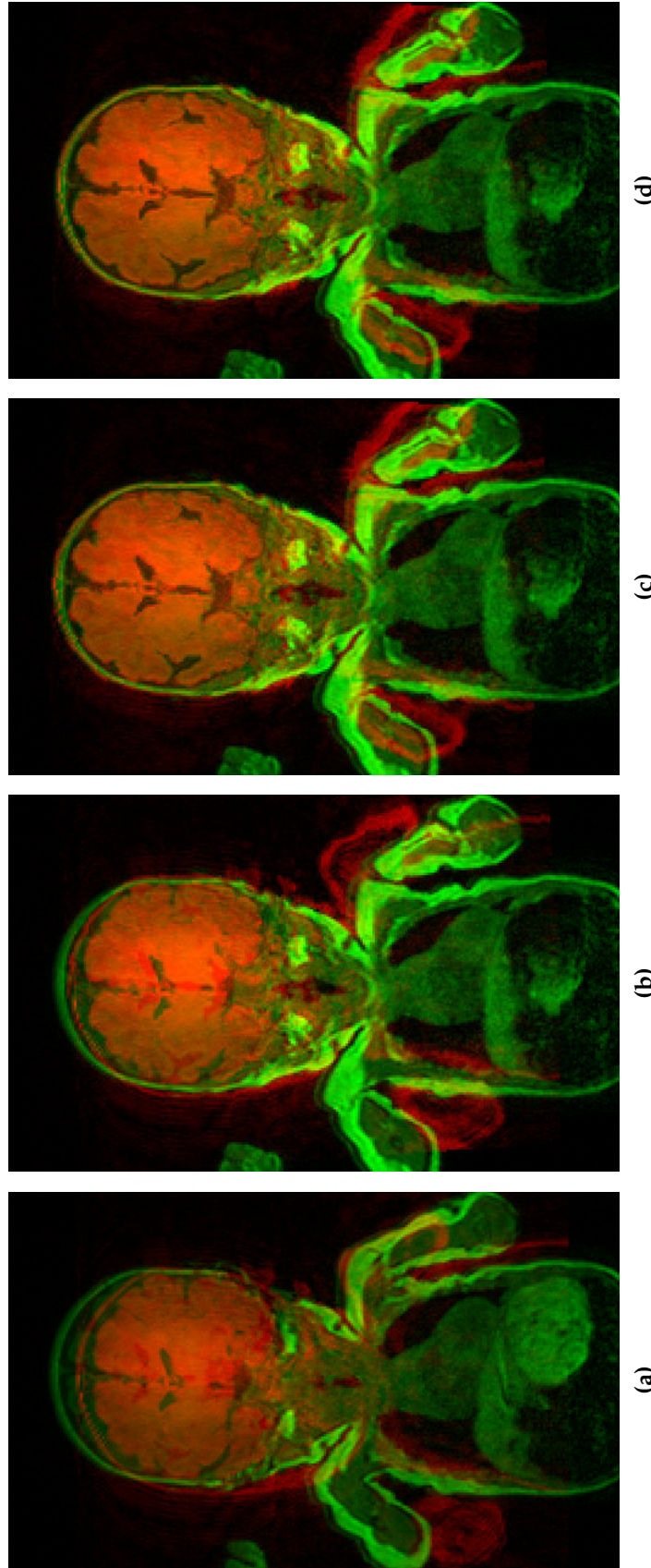


Figure 7.16: Registration results obtained using original particle swarm optimizer (PSO), the linear dynamic system Kalman filter PSO (LDS-KFPSO) and the nested unscented Kalman filter PSO (UKFPSO): (a) before registration; (b) registered using original PSO; (c) registered using LDS-KFPSO; (d) registered using nested UKFPSO. The registration is performed to align the T2 weighted dark fluid and T1 MRPAGE images of the patient (No. 2956) which makes all the registration methods tested in chapter 5 fail. The results are visualized in overlapped red and green colour channels.

Table 7.4: Comprehensive evaluation of the particle swarm optimizers applied to the Retrospective Image Registration Evaluation (RIRE) Project data using target registration errors measured in mm: best results are shown in bold font. The right column shows the average runtime measured in second.

Modality	Method	mean	median	max	STD	Run Time
CT to MR_T2	original PSO	6.2158	6.2047	10.9677	2.2740	112.33s
	DRQ -PSO	4.5297	4.4752	6.0673	0.8503	97.69s
	bare bones PSO	10.3678	12.0473	14.9192	3.6121	92.40s
	Kalman filter PSO	5.5092	5.6158	6.8900	1.0642	73.58s
	LDS -KFPSO	3.5898	3.5980	4.8410	1.0607	83.68s
	SPO -UKFPSO	1.7407	1.8617	2.7761	0.6932	135.89s
	nested -UKFPSO	1.1829	1.1718	1.7320	0.3326	138.67s
PET to MR_PD	original PSO	3.5883	3.1755	5.5919	1.0313	105.94s
	DRQ -PSO	3.9001	3.5118	6.2657	1.4400	78.12s
	bare bones PSO	3.6822	3.7254	4.1755	0.3322	106.67s
	Kalman filter PSO	6.2004	6.1185	8.2318	1.6303	59.83s
	LDS -KFPSO	3.5112	3.1472	6.2145	1.5786	78.03s
	SPO -UKFPSO	3.1409	3.1971	4.2629	0.8860	96.91s
	nested -UKFPSO	2.9810	3.0962	4.4413	1.0489	108.31s

Table 7.5: *Registration quality evaluation for CRIC Neonatal Data. Statistics of target registration errors (TRE) is measured in mm and calculated from succeeded registrations. Registrations with TRE larger than 8mm is considered as failures as they can be easily detected by visual assessments. The average run time of each registration is measured in second.*

	PSO	LDS-KFPSO	nested-UKFPSO
Average Run Time	92.48s	100.19s	144.83s
Mean	3.25	2.80	2.72
Median	1.88	1.93	1.82
Standard deviation	3.41	1.71	1.56
Number of Failures	1	0	0

7.7 Conclusion and Discussion

In this chapter, we proposed three new UKF-guided registration-oriented optimization models based on a comprehensive review of the state-of-art PSO methods in the previous chapter. The new PSO models were evaluated and compared to other methods using common benchmark functions and real medical data, and demonstrated improved convergence properties and registration accuracy in both applications.

This new type of UKF-based PSO algorithm provides an efficient mechanism to encode prior knowledge of the searching space into the optimization process. Different from other PSO methods, the proposed methods update the probabilistic distribution of the whole searching space rather than storing the distribution for each particle. Furthermore, this mechanism that updates the knowledge of the searching space can also be applied to other population based optimization methods, for example, other swarm intelligence methods.

Conclusion and Future Work

8.1 Introduction

The purpose of this PhD project is to solve image alignment problems for several ongoing clinical research projects in the Clinical Research Imaging Centre (CRIC), the University of Edinburgh (UoE). These cutting-edge clinical trials involve X-ray computed tomography (CT), multi-parametric magnetic resonance (MR) and positron emission tomography (PET) data acquired using state-of-the-art clinical scanners. The imaged objects include abdominal aortic aneurysm (AAA), heart, and brain. This thesis presents validated image registration solutions provided for three clinical trials. In this section, the academic contributions of this thesis are summarized, and the general conclusions from the registration works described in the previous chapters are made. Furthermore, suggestions for future work are presented based on considerations about the strengths and limitations of the proposed methods.

8.2 Multi-modality and Multi-parametric Registration of Clinical Data

Based on the comprehensive review study in chapter 2, a region of interest (ROI) based semi-automatic rigid registration framework is first proposed to register CT and MR AAA data for the *MA³RS* clinical trial as introduced in chapter 3. This framework is designed following the classical four-step structure with a multiresolution registration strategy. With simple user interactions, the ROI that covered the whole imaged object in a 3D coordinate system can automatically generated. Multi-modality and multi-parametric/contrast images is initially aligned using a novel topological feature and a simplified random sample census (RANSAC) method. Then the data can be registered using an asymmetric cluster-to-image registration method with mutual information (MI) calculated with my own implementation of “bottom-up” k-means clustering. The algorithm is integrated into a set of user friendly graphic user interfaces (GUIs) for registration and validation purposes, and has been applied to data collected from 445 patients. Evaluated against manual registration results, over half of the performed registrations achieved sub-voxel accuracy. The algorithm obtained better results registering anatomical and functional MR images, than registering multi-contrast MR or multi-modality CT-MR data. Positive feedbacks have been received for the invented registration software from more than four users involved in the *MA³RS* study.

The registration framework proposed in chapter 3 is then improved with wavelet image pyramid and particle swarm optimizer (PSO) to solve the cardiac MR (CMR) image alignment problem for the *IRNMAN* clinical trial which has a similar imaging protocol with the *MA³RS* project. A pre-processing step is developed to correct the image contrast distribution. Based on the comparison study presented in chapter 4, and the study specific prior knowledge discussed in chapter 5, a new parameter called

homogeneous dynamic intensity ratio (HDIR) is defined as a quantitative measure of MR imaging quality. Then intensity of the data is then corrected using a new rearranged histogram specification (RHS) method to reduce intensity inhomogeneity. This improved registration algorithm, with the new preprocessing step integrated, is evaluated against the previous registration algorithm using a similar evaluation procedure shown in chapter 3. Furthermore, multi-parametric neonatal data with manually picked landmarks is also used to compare the performance of the new registration method with several other methods. In both experiments, the new method obtained more accurate alignments and displayed better robustness to intensity inhomogeneity. The newly applied PSO also shows better alignments than the DIRECT optimizer used in the previous method. But all the compared methods failed to register a pair of multi-parametric MR images due to the obvious artefacts caused by patient motion which introduced extra local optima in the problem space.

To enhance the robustness of the optimization process to non-convex searching space introduced by common artefacts in MR data, a new type of optimizer is proposed in chapter 7. This unscented Kalman filter PSO (UKFPSO) algorithm encoded registration-oriented prior knowledge of the problem space. Three implementations of the UKFPSO model are proposed based on Bayesian probabilistic model as shown in the literature review presented in chapter 6. These three UKFPSO methods are intensively validated with widely used benchmark functions and benchmark dataset, as well as the neonatal data used in chapter 5. The performances have been compared with several selected PSO based optimizers in both function value minimization and registration experiments. The UKFPSO model achieved best performances when minimizing most benchmark functions and when registering both the benchmark and our own neonatal datasets.

To sum up, all the registration methods presented in this thesis follow an uniform analysis procedure: 1) definition 2D ROI on one slice; 2) automatic generation of ROIs on other slices of the data; 3) initial alignment using the automatic tracked ROI centres;

4) coarse level cluster-to-cluster registration; 5) fine level cluster-to-image registration. This procedure is implemented with application specific preprocessing, feature extraction, transformation, similarity measure and optimization methods. Different from most registration algorithms reviewed in chapter 2. The proposed methods encoded application- and registration-oriented prior knowledge. Evaluation results obtained with multi-modality and multi-parametric AAA, cardiac and neonatal data have shown that these prior knowledge help to achieve higher registration accuracy and better robustness to local optima in the problem space.

8.3 Strengths of This Project

This PhD project aims to solve realistic image alignment problems for several ongoing clinical research projects. Co-funded by the University of Edinburgh (UoE) and Toshiba Medical Visualization System - Europe (TMVSE), a wide range of commercial image analysis tool and various clinical data acquired from a large amount of different patients are available in this PhD project. The newly developed registration and analysis methods thus can be validated with data acquired with state-of-the-art imaging techniques, and can receive direct feedback from multiple clinical researchers. This gives strong evidence of the performance and applicability of the proposed registration methods.

The presented registration methods were designed specifically for the associated clinical research objectives. This means the more application-specific information can be integrated in the algorithms, which boost both the accuracy and robustness of the methods when applied to several specific types of registration problems. The triangulation topological feature and simplified RANSAC method are easy to implement, and can efficiently transform the imaged object which has a tubular shape to a position close to the global optimum. This effectively reduced the work load of later voxel based registration. The automatic ROI tracking method avoids intense user interactions and reliably located the imaged object, thus also reduced the size of the searching space. The HDIR provides a quantitative criterion to compare the imaging quality of MR data in terms of intensity homogeneity, and RHS shows better robustness to intensity differences than the conventional histogram specification technique when dealing with multi-modality and multi-parametric data. The UKFPSO model provides a new way to encode registration-oriented prior knowledge, thus leads to more accurate, robust and efficient registrations compared to other general-purpose optimization algorithms. The applicability of this UKFPSO model is not limited by specific application, and can be used for most rigid registration

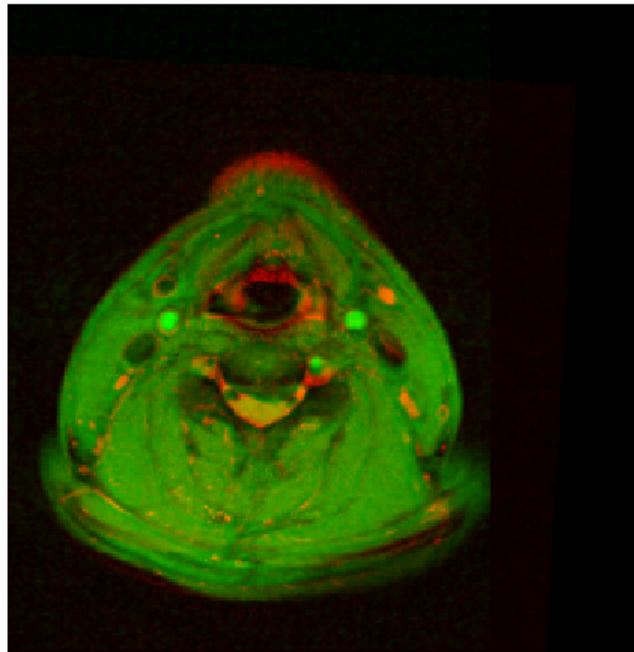


Figure 8.1: *Example of a pair of carotid images registered by the registration method presented in chapter 5 integrated in the GUIs, visualized by overlapped red and green colour channels. The GUIs and ROI tracking method are slightly modified to locate the central “frog face” structure.*

problems. Furthermore, the graphic user interfaces demonstrated in this thesis make image registration a easy work for users from different backgrounds, and can help to collect large amounts of manually obtained results. Finally the uniform ROI structure of the proposed methods, integrated in our GUIs, is applicable to a wider range of clinical data thus enables quick development of user friendly registration and validation software for a specific clinical research project. Figure 8.1 shows an example of a pair of carotid images registered by the registration method presented in chapter 5 integrated in the GUIs. The GUIs and ROI tracking method are slightly modified to locate the central “frog face” structure.

8.4 Limits and Weaknesses of This Study

Because of the integration of application-specific information, each registration method presented in this thesis has limited applicability. For example, because the involved PET data are acquired using a PET-CT clinical scanner, the methods have not been used to register multi-modality PET-MR or PET-CT data. The ROI tracking method based on circular Hough transformation (CHT), presented in chapter 3, can be only applied to generate 3D ROI for tubular structures. When registering other types of data, for example the cardiac and brain data, interpolated slices have to be introduced for robust tracking of 2D ROIs. Similarly, the preprocessing method based on HDIR and RHS lead to more accurate registration only in the case that the reference and floating images have different imaging qualities. Also, the global optimization methods presented in this thesis are most applied to transformation model with limited numbers of degrees of freedom. For complicated transformation models, global optimizations can slow down the registration or fail to converge. Furthermore, due to the requirements of the clinical research projects, all the data are only rigidly registered. Although this enabled flexible evaluation of the performances of these methods, but for non-rigid registration tasks they have not been validated.

Another obvious limit of this study is that, unless the whole scope of an image is included in the ROI, the registration process still requires user interaction. To make reasonable comparison between performances of different methods, the same piece of ROI has to been used in different registration processes because variation of ROI definition can be a possible source of the differences of performances.

Finally, due to lack of “gold standard”, the manual registration results and corrections have been used for evaluation purposes. The axis-angle representation of transformations were used as errors. Although this method has been widely used, it cannot reflect the performance of registration through one single quantity as target registration error (TRE). However, calculating TRE requires manual selection of

8.4 Limits and Weaknesses of This Study

anatomical landmarks that are well distributed on the imaged objects. This requires precise and large amounts of work from multiple clinical experts. In this study, these landmarks are only available in the neonatal data. Although calculation of TRE is possible using the benchmark datasets from *the Retrospective Image Registration Evaluation (RIRE) Project* [193], to speed up the registration experiments, only down-sampled data were registered. This makes the results presented in chapter 7 not comparable to other methods proposed by others that have been evaluated using the RIRE data.

8.5 Future Directions

Based on the limits of this study discussed above, the proposed methods can be extended in a few directions. First, transformation models that allow more numbers of degrees of freedom can be used to enable non-rigid registration. Specifically, the *IRNMAN* data were rigidly registered, but non-rigid deformation can still be found in the ECG-gated short-axis MR data. This deformation mainly happened between the neighbouring slices. In this case, with a rigid transformation model, the short-axis data cannot be well aligned at the same time. This can be visualized as shown at the bottom of figure which present an example of a pair triple-slice short axis T1 weighted (T1W) Gadolinium-enhanced CMR data registered using rigid transformation model. The simplest transformation model that can solve this problem is represented by three transformation matrices (one for each slice) where the relative shift between each slice is constraint by adding a regularization term [190], as shown at the top of Figure 8.2. Difference of the registration results obtained using single-matrix transformation model and the transformation allow more degrees of freedom can be visually detected. The more complicated transformation model leads to better alignment as it allows non-rigid deformation along just one dimension in the problem space. In the future, the registration methods can be evaluated for non-rigid registration applications by using different non-rigid deformation models.

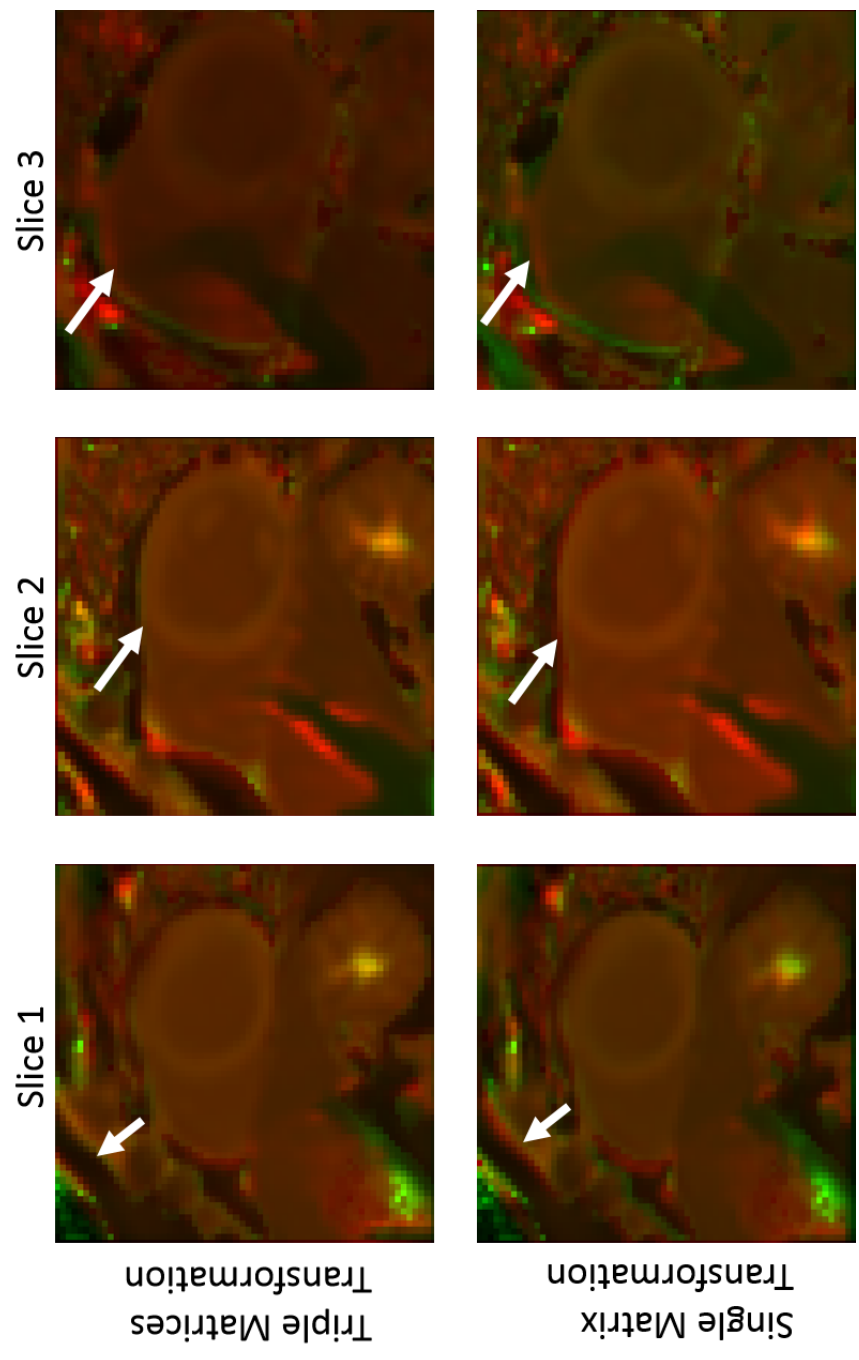


Figure 8.2: Example of registration results of a triple-slice short-axis T1 weighted (T1W) CMR data, visualized by overlapped red and green colour channels: the results obtained using single transformation matrix is at the bottom, and the results obtained using the triple matrices transformation model is shown at the top. The white arrows point to the visual clues that indicate the difference between the registration results.

Second, considering registration as a machine learning problem, a recently new direction of improving the robustness and speed of registration is to use supervised learning. For example, registration methods based on neural networks have been proposed recently [323, 324, 325]. All the methods proposed in this thesis can be classified as unsupervised learning as there is no ground truth registration results which is required by the “training” process of supervised learning. However, after applied my registration methods to the clinical research projects during this PhD project, a large amount of manual registration results have been provided by multiple clinical experts. This provides abundant materials for the development of my future supervised learning based similarity measures. Application-specific information can be encoded in these new similarity measures which will be compared with the recently proposed learning-based measures, such as Kullback-Leibler divergence (KLD) [156] and weighted MI [158]. Furthermore, although the ground truth of registration results is hard to collect in some applications, a number of benchmark image segmentation datasets are available for different imaged objects. For non-rigid registration, a commonly used evaluation criteria is the overlapping rate of the segmentation of the imaged objects. Based on supervised learning theory, this indicate a new type of learning-based methods which use segmentation ground truths in the training stage of registration algorithms.

Supervised learning technique is also a potential solution for fully automatic registrations. As presented in chapter 3, I use shape features for automatic tracking of aorta after it is manually located at the beginning of registration. Using supervised learning, I can develop object recognition algorithms which can detect the targeted object within the image, and thus user interactions can be completely avoid. An example of potential object detection solution is the face recognition algorithm proposed by Viola and Jones [326]. Different features can be used in this process. Following these directions, the future registration algorithms should be more intelligent without losing effectiveness and efficiency, thus labour of clinicians can be

8.5 Future Directions

relieved from unnecessary image analysis works.

Bibliography

- [1] D C Lee and T J Carroll. Magnetic resonance imaging. *Practical Signal and Image Processing in Clinical Cardiology*, pages 251–273, 2010.
- [2] R Szeliski. Image alignment and stitching: A tutorial. *Foundations and Trends in Computer Graphics and Vision*, 2(1):1–104, 2006.
- [3] Jennifer MJ Richards, Scott I Semple, Thomas J MacGillivray, Calum Gray, Jeremy P Langrish, Michelle Williams, Marc Dweck, William Wallace, Graham McKillop, Roderick TA Chalmers, et al. Abdominal aortic aneurysm growth predicted by uptake of ultrasmall superparamagnetic particles of iron oxideclinical perspective a pilot study. *Circulation: Cardiovascular Imaging*, 4(3): 274–281, 2011.
- [4] Clay Robert Hinrichs and Great Vessels. *Clinical Cardiac MRI*. Secaucus, NJ, 2005.
- [5] Boubakeur Belaroussi, Julien Milles, Sabin Carne, Yue Min Zhu, and Hugues Benoit-Cattin. Intensity non-uniformity correction in MRI: existing methods and their validation. *Medical image analysis*, 10(2):234–46, April 2006. ISSN 1361-8415. doi: 10.1016/j.media.2005.09.004. URL <http://www.ncbi.nlm.nih.gov/pubmed/16307900>.
- [6] J G Sled, a P Zijdenbos, and a C Evans. A nonparametric method for automatic correction of intensity nonuniformity in MRI data. *IEEE transactions on medical imaging*, 17(1):87–97, February 1998. ISSN 0278-0062. doi: 10.1109/42.668698. URL <http://www.ncbi.nlm.nih.gov/pubmed/9617910>.

- [7] Karl J Friston, John T Ashburner, Stefan J Kiebel, Thomas E Nichols, and William D Penny. *Statistical Parametric Mapping: The Analysis of Functional Brain Images: The Analysis of Functional Brain Images*. Academic Press, 2011.
- [8] Christopher K Monson and Kevin D Seppi. Bayesian optimization models for particle swarms. In *Proceedings of the 7th annual conference on Genetic and evolutionary computation*, pages 193–200. ACM, 2005.
- [9] D Mietchen, M Aberhan, B Manz, O Hampe, B Mohr, C Neumann, and F Volke. Three-dimensional magnetic resonance imaging of fossils across taxa. *Biogeosciences*, 5:25–41, 2008.
- [10] Y Wu, D A Chesler, M J Glimcher, L Garrido, J Wang, H J Jiang, and J L Ackerman. Multinuclear solid-state three-dimensional MRI of bone and synthetic calcium phosphates. *Proceedings of the National Academy of Sciences*, 96(4):1574, 1999.
- [11] E D Allen, S E Byrd, C F Darling, T Tomita, and M A Wilczynski. The clinical and radiological evaluation of primary brain neoplasms in children, Part II: Radiological evaluation. *Journal of the National Medical Association*, 85(7):546, 1993.
- [12] M D F Deck, C Henschke, B C P Lee, R D Zimmerman, R A Hyman, J Edwards, L A Saint Louis, P T Cahill, H Stein, and J P Whalen. Computed tomography versus magnetic resonance imaging of the brain a collaborative interinstitutional study. *Clinical Imaging*, 13(1):2–15, 1989.
- [13] European Commission. Radiation protection 118: referral guidelines for imaging. *Luxemburg: Office for Official Publications of the European Communities*, 2001. URL <http://europa.eu.int/comm/environment/radprot/118/rp-118-en.pdf>.

-
- [14] H Sakuma. Coronary CT versus MR angiography: the role of MR angiography. *Radiology*, 258(2):340–349, 2011.
- [15] M R Prince and J F M Meaney. Expanding role of MR angiography in clinical practice. *European Radiology Supplements*, 16:3–8, 2006.
- [16] A de Roos. Myocardial Perfusion Imaging with Multidetector CT: Beyond Lumenography¹. *Radiology*, 254(2):321–323, 2010.
- [17] W A Kalender. X-ray computed tomography. *Physics in medicine and biology*, 51: R29, 2006.
- [18] D W McRobbie, E A Moore, and M J Graves. *MRI from Picture to Proton*. Cambridge Univ Pr, 2007.
- [19] L J Erasmus, D Hurter, M Naudé, H G Kritzing, and S Acho. A short overview of MRI artefacts. *South African Journal of Radiology*, 8(2), 2009.
- [20] D L Hill, P G Batchelor, M Holden, and D J Hawkes. Medical image registration. *Physics in medicine and biology*, 46(3):R1—45, March 2001. ISSN 0031-9155. URL <http://www.ncbi.nlm.nih.gov/pubmed/11277237>.
- [21] Graeme P Penney, Jürgen Weese, John A Little, Paul Desmedt, Derek LG Hill, et al. A comparison of similarity measures for use in 2-D-3-D medical image registration. *IEEE transactions on medical imaging*, 17(4):586–595, 1998.
- [22] J N Ulysses. Measuring Similarity in Medical Registration. *Image Processing*, 2010.
- [23] Bernd Fischer and Jan Modersitzki. Ill-posed medicine—an introduction to image registration. *Inverse Problems*, 24(3):034008, June 2008. ISSN 0266-5611. doi: 10.1088/0266-5611/24/3/034008.

- [24] Ramtin Shams, Parastoo Sadeghi, and R Kennedy. A survey of medical image registration on multicore and the GPU. *Signal Processing*, 27(March):50–60, 2010. URL http://ieeexplore.ieee.org/xpls/abs_all.jsp?arnumber=5438962.
- [25] S Damas, O Cordon, and J Santamaria. Medical Image Registration Using Evolutionary Computation: An Experimental Survey. *Computational Intelligence Magazine, IEEE*, 6(4):26–42, 2011.
- [26] Milan Sonka and J Michael Fitzpatrick. Handbook of medical imaging (volume 2, medical image processing and analysis). SPIE- The international society for optical engineering, 2000.
- [27] Barbara Zitová and Jan Flusser. Image registration methods: a survey. *Image and Vision Computing*, 21(11):977–1000, October 2003. ISSN 02628856. doi: 10.1016/S0262-8856(03)00137-9. URL <http://linkinghub.elsevier.com/retrieve/pii/S0262885603001379>.
- [28] Russ C Eberhart and James Kennedy. A new optimizer using particle swarm theory. In *Proceedings of the sixth international symposium on micro machine and human science*, volume 1, pages 39–43. New York, NY, 1995.
- [29] Zhi-Hui Zhan, Jun Zhang, Yun Li, and Henry Shu-Hung Chung. Adaptive particle swarm optimization. *Systems, Man, and Cybernetics, Part B: Cybernetics, IEEE Transactions on*, 39(6):1362–1381, 2009.
- [30] JV Hajnal and DLG Hill. *Medical image registration*. CRC Press, 2010, 2010. ISBN 0849300649. URL <http://medcontent.metapress.com/index/A65RM03P4874243N.pdf><http://books.google.com/books?hl=en&lr=&id=2dtQNsk-qBQC&oi=fnd&pg=PP1&dq=Medical+Image+Registration&ots=f7FvNiDse3&sig=E7xI3P8g5zycA8bUrDhnt6BWjGI>http://books.google.com/books?hl=en&lr=&id=2dtQNsk-qBQC&oi=fnd&pg=PP1&dq=Medical+image+registration&ots=f7FvNiDuj3&sig=Nsu1P5wwTTMK0E-o4Lg94_Oo1CY.

-
- [31] Yasmina Chenoune, Yasmina Bouaoune, Eric Delechelle, Eric Petit, Jerome Garot, and Alain Rahmouni. MR/CT multimodal registration of short-axis slices in CT volumes. In *2007 29th Annual International Conference of the IEEE Engineering in Medicine and Biology Society*, pages 4496–4499. IEEE, 2007.
- [32] B Likar, M A Viergever, and F Pernus. Retrospective correction of MR intensity inhomogeneity by information minimization. *Medical Imaging, IEEE Transactions on*, 20(12):1398–1410, 2001.
- [33] G T Herman. *Fundamentals of Computerized Tomography: Image Reconstruction from Projections*. Springer Verlag, 2009.
- [34] IA Cunningham. Handbook of medical imaging. *Physics and Psychophysics (SPIE, 2000)*, pages 675–710, 2000. URL <http://scholar.google.com/scholar?hl=en&btnG=Search&q=intitle:Handbook+of+Medical+Imaging#6>.
- [35] Matt A Bernstein, Kevin F King, and Xiaohong Joe Zhou. *Handbook of MRI pulse sequences*. Elsevier, 2004.
- [36] R H Hashemi, W G Bradley, and C J Lisanti. *MRI: the basics*. Lippincott Williams & Wilkins, 2010.
- [37] A C Kak and M Slaney. Principles of Computerized Tomographic Imaging. *Engineering*, 33(1):327, 1988. ISSN 00942405. doi: 10.1118/1.1455742. URL http://www.osti.gov/energycitations/product.biblio.jsp?osti_id=5813672.
- [38] M C Williams, J H Reid, G McKillop, N W Weir, E J R van Beek, N G Uren, and D E Newby. Cardiac and coronary CT comprehensive imaging approach in the assessment of coronary heart disease. *Heart (British Cardiac Society)*, 97(15):1198–1205, August 2011. ISSN 1468-201X. doi: 10.1136/heartjnl-2011-300037. URL <http://www.ncbi.nlm.nih.gov/pubmed/21742616>.

Bibliography

- [39] W R Hendee and C J Morgan. Magnetic Resonance Imaging Part I-Physical Principles. *Western Journal of Medicine*, 141(4):491, 1984.
- [40] R K Dortzbach, J W Kronish, and L R Gentry. Magnetic Resonance Imaging of the Orbit: Part I. Physical Principles. *Ophthalmic Plastic & Reconstructive Surgery*, 5(3):151, 1989.
- [41] John P Ridgway. Cardiovascular magnetic resonance physics for clinicians: part i. *J Cardiovasc Magn Reson*, 12(1):71, 2010.
- [42] LJ Anderson, S Holden, B Davis, E Prescott, CC Charrier, NH Bunce, DN Firmin, B Wonke, J Porter, JM Walker, et al. Cardiovascular T2-star (T2*) magnetic resonance for the early diagnosis of myocardial iron overload. *European heart journal*, 22(23):2171–2179, 2001.
- [43] Jintong Mao, Hong Yan, WW Brey, WD Bidgood, JJ Steinbach, and A Mancuso. Fat tissue and fat suppression. *Magnetic resonance imaging*, 11(3):385–393, 1993.
- [44] N Strumas, O Antonyshyn, M J Yaffe, G Mawdsley, and P Cooper. Computed tomography artefacts: An experimental investigation of causative factors. *Canadian Journal of Plastic Surgery*, 6:23–29, 1998.
- [45] A C Gordon, J Branson, C Simmons, K A Berland, D S Willsey, A L Andrews, and Others. Over-utilization of MRI in the osteoarthritis patient. In *AAOS meeting*, page P145, 2008.
- [46] JB Maintz. A survey of medical image registration. *Medical image analysis*, 2(1):1–36, 1998. URL [http://www.sciencedirect.com/science/article/pii/S1361-8415\(01\)80026-8](http://www.sciencedirect.com/science/article/pii/S1361-8415(01)80026-8).
- [47] L G Brown. A survey of image registration techniques. *ACM computing surveys (CSUR)*, 1992. URL <http://dl.acm.org/citation.cfm?id=146374>.

- [48] J Salvi, C Matabosch, D Fofi, and J Forest. A review of recent range image registration methods with accuracy evaluation. *Image and Vision Computing*, 25(5):578–596, 2007.
- [49] M V Wyawahare, P M Patil, and H K Abhyankar. Image registration techniques: an overview. *International Journal of Signal Processing, Image Processing and Pattern Recognition*, 2(3):1–5, 2009.
- [50] MP Deshmukh. A Survey OF Image Registration. *International Journal of Image Processing (IJIP)*, 4(5):245–269, 2011. URL <http://www.cscjournals.org/csc/manuscriptinfo.php?ManuscriptCode=71.72.71.78.43.49.52.50.100>.
- [51] D J Hawkes. Algorithms for radiological image registration and their clinical application. *Journal of anatomy*, 193(3):347–361, 1998.
- [52] H Lester and S R Arridge. A survey of hierarchical non-linear medical image registration. *Pattern recognition*, 32(1):129–149, 1999.
- [53] Gary E Christensen, Xiujuan Geng, Jon G Kuhl, Joel Bruss, Thomas J Grabowski, Imran A Pirwani, Michael W Vannier, John S Allen, and Hanna Damasio. Introduction to the non-rigid image registration evaluation project. *Biomedical Image Registration*, 4057:128–135, 2006. doi: 10.1007/11784012. URL <http://www.springerlink.com/index/10.1007/11784012>.
- [54] Piotr J Slomka and Richard P Baum. Multimodality image registration with software: state-of-the-art. *European journal of nuclear medicine and molecular imaging*, 36 Suppl 1:S44—55, March 2009. ISSN 1619-7089. doi: 10.1007/s00259-008-0941-8. URL <http://www.ncbi.nlm.nih.gov/pubmed/19104803>.
- [55] Timo Mäkelä, Patrick Clarysse, Outi Sipilä, Nicoleta Pauna, Quoc Cuong Pham, Toivo Katila, and Isabelle E Magnin. A review of cardiac image registration methods. *IEEE transactions on medical imaging*, 21(9):1011–21, September 2002.

- ISSN 0278-0062. doi: 10.1109/TMI.2002.804441. URL <http://www.ncbi.nlm.nih.gov/pubmed/12564869>.
- [56] P J Kostelec and S Periaswamy. Image registration for MRI. *Modern signal processing*, 46:161–184, 2003.
- [57] A Collignon, F Maes, and D Delaere. Automated multi-modality image registration based on information theory. *Information*, 3:264–274, 1995. doi: 10.1007/11784012_16. URL <http://scholar.google.com/scholar?hl=en&btnG=Search&q=intitle:AUTOMATED+MULTI-MODALITY+IMAGE+REGISTRATION+BASED+ON+INFORMATION+THEORY#0>.
- [58] C J Dean, J R Sykes, R a Cooper, P Hatfield, B Carey, S Swift, S E Bacon, D Thwaites, D Sebag-Montefiore, and a M Morgan. An evaluation of four CT-MRI co-registration techniques for radiotherapy treatment planning of prone rectal cancer patients. *The British journal of radiology*, 85(1009):61–68, January 2012. ISSN 1748-880X. doi: 10.1259/bjr/11855927. URL <http://www.ncbi.nlm.nih.gov/pubmed/22190750>.
- [59] G L Sannazzari, R Ragona, M G R Redda, F R Giglioli, G Isolato, and A Guarneri. CT-MRI image fusion for delineation of volumes in three-dimensional conformal radiation therapy in the treatment of localized prostate cancer. *British journal of radiology*, 75(895):603–607, 2002.
- [60] C Rasch, I Barillot, P Remeijer, A Touw, M van Herk, and J V Lebesque. Definition of the prostate in CT and MRI: a multi-observer study. *International Journal of Radiation Oncology* Biology* Physics*, 43(1):57–66, 1999.
- [61] K Kagawa, W R Lee, T E Schultheiss, M A Hunt, A H Shaer, and G E Hanks. Initial clinical assessment of CT-MRI image fusion software in localization of the prostate for 3D conformal radiation therapy. *International Journal of Radiation Oncology* Biology* Physics*, 38(2):319–325, 1997.

-
- [62] PD Kotsas. A Review of Methods for 2D/3D Registration. *World Academy of Science, Engineering and Technology*, pages 606–609, 2011. URL http://www.orth.gr/UsersFiles/WASET_v59-117.pdf.
- [63] P A den Elsen, E J D Pol, and M A Viergever. Medical image matching-a review with classification. *Engineering in Medicine and Biology Magazine, IEEE*, 12(1): 26–39, 1993.
- [64] L Chmielewski and D Kozinska. Image registration. In *Proceedings of the 3rd Polish Conference on Computer Pattern Recognition Systems. MiBk{ó}w (Poland): KOSYR*, pages 163–168, 2003.
- [65] W Rui and L Minglu. An overview of medical image registration. In *Computational Intelligence and Multimedia Applications, 2003. ICCIMA 2003. Proceedings. Fifth International Conference on*, pages 385–390. IEEE, 2003.
- [66] Sigurd Angenent, Eric Pichon, and Allen Tannenbaum. Mathematical methods in medical image processing. *Bulletin of the American Mathematical Society*, 43 (03):365–397, April 2006. ISSN 0273-0979. doi: 10.1090/S0273-0979-06-01104-9. URL <http://www.ams.org/journal-getitem?pii=S0273-0979-06-01104-9>.
- [67] O Péria, L Chevalier, A François-Joubert, J P Caravel, S Dalsoglio, S Lavallée, and P Cinquin. Using a 3D position sensor for registration of SPECT and US images of the kidney. In *Computer vision, virtual reality and robotics in medicine*, pages 23–29. Springer, 1995.
- [68] H Erbe, A Kriete, A Jödicke, W Deinsberger, and D K Böker. 3D-ultrasonography and image matching for detection of brain shift during intracranial surgery. In *Computer assisted radiology*, volume 1124, pages 225–230, 1996.

Bibliography

- [69] P Potamianos, B L Davies, and R D Hibberd. Intra-operative registration for percutaneous surgery. In *Proc. Second Int. Symposium on Medical Robotics and Computer Assisted Surgery*, pages 156–164, 1995.
- [70] S Lavallee and Others. Registration for computer-integrated surgery: methodology, state of the art. *Computer Integrated Surgery*, 5:77–97, 1996.
- [71] D Vandermeulen. Methods for registration, interpolation and interpretation of three-dimensional medical image data for use in 3-D display, 3-D modeling and therapy planning. *status: published*, 1991.
- [72] L Lemieux, N D Kitchen, S W Hughes, and D G T Thomas. Voxel-based localization in frame-based and frameless stereotaxy and its accuracy. *Medical physics*, 21:1301, 1994.
- [73] L Lemieux and R Jagoe. Effect of fiducial marker localization on stereotactic target coordinate calculation in CT slices and radiographs. *Physics in medicine and biology*, 39:1915, 1994.
- [74] S C Strother, J R Anderson, X L Xu, J S Liow, D C Bonar, D A Rottenberg, and Others. Quantitative comparisons of image registration techniques based on high-resolution MRI of the brain. *Journal of computer assisted tomography*, 18(6): 954, 1994.
- [75] T S SUMANAWEEERA, S NAPEL, J DRACE, and J R ADLER. A quantitative comparison of residual error for three different multimodality registration techniques. In *Information processing in medical imaging*, volume 3, page 251. Springer, 1995.
- [76] D.V.A.C.J. Michieis and H B P Suetens. Multi-modality image registration within COVIRA. *Medical imaging: analysis of multimodality 2D/3D images*, 19: 29, 1995.

-
- [77] T Peters, B Davey, P Munger, R Comeau, A Evans, and A Olivier. Three-dimensional multimodal image-guidance for neurosurgery. *Medical Imaging, IEEE Transactions on*, 15(2):121–128, 1996.
- [78] C R Maurer Jr, R J Maciunas, and J M Fitzpatrick. Registration of head CT images to physical space using a weighted combination of points and surfaces [image-guided surgery]. *Medical Imaging, IEEE Transactions on*, 17(5):753–761, 1998.
- [79] R Ellis, S TOKSVIG-LARSEN, M Marcacci, D Caramella, and M Fadda. Use of a biocompatible fiducial marker in evaluating the accuracy of computed tomography image registration. *Investigative radiology*, 31(10):658, 1996.
- [80] M Y Wang, C R Maurer Jr, J M Fitzpatrick, and R J Maciunas. An automatic technique for finding and localizing externally attached markers in CT and MR volume images of the head. *Biomedical Engineering, IEEE Transactions on*, 43(6):627–637, 1996.
- [81] C R Maurer Jr, G B Aboutanos, B M Dawant, S Gadamsetty, R A Margolin, R J Maciunas, and J M Fitzpatrick. Technical note. Effect of geometrical distortion correction in MR on image registration accuracy. *Journal of computer assisted tomography*, 20(4):666, 1996.
- [82] L R Schad, R Boesecke, W Schlegel, G H Hartmann, V Sturm, L G Strauss, W J Lorenz, and Others. Three dimensional image correlation of CT, MR, and PET studies in radiotherapy treatment planning of brain tumors. *Journal of computer assisted tomography*, 11(6):948, 1987.
- [83] David J Hawkes, Derek LG Hill, and Emma CML Bracey. Multi-modal data fusion to combine anatomical and physiological information in the head and heart. In *Cardiovascular nuclear medicine and MRI*, pages 113–130. Springer, 1992.

Bibliography

- [84] R T Malison, E G Miller, R Greene, G McCarthy, D S Charney, R B Innis, and Others. Computer-assisted coregistration of multislice SPECT and MR brain images by fixed external fiducials. *Journal of computer assisted tomography*, 17(6): 952, 1993.
- [85] R L Wahl, L E Quint, R D Cieslak, A M Aisen, R A Koeppe, C R Meyer, and Others. "Anatomometabolic" tumor imaging: fusion of FDG PET with CT or MRI to localize foci of increased activity. *Journal of nuclear medicine: official publication, Society of Nuclear Medicine*, 34(7):1190, 1993.
- [86] M Y Wang, J M Fitzpatrick, and C R Maurer Jr. Design of fiducials for accurate registration of CT and MR volume images. In *Proceedings of SPIE*, volume 2434, page 96, 1995.
- [87] D L G Hill, D J Hawkes, J E Crossman, M J Gleeson, T C S Cox, E Brace, A J Strong, and P Graves. Registration of MR and CT images for skull base surgery using point-like anatomical features. *British journal of radiology*, 64(767):1030–1035, 1991.
- [88] A C Evans, S Marrett, J Torrescorzo, S Ku, and L Collins. MRI-PET correlation in three dimensions using a volume-of-interest (VOI) atlas. *Journal of Cerebral Blood Flow & Metabolism*, 11:A69—A78, 1991.
- [89] G Q Maguire Jr, M E Noz, H Rusinek, J Jaeger, E L Kramer, J J Sanger, and G Smith. Graphics applied to medical image registration. *Computer Graphics and Applications, IEEE*, 11(2):20–28, 1991.
- [90] C J Henri, A Cukiert, D L Collins, A Olivier, and T M Peters. Toward frameless stereotaxy: Anatomical-vascular correlation and registration. In *Proceedings of SPIE*, volume 214, 1808.
- [91] P Neelin, J Crossman, D J Hawkes, Y Ma, and A C Evans. Validation of an MRI/PET landmark registration method using 3D simulated PET images and

- point simulations. *Computerized medical imaging and graphics*, 17(4-5):351–356, 1993.
- [92] Y Ge, J M Fitzpatrick, J R Votaw, S Gadamssetty, R J Maciunas, R M Kessler, R A Margolin, and Others. Retrospective registration of PET and MR brain images: an algorithm and its stereotactic validation. *Journal of computer assisted tomography*, 18(5):800, 1994.
- [93] U Pietrzyk, G F KarlHerholz, and R M AndreasJacobs. Image Registration: Validation for PET, SPECT, MRI and CT Brain Studies. 1994.
- [94] M van Herk and H M Kooy. Automatic three-dimensional correlation of CT-CT, CT-MRI, and CT-SPECT using chamfer matching. *Medical physics*, 21:1163, 1994.
- [95] A M Scott, H A Macapinlac, C R Divgi, J J Zhang, H Kalaigian, K Pentlow, S Hilton, M C Graham, G Sgouros, C Pelizzari, and Others. Clinical validation of SPECT and CT/MRI image registration in radiolabeled monoclonal antibody studies of colorectal carcinoma. *Journal of nuclear medicine: official publication, Society of Nuclear Medicine*, 35(12):1976, 1994.
- [96] B A Ardekani, M Braun, B F Hutton, I Kanno, H Iida, and Others. A fully automatic multimodality image registration algorithm. *Journal of computer assisted tomography*, 19(4):615, 1995.
- [97] C A Pelizzari, G T Chen, D R Spelbring, R R Weichselbaum, C T Chen, and Others. Accurate three-dimensional registration of CT, PET, and/or MR images of the brain. *Journal of computer assisted tomography*, 13(1):20, 1989.
- [98] D MacDonald, D Avis, and A C Evans. Multiple surface identification and matching in magnetic resonance images. In *Proceedings of SPIE*, volume 2359, page 160, 1994.

- [99] G. Borgefors. Hierarchical chamfer matching: a parametric edge matching algorithm. *IEEE Transactions on Pattern Analysis and Machine Intelligence*, 10(6): 849–865, 1988. ISSN 01628828. doi: 10.1109/34.9107. URL <http://ieeexplore.ieee.org/lpdocs/epic03/wrapper.htm?arnumber=9107>.
- [100] O Cuisenaire, J P Thiran, B Macq, C Michel, A De Volder, and F Marques. Automatic registration of 3D MR images with a computerized brain atlas. *Medical imaging*, 2710:438–448, 1996.
- [101] G J Wang, N D Volkow, A V Levy, J S Fowler, J Logan, D Alexoff, R J Hitzemann, and D J Schyler. MR-PET image coregistration for quantitation of striatal dopamine D2 receptors. *Journal of computer assisted tomography*, 20(3):423, 1996.
- [102] M Berger and M Cole. *Geometry*, volume 1. Springer Verlag, 1987.
- [103] T S Huang, S D Blostein, and E A Margerum. Least-squares estimation of motion parameters from 3-D point correspondences. In *Proc. IEEE Conf. Computer Vision and Pattern Recognition*, pages 198–201, 1986.
- [104] M R Kaus, K K Brock, V Pekar, L A Dawson, A M Nichol, and D A Jaffray. Assessment of a model-based deformable image registration approach for radiation therapy planning. *International Journal of Radiation Oncology* Biology* Physics*, 68(2):572–580, 2007.
- [105] L Zagorchev and A Goshtasby. A comparative study of transformation functions for nonrigid image registration. *Image Processing, IEEE Transactions on*, 15(3):529–538, 2006.
- [106] Joseph V Hajnal. *Medical image registration*. CRC PressI Llc, 2001.
- [107] A Goshtasby. Image registration by local approximation methods. *Image and Vision Computing*, 6(4):255–261, 1988.

-
- [108] A Goshtasby. Piecewise linear mapping functions for image registration. *Pattern Recognition*, 19(6):459–466, 1986.
- [109] R Wiemker, K Rohr, L Binder, R Sprengel, and H S Stiehl. Application of elastic registration to imagery from airborne scanners. *International Archives of Photogrammetry and Remote Sensing*, 31:949–954, 1996.
- [110] J A Little, D L G Hill, and D J Hawkes. Deformations incorporating rigid structures [medical imaging]. In *Mathematical Methods in Biomedical Image Analysis, 1996., Proceedings of the Workshop on*, pages 104–113. IEEE, 1996.
- [111] M Fornefett, K Rohr, and H S Stiehl. Radial basis functions with compact support for elastic registration of medical images. *Image and Vision Computing*, 19(1):87–96, 2001.
- [112] G Wahba. *Spline models for observational data*, volume 59. Society for Industrial Mathematics, 1990.
- [113] R L Harder and R N Desmarais. Interpolation using surface splines. *Journal of Aircraft*, 9(2):189–191, 1972.
- [114] J Meinguet. An intrinsic approach to multivariate spline interpolation at arbitrary points. 1978.
- [115] M D Buhmann. Multivariate cardinal interpolation with radial-basis functions. *Constructive Approximation*, 6(3):225–255, 1990.
- [116] R Franke. Scattered data interpolation: tests of some methods. *Math. Comput.*, 38(157):181–200, 1982.
- [117] M R Kaus and K K Brock. Deformable Image Registration for radiation therapy planning: Algorithms and Applications. *Biomechanical Systems Technology*, 1:1–28, 2009.

- [118] F L Bookstein. Principal warps: Thin-plate splines and the decomposition of deformations. *Pattern Analysis and Machine Intelligence, IEEE Transactions on*, 11(6):567–585, 1989.
- [119] K Rohr, H S Stiehl, R Sprengel, T M Buzug, J Weese, and M H Kuhn. Landmark-based elastic registration using approximating thin-plate splines. *Medical Imaging, IEEE Transactions on*, 20(6):526–534, 2001.
- [120] K Rohr. Elastic registration of multimodal medical images: A survey. *KI*, 14(3): 11–17, 2000.
- [121] K Rohr. *Landmark-based image analysis: using geometric and intensity models*, volume 21. Springer, 2001.
- [122] E V Shikin and A I Plis. *Handbook on Splines for the User*. CRC, 1995.
- [123] M H Davis, A Khotanzad, D P Flamig, and S E Harms. Elastic body splines: A physics based approach to coordinate transformation in medical image matching. In *Computer-Based Medical Systems, 1995., Proceedings of the Eighth IEEE Symposium on*, pages 81–88. IEEE, 1995.
- [124] H Wendland. Piecewise polynomial, positive definite and compactly supported radial functions of minimal degree. *Advances in computational Mathematics*, 4(1): 389–396, 1995.
- [125] R Bajcsy and S Kovačič. Multiresolution elastic matching. *Computer vision, graphics, and image processing*, 46(1):1–21, 1989.
- [126] M Bro-Nielsen and C Gramkow. Fast fluid registration of medical images. In *Visualization in Biomedical Computing*, pages 265–276. Springer, 1996.
- [127] G Wollny and F Kruggel. Computational cost of nonrigid registration algorithms based on fluid dynamics [mri time series application]. *Medical Imaging, IEEE Transactions on*, 21(8):946–952, 2002.

-
- [128] J P Thirion. Image matching as a diffusion process: an analogy with Maxwell's demons. *Medical image analysis*, 2(3):243–260, 1998.
- [129] S S Beauchemin and J L Barron. The computation of optical flow. *ACM Computing Surveys (CSUR)*, 27(3):433–466, 1995.
- [130] B D Lucas and T Kanade. An iterative image registration technique with an application to stereo vision. In *Proceedings of the 7th international joint conference on Artificial intelligence*, 1981.
- [131] B K P Horn and B G Schunck. Determining optical flow. *Artificial intelligence*, 17(1-3):185–203, 1981.
- [132] G W Humphreys and V Bruce. *Visual cognition: Computational, experimental, and neuropsychological perspectives*. Lawrence Erlbaum Associates, Inc, 1989.
- [133] S X Ju, M J Black, and A D Jepson. Skin and bones: Multi-layer, locally affine, optical flow and regularization with transparency. In *Computer Vision and Pattern Recognition, 1996. Proceedings CVPR'96, 1996 IEEE Computer Society Conference on*, pages 307–314. IEEE, 1996.
- [134] J L Barron, D J Fleet, and S S Beauchemin. Performance of optical flow techniques. *International journal of computer vision*, 12(1):43–77, 1994.
- [135] M Lefébure and L D Cohen. Image registration, optical flow and local rigidity. *Journal of Mathematical Imaging and Vision*, 14(2):131–147, 2001.
- [136] J R Cooper and N Ritter. Optical flow for validating medical image registration. In *Proceedings of the 9th IASTED International Conference on Signal and Image Processing*, pages 502–506. Citeseer, 2003.
- [137] T Pock, M Urschler, C Zach, R Beichel, and H Bischof. A duality based algorithm for TV-L1-optical-flow image registration. In *Proceedings of the 10th international*

- conference on Medical image computing and computer-assisted intervention*, pages 511–518. Springer-Verlag, 2007.
- [138] M Urschler, M Werlberger, E Scheurer, and H Bischof. Robust optical flow based deformable registration of thoracic CT images. *Medical Image Analysis for the Clinic: A Grand Challenge*, pages 195–204, 2010.
- [139] V Markandey. System and method for determining optical flow, 1997.
- [140] B Glocker, N Komodakis, G Tziritas, N Navab, and N Paragios. Dense image registration through MRFs and efficient linear programming. *Medical Image Analysis*, 12(6):731–741, 2008.
- [141] B C Vemuri, J Ye, Y Chen, and C M Leonard. Image registration via level-set motion: Applications to atlas-based segmentation. *Medical image analysis*, 7(1): 1–20, 2003.
- [142] D I Barnea and H F Silverman. A class of algorithms for fast digital image registration. *Computers, IEEE Transactions on*, 100(2):179–186, 1972.
- [143] W S Hoge. A subspace identification extension to the phase correlation method [MRI application]. *Medical Imaging, IEEE Transactions on*, 22(2):277–280, 2003.
- [144] V Argyriou and T Vlachos. Estimation of sub-pixel motion using gradient cross-correlation. *Electronics letters*, 39(13):980–982, 2003.
- [145] F Maes, a Collignon, D Vandermeulen, G Marchal, and P Suetens. Multimodality image registration by maximization of mutual information. *IEEE transactions on medical imaging*, 16(2):187–98, April 1997. ISSN 0278-0062. doi: 10.1109/42.563664. URL <http://www.ncbi.nlm.nih.gov/pubmed/9101328>.
- [146] Alexis Roche, G Malandain, and Xavier Pennec. The correlation ratio as a new similarity measure for multimodal image registration. *Medical Image*

- Computing*, 1496:1115–1124, 1998. URL <http://www.springerlink.com/index/e76058821mp3v143.pdf>.
- [147] R P Woods, J C Mazziotta, S R Cherry, and Others. MRI-PET registration with automated algorithm. *Journal of computer assisted tomography*, 17(4):536, 1993.
- [148] P Viola and W M Wells. Alignment by maximization of mutual information. *International journal of computer vision*, 24(2):137–154, 1997.
- [149] P E Anuta. Spatial registration of multispectral and multitemporal digital imagery using fast Fourier transform techniques. *Geoscience Electronics, IEEE Transactions on*, 8(4):353–368, 1970.
- [150] T M Buzug and J Weese. Image registration for DSA quality enhancement. *Computerized medical imaging and graphics*, 22(2):103–113, 1998.
- [151] Josien P W Pluim, J B Antoine Maintz, and Max a Viergever. Mutual-information-based registration of medical images: a survey. *IEEE transactions on medical imaging*, 22(8):986–1004, August 2003. ISSN 0278-0062. doi: 10.1109/TMI.2003.815867. URL <http://www.ncbi.nlm.nih.gov/pubmed/12906253>.
- [152] C Studholme, D L G Hill, D J Hawkes, and Others. An overlap invariant entropy measure of 3D medical image alignment. *Pattern recognition*, 32(1):71–86, 1999.
- [153] M Holden, D L G Hill, E R E Denton, J M Jarosz, T C S Cox, T Rohlfing, J Goodey, and D J Hawkes. Voxel similarity measures for 3-D serial MR brain image registration. *Medical Imaging, IEEE Transactions on*, 19(2):94–102, 2000.
- [154] Dirk Loeckx, Pieter Slagmolen, and Frederik Maes. Nonrigid image registration using conditional mutual information. *Medical Imaging*, 29(1):19–29, 2010. URL http://ieeexplore.ieee.org/xpls/abs_all.jsp?arnumber=4915793.

- [155] Michael E Leventon and W Eric L Grimson. Multi-modal volume registration using joint intensity distributions. In *International Conference on Medical Image Computing and Computer-Assisted Intervention*, pages 1057–1066. Springer, 1998.
- [156] Christoph Guetter, Chenyang Xu, Frank Sauer, and Joachim Hornegger. Learning based non-rigid multi-modal image registration using Kullback-Leibler divergence. *Medical image computing and computer-assisted intervention : MICCAI ... International Conference on Medical Image Computing and Computer-Assisted Intervention*, 8(Pt 2):255–62, January 2005. URL <http://www.ncbi.nlm.nih.gov/pubmed/16685967>.
- [157] Jeff Orchard. Multimodal image registration using floating regressors in the joint intensity scatter plot. *Medical image analysis*, 12(4):385–96, August 2008. ISSN 1361-8423. doi: 10.1016/j.media.2007.12.002. URL <http://www.ncbi.nlm.nih.gov/pubmed/18262460>.
- [158] Yongning Lu, Rui Liao, Li Zhang, Ying Sun, Christophe Chef d’Hotel, and Sim Heng Ong. Learning-based deformable registration using weighted mutual information. In *Pattern Recognition (ICPR), 2012 21st International Conference on*, pages 2626–2629. IEEE, 2012.
- [159] Ronald WK So and Albert CS Chung. Learning-based multi-modal rigid image registration by using bhattacharyya distances. In *2011 Annual International Conference of the IEEE Engineering in Medicine and Biology Society*, pages 2642–2645. IEEE, 2011.
- [160] R P Woods, S R Cherry, J C Mazziotta, and Others. Rapid automated algorithm for aligning and reslicing PET images. *Journal of computer assisted tomography*, 16(4):620, 1992.
- [161] J Weese, P, T Netsch, and T Blaffert. Gray-value based registration of CT and MR images by maximization of local correlation. *Medical Image*

-
- Computing*, pages 656–664, 1999. URL <http://www.springerlink.com/index/U87R736629U617G7.pdf>.
- [162] W H Press, S A Teukolsky, W T Vetterling, and B P Flannery. Numerical Recipes 3rd Edition: The Art of Scientific Computing, 2007.
- [163] J A Nelder and R Mead. A simplex method for function minimization. *The computer journal*, 7(4):308–313, 1965.
- [164] R Shams, R A Kennedy, P Sadeghi, and R Hartley. Gradient intensity-based registration of multi-modal images of the brain. In *Computer Vision, 2007. ICCV 2007. IEEE 11th International Conference on*, pages 1–8. IEEE, 2007.
- [165] J E Dennis Jr and V Torczon. Direct search methods on parallel machines. Technical report, DTIC Document, 1991.
- [166] D R Jones, C D Perttunen, and B E Stuckman. Lipschitzian optimization without the Lipschitz constant. *Journal of Optimization Theory and Applications*, 79(1):157–181, 1993.
- [167] E Cantú-Paz. A survey of parallel genetic algorithms. *Calculateurs paralleles, reseaux et systems repartis*, 10(2):141–171, 1998.
- [168] Simon Garnier, Jacques Gautrais, and Guy Theraulaz. The biological principles of swarm intelligence. *Swarm Intelligence*, 1(1):3–31, 2007.
- [169] W H Press and S A Teukolsky. WTV: Numerical Recipes in C: The Art of Scientific Computing, 1992.
- [170] Z Zhang. Iterative point matching for registration of free-form curves. 1992.
- [171] Olivia MB McBride, Colin Berry, Paul Burns, Roderick TA Chalmers, Barry Doyle, Rachael Forsythe, O James Garden, Kirsteen Goodman, Catriona Graham, Peter Hoskins, et al. MRI using ultrasmall superparamagnetic particles

- of iron oxide in patients under surveillance for abdominal aortic aneurysms to predict rupture or surgical repair: MRI for abdominal aortic aneurysms to predict rupture or surgery—the MA3RS study. *Open heart*, 2(1):e000190, 2015.
- [172] Frans L Moll, JT Powell, G Fraedrich, F Verzini, S Haulon, M Waltham, JA van Herwaarden, PJE Holt, JW van Keulen, B Rantner, et al. Management of abdominal aortic aneurysms clinical practice guidelines of the European society for vascular surgery. *European Journal of Vascular and Endovascular Surgery*, 41: S1–S58, 2011.
- [173] Chengjia Wang, Georgia Koutraki, Olivia McBride, Alex Vesey, Tom MacGillivray, Calum Gray, David Newby, Keith Goatman, and Scott Semple. A robust automated multi-modality registration tool applied to abdominal aortic aneurysm [abstract]. In *Joint Annual Meeting ISMRM-ESMRMB 2014, Milano, Italy*, 2014.
- [174] HK Yuen, J Princen, J Illingworth, and J Kittler. Comparative study of Hough transform methods for circle finding. *Image and Vision Computing*, 8(1):71–77, 1990.
- [175] Paul VC Hough. Method and means for recognizing complex patterns. Technical report, 1962.
- [176] Richard O Duda and Peter E Hart. Use of the Hough transformation to detect lines and curves in pictures. *Communications of the ACM*, 15(1):11–15, 1972.
- [177] Tao Peng, Arvind Balijepalli, Satyandra K Gupta, and Tom LeBrun. Algorithms for on-line monitoring of micro spheres in an optical tweezers-based assembly cell. *Journal of computing and information science in engineering*, 7(4):330–338, 2007.
- [178] John Illingworth and J Kittler. The adaptive Hough transform. *Pattern Analysis and Machine Intelligence, IEEE Transactions on*, (5):690–698, 1987.

-
- [179] Bastian Leibe, Ales Leonardis, and Bernt Schiele. Combined object categorization and segmentation with an implicit shape model. In *Workshop on statistical learning in computer vision, ECCV*, volume 2, page 7, 2004.
- [180] Timothée Jost and Heinz Hügli. *Pattern Recognition*, volume 2449 of *Lecture Notes in Computer Science*. Springer Berlin Heidelberg, Berlin, Heidelberg, October 2002. ISBN 978-3-540-44209-7. doi: 10.1007/3-540-45783-6. URL <http://www.springerlink.com/index/10.1007/3-540-45783-6>.
- [181] Jacob Beutel, J Michael Fitzpatrick, Steven C Horii, Yongmin Kim, Harold L Kundel, Milan Sonka, and Richard L Van Metter. *Handbook of Medical Imaging, Volume 3. Display and PACS*. Washington, DC: SPIE Press, 2002.
- [182] Shinji Umeyama. Least-squares estimation of transformation parameters between two point patterns. *IEEE Transactions on Pattern Analysis and Machine Intelligence*, (4):376–380, 1991.
- [183] Guillermo Sapiro. *Geometric partial differential equations and image analysis*. Cambridge university press, 2006.
- [184] Bengt Fornberg. Generation of finite difference formulas on arbitrarily spaced grids. *Mathematics of computation*, 51(184):699–706, 1988.
- [185] Jian Chen, Dan Zeng, Chen Kang, and Zhi Jiang Zhang. A triangle division based point matching for image registration. In *Advanced Materials Research*, volume 765, pages 726–729. Trans Tech Publ, 2013.
- [186] Hongwei Zheng, Ioan Cleju, and Dietmar Saupe. Highly-automatic mi based multiple 2d/3d image registration using self-initialized geodesic feature correspondences. In *Asian Conference on Computer Vision*, pages 426–435. Springer, 2009.

- [187] Martin A Fischler and Robert C Bolles. Random sample consensus: a paradigm for model fitting with applications to image analysis and automated cartography. *Communications of the ACM*, 24(6):381–395, 1981.
- [188] Yixun Liu and Nikos Chrisochoides. Using K-means clustering and MI for non-rigid registration of MRI and CT. In *International Workshop on Machine Learning in Medical Imaging (MLMI), the 13th International Conference on Medical Image Computing and Computer Assisted Intervention (MICCAI)*, September 2010.
- [189] Z F Knops, J B a Maintz, M a Viergever, and J P W Pluim. Normalized mutual information based registration using k-means clustering and shading correction. *Medical image analysis*, 10(3):432–439, June 2006. ISSN 1361-8415. doi: 10.1016/j.media.2005.03.009. URL <http://www.ncbi.nlm.nih.gov/pubmed/16111913>.
- [190] CM Bishop. *Pattern recognition and machine learning*. 2006. ISBN 9780387310732. URL <http://www.library.wisc.edu/selectedtocs/bg0137.pdf>.
- [191] James MacQueen et al. Some methods for classification and analysis of multivariate observations. In *Proceedings of the fifth Berkeley symposium on mathematical statistics and probability*, volume 1, pages 281–297. Oakland, CA, USA., 1967.
- [192] J Michael Fitzpatrick. *Detecting failure, assessing success*. CRS Press, 2001.
- [193] J West, J M Fitzpatrick, M Y Wang, B M Dawant, C R Maurer, R M Kessler, R J Maciunas, C Barillot, D Lemoine, a Collignon, F Maes, P Suetens, D Vandermeulen, P a van den Elsen, S Napel, T S Sumanaweera, B Harkness, P F Hemler, D L Hill, D J Hawkes, C Studholme, J B Maintz, M a Viergever, G Malandain, and R P Woods. Comparison and evaluation of retrospective intermodality brain image registration techniques. *Journal of computer assisted*

- tomography*, 21(4):554–566, 1996. ISSN 0363-8715. URL <http://www.ncbi.nlm.nih.gov/pubmed/9216759>.
- [194] J Michael Fitzpatrick, Derek LG Hill, Yu Shyr, Jay West, Colin Studholme, and Calvin R Maurer. Visual assessment of the accuracy of retrospective registration of mr and ct images of the brain. *IEEE Transactions on Medical Imaging*, 17(4): 571–585, 1998.
- [195] Thomas L Curtright, David B Fairlie, Cosmas K Zachos, et al. A compact formula for rotations as spin matrix polynomials. *SIGMA*, 10(084):084, 2014.
- [196] John Canny. A computational approach to edge detection. *IEEE Transactions on pattern analysis and machine intelligence*, (6):679–698, 1986.
- [197] John G Sled and G Bruce Pike. Standing-wave and RF penetration artifacts caused by elliptic geometry: an electrodynamic analysis of MRI. *Medical Imaging, IEEE Transactions on*, 17(4):653–662, 1998.
- [198] L G Hanson and T Dyrby. RF inhomogeneity correction: Validity of the smooth-bias approximation. In *Proceeding International Society for Magnetic Resonance in Medicine*, 2002.
- [199] Z Hou. A review on MR image intensity inhomogeneity correction. *International Journal of Biomedical Imaging*, 2006, 2006.
- [200] Zin Yan Chua, Weili Zheng, Michael W L Chee, and Vitali Zagorodnov. Evaluation of performance metrics for bias field correction in MR brain images. *Journal of magnetic resonance imaging : JMRI*, 29(6):1271–1279, June 2009. ISSN 1053-1807. doi: 10.1002/jmri.21768. URL <http://www.ncbi.nlm.nih.gov/pubmed/19472380>.

Bibliography

- [201] G Collewet, A Davenel, C Toussaint, and S Akoka. Correction of intensity nonuniformity in spin-echo T1-weighted images. *Magnetic resonance imaging*, 20(4):365–373, 2002.
- [202] Sfibastien Gilles, Michael Brady, and J Declerck. Bias field correction of breast MR images. *Visualization in Biomedical Computing*, 1996. URL <http://www.springerlink.com/index/04n837944876j116.pdf>.
- [203] G P Liney, L W Turnbull, and A J Knowles. A simple method for the correction of endorectal surface coil inhomogeneity in prostate imaging. *Journal of Magnetic Resonance Imaging*, 8(4):994–997, 2005.
- [204] H Mihara, N Iriguchi, and S Ueno. A method of RF inhomogeneity correction in MR imaging. *Magnetic Resonance Materials in Physics, Biology and Medicine*, 7(2):115–120, 1998.
- [205] E A Vokurka, N A Thacker, A Jackson, and Others. A fast model independent method for automatic correction of intensity nonuniformity in MRI data. *Journal of Magnetic Resonance Imaging*, 10(4):550–562, 1999.
- [206] B M Dawant, A P Zijdenbos, and R A Margolin. Correction of intensity variations in MR images for computer-aided tissue classification. *Medical Imaging, IEEE Transactions on*, 12(4):770–781, 1993.
- [207] S H Lai and M Fang. A new variational shape-from-orientation approach to correcting intensity inhomogeneities in magnetic resonance images. *Medical Image Analysis*, 3(4):409–424, 1999.
- [208] M Tincher, C R Meyer, R Gupta, and D M Williams. Polynomial modeling and reduction of RF body coil spatial inhomogeneity in MRI. *Medical Imaging, IEEE Transactions on*, 12(2):361–365, 1993.

-
- [209] C R Meyer, P H Bland, and J Pipe. Retrospective correction of intensity inhomogeneities in MRI. *Medical Imaging, IEEE Transactions on*, 14(1):36–41, 1995.
- [210] M Styner, C Brechbühler, G Székely, and G Gerig. Parametric estimate of intensity inhomogeneities applied to MRI. *IEEE transactions on medical imaging*, 19(3):153–65, March 2000. ISSN 0278-0062. doi: 10.1109/42.845174. URL <http://www.ncbi.nlm.nih.gov/pubmed/10875700>.
- [211] K O Lim, A Pfefferbaum, and Others. Segmentation of MR brain images into cerebrospinal fluid spaces, white and gray matter. *Journal of Computer Assisted Tomography*, 13(4):588, 1989.
- [212] G J Harris, P E Barta, L W Peng, S Lee, P D Brettschneider, A Shah, J D Henderer, T E Schlaepfer, and G D Pearlson. MR volume segmentation of gray matter and white matter using manual thresholding: dependence on image brightness. *American journal of neuroradiology*, 15(2):225–230, 1994.
- [213] P A Narayana and A Borthakur. Effect of radio frequency inhomogeneity correction on the reproducibility of intra-cranial volumes using MR image data. *Magnetic Resonance in Medicine*, 33(3):396–400, 2005.
- [214] A Koivula, J Alakuijala, and O Tervonen. Image feature based automatic correction of low-frequency spatial intensity variations in MR images. *Magnetic resonance imaging*, 15(10):1167–1175, 1997.
- [215] L Q Zhou, Y M Zhu, C Bergot, A M Laval-Jeantet, V Bousson, J D Laredo, and M Laval-Jeantet. A method of radio-frequency inhomogeneity correction for brain tissue segmentation in MRI. *Computerized medical imaging and graphics*, 25(5):379–389, 2001.

Bibliography

- [216] B H Brinkmann, A Manduca, and R A Robb. Optimized homomorphic unsharp masking for MR grayscale inhomogeneity correction. *Medical Imaging, IEEE Transactions on*, 17(2):161–171, 1998.
- [217] M S Cohen, R M DuBois, and M M Zeineh. Rapid and effective correction of RF inhomogeneity for high field magnetic resonance imaging. *Human Brain Mapping*, 10(4):204–211, 2000.
- [218] Muqing Lin, Siwa Chan, Jeon-Hor Chen, Daniel Chang, Ke Nie, Shih-Ting Chen, Cheng-Ju Lin, Tzu-Ching Shih, Orhan Nalcioglu, and Min-Ying Su. A new bias field correction method combining N3 and FCM for improved segmentation of breast density on MRI. *Medical physics*, 38(1):5–14, January 2011. ISSN 0094-2405. URL <http://www.pubmedcentral.nih.gov/articlerender.fcgi?artid=3017578&tool=pmcentrez&rendertype=abstract>.
- [219] Mohamed N Ahmed, Sameh M Yamany, Nevin Mohamed, Aly a Farag, and Thomas Moriarty. A modified fuzzy C-means algorithm for bias field estimation and segmentation of MRI data. *IEEE transactions on medical imaging*, 21(3):193–199, March 2002. ISSN 0278-0062. doi: 10.1109/42.996338. URL <http://www.ncbi.nlm.nih.gov/pubmed/11989844>.
- [220] J G Sled and G B Pike. Standing-wave and RF penetration artifacts caused by elliptic geometry: an electrodynamic analysis of MRI. *Medical Imaging, IEEE Transactions on*, 17(4):653–662, 1998.
- [221] J F Mangin. Entropy minimization for automatic correction of intensity nonuniformity. In *Mathematical Methods in Biomedical Image Analysis*, 2000. *Proceedings. IEEE Workshop on*, pages 162–169. IEEE, 2000.
- [222] Eduard Solanas. Exploiting voxel correlation for automated MRI bias field correction by conditional entropy minimization. *Medical Image Computing and*

- Computer-Assisted*, pages 1220–1221, 2001. URL <http://www.springerlink.com/index/bb8ekek9trc8tmqg.pdf>.
- [223] J Milles, Y M Zhu, G Gimenez, C R Guttmann, I E Magnin, and Others. MRI intensity nonuniformity correction using simultaneously spatial and gray-level histogram information. *Computerized medical imaging and graphics: the official journal of the Computerized Medical Imaging Society*, 31(2):81, 2007.
- [224] U Vovk, F Pernuš, and B Likar. MRI intensity inhomogeneity correction by combining intensity and spatial information. *Physics in Medicine and Biology*, 49(17):4119, 2004.
- [225] Nicholas J Tustison, Brian B Avants, Philip a Cook, Yuanjie Zheng, Alexander Egan, Paul a Yushkevich, and James C Gee. N4ITK: improved N3 bias correction. *IEEE transactions on medical imaging*, 29(6):1310–1320, June 2010. ISSN 1558-254X. doi: 10.1109/TMI.2010.2046908. URL <http://www.pubmedcentral.nih.gov/articlerender.fcgi?artid=3071855&tool=pmcentrez&rendertype=abstract>.
- [226] N A Thacker, A J Lacey, and P A Bromiley. Validating MRI field homogeneity correction using image information measures. In *Proc. BMVC*, volume 2, pages 626–635, 2002.
- [227] A P Zijdenbos, B M Dawant, and R A Margolin. Intensity correction and its effect on measurement variability in the computer-aided analysis of MRI. In *Proc. 9th Int. Symp. Exhibition Computer Assisted Radiology (CAR'95)*, pages 216–221, 1995.
- [228] J B Arnold, J S Liow, K A Schaper, J J Stern, J G Sled, D W Shattuck, A J Worth, M S Cohen, R M Leahy, J C Mazziotta, and Others. Qualitative and quantitative evaluation of six algorithms for correcting intensity nonuniformity effects. *NeuroImage*, 13(5):931–943, 2001.

Bibliography

- [229] Sylvain Prima, Nicholas Ayache, Tom Barrick, and Neil Roberts. Maximum likelihood estimation of the bias field in MR brain images: Investigating different modelings of the imaging process. *Medical Image Computing and ...*, pages 811–819, 2001. URL <http://www.springerlink.com/index/95cb8rtw2uwpqf44.pdf>.
- [230] E B Lewis, N C Fox, and Others. Correction of differential intensity inhomogeneity in longitudinal MR images. *Neuroimage*, 23(1):75–83, 2004.
- [231] L Devroye. *Non-uniform random variate generation*, volume 4. Springer-Verlag New York, 1986.
- [232] NJ Tustison and JC Gee. N4ITK: Nick’s N3 ITK implementation for MRI bias field correction. *Insight Journal*, pages 1–8, 2009. URL http://www.insight-journal.org/download/pdf/18880/IJ_640_1_n3.pdf.
- [233] N Otsu. A threshold selection method from gray-level histograms. *Automatica*, 11(285-296):23–27, 1975.
- [234] John Ashburner, Gareth Barnes, C Chen, Jean Daunizeau, Guillaume Flandin, Karl Friston, D Gitelman, S Kiebel, J Kilner, V Litvak, et al. Spm8 manual. *Functional Imaging Laboratory, Institute of Neurology*, page 41, 2008.
- [235] Francisco Varela, Jean-Philippe Lachaux, Eugenio Rodriguez, and Jacques Martinerie. The Brainweb: phase synchronization and large-scale integration. *Nature reviews neuroscience*, 2(4):229–239, 2001.
- [236] P A Bromiley. Problems with the Brainweb MRI Simulator in the Evaluation of Medical Image Segmentation Algorithms, and an Alternative Methodology.
- [237] Jia-Xiu Liu, Yong-Sheng Chen, and Li-Fen Chen. Fast and accurate registration techniques for affine and nonrigid alignment of MR brain images. *Annals of*

-
- biomedical engineering*, 38(1):138–57, January 2010. ISSN 1521-6047. doi: 10.1007/s10439-009-9840-9. URL <http://www.ncbi.nlm.nih.gov/pubmed/19936927>.
- [238] Dinu Coltuc, Philippe Bolon, and J-M Chassery. Exact histogram specification. *Image Processing, IEEE Transactions on*, 15(5):1143–1152, 2006.
- [239] Chengjia Wang, Georgia Koutraki, Olivia McBride, Alex Vesey, Tom MacGillivray, Calum Gray, David Newby, Keith Goatman, and Scott Semple. A robust automated multi-modality registration tool applied to abdominal aortic aneurysm [abstract]. In *Joint Annual Meeting ISMRM-ESMRMB 2014, Milano, Italy*, 2014.
- [240] Daniel E Finkel. Direct optimization algorithm user guide. *Center for Research in Scientific Computation, North Carolina State University*, 2, 2003.
- [241] Hans J Johnson, Matt McCormick, and Luis Ibanez. The itk software guide third edition updated for itk version 4.5. 2013.
- [242] Stefan Klein, Marius Staring, and Josien P W Pluim. Evaluation of optimization methods for nonrigid medical image registration using mutual information and B-splines. *IEEE transactions on image processing : a publication of the IEEE Signal Processing Society*, 16(12):2879–2890, December 2007. ISSN 1057-7149. URL <http://www.ncbi.nlm.nih.gov/pubmed/18092588>.
- [243] Mark Jenkinson and Stephen Smith. A global optimisation method for robust affine registration of brain images. *Medical image analysis*, 5(2):143–156, 2001.
- [244] Mark P Wachowiak, Renata Smolíková, Yufeng Zheng, Jacek M Zurada, and Adel Said Elmaghraby. An approach to multimodal biomedical image registration utilizing particle swarm optimization. *IEEE Transactions on evolutionary computation*, 8(3):289–301, 2004.

- [245] Lawrence J Fogel, Alvin J Owens, and Michael J Walsh. *Artificial intelligence through simulated evolution*. John Wiley, 1966.
- [246] Radha Thangaraj, Millie Pant, Ajith Abraham, and Pascal Bouvry. Particle swarm optimization: hybridization perspectives and experimental illustrations. *Applied Mathematics and Computation*, 217(12):5208–5226, 2011.
- [247] John Henry Holland. *Adaptation in natural and artificial systems: an introductory analysis with applications to biology, control, and artificial intelligence*. MIT press, 1992.
- [248] Emile Aarts and Jan Korst. Simulated annealing and Boltzmann machines. 1988.
- [249] Marco Dorigo, Vittorio Maniezzo, Alberto Colorni, and Vittorio Maniezzo. Positive feedback as a search strategy. 1991.
- [250] Jean-Michel Rouet, Jean-José Jacq, and Christian Roux. Genetic algorithms for a robust 3-D MR-CT registration. *Information Technology in Biomedicine, IEEE Transactions on*, 4(2):126–136, 2000.
- [251] Alan Liu, Stephen M Pizer, David H Eberly, Bryan S Morse, Julian G Rosenman, Edward L Chaney, Elizabeth Bullitt, and Vincent Carrasco. Volume registration using the 3D core. In *Visualization in Biomedical Computing 1994*, pages 217–226. International Society for Optics and Photonics, 1994.
- [252] Mark P Wachowiak and Adel S Elmaghraby. The continuous tabu search as an optimizer for 2D-to-3D biomedical image registration. In *Medical Image Computing and Computer-Assisted Intervention–MICCAI 2001*, pages 1273–1274. Springer, 2001.
- [253] George K Matsopoulos, Pantelis A Asvestas, Nicolaos A Mouravliansky, and Konstantinos K Delibasis. Multimodal registration of retinal images using self organizing maps. *IEEE Transactions on Medical Imaging*, 23(12):1557–1563, 2004.

-
- [254] Yen-Wei Chen, Chen-Lun Lin, and Aya Mimori. Multimodal medical image registration using particle swarm optimization. *2008 Eighth International Conference on Intelligent Systems Design and Applications*, 1:127–131, November 2008. doi: 10.1109/ISDA.2008.321. URL <http://ieeexplore.ieee.org/lpdocs/epic03/wrapper.htm?arnumber=4696449>.
- [255] Yen-Wei Chen, Aya Mimori, and Chen-Lun Lin. Hybrid particle swarm optimization for 3-D image registration. *2009 16th IEEE International Conference on Image Processing (ICIP)*, pages 1753–1756, November 2009. doi: 10.1109/ICIP.2009.5414613. URL <http://ieeexplore.ieee.org/lpdocs/epic03/wrapper.htm?arnumber=5414613>.
- [256] Chen-Lun Lin, Aya Mimori, and Yen-Wei Chen. Hybrid particle swarm optimization and its application to multimodal 3D medical image registration. *Computational intelligence and neuroscience*, 2012:561406, January 2012. ISSN 1687-5273. doi: 10.1155/2012/561406. URL <http://www.pubmedcentral.nih.gov/articlerender.fcgi?artid=3432335&tool=pmcentrez&rendertype=abstract>.
- [257] Nemir Al-azzawi, Harsa A Mat Sakim, Wan Ahmed, K Wan Abdullah, and Yasmin Mohd Yacob. Efficient Feature-Based Registration for CT-MR Images Based on NSCT and PSO. *World Academy of Science Engineering and Technology*, 74:535–539, 2011.
- [258] M. Khalid Khan and Ingela Nystrom. A modified particle swarm optimization applied in image registration. *2010 20th International Conference on Pattern Recognition*, pages 2302–2305, August 2010. doi: 10.1109/ICPR.2010.563. URL <http://ieeexplore.ieee.org/lpdocs/epic03/wrapper.htm?arnumber=5595978>.
- [259] Hua Li, Ying Lin, and Anna Wang. An medical image registration approach using improved Hausdorff distance combined with particle swarm

- optimization. *2008 Fourth International Conference on Natural Computation*, pages 428–432, 2008. doi: 10.1109/ICNC.2008.444. URL <http://ieeexplore.ieee.org/lpdocs/epic03/wrapper.htm?arnumber=4667470>.
- [260] Hua Li, Yu Zhang, and Anna Wang. Medical image registration based on JS measure and niche chaotic mutation quantum-behaved particle swarm optimization. In *2010 6th International Conference on Wireless Communications Networking and Mobile Computing (WiCOM)*, pages 1–4. IEEE, 2010.
- [261] Souham Meshoul and Mohamed Batouche. A novel quantum behaved particle swarm optimization algorithm with chaotic search for image alignment. In *IEEE congress on evolutionary computation*, pages 1–6. IEEE, 2010.
- [262] H Talbi and Mohamed Batouche. Hybrid particle swarm with differential evolution for multimodal image registration. *Industrial Technology, 2004. IEEE ICIT'04 ...*, pages 1567–1572, 2004. URL http://ieeexplore.ieee.org/xpls/abs_all.jsp?arnumber=1490800.
- [263] Benzhenh Wei, Xin Peng, and Zhimin Zhao. An improved PSO algorithm based multimodality medical image automatic registration. In *Natural Computation, 2008. ICNC'08. Fourth International Conference on*, volume 7, pages 574–578. IEEE, 2008.
- [264] P Andras. A bayesian interpretation of the particle swarm optimization and its kernel extension. *PloS one*, 7(11):e48710–e48710, 2011.
- [265] Riccardo Poli. An analysis of publications on particle swarm optimization applications. *Essex, UK: Department of Computer Science, University of Essex*, 2007.
- [266] Maurice Clerc and James Kennedy. The particle swarm-explosion, stability, and convergence in a multidimensional complex space. *Evolutionary Computation, IEEE Transactions on*, 6(1):58–73, 2002.

- [267] Yuhui Shi and Russell Eberhart. A modified particle swarm optimizer. In *Evolutionary Computation Proceedings, 1998. IEEE World Congress on Computational Intelligence., The 1998 IEEE International Conference on*, pages 69–73. IEEE, 1998.
- [268] Yuhui Shi, J Kennedy, and RC Eberhart. Swarm intelligence. In *Proc of Swarm Intelligence Symposium. San Mateo: Morgan Kaufman Publishers*, pages 50–60, 2001.
- [269] Maurice Clerc. The swarm and the queen: towards a deterministic and adaptive particle swarm optimization. In *Evolutionary Computation, 1999. CEC 99. Proceedings of the 1999 Congress on*, volume 3. IEEE, 1999.
- [270] James Kennedy. Bare bones particle swarms. In *Swarm Intelligence Symposium, 2003. SIS'03. Proceedings of the 2003 IEEE*, pages 80–87. IEEE, 2003.
- [271] Renato A Krohling and Eduardo Mendel. Bare bones particle swarm optimization with Gaussian or Cauchy jumps. In *2009 IEEE Congress on Evolutionary Computation*, pages 3285–3291. IEEE, 2009.
- [272] Jacques Riget and Jakob S Vesterstrøm. A diversity-guided particle swarm optimizer-the ARPSO. *Dept. Comput. Sci., Univ. of Aarhus, Aarhus, Denmark, Tech. Rep*, 2:2002, 2002.
- [273] James Kennedy and Rui Mendes. Population structure and particle swarm performance. 2002.
- [274] James Kennedy and Rui Mendes. Neighborhood topologies in fully informed and best-of-neighborhood particle swarms. *IEEE Transactions on Systems Man and Cybernetics Part C Applications and Reviews*, 36(4):515, 2006.
- [275] Ponnuthurai N Suganthan. Particle swarm optimiser with neighbourhood operator. In *Evolutionary Computation, 1999. CEC 99. Proceedings of the 1999 Congress on*, volume 3. IEEE, 1999.

- [276] Xiaohui Hu and Russell Eberhart. Multiobjective optimization using dynamic neighborhood particle swarm optimization. In *wcci*, pages 1677–1681. Ieee, 2002.
- [277] JJ Liang and Ponnuthurai Nagaratnam Suganthan. Dynamic multi-swarm particle swarm optimizer. In *Swarm Intelligence Symposium, 2005. SIS 2005. Proceedings 2005 IEEE*, pages 124–129. IEEE, 2005.
- [278] Rui Mendes, James Kennedy, and José Neves. The fully informed particle swarm: simpler, maybe better. *Evolutionary Computation, IEEE Transactions on*, 8(3):204–210, 2004.
- [279] Jing J Liang, A Kai Qin, Ponnuthurai Nagaratnam Suganthan, and S Baskar. Comprehensive learning particle swarm optimizer for global optimization of multimodal functions. *Evolutionary Computation, IEEE Transactions on*, 10(3):281–295, 2006.
- [280] Jun Sun, Wenbo Xu, and Bin Feng. A global search strategy of quantum-behaved particle swarm optimization. In *Cybernetics and Intelligent Systems, 2004 IEEE Conference on*, volume 1, pages 111–116. IEEE, 2004.
- [281] Wei Fang, Jun Sun, Yanrui Ding, Xiaojun Wu, and Wenbo Xu. A review of quantum-behaved particle swarm optimization. *IETE Technical Review*, 27(4): 336–348, 2010.
- [282] Jun Sun, Wenbo Xu, and Bin Feng. Adaptive parameter control for quantum-behaved particle swarm optimization on individual level. In *Systems, Man and Cybernetics, 2005 IEEE International Conference on*, volume 4, pages 3049–3054. IEEE, 2005.
- [283] Jun Sun, Wenbo Xu, and Jing Liu. Parameter selection of quantum-behaved particle swarm optimization. In *Advances in Natural Computation*, pages 543–552. Springer, 2005.

-
- [284] Jun Sun, Bin Feng, and Wenbo Xu. Particle swarm optimization with particles having quantum behavior. In *Congress on Evolutionary Computation*, 2004.
- [285] Jun Sun, Wenbo Xu, and Wei Fang. Enhancing global search ability of quantum-behaved particle swarm optimization by maintaining diversity of the swarm. In *Rough Sets and Current Trends in Computing*, pages 736–745. Springer, 2006.
- [286] Q Baida, J Zhuqing, and X Baoguo. Research on quantum-behaved particle swarms cooperative optimization. *Computer Engineering and Applications*, 44(7): 72–4, 2008.
- [287] Leandro dos Santos Coelho. Gaussian quantum-behaved particle swarm optimization approaches for constrained engineering design problems. *Expert Systems with Applications*, 37(2):1676–1683, 2010.
- [288] Jacob Robinson, Seelig Sinton, and Yahya Rahmat-Samii. Particle swarm, genetic algorithm, and their hybrids: optimization of a profiled corrugated horn antenna. In *Antennas and Propagation Society International Symposium, 2002. IEEE*, volume 1, pages 314–317. IEEE, 2002.
- [289] Shu-Kai S Fan, Yun-chia Liang, and Erwie Zahara. Hybrid simplex search and particle swarm optimization for the global optimization of multimodal functions. *Engineering Optimization*, 36(4):401–418, 2004.
- [290] Morten Lovbjerg, Thomas Kiel Rasmussen, and Thiemo Krink. Hybrid particle swarm optimiser with breeding and subpopulations. In *Proceedings of the Genetic and Evolutionary Computation Conference*, volume 2001, pages 469–476. Citeseer, 2001.
- [291] Jing Liu, Jun Sun, and Wenbo Xu. Improving quantum-behaved particle swarm optimization by simulated annealing. In *Computational Intelligence and Bioinformatics*, pages 130–136. Springer, 2006.

- [292] Jing Liu, Jun Sun, and Wenbo Xu. Quantum-behaved particle swarm optimization with immune operator. In *Foundations of Intelligent Systems*, pages 77–83. Springer, 2006.
- [293] Wei Fang, Jun Sun, and Wen-bo Xu. Improved quantum-behaved particle swarm optimization algorithm based on differential evolution operator and its application. *Journal of System Simulation*, 20(24):6740–4, 2008.
- [294] Leandro dos Santos Coelho. A quantum particle swarm optimizer with chaotic mutation operator. *Chaos, Solitons & Fractals*, 37(5):1409–1418, 2008.
- [295] YANG Kaiqiao and Hirosato Nomura. Quantum-behaved particle swarm optimization with chaotic search. *IEICE TRANSACTIONS on Information and Systems*, 91(7):1963–1970, 2008.
- [296] Fang Liu, Haibin Duan, and Yimin Deng. A chaotic quantum-behaved particle swarm optimization based on lateral inhibition for image matching. *Optik-International Journal for Light and Electron Optics*, 123(21):1955–1960, 2012.
- [297] Antonio Fernández-Caballero, María T López, Enrique J Carmona, and Ana E Delgado. A historical perspective of algorithmic lateral inhibition and accumulative computation in computer vision. *Neurocomputing*, 74(8):1175–1181, 2011.
- [298] Hadi Rezaei, Sassan Azadi, and Mina Ghorbani. A hybrid particle swarm steepest gradient algorithm for elastic brain image registration. In *Machine Vision, 2009. ICMV'09. Second International Conference on*, pages 54–58. IEEE, 2009.
- [299] Anbang Xu, Xin Jin, and Ping Guo. Two-dimensional PCA combined with PCA for neural network based image registration. *Advances in Natural Computation*, pages 696–705, 2006. URL http://link.springer.com/chapter/10.1007/11881223_87.

-
- [300] Jing Jin, Qiang Wang, and Yi Shen. High-performance medical image registration using improved particle swarm optimization. In *Instrumentation and Measurement Technology Conference Proceedings, 2008. IMTC 2008. IEEE*, pages 736–740. IEEE, 2008.
- [301] Hakjae Lee, Kisung Lee, Yongkwon Kim, Jinhun Joung, Kookhyun Moon, Sung-Kwan Joo, Kyeong-Min Kim, and Gi-Jeong Chun. Image registration for PET/CT and CT images with particle swarm optimization. In *Nuclear Science Symposium Conference Record (NSS/MIC), 2009 IEEE*, pages 3717–3720. IEEE, 2009.
- [302] Aiping Wang, Zhe Wang, Dan Lv, and Zhizhen Fang. Research on a novel non-rigid registration for medical image based on surf and apso. In *Image and Signal Processing (CISP), 2010 3rd International Congress on*, volume 6, pages 2628–2633. IEEE, 2010.
- [303] C Wang, KA Goatman, T MacGillivray, E Beveridge, Y Koutraki, J Boardman, C Stirrat, S Sparrow, E Moore, R Paraky, et al. Automatic multi-parametric MR registration method using mutual information based on adaptive asymmetric k-means binning. In *Biomedical Imaging (ISBI), 2015 IEEE 12th International Symposium on*, pages 1089–1092. IEEE, 2015.
- [304] Di Zhou, Jun Sun, Choi-Hong Lai, Wenbo Xu, and Xiaoguang Lee. An improved quantum-behaved particle swarm optimization and its application to medical image registration. *International Journal of Computer Mathematics*, 88(6):1208–1223, 2011.
- [305] Yang Xuan and Pei Jihong. Elastic image registration using attractive and repulsive particle swarm optimization. In *Simulated Evolution and Learning*, pages 782–789. Springer, 2006.

- [306] Anna Wang, Zhe Wang, Dan Lv, and Zhizhen Fang. Research on a novel non-rigid registration for medical image based on SURF and APSO. *2010 3rd International Congress on Image and Signal Processing*, pages 2628–2633, October 2010. doi: 10.1109/CISP.2010.5648148. URL <http://ieeexplore.ieee.org/lpdocs/epic03/wrapper.htm?arnumber=5648148>.
- [307] Qi Li and Isao Sato. Multimodality image registration by particle swarm optimization of mutual information. In *Advanced Intelligent Computing Theories and Applications. With Aspects of Artificial Intelligence*, pages 1120–1130. Springer, 2007.
- [308] J Senthilnath, SN Omkar, V Mani, and T Karthikeyan. Multiobjective discrete particle swarm optimization for multisensor image alignment. *Geoscience and Remote Sensing Letters, IEEE*, 10(5):1095–1099, 2013.
- [309] Hadi Rezaei and Sassan Azadi. Nonrigid medical image registration using hierarchical particle swarm optimization. In *Soft Computing, Computing with Words and Perceptions in System Analysis, Decision and Control, 2009. ICSCCW 2009. Fifth International Conference on*, pages 1–4. IEEE, 2009.
- [310] Yang Lu, ZW Liao, and WF Chen. An automatic registration framework using quantum particle swarm optimization for remote sensing images. In *Wavelet Analysis and Pattern Recognition, 2007. ICWAPR'07. International Conference on*, volume 2, pages 484–488. IEEE, 2007.
- [311] B Feng, Z Wang, and J Sun. Niche chaotic mutation quantum-behaved partical swarm optimization. *Comput Appl Software*, 26:50–52, 2009.
- [312] Toby J Richer and Tim M Blackwell. The Lévy particle swarm. In *Evolutionary Computation, 2006. CEC 2006. IEEE Congress on*, pages 808–815. IEEE, 2006.
- [313] James Kennedy. Probability and dynamics in the particle swarm. In *Congress on evolutionary computation*, 2004.

-
- [314] Christopher K Monson and Kevin D Seppi. The Kalman swarm. In *Genetic and Evolutionary Computation–GECCO 2004*, pages 140–150. Springer, 2004.
- [315] Rudolph Emil Kalman. A new approach to linear filtering and prediction problems. *Journal of Fluids Engineering*, 82(1):35–45, 1960.
- [316] Simon J Julier and Jeffrey K Uhlmann. New extension of the Kalman filter to nonlinear systems. In *AeroSense’97*, pages 182–193. International Society for Optics and Photonics, 1997.
- [317] Dragan Jukić and Rudolf Scitovski. Least squares fitting gaussian type curve. *Applied mathematics and computation*, 167(1):286–298, 2005.
- [318] Garry A Einicke and Langford B White. Robust extended Kalman filtering. *IEEE Transactions on Signal Processing*, 47(9):2596–2599, 1999.
- [319] Rudolph E Kalman. An introduction to Kalman filter. *University of North Carolina at Chapel Hill, Department of Computer Science, TR*, pages 95–041, 1995.
- [320] J Uhlmann, S Julier, and HF Durrant-Whyte. A new method for the non linear transformation of means and covariances in filters and estimations. *IEEE Transactions on automatic control*, 45, 2000.
- [321] Momin Jamil and Xin-She Yang. A literature survey of benchmark functions for global optimisation problems. *International Journal of Mathematical Modelling and Numerical Optimisation*, 4(2):150–194, 2013.
- [322] Josien PW Pluim, JB Antoine Maintz, and Max A Viergever. Image registration by maximization of combined mutual information and gradient information. In *Medical Image Computing and Computer-Assisted Intervention–MICCAI 2000*, pages 452–461. Springer, 2000.
- [323] Antoine B Abche, Fadi Yaacoub, Aldo Maalouf, and Elie Karam. Image registration based on neural network and fourier transform. In *Engineering in*

- Medicine and Biology Society*, 2006. *EMBS'06. 28th Annual International Conference of the IEEE*, pages 4803–4806. IEEE, 2006.
- [324] J Jiang, P Trundle, and J Ren. Medical image analysis with artificial neural networks. *Computerized medical imaging and graphics : the official journal of the Computerized Medical Imaging Society*, 34(8):617–31, December 2010. ISSN 1879-0771. doi: 10.1016/j.compmedimag.2010.07.003. URL <http://www.ncbi.nlm.nih.gov/pubmed/20713305>.
- [325] Lifeng Shang, Jian Cheng Lv, and Zhang Yi. Rigid medical image registration using PCA neural network. *Neurocomputing*, 69(13-15):1717–1722, August 2006. ISSN 09252312. doi: 10.1016/j.neucom.2006.01.007. URL <http://linkinghub.elsevier.com/retrieve/pii/S092523120600083X>.
- [326] Paul Viola and Michael J Jones. Robust real-time face detection. *International journal of computer vision*, 57(2):137–154, 2004.

Appendices

A Publications related to this thesis

ABSTRACT

Some of the material presented in chapter 3 has been published as a conference abstract and presented as an electronic poster at the International Society for Magnetic Resonance in Medicine (ISMRM) annual scientific meeting 2014, Milan, Italy. A patent (20150131880) was published in May 2015. A paper-based poster was produced and presented at Edinburgh BioQuarter Centre 4 Cardiovascular Science Symposium. The image analysis method and results presented in chapter 5 were published at The Institute of Electrical and Electronics Engineers (IEEE) International Symposium on Biomedical Imaging (ISBI) 2015, New York, USA. The application of the image analysis software to cardiac and neonatal MR data was presented separately at the European Society for Magnetic Resonance in Medicine and Biology (ESMRMB) annual meeting 2015, Edinburgh, UK. Journal papers about analysis methods and results presented in chapter 3 and chapter 7 are still in print and not yet published. In this chapter, the published materials mentioned in abstracts of chapter 3 and chapter 5 are presented.

A.1 Conference abstract of ISMRM2014

A robust automated multi-modality registration tool applied to abdominal aortic aneurysm

Chengjia Wang^{1,2}, Georgia Koutraki^{1,3}, Olivia McBride³, Alex Vesey³, Tom MacGillivray¹, Calum Gray¹, David Newby^{1,3}, Keith Goatman², and Scott Semple^{1,3}
¹Clinical Research Imaging Centre, University of Edinburgh, Edinburgh, United Kingdom, ²Toshiba Medical Visualization System-Europe, Edinburgh, United Kingdom, ³Centre for Cardiovascular Science, University of Edinburgh, Edinburgh, United Kingdom

PURPOSE

This study aims to evaluate the accuracy of a new method for multimodality registration of vascular structure. Registration of multi-modality and multi-parameter imaging is challenging because of the large variations in image contrast and non-stationary artifacts. This paper presents an accuracy evaluation for an automatic registration method for T2 weighted (T2W), pre- and post-contrast T2* weighted (T2*W) MR images, and CT images used in a study of abdominal aortic aneurysms (AAA).

METHODOLOGY

Data acquisition: The MA3RS study, led by the Clinical Research Imaging Centre, University of Edinburgh is investigating inflammatory markers for AAA growth and rupture¹. 71 patients currently under the UK aneurysm surveillance programme with aneurysm diameter >4cm were imaged. Imaging protocol: 3D isotropic axial T2W fast spin echo with and without fat suppression, and T2*W multi-gradient-echo multi-slice axial 2D images acquired at baseline (3T Verio, Siemens Healthcare, Germany), followed by administration of 4mg/kg of ultra-small superparamagnetic iron oxide (USPIO) contrast agent (Rienso, Advanced Magnetix Inc, USA). MRI coverage was obtained from above AAA to aortic bifurcation. 36 hours later the MRI protocol was repeated. Uptake of USPIO in AAA on the post-infusion T2*W images indicates inflammatory macrophage uptake¹. A standard contrast enhanced CT dataset covering the aorta was acquired at baseline (Aquilion ONE, Toshiba Medical Systems, Japan). Figure 1 shows the variation in appearance and artifacts between acquisitions. To quantify USPIO uptake, pre- and post-contrast T2*W images must be spatially registered, along with the T2W images and CT images to provide USPIO localisation.

Registration and Evaluation: For the purposes of this study the abdominal aorta could be adequately aligned using a rigid-body transform. To account for differences in contrast between images a mutual information similarity metric with top-down k-means binning strategy was used. The DIRECT global optimization was used to search for the optimal transform. A multi-resolution framework was adopted for efficiency, together with an axial-ROI tracking method all implemented in MATLAB. To access registration accuracy, a graphical user interface (GUI), shown in figure 2, was developed to allow a suitably experienced clinician to manually "correct" registration (if required), by adjustments to the translations and rotations. Differences between manual and automatic registration transforms were then analysed for T2W-T2*W registration, T2*W_{baseline}-T2*W_{post-contrast}, and T2W-CT.

RESULTS

Mean translational and rotational errors in x, y, z and mean Euclidean error for MR registrations are shown in Table 1. The mean translational error is 2.56mm, and 59.6% T2W-T2*W and 54.5% T2*W-T2*W registrations achieved sub-pixel accuracy. The largest translational error is <7.0 mm, >50% of the registration results require no manual correction. Results of registering pre-contrast-T2*W to CT are shown in Table 2. The mean translational error is 4.2 mm, and mean rotational error is <0.7° in all dimensions. >35% of results require no manual adjusting and in >50% cases the manual correction along each axis was ≤1 pixel.

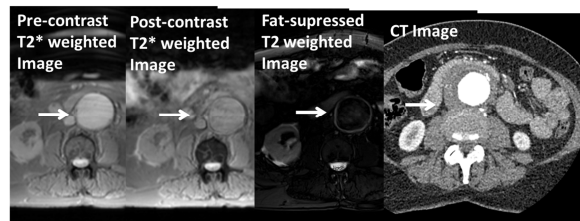


Figure 1 Images involved: from left to right, pre- and post-contrast T2*W image, T2W image with fat-suppression, CT image, white arrow pointing to aorta.

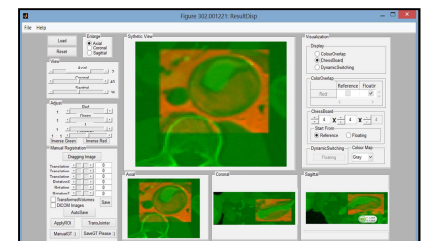


Figure 2 The GUI used to collect manual registration results showing aligned CT-MR volume using overlapped colour channel.

DISCUSSION

We have investigated the accuracy of a new method for aligning AAA in multi-modality and multi-parametric imaging. >50% of performed registrations gained sub-pixel accuracy. Using manual "corrections" to validate the results may cause over-estimated errors when rotational adjusting involved. Inter-parametric MR registration gained better results than MR-CT registrations because of larger non-rigid distortion and morphological irrelevances in the latter case. However, this may also be caused by the larger coverage of the CT volumes. As a result, small rotations will cause relatively larger changes in translation. Performance of registration can be improved by modifying parametric settings, e.g., increasing number of iterations, searching space, bin numbers, etc. Non-rigid registration can be easily integrated into this registration framework.

ACKNOWLEDGEMENTS

This work was funded from contributions by the Medical Research Council, British Heart Foundation and the Scottish Universities Physics Alliance INSPIRE award.

REFERENCES

- Richards J, et al. Abdominal aortic aneurysm growth predicted by uptake of ultrasmall superparamagnetic particles of iron oxide: a pilot study. *Circulation: Cardiovascular Imaging*, 2011; 4(3):274-281.
- Knops Z, et al. Normalized mutual information based registration using k-means clustering and shading correction. *Medical Image Analysis*, 2006;10(3):432-439.
- Finkel D. DIRECT optimization algorithm user guide. Center for Research in Scientific Computation, North Carolina State University, 2003.


Table 1 MR image registration errors, including, translational and rotational errors in x, y, z and mean Euclidean errors and rotational errors calculated as the an equivalent single rotation resulted by the rotational errors of x, y, and z. Translational error represents in number of pixels and rotational error in degrees where all images were down sampled to 1.5625mm per pixel.

axis	T2*W-T2*W				T2W-T2*W			
	Translation	Rotation	Euclidean Translation	Rotation Angle	Translation	Rotation	Euclidean Translation	Rotation Angle
x	1.0556	0.7037	1.76	0.81	0.9032	0	1.55	0.04
y	1.1296	0.2407			1.2984	0		
z	1.0833	0.5556			0.4919	0.0323		


Table 2 T2*W-CT registration errors, including translational and rotational errors in x, y, z and final Euclidean errors and rotational errors calculated as an single rotation composed by rotation errors around x, y and z. Translational error represents in number of pixels and rotational error in degrees where all images were down sampled to 1.5625mm per pixel.


Axis	Translation	Rotation	Euclidean Translation	Rotation Angle
x	1.0455	0.3409	2.70	0.69
y	1.7500	0.0909		
z	0.9091	0.3182		

A.2 Electronic poster presented in ISMIRM2014



A Robust Automated Multi-modality Registration Tool Applied to Abdominal Aortic Aneurysm





Author: Chengjia Wang¹, Georgia Koutraki¹, Olivia McBride¹, Alex Vesey¹, Tom MacGillivray¹, Calum Gray¹, David Newby¹, Keith Goatman², Scott Semple¹

¹University of Edinburgh, ²Toshiba Medical Visualization System-Europe


TOSHIBA
Leading Innovation

14:30, 13 MAY 2014
Computer No.: 31


Contents	
	Introduction
	Methodology
	Results
	Conclusion and Discussion

Introduction

Surveillance for abdominal aortic aneurysms (AAA) using Magnetic Resonance (MR) Imaging and Image Registration



scan to watch on phone



Introduction -- Summary

MA3RS Clinical Trial

- Other than using ultrasound, a novel clinical trial using Magnetic Resonance (MR) Imaging with Ultrasmall Superparamagnetic Particles of Iron Oxide (USPIO) were developed in Clinical Research Imaging Centre (CRIC), University of Edinburgh (UoE) to predict clinical outcome in patients under surveillance for AAA;

Image Registration

- A new multimodality 3D image registration method was developed to mix the information of different types of images in this study.

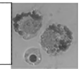
Contents	
	Introduction
	Methodology
	Results
	Conclusion and Discussion

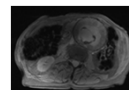
Method – MA3RS

Theory

Uptake of USPIO in the aortic wall (shown in blue):

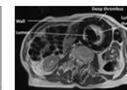
- Correlates with macrophage activity, identifies cellular inflammation
- Distinguishes aneurysms with higher growth rates





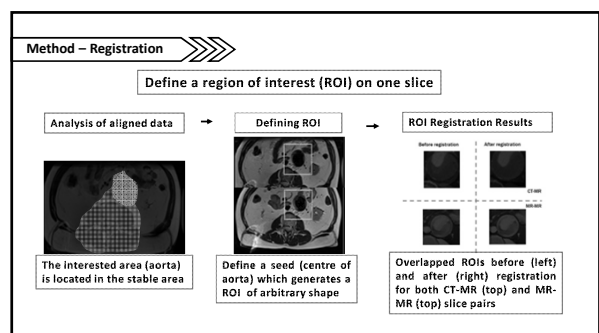
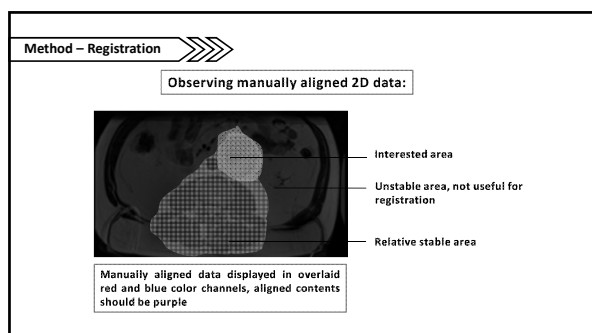
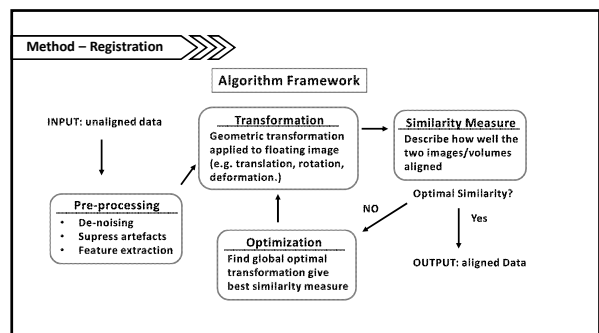
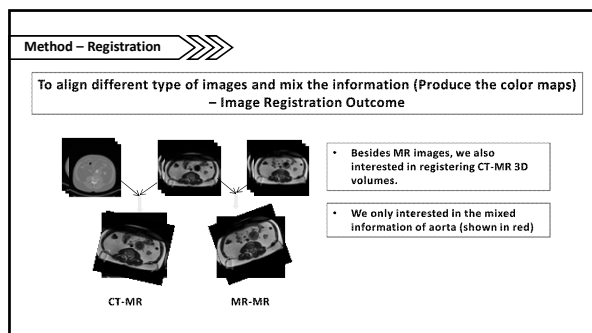
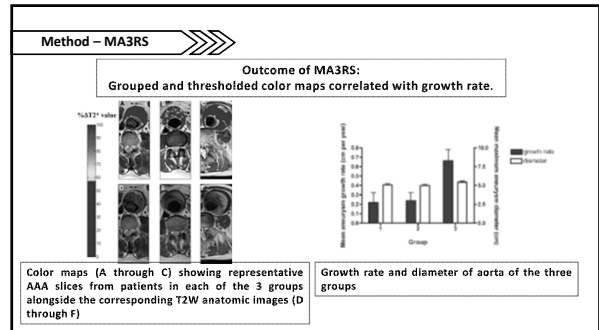
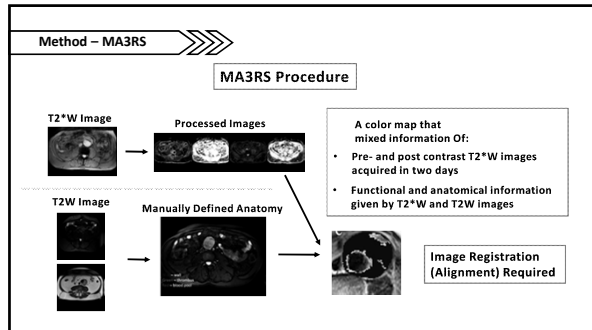
T2*W Image:

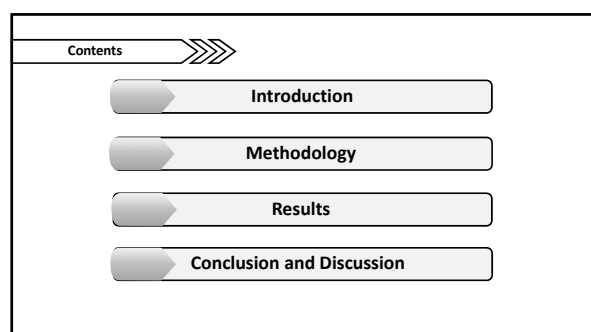
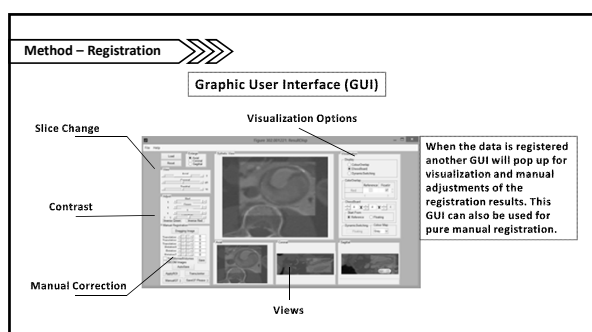
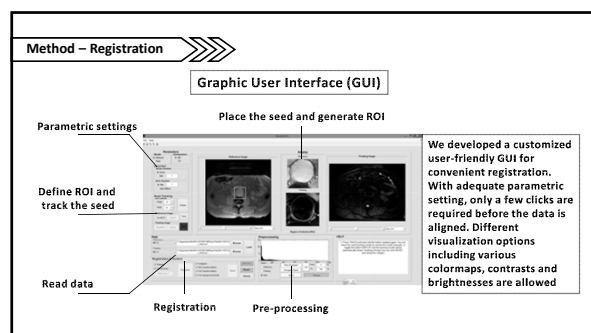
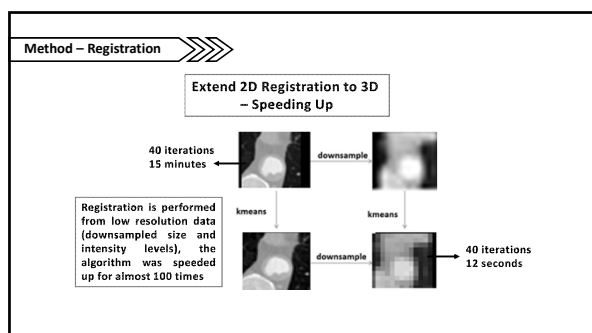
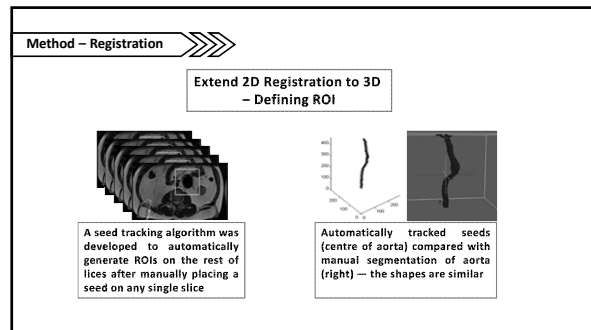
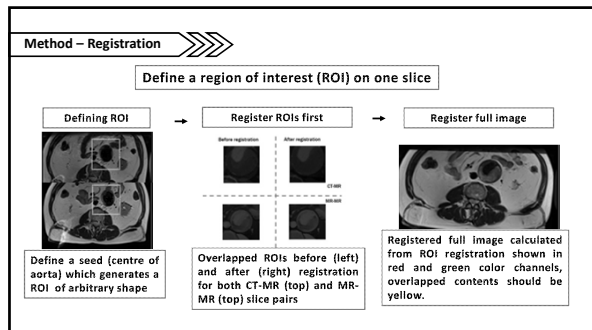
- Functional Information
- Better for observing USPIO uptake

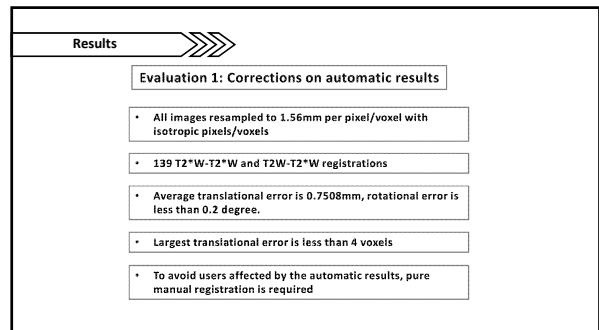
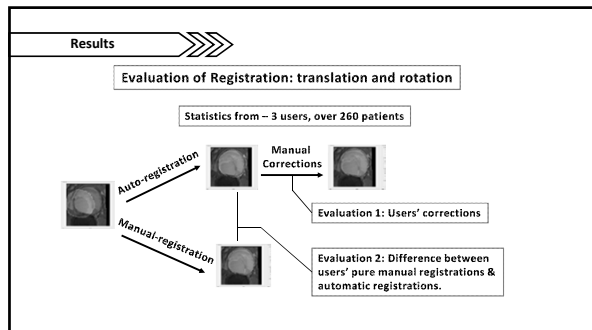


T2W Image:

- Anatomical Information
- Better for defining different anatomical structures







Results

Evaluation 2: using Pure Manual Registration

- All images resampled to 1.56mm per pixel/voxel with isotropic pixels/voxels
- 78 T2*W-T2*W and T2W-T2*W registrations, 78 CT-T2*W registrations
- Over 55% MR-MR registrations and 35% CT-MR registrations achieved sub-pixel accuracy

Pre-contrast T2*W - Post-contrast T2*W					
Axis	Translation	Rotation	Euclidean Translation	Euclidean Angle	Sub-pixel Accuracy
x	1.0556	0.3027	1.76	0.81	
y	1.1296	0.2607			
z	1.0833	0.1556			

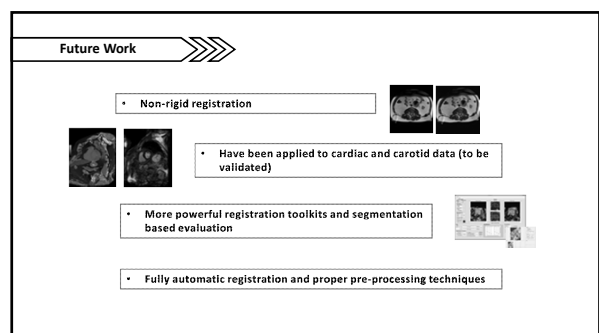
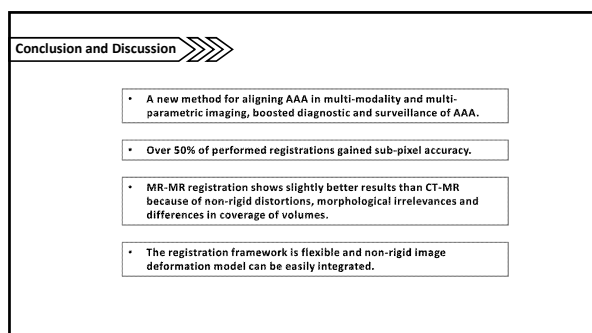
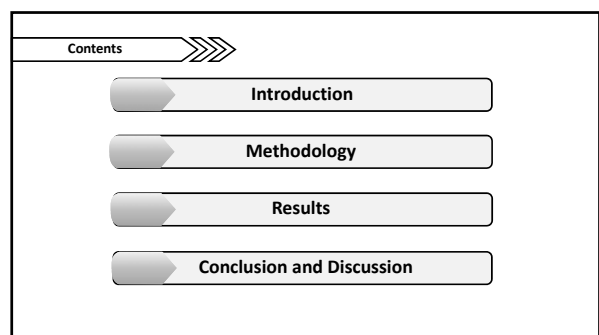
T2*W registration errors

T2W - T2*W					
Axis	Translation	Rotation	Euclidean Translation	Euclidean Angle	Sub-pixel Accuracy
x	0.9032	0	1.55	0.04	
y	1.2944				
z	0.4919	0.0323			

T2W-T2*W registration errors

CT-T2*W					
Axis	Translation	Rotation	Euclidean Translation	Euclidean Angle	Sub-pixel Accuracy
x	1.0403	0.3409	2.70	0.69	
y	1.7500	0.0909			
z	0.9091	0.3162			

CT-T2*W registration errors



Acknowledgements

LOGOs for all the following companies

- SUPA
- Toshiba
- University of Edinburgh
- CRIC
- MRC (medical research council)
- BHF (British Heart Foundation)
- List of names that involves in MA3RS and my PHD

Thank you !



A.3 Conference paper published of IEEE ISBI2015

AUTOMATIC MULTI-PARAMETRIC MR REGISTRATION METHOD USING MUTUAL INFORMATION BASED ON ADAPTIVE ASYMMETRIC K-MEANS BINNING

C. Wang^{1,2,3}, K. A. Goatman³, T. MacGillivray^{1,4}, E. Beveridge³, Y. Koutraki², J. Boardman⁵,
C. Stirrat², S. Sparrow⁵, E. Moore⁵, R. Paraky⁵, S. Alam², M. Dweck², C. Chin², C. Gray^{1,2},
D. Newby^{1,2}, S. Semple^{1,2}

¹ Clinical Research Imaging Centre, University of Edinburgh, Edinburgh, UK

² BHF Centre for Cardiovascular Science, University of Edinburgh, Edinburgh, UK

³ Toshiba Medical Visualization System - Europe, Edinburgh, UK

⁴ Centre for Clinical Brain Sciences, University of Edinburgh, Edinburgh, UK

⁵ MRC Centre for Reproductive Health, University of Edinburgh, Edinburgh, UK

ABSTRACT

Multi-parametric MR image registration combines different imaging sequences to enhance visualisation and analysis. However, alignment of the different acquisitions is challenging, due to contrast-dependent anatomical information and abundant artefacts. For two decades, voxel-based registration has been dominated by methods based on mutual information, calculated from the joint image histogram. In this paper, we propose a modified framework — based on an asymmetric cluster-to-image mutual information metric — that increases registration speed and robustness. A new parameter, the homogeneous dynamic intensity range, is used to determine to which image clustering is applied. The framework also includes a semi-automatic 3D region of interest, multi-resolution wavelet decomposition, and particle swarm optimization. Performance of the framework, and its individual components, were evaluated on two diverse datasets, comprising cardiac and neonatal brain datasets. The results demonstrated the method was more robust and accurate than mutual information alone.

Index Terms— Multi-parametric registration, k-means binning, histogram specification, ROI-tracking.

1. INTRODUCTION

For two decades, research on multi-modal and multi-parametric registration of 3D CT and MRI data has relied on entropy-based voxel similarity measures, such as mutual information (MI)[1]. Mutual information is usually calculated from the joint intensity histogram, calculated by equidistant binning of the image intensities. However, with equidistant bins the quality of the result depends critically on the number of bins chosen to quantise the data: too many bins results in the dispersion of single anatomical structures across multiple bins — due to intensity inhomogeneities — while too few bins results in the combination of disparate anatomical structures

within the same bin. There are many non-equidistant binning strategies, for example histogram equalization or k-means clustering[2]. However, important information can also be lost by inappropriate clustering. An asymmetric cluster-to-image non-rigid registration method was proposed to reduce this problem for multi-modal CT-MR alignment. It only performs k-means clustering on the CT data[3]. However, when registering multi-parametric MR data it is unclear which dataset should be the target for k-means binning, and experiments demonstrate that the selection of which image to cluster has a significant effect on accuracy.

This paper presents a novel co-registration framework that is shown to be more robust to intensity differences between images than using mutual information alone. The performance of the framework is demonstrated using two quite different sets of data from ongoing clinical studies (cardiac data and neonatal brain data). Experiments were performed to show how the different stages of the proposed framework are important to the accuracy and robustness of the results.

2. METHODS

Given a floating image, \mathcal{F} , and a reference image, \mathcal{R} , registration aims to find the transformation, $\hat{\mathcal{T}}$, that optimizes a given similarity measure, $\mathcal{S}\{\mathcal{R}, \mathcal{F} \circ \mathcal{T}\}$, where \mathcal{T} is the transformation applied to \mathcal{F} . Our method constrains \mathcal{T} to be a rigid-body transformation, which is calculated within a semi-automatic 3D region of interest (ROI), described in section 2.1.

One of the images (either the reference or floating image) is chosen to undergo k-means intensity binning. A new parameter, the homogeneous dynamic intensity ratio (HDIR) described in section 2.2, is used to determine which image the k-means binning is applied to. The data with the larger dynamic range is chosen for asymmetric k-means binning. Meanwhile, the non-clustered image is corrected by ranked histogram specification to achieve similar intensity homogene-

ity with the clustered image. The similarity between \mathcal{R} and $\mathcal{F} \circ \mathcal{T}$ (one of which has undergone k-means binning, the other ranked histogram specification) is measured using mutual information. The optimal transformation is estimated using a particle swarm optimizer (PSO) [4]. Finally, a wavelet decomposition-based multi-resolution scheme is incorporated to increase the speed and robustness of the result.

2.1. Registration region of interest

Limiting the registration calculation to a specific region of interest can greatly improve registration robustness. Indeed, it may be essential where different regions of the image undergo separate transformations. Two strategies were used for semi-automatic definition of the regions of interest on the data in this project: for the neonatal brain datasets a fixed-size enclosing cuboid was placed over the brain; for the cardiac data an adaptive scheme was developed that is described below.

For the cardiac data, a square ROI is first defined on the k th slice, μ_k , of the K -slice 3D data $\mu = \{\mu_k\}, k = 1, 2, \dots, K$. Once the ROI, \mathcal{R}_{μ_k} , is picked on μ_k , the optimal ROI, \mathcal{R}_{μ_j} , on the neighbouring slice, $\mu_j, j \in \{k-1, k+1\}$, is tracked by minimizing the sum of square difference (SSD) of intensities:

$$\hat{\mathcal{R}}_{\mu_j} = \arg \min_{\mathcal{R}_{\mu_j} \in \Omega_{\mu_j}} \sum |\hat{\mathcal{R}}_{\mu_k} - \mathcal{R}_{\mu_j}|^2, \quad (1)$$

where Ω_{μ_j} is the search area, defined on μ_j but centred on the same coordinate with $\hat{\mathcal{R}}_{\mu_k}$. This results in a bi-directional growth of the 3D ROI, starting from μ_k and ending when it covers the entire 3D dataset.

These 2D ROIs may then be refined, for example using a circular Hough Transform [5] to automatically detect objects, such as the aortic wall in abdominal data, or the left-ventricle in short-axis cardiac data, as shown in figure 1(a)). Figure 1(b) shows the trajectory of the automatically tracked 2D-ROI centres from a standard contrast enhanced CT dataset acquired in a clinical trial on an Aquilion ONE (Toshiba Medical Systems, Japan).

Initial alignment can be achieved by registering the 2D-ROI centres using the iterative closest points (ICP) algorithm [6]. Alternatively, if the correspondences between slices are known, least square methods can be applied to solve this problem analytically, using singular value decomposition (SVD)[7]. Figure 1(c) and 1(d) show examples of initial alignments obtained on T2*-weighted (T2*W) and delayed enhancement cardiac MR data.

2.2. Intensity Distribution Correction and K-means Binning

The motivation for calculating MI using asymmetric k-means binning in CT-MR multi-modality registration is to overcome the histogram dispersion problem, without breaking the ability

to distinguish detailed structures [3]. When applying asymmetric k-means binning to multi-parametric MR data the optimal target for the k-means binning needs to be selected carefully. Clustering the image with less dynamic intensity range, and more severe inhomogeneities, may emphasize the dispersion effects on histograms. A histogram-based measure, HDIR, was derived to measure the dynamic intensity ranges and inhomogeneities of the reference and floating images.

Let $\rho_\mu(\bullet)$ be the probability densities function (PDF) of the normalized voxel intensity, $i \in [0, 1]$, of image μ . A probability $\hat{\mathcal{P}}_\mu$ is defined as:

$$\hat{\mathcal{P}}_\mu = \sum_{i \in [b_L, b_U]} \rho_\mu(i), \quad (2)$$

where b_L and b_U are two thresholds defined on image intensity. Given two images, μ and ν , the HDIR is:

$$\text{HDIR} = \frac{\text{std}(\hat{\mathcal{H}}_\mu) \hat{\mathcal{P}}_\mu}{\text{std}(\hat{\mathcal{H}}_\nu) \hat{\mathcal{P}}_\nu}, \quad (3)$$

where $\hat{\mathcal{H}}_\mu$ is the intensity histogram for image μ , excluding the intensity values larger than b_U or smaller than b_L , and similarly $\hat{\mathcal{H}}_\nu$ is the truncated histogram for ν . $\text{std}(\bullet)$ represents the standard deviation of the histogram. $\hat{\mathcal{P}}_\mu$ and $\hat{\mathcal{P}}_\nu$ are the probabilities calculated using equation 2 for μ and ν . Here $b_L = 0.05$ and $b_U = 0.95$ were used.

If the $\text{HDIR} \geq 1$ then the k-means binning is applied to image μ , otherwise to ν . Ranked histogram specification is applied to the other image to correct its intensity distribution. Let ϕ_μ and ϕ_ν the cumulative density function (CDF) of the two images. When $\text{HDIR} \geq 1$, conventional histogram specification [8] maps the intensity distribution of ν by a transformation function $\psi_{\nu \rightarrow \mu} = \phi_\mu^{-1}(\phi_\nu(\bullet))$. But different from [8], here we introduce transformation functions $f_\mu(\bullet)$ and $f_\nu(\bullet)$ which re-arranges the histograms of image μ and ν in descending order by ρ_μ and ρ_ν . Then calculate the CDFs of both re-arranged histograms, denoted as $\phi_{f_\mu}(\bullet)$ and $\phi_{f_\nu}(\bullet)$. The transformation function of this re-arranged histogram specification then becomes $\psi_{\nu \rightarrow \mu} = f_\nu^{-1}(\phi_{f_\nu}^{-1}(\phi_{f_\mu}(\psi_{\nu \rightarrow \mu})))$.

To reduce the sensitivity of k-means to initialization of cluster centres, we deployed the ‘‘top-to-down’’ k-means method[3], except that we uniformly initialize a large number of cluster centres at the start. Then neighbouring clusters with distances smaller than a threshold are merged. This framework performs k-means clustering and intensity distribution correction simultaneously, as shown in figure 2.

2.3. Registration Framework Implementation

To improve speed and robustness, a multi-resolution approach based on the discrete wavelet transformation, was used. Registration starts from the lowest to the highest resolution. When performing k-means clustering, with an L -level wavelet pyramid, the largest number of cluster centres, \mathcal{N}_k , on the k th layer of the pyramid is limited to $\max(48, 8 * k), k = 1, 2, \dots, L$.

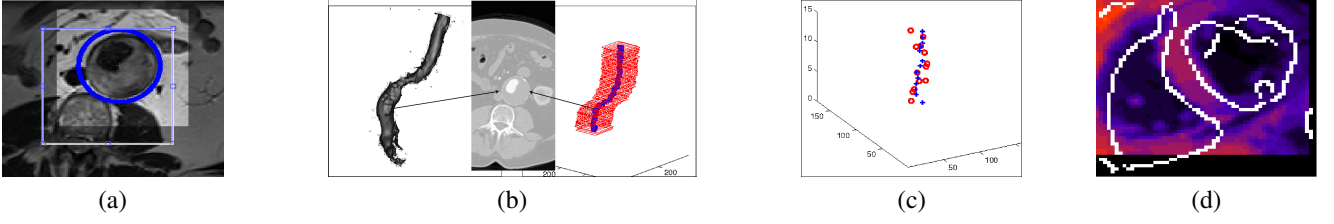


Fig. 1. Automatic 3D ROI tracking: (a) Automatically tracked aorta (blue circle) and the adjusted 2D ROI (brightened area); (b) Manually segmented aorta (left) on CT data (centre) compared with automatic ROI (right); (c) ROI centres following initial alignment; (d) Result of initial alignment on cardiac data.

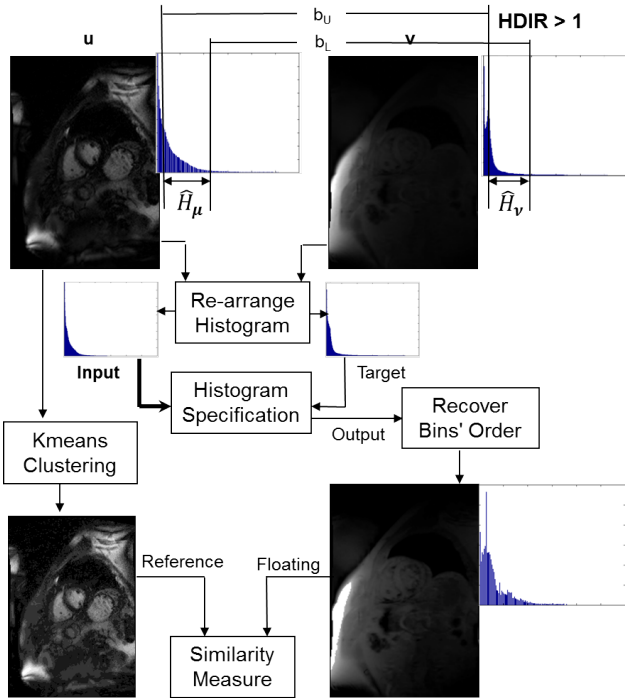


Fig. 2. K-means binning and intensity distribution correction.

For robust registration and efficient searching, we use global, gradient-independent, optimizers. In our previous work [9], the DIRECT optimization algorithm [10] was used. Despite various improvements it still struggles to avoid local optima. In this work we use a PSO [4] to search for the optimal transformation. Experiments show that only 60 initial particles are necessary to solve these rigid-body registration problems.

3. EXPERIMENTS AND VALIDATION

The registration method was validated using two diverse datasets, both acquired as part of on-going clinical trials. Both sets of data were registered using the three-level multi-

resolution framework described above.

3.1. Cardiac Data

Multi-parametric MR data was acquired from 30 patients. Data were contiguous throughout the short axis, and were ECG-gated for diastole during an expired breath-hold. These constraints mean a rigid-body transform was sufficient for this application. Each subject had one delayed enhancement volume, one pre-contrast, and at least three post-contrast T2*W volumes. All data have a resolution of $1.56 \times 1.56 \times 10$ mm, and suffer from significant inhomogeneities and motion-related artefacts. The ROI was defined to cover the whole left ventricle and main structures of the heart. We tested 45 post-to-pre-contrast T2*W image registrations, and 53 T2*W to delayed enhancement image registrations.

The registration performance was evaluated by manual corrections performed by experienced clinicians. Errors were calculated in the form of Euclidean distances and Euler angles.

3.2. Neonatal Data

Thirty-one neonatal brain volumes were acquired at 38–44 weeks post-menstrual age during natural sleep. Data with different contrasts (T1-weighted MPRAGE, T2-weighted SPACE) were obtained. Some neonatal motion between scans, and repositioning of waking neonates between acquisitions, was experienced. The data were aligned using a rigid-body transform, calculated within a $51 \times 51 \times 41$ mm ROI, manually centred on the brain. Registration accuracy was assessed using the target registration error (TRE), calculated from 18 corresponding landmarks placed on each volume (giving a total of 1908 corresponding landmarks).

	Translation	Rotation
T2*W to T2*W	1.76	0.81
T2*W to DE	1.55	0.04

Table 1. Translational and Rotational Errors of Cardiac Registration: voxels and degrees of manual correction.

Furthermore, to test the importance of each step in the

Method	This Method	Gaussian-pyramid	No-kmeans	No-Histogram Specification	DIRECT [10]	Reverse-clustering	Method [9]
Median	1.88	2.11	3.29	1.97	2.45	1.99	2.14
STD	1.72	1.82	4.40	3.32	4.04	4.42	4.15
Failures	1	1	2	2	3	4	2

Table 2. Registration Accuracy Evaluated by median and standard deviation (STD) of TREs.

overall registration framework, several components were either omitted completely or exchanged with alternative methods. The changes were: (a) Gaussian pyramid instead of the wavelet pyramid; (b) omitting the k-means step; (c) omitting the histogram specification step; (d) replacing the with the DIRECT optimizer; and (e) reversing the decision of clustered and non-clustered image. Finally, the results were also compared with our previous algorithm [9]. Registrations with TREs larger than 8 mm are easy to detect by visual inspection, and are considered failures.

4. RESULTS

4.1. Cardiac Data

The average rotational and translational errors across the 98 registrations are shown in table 1. The mean translational and rotational errors are 1.61 voxels (approximately 2.66 mm) and 0.68 degrees, respectively. 55% of the registrations achieved sub-pixel accuracy, and 40% could not be improved further by manual adjustment.

4.2. Neonatal Data

Table 2 illustrates the results from the 31 T2W–T1W MR registrations. The new algorithm presented here gave smaller TREs than our previous methodology, and produced fewer complete failures. Omitting or exchanging any of the algorithm steps described earlier resulted in worse registration accuracy.

5. DISCUSSION

We have introduced a multi-parametric MR data registration framework that is more robust to data intensity differences than mutual information alone. Registration performance was evaluated using multi-parametric cardiac and neonatal data. Omitting or exchanging any of the algorithm steps led to larger registration errors. Many parts of the algorithm may be trivially parallelized.

6. REFERENCES

- [1] Timo Mäkelä, Patrick Clarysse, Outi Sipilä, Nicoleta Pauna, Quoc Cuong Pham, Toivo Katila, and Isabelle E Magnin, “A review of cardiac image registration methods,” *IEEE transactions on medical imaging*, vol. 21, no. 9, pp. 1011–21, Sept. 2002.
- [2] Z F Knops, J B a Maintz, M a Viergever, and J P W Pluim, “Normalized mutual information based registration using k-means clustering and shading correction,” *Medical image analysis*, vol. 10, no. 3, pp. 432–9, June 2006.
- [3] Yixun Liu and Nikos Chrisochoides, “Using k-means clustering and mi for non-rigid registration of mri and ct,” in *International Workshop on Machine Learning in Medical Imaging (MLMI), the 13th International Conference on Medical Image Computing and Computer Assisted Intervention (MICCAI)*, September 2010.
- [4] Russ C Eberhart and James Kennedy, “A new optimizer using particle swarm theory,” in *Proceedings of the sixth international symposium on micro machine and human science*. New York, NY, 1995, vol. 1, pp. 39–43.
- [5] HK Yuen, J Princen, J Illingworth, and J Kittler, “Comparative study of hough transform methods for circle finding,” *Image and Vision Computing*, vol. 8, no. 1, pp. 71–77, 1990.
- [6] Timothée Jost, “Fast icp algorithms for shape registration,” *Pattern Recognition*, vol. 2449, pp. 1–8, Oct. 2002.
- [7] Jacob Beutel, J Michael Fitzpatrick, Steven C Horii, Yongmin Kim, Harold L Kundel, Milan Sonka, and Richard L Van Metter, *Handbook of Medical Imaging, Volume 3. Display and PACS*, Washington, DC: SPIE Press, 2002.
- [8] Dinu Coltuc, Philippe Bolon, and J-M Chassery, “Exact histogram specification,” *Image Processing, IEEE Transactions on*, vol. 15, no. 5, pp. 1143–1152, 2006.
- [9] Chengjia Wang, Georgia Koutraki, Olivia McBride, Alex Vesey, Tom MacGillivray, Calum Gray, David Newby, Keith Goatman, and Scott Semple, “A robust automated multi-modality registration tool applied to abdominal aortic aneurysm [abstract],” in *Joint Annual Meeting ISMRM-ESMRMB 2014, Milano, Italy*, 2014.
- [10] Daniel E Finkel, “Direct optimization algorithm user guide,” *Center for Research in Scientific Computation, North Carolina State University*, vol. 2, 2003.

A.4 Poster presented in IEEE ISBI2015

Automatic Multi-Parametric MR Registration Method Using Mutual Information Based on Adaptive Asymmetric K-means Binning

C. Wang^{1,2}, K. A. Goatman², T. MacGillivray¹, E. Beveridge¹, Y. Koutraki¹, J. Boardman¹, C. Stirrat¹, S. Sparrow¹, E. Moore¹, R. Paraky¹, S. Alam¹, M. Dweck¹, C. Chin¹, C. Gray¹, D. Newby¹, and S. Semple¹

¹University of Edinburgh, ²Toshiba Medical Visualization System-Europe



Introduction

Purpose

A robust multi-parametric MR image co-registration framework, based on an adaptive asymmetric cluster-to-image mutual information (MI) metric.

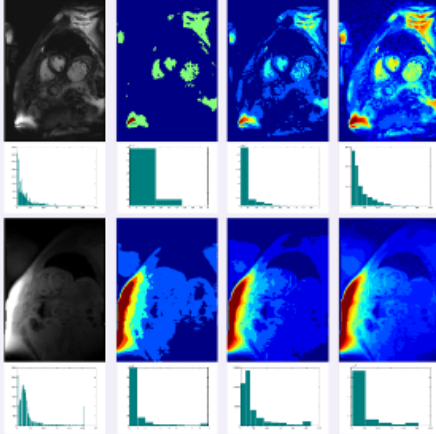


Figure 1 : Different binning strategies with different imaging qualities: the middle two columns show situations of equidistant binning, the right column displays k-means binning.

Why? – failed registrations using MI

MI is usually calculated from the joint intensity histogram. Because of bad image quality, inadequate equidistant or in-equidistant binning can cause failed registrations, as shown in figure 1. Asymmetric k-means binning [1] for CT-MR registration can't be directly applied to multi-parametric MR registration as it's unclear which MR image should be the target of k-means binning.

Method: Algorithm

Framework: (as shown in figure 2):

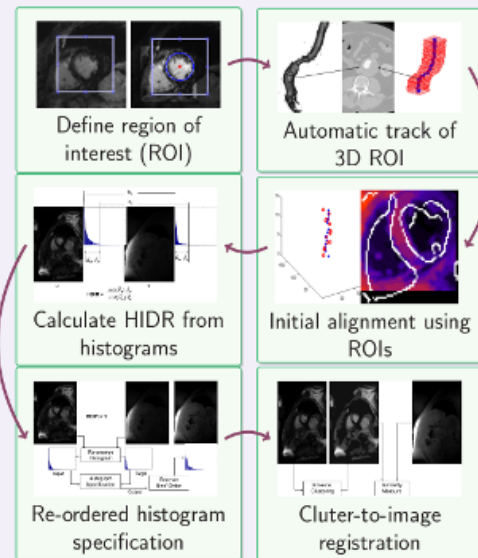


Figure 2 : Algorithm framework: given the floating and reference images, this framework searches for a rigid transformation that optimizes cluster-to-image MI.

Main contributions:

1. A new parameter, the homogeneous dynamic intensity ratio (HDR), used to determine which image has intensity homogeneity suitable for k-means binning;
2. A ranked histogram specification method (RHS) used to improve the intensity homogeneity of the non-clustered image.

Method: Details

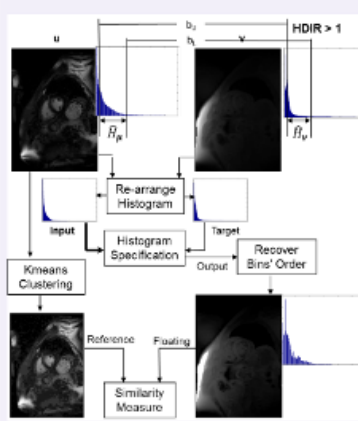


Figure 3 : Algorithm framework

Adaptive asymmetric cluster-to-image registration:

1. Given reference image, μ , and floating image, ν : Let ρ_μ be the probability densities function (PDF) of the normalized voxel intensity. A probability \hat{P}_μ is defined as:

$$\hat{P}_\mu = \sum_{i \in [b_L, b_U]} \rho_\mu(i), \quad (1)$$

where b_L and b_U are two thresholds defined on image intensity, the HDR is:

$$HDR = \frac{\text{std}(\hat{H}_\mu) \hat{P}_\mu}{\text{std}(\hat{H}_\nu) \hat{P}_\nu}, \quad (2)$$

where \hat{H}_μ is the intensity histogram between b_L and b_U ;

2. If $HDR \geq 1$, k-means binning is applied to μ , otherwise to ν . Ranked histogram specification is applied to the other image to correct its intensity distribution;
3. Particle swarm optimizer (PSO) and a wavelet-based image pyramid are used to search for optimal transformation.

Implementation & Experiments

Images to be registered:

1. Short axis cardiac data: T2*W pre- and post-contrast data, and standard clinical delayed enhancement (DE) data. 45 post-contrast T2*W image registrations, and 53 T2*W to DE image registrations were tested.
2. Neonatal brain sMRI and dMRI: T1W MPRAGE and T2W SPACE data. 30 Registrations were performed.

Registration software:

We developed a user-friendly graphic user interface (GUI), as shown in figure 4, for experiments above.

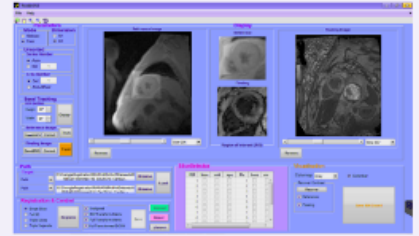


Figure 4 : The Registration GUI

Results

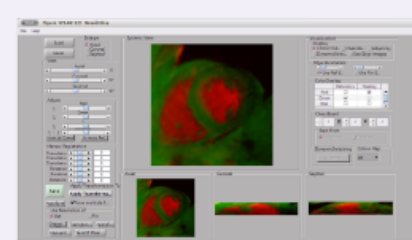


Figure 5 : The GUI used for visualizing the registration results.

Cardiac Data (Table 1):

The registration performance was evaluated by manual corrections performed by experienced clinicians using GUI shown in figure 5, in the form of Euclidean distances and Euler angles.

	Translation	Rotation
T2*W to T2*W	1.76	0.81
T2*W to DE	1.55	0.04

Table 1 : Translational and Rotational Errors of Cardiac Registrations: voxels and degrees of manual correction.

Neonatal Data (Table 2):

Method	This Method	Gaussian-pyramid	No-kmeans	No-Histogram Specification	DIRECT [2]	Reverse-clustering	Method [3]
Median	1.88	2.11	3.29	1.97	2.45	1.99	2.14
STD	1.72	1.82	4.40	3.32	4.04	4.42	4.15
Failures	1	1	2	2	3	4	2

Table 2 : Registration Accuracy Evaluated by median and standard deviation (STD) of TREs: The method proposed in this work is underlined. Gaussian-pyramid method replaces wavelet image pyramid with Gaussian pyramid. No-Kmeans method simply uses linear binning when calculating mutual information. No-HS method does not perform histogram specification. DIRECT was used to replace the PSO searching. Finally, our previous method [3] was also evaluated.

1. Registration accuracy was assessed using the target registration error (TRE), calculated from 18 corresponding landmarks placed on each volume.
2. To test the importance of each step in the overall registration framework, several components were either omitted completely or exchanged with alternative methods.

Conclusion and Discussion

We introduced a multi-parametric MR data registration framework that is more robust to intensity differences than mutual information alone.

Non-rigid transformation model will be adopted. And more the method will be tested on various applications, for example, as shown in figure 6.

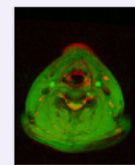


Figure 6 : Carotid registration example

References

1. Liu Y, et al. 2010.
2. Finkel D, 2003.
3. Wang C, et al. 2014.

Want to watch a video about another application of this registration software? Scan the binary code on the left.



A.5 Posters presented in ESMRMB2015

Introduction

Purpose

In this work we demonstrate a software for automatically registering multi-parametric and multi-contrast Cardiac MR (CMR) data. This tool is robust to common artefacts which can lead to failure of automatic analysis. An example is shown in figure 1. It has been applied to the IRNMAN study, led by the Clinical Research Imaging Centre (CRIC) and the Centre for Cardiovascular Science (CVS), University of Edinburgh, aiming to assess inflammation in the myocardium post-myocardial infarction, through a combination of multi-contrast MR images.

Difficulties

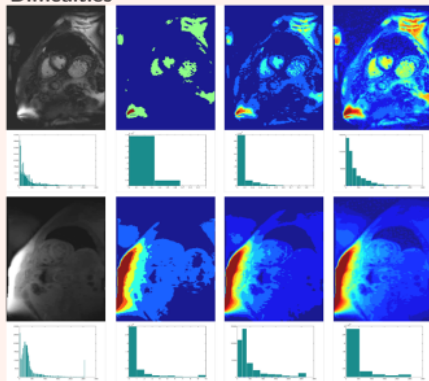


Figure 1: Pre-processing used in our previously proposed registration algorithm: different binning strategies with different imaging qualities. The middle two columns show histograms of equidistant binning and k-means binning.

Mutual information (MI) is a common technique used in many registration methods, calculated from the joint intensity histogram. However, common artefacts in MR images, for example, the intensity inhomogeneity shown in figure 1 may cause wrong calculation of histogram which may destroy registration performance.

Solution Framework

Workflow (Figure 2)

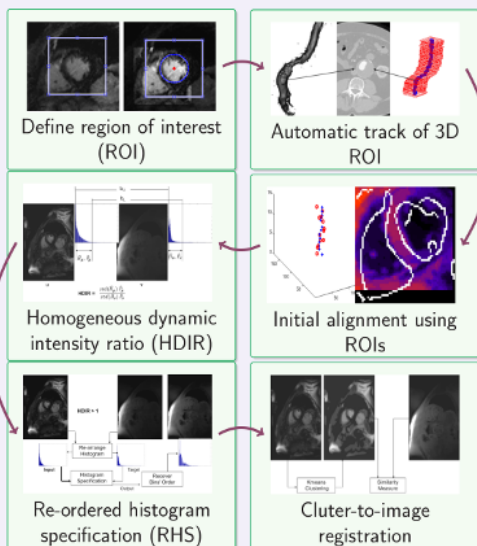


Figure 2: Rigid Registration Workflow

As shown in figure 2, user selects a ROI on once slice. The heart is automatically tracked on other slices. Rough registration is performed using ROI centres. Then the images are evaluated using the homogeneous dynamic intensity ratio (HDIR) to determine which one has better quality. Image appearance of the image with worse quality is corrected. Registration used our cluster-to-image method [1].

Technical contributions:

- 1.HDIR, used to determine which image has better intensity homogeneity;
- 2.Ranked histogram specification method (RHS) was used to improve the intensity homogeneity.

Graphic User Interface (GUI)

Registration Window (Figure 3)



Figure 3: The Registration GUI

In this window, you can: 1. Select parameters pre-configuration; 2. Load both images; 3. Select ROI centre to generate a ROI of an arbitrary shape, and save its co-ordinate; 4. Perform simple pre-processing; 5. Launch the registration.

Visualization Window (Figure 4)

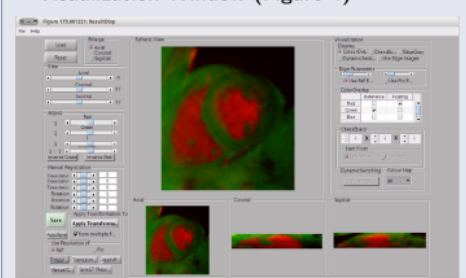


Figure 4: The Visualization GUI

In this window, you can: 1. Visualize the data from a 3D view using different techniques; 2. Manually perform/adjust rigid registrations and save results; 3. Apply a transformation to any data; 4. Enjoy customized button for your specific clinical trials.

Experiment on IRNMAN Data

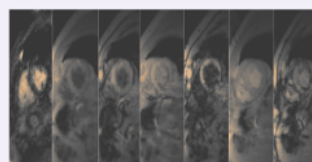


Figure 5: IRNMAN CMR data example: from left to right, delayed enhancement data (1), multi-echo pre-contrast (2-3) and post-contrast (4-7) data.

Data were collected and processed as follows:

1. Data from 30 patients with a dedicated 32-channel body matrix array;
2. ECG-gated data acquired during diastole and expired breath-holding;
3. Each subject had: 1 delayed enhancement volume, 1 pre-contrast, and at least 3 post-contrast T2*W volumes, as shown in figure 5, acquired on different days after infusion of a USPIO-based contrast agent;
4. Data were acquired contiguously throughout the short axis, with 10mm slice width and an in-plane resolution of 1.56mm².
5. Rigid body registration allowed transformation of 6 degree-of-freedom.

Experiment Results

Visualization of Results (Figure 6)

We provide a variety of options so that our users can choose the best one based on specific applications:

1. Overlapped colour channels;
2. Chess board visualization;
3. Edge image overlapped with gray image;
4. Multiple choices of colour maps.

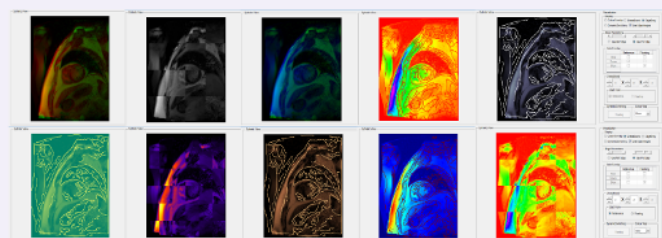


Figure 6: Visualizations of Registered Images

Performance of Automatic Registration (Table 1)

Table 1: Registration errors obtained from 16 patients, includes, translational and rotational errors in x, y, z and mean Euclidean errors and rotational errors calculated the equivalent Euler angle resulted by single rotation. Translational error is represented in number of pixels and rotational error in degrees where all images were down sampled to 1.5625mm per pixel.

axis	Post- to Pre-contrast T2*W				T2*W to Delayed Enhancement			
	Translation	Rotation	Euclidean Translation	Rotation Angle	Translation	Rotation	Euclidean Translation	Rotation Angle
x	0.6567	0.1657	1.34	0.38	1.125	0.1364	1.83	0.95
y	1.375	0.0834			1.1563	0		
z	0	0.3333			0.0455	1.0625		

1. The performance was evaluated by comparing the automatic results with the corresponding pure manual alignments performed by different clinicians;
2. 45 pre- to post-contrast T2*W and 53 T2*W to Delayed enhancement registrations were performed;
3. 55% of all achieved sub-pixel accuracy, and 40% couldn't be improved further by any manual adjustment.

Conclusion and Discussion

We developed an automatic multi-contrast and multi-parametric CMR registration software with our a robust registration algorithm integrated. This tool has been applied to a real clinical trial. The future work includes:

1. Adopt non-rigid transformation model;
2. Organ detection methods for fully automatic registration;
3. More algorithms will be tested on various applications, for example, the carotid data shown in figure 7.

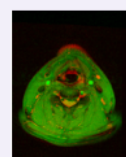


Figure 7: Carotid registration example

References

1. Wang et al., "Automatic multi-parametric MR registration method using mutual information based on adaptive asymmetric k-means binning", IEEE ISBI 2015.

Acknowledgements: This work is funded by the Medical Research Council, British Heart Foundation Centre of Research Excellence award and the Scottish Universities Physics Alliance INSPIRE award.

Want to watch a video about another application of this registration software? Scan the binary code on the right.



A robust automated multi-parametric registration software applied to neonatal MR neuro data

C. Wang¹, T. MacGillivray², Y. Koutraki¹, J.P. Boardman³, S. Sparrow³, R. Pataky³, and S. Semple²

¹BHF Centre for Cardiovascular Science, ²Clinical Research Imaging Centre, ³MRC Centre for Reproductive Health, University of Edinburgh

Introduction

A lot of magnetic resonance (MR) imaging protocols now acquire data with a range of contrasts and parametric settings. Combining the information obtained from multi-parametric neonatal MR data by image registration is, for example, a useful first step in tissue segmentation. But it is challenging due to patient motion between acquisitions and non-stationary artifacts. We present here an automatic registration software that is robust to significant levels of noise and non-homogeneity.

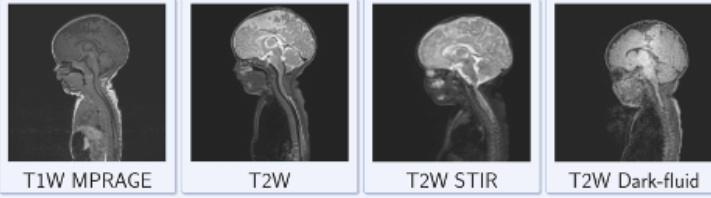


Figure 1 : Neonatal brain sMRI and dMRI images used for validation

Validation Data

This software is tested using a development dataset acquired as part of a study investigating the effect of preterm birth on brain structure and long term outcome, in a collaboration between the Clinical Imaging Centre (CRIC) and the Centre for Reproductive Health (CRH), University of Edinburgh.

1. Isotropic anatomical data with a range of contrasts, as shown in figure 1;
2. Acquired at 38-44 weeks postmenstrual age in natural sleep;
3. Some neonatal motion and repositioning of waking neonates between acquisitions;

Software User Interface

The software is designed with a new efficient registration algorithm [1] and a user-friendly interface which is displayed by figure 2 and figure 3..

Registration (Figure 2)

1. Parameters preconfiguration;
2. Load both images;
3. Select ROI centre to generate a ROI of an arbitrary shape, and save its coordinate;
4. Perform simple pre-processing;
5. Launch the registration.

Visualization (Figure 3)

1. Visualize the data from a 3D view using different techniques;
2. Manually perform/adjust rigid registrations and save results;
3. Apply a transformation to any data;
4. Enjoy customized button for your specific clinical trials.

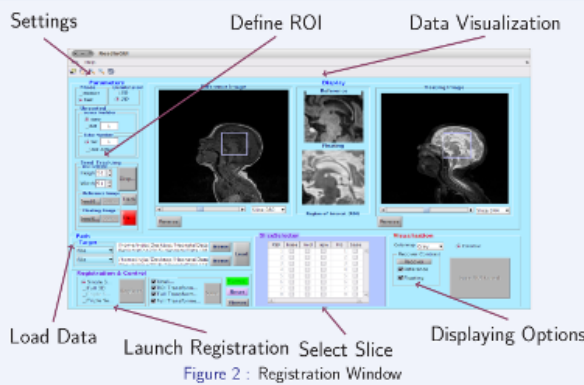


Figure 2 : Registration Window

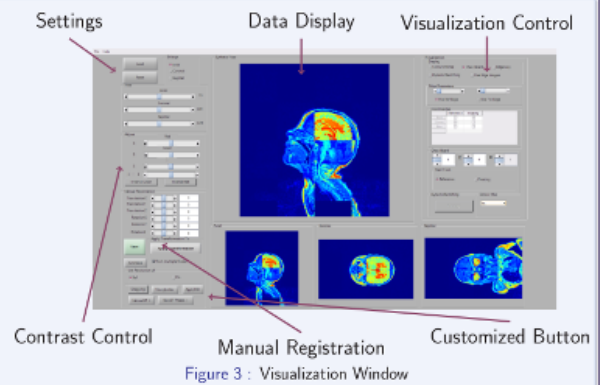


Figure 3 : Visualization Window

Technical Details

The registration algorithm integrated in the software is an adaptive asymmetric cluster-to-image registration we developed for processing multi-contrast and multi-parametric cardiac MR data [1]. The brief workflow of the algorithm is as follows:

1. Given the fixed image, μ , and the moving image, ν , we evaluate the quality of the images using a measure called homogeneous dynamic image ratio (HDIR) which is calculated from the image histograms;
2. The image of worst imaging quality, or with smaller HDIR, is then pre-processed using a reordered histogram specification (RHS) method, as shown in figure 4;

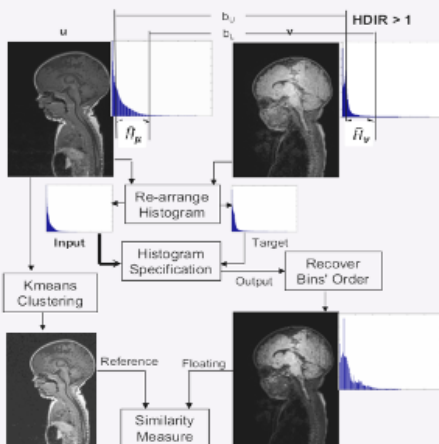


Figure 4 : Pre-processing Details [1]

3. Define cubic regions of interest (ROI) in both image which have abundant anatomical structures, for example, a cubic region that includes structures like corpus callosum, thalamus, hypothalamus and pituitary;
4. Calculate the mutual information using image histograms, where the image has higher HDIR is processed using k-means binning and the other image using equidistant binning;
5. Particle swarm optimizer (PSO) and a wavelet-based image pyramid are used to search for optimal transformation.

Experiment and Results

The data were aligned using a rigid-body transform, calculated within a $51 \times 51 \times 51 \text{mm}^3$ user-positioned ROI. The performance was evaluated by target registration error calculated using 1908 pairs of corresponding landmarks manually picked on by clinical experts on 40 brain volumes (18 on each volume). To test the importance of each step in the overall registration framework, several components were either omitted completely or exchanged with alternative methods. A old algorithm we used to register multi-modality aortic data is also involved in the experiment. The results are shown in figure 5 and table 1. An example of data before and after registration is shown in figure 6.

Method	This method	Gaussian-pyramid	No-kmeans	No-Histogram Specification	DIRECT Search	Reverse clustering	Method [2]
Median	1.88	2.11	3.29	1.97	2.45	1.99	2.14
STD	1.72	1.82	4.40	3.32	4.04	4.42	4.15
Failures	1	1	2	2	3	4	2

Table 1 : Registration Accuracy Evaluated by median and standard deviation (STD) of TREs.

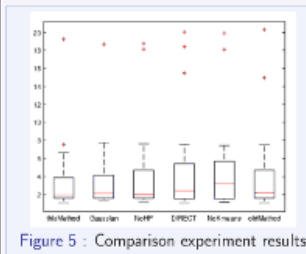


Figure 5 : Comparison experiment results

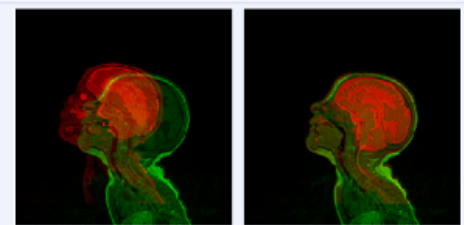


Figure 6 : Example data before and after registration

Conclusion and Future Work

In this study we have demonstrated a multi-parametric neonatal brain MR data registration software, and tested its performance in a real clinical trial.

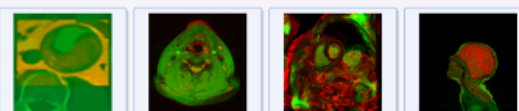


Figure 7 : Applications of This Software

We've developed a family of software targeting different applications, including multi-modality and multi-parametric registration of aortic, neonatal, cardiac and carotid data, as shown in figure 7. These works will be merged into a multi-functional user interface that is applicable to different registration tasks.

References

1. Wang et al., "Automatic multi-parametric MR registration method using mutual information based on adaptive asymmetric k-means binning", IEEE ISBI 2015.
3. Wang et al., "A robust automated multi-modality registration tool applied to abdominal aortic aneurysm", ISMRM 2014.

Acknowledgements: This work is funded by the Medical Research Council, British Heart Foundation Centre of Research Excellence award, and the Scottish Universities Physics Alliance INSPIRE award. Data were acquired with funding from Theirworld.